INTERNATIONAL TABLES FOR CRYSTALLOGRAPHY

ISSN 1574-8707
it.iucr.org

Volume I, X-ray Absorption Spectroscopy
and Related Techniques
ISBN: 978-1-119-43394-1

Chapter 7.4

Keywords: XAFS data; XANES data; data quality.

Related chapters

Volume I: 1.3, 3.14, 3.43, 3.46, 3.49, 4.6, 4.7

Tables and supplementary material for X-ray absorption spectroscopy, pre-edge, XANES and XAFS

Christopher T. Chantler*

School of Physics, University of Melbourne, Australia. *Correspondence e-mail: chantler@unimelb.edu.au

This chapter attempts to address two challenges: to present a representative set of reduced XAFS data sets, including illustrative pre-edge and XANES; and to discuss scientific purposes to which each may – or may not – properly be put, as we understand at the current time. Comparisons of standards of quality and portability of data sets for different purposes are therefore core to this. The user can happily extract ideas, applications or data for their purposes from this selection, and one hopes this chapter can thereby inform data-collection and quality-control procedures that more readily allow a particular experiment to address a particular scientific purpose. The illustrations herein are arranged mainly in time order. The illustrations and discussion included in tables and the online supporting information can be used as guides towards templates for XAFS, XANES and pre-edge data standards in CIF, *eFEFFit* or *iFEFFit* formats.

1. Introduction

X-ray diffraction and crystallography in general have for a long time defined standards for reporting crystal and diffraction data, allowing these to be checked automatically according to important criteria to judge the suitability, accuracy and self-consistency of the data with the scientific result that was sought and is claimed in a publication. X-ray absorption spectroscopy (XAS) and X-ray fluorescence spectroscopy (XFS) or X-ray emission spectroscopy (XES) have been developing in this respect, and it is the intention of this chapter to discuss and illustrate some of the opportunities, needs and requirements to develop this further, especially for X-ray absorption fine structure (XAFS) studies, X-ray absorption near-edge structure (XANES) studies and pre-edge studies.

The illustrations herein are clearly only a selection, which one hopes will nonetheless be useful and lead to further development and discussion. Since there are several thousand XAFS and XANES publications a year, there is no possibility that this can or should be exhaustive. Many publications do not provide reduced data in a form that is portable for other researchers to use, and in addition the dominant modes of presentation are $\chi(k)$ versus *k plots* or transformed $\chi(r)$ versus *r plots*, thus representing the data after extensive reduction and transformation, and without presentation of the uncertainties. For most purposes, these studies have made many assumptions regarding the science which could and should be questioned, including uncertainties, grid spacing, background subtraction, normalization, interpolation, definition of edge energy and spline fitting, among others. Less common are publications with *plots* of scaled or normalized μ versus E

https://doi.org/10.1107/S1574870721011010

values or $[\mu/\rho]$ versus E values. For many purposes there remains a critical need for *tabulations* of pre-processed data which can be ported to and from a database, preferably with defined uncertainties. The present chapter might hopefully encourage further work towards this goal.

2. Pre-synchrotron and early synchrotron studies. Purpose – XAFS: developing ideas of spherical wavefronts and phase offsets, presenting processed figures and illustrations

XAFS began with local sources (Fricke, 1920; Kievit & Lindsay, 1930; Lindsay, 1931; Coster & Veldkamp, 1931; Lytle, 1965, 1966; Lytle *et al.*, 1975), but it was soon understood that synchrotron sources would dominate for the acquisition of high-flux, high-precision data sets (Lapeyre *et al.*, 1983; Doniach *et al.*, 1997; Lynch, 1997). Indirectly, this focus led to the development of some standard practices at synchrotron beamlines for sample preparation and data collection (Newville, 2004; Bunker, 2010). In early publications there are few tables. Papers report plots, usually without supplementary material, *e.g.* Chantler *et al.* (2001*c*). There tended to be individual, personal collections of spectra of mixed statistical quality and characterization, including the Farrel Lytle database (http://ixs.iit.edu/database/data/Farrel_Lytle_data) and spectral profiles of Wong (1999) used as standards by numerous beamlines, but without absolute calibration. [Note that the results of Wong (1999) have a very fine grid giving the local structure with greater detail than most published results. These data, after scaling to give absolute results, are excellent for testing reproducibility of structure in XAFS.] Following the pioneers and founders of the modern XAFS data collection and analysis techniques, different beamlines developed raw or fully processed reference data sets, usually for their internal processes and usually not suitable for cross-portability. This early work and history was discussed recently by Chantler *et al.* (2018).

3. Early work with the purpose of determining absolute attenuation coefficients

The International Union of Crystallography (IUCr) and the extended XAFS community began to develop a series of recommendations of methodology, in separate works and meetings and as part of the IUCr Attenuation Project. This produced a number of excellent works by Barnea, Creagh and others (Mika *et al.*, 1985; Creagh & Hubbell, 1987, 1990), particularly focused on attenuation on the one hand, and on processed data on the other hand, as synchrotron science developed.

Some work, translated from high-accuracy fields, focused on the determination of absolute coefficients of attenuation or photoelectric absorption for ideal systems, with the early development of the X-ray extended range technique (XERT), such as shown in Table 2 (Gerward *et al.*, 1989, 1981; Chantler *et al.*, 2001*a*).

A particular purpose of these studies was to compare these data with recent theoretical tabulations of mass attenuation coefficients, mass absorption coefficients and atomic form factors, including comparisons with data from XCOM (Scofield, 1973; Berger & Hubbell, 1987; Gerward *et al.*, 2004), FFAST (Chantler, 1995, 2000; Chantler *et al.*, 2000), *International Tables for Crystallography* Volume C (Creagh, 1999) and other tabulations (Hubbell & Øverbø, 1979; Schaupp *et al.*, 1983). The data were also compared with experimental data and mixed experimental–theoretical tabulations and databases of elemental attenuation coefficients (Hubbell *et al.*, 1980; Hubbell, 1994, 1996; Perkins *et al.*, 1991; Henke *et al.*, 1993; Cullen *et al.*, 1997) and to individual measurements (Wang *et al.*, 1992; Sandiago *et al.*, 1997; Stanglmeier *et al.*, 1992). This effort culminated in achieving accuracies of attenuation coefficients to 0.27% with reproducibility (precision) to 0.02%. For many materials, and even for reference materials, a typical best level of accuracy is no better than 1–15% even now (2024). This led very clearly to a call for a round-robin project to investigate data quality, reproducibility, cross-portability, optimized experimental methodologies and analytic approaches (Chantler *et al.*, 2018).

Comparison was made of the X-ray absorption fine structure, at least in the XANES region, with data (Wong, 1999; Aberdam *et al.*, 1980) and theory (Joly *et al.*, 1999; Joly, 2001). A key issue during this period was the selection of an optimal thickness of material or ideal foil (Chantler *et al.*, 2001*a*) and the optimization of this remains ongoing. A good statistical accuracy of the data can be obtained over a wide range of thicknesses ($0.5 \leq [\mu/\rho][\rho t] \leq 6$) with similar data-collection times, well beyond the Nordfors attenuation criterion ($2 \leq [\mu/\rho][\rho t] \leq 4$) (Nordfors, 1960; Creagh & Hubbell, 1987; Chantler *et al.*, 2001*a*). However, it is well known that dominant systematic errors arise either for thin or for thick samples. The nature of different systematic effects and errors and the magnitudes of corrections are a key theme of this volume of *International Tables for Crystallography*. An early conclusion was that multiple samples across a range of thicknesses will best achieve an accurate result in the face of common systematic errors.

For more recent work, see the remainder of this chaper and other chapters in this volume. One should also note the current joint efforts of the round-robin collaboration of the IUCr Commission on XAFS and the International XAFS Society (Chantler *et al.*, 2018), the compilation efforts of the Japanese XAFS Society (Asakura *et al.*, 2018) and the IXAS Lytle compendium (http://ixs.iit.edu/database/), restricted or open local synchrotron databases (http://cars.uchicago.edu/xaslib/search, https://sp8dr.spring8.or.jp/portal/dspace, https://www.esrf.eu/home/UsersAndScience/Experiments/XNP/ID21/php.html), an ongoing effort to aggregate experimental spectra within the XAS part of the Materials Genome Initiative (Strange & Feiters, 2008; Chantler *et al.*, 2019), and the recent development of immense populations of theoretical spectra that are being created, (usually) catalogued and made public, typically with the goal of use in machine-learning applications (Timoshenko *et al.*,

Table 1
A checklist of corrections and purposes for the data sets featured in this chapter.

Column (A): dark-current correction? Column (B): blank measurement normalization for XERT or solvent measurement normalization for hybrid method? Column (C): fluorescence correction for XAS data; absorption and self-absorption correction for fluorescence data? Column (D): energy calibration? Column (E): absolute measurement/calibration? Column (F): harmonics determination and correction? Column (G): bandwidth determination and correction? Column (H): roughness determination and correction? (See Section 4 for more details on each of these.)

Section for this data set; substance or material; [edge(s) measured]	Tables	Figures	*E* (keV)	Reference	XAS?	XAFS?	(A)	(B)	(C)	(D)	(E)	(F)	(G)	(H)
(5), Cu metal	2–4		8.9–20.0	Chantler *et al.* (2001*a*)	XAS	—	Y	Y	Y	Y	Y	Y	N	N
(6), Si crystal	5, 6		5.0–20.0	Tran *et al.* (2003*c*)	XAS	—	Y	Y	Y	Y	Y	Y	N	N
(7), Ag metal	7, 8	1	15.3–49.9	Tran *et al.* (2005)	XAS	‘*K*’†	Y	Y	Y	Y	Y	Y	N	N
(8), Mo metal	9, 10	2	13.5–41.5	de Jonge *et al.* (2005)	XAS	*K*	Y	Y	Y	Y	Y	Y	Y	Y
(9), Sn metal	11, 12	3	29.0–60.1	de Jonge *et al.* (2007)	XAS	*K*	Y	Y	Y	Y	Y	Y	Y	Y
(10), Cu metal	13–15		5.0–20.1	Glover *et al.* (2008)	XAS	*K*	Y	Y	Y	Y	Y	Y	Y	Y
(11), Zn metal	16		7.2–15.2	Rae *et al.* (2010*a*)	XAS	—	Y	Y	Y	Y	Y	Y	Y	Y
(12), Au metal	17		38.0–49.9	Islam *et al.* (2010*b*)	XAS	—	Y	Y	Y	Y	Y	Y	N	N
(13), Au metal	18, 19	4, 5	14.2–21.1	Glover *et al.* (2010)	XAS	$L_{\rm I}$	Y	Y	Y	Y	Y	Y	N	Y
(14), Ag metal	20		5.0–20.1	Islam *et al.* (2014)	XAS	—	Y	Y	Y	Y	Y	Y	N	Y
(15), Ag metal	21	6, 7	11.0–28.1	Tantau *et al.* (2015)	XAS	*K*	Y	Y	Y	Y	Y	Y	Y	N
(16), 15 m*M* *i*-pr Ni [Ni]	22–24	8–14	7.02–9.52	Chantler *et al.* (2015)	XAS	*K*	Y	Y	Y	Y	Y	Y	N	N
(16), 1.5 m*M* *i*-pr Ni [Ni]			8.10–9.02	Chantler *et al.* (2015)	XAS	*K*	Y	Y	Y	Y	Y	Y	N	N
(16), 15 m*M* *n*-pr Ni [Ni]			7.92–9.52	Chantler *et al.* (2015)	XAS	*K*	Y	Y	Y	Y	Y	Y	N	N
(17), 15 m*M* Fc [Fe]	25–28	15–19	6.91–9.01	Islam *et al.* (2016)	XAS	*K*	Y	Y	Y	Y	Y	Y	N	N
(17), 3 m*M* Fc [Fe]			6.91–7.80	Islam *et al.* (2016)	XAS	*K*	Y	Y	Y	Y	Y	Y	N	N
(17), 15 m*M* DMFc [Fe]			7.01–8.52	Islam *et al.* (2016)	XAS	*K*	Y	Y	Y	Y	Y	Y	N	N
(17), 3 m*M* DMFc [Fe]			7.01–8.52	Islam *et al.* (2016)	XAS	*K*	Y	Y	Y	Y	Y	Y	N	N
(18), 15 m*M* *n*-pr Ni [Ni]	29	20, 21	7.91–9.52	Schalken & Chantler (2018)	XAS	*K*	Y	Y	Y	Y	Y	Y	N	N
(19), 15 m*M* *n*-pr Ni [Ni]	30, 31	22, 23	8.14–9.32	Trevorah *et al.* (2019)	XFS	*K*	Y	Y	Y	Y	Y	Y	—	—
(19), 15 m*M* *i*-pr Ni [Ni]			8.14–9.32	Trevorah *et al.* (2019)	XFS	*K*	Y	Y	Y	Y	Y	Y	—	—
(20), ZnSe crystal [Zn, Se]	32, 33	24–27	6.82–15.07	Sier *et al.* (2020)	XAS	*K*	Y	Y	Y	Y	Y	Y	Y	N
(21), Zn metal	34, 35	28–30	8.51–11.59	Ekanayake *et al.* (2021*a*)	XAS	*K*	Y	Y	Y	Y	Y	Y	Y	Y

† Based around the *K* edge but not directly including the edge region.

2017, 2018; Mathew *et al.*, 2018; Zheng *et al.*, 2018; Guda *et al.*, 2019, 2020; Martini *et al.*, 2020).

4. Summary of data sets featured in this chapter and their purposes

All the data sets discussed herein are appropriate for use as reference standards and for calibration purposes, and all formats are suitable for deposition – indeed all have been deposited in these forms. However, discussions within the international community, the International XAFS Society, the IUCr Commission on XAFS and the Q2XAFS meetings, and the associated reports have led to the recommendation of text-based and computer-readable forms, in particular the .dat (*eFEFFit* or *iFEFFit*) or .cif formats described in later sections. All of the data sets are available as supplementary files at https://it.iucr.org/I as specified in each section below. Some of these data sets have been measured following the principles of XERT; some following hybrid methodology [as explained in Chapter 3.14 (Best & Chantler, 2024)].

Some are primarily useful for measurement and determination of the mass attenuation coefficient, the mass absorption coefficient and the imaginary component of the (atomic) form factor. These XAS studies and data sets are also particularly useful for investigating theory and for comparison with form factors in crystallographic and attenuation databases. In general these data sets attempt to quantify an uncertainty in the X-ray energy, an uncertainty in the absolute value of the mass attenuation, a pointwise uncertainty in the mass attenuation coefficient, an uncertainty in the extracted mass absorption coefficient, and hence in the imaginary component of the (atomic) form factor. Near any absorption edge any extracted form factor is just that – solid-state effects typically exceed 1% and hence the accuracy of the form factor in an *atomic* sense is reduced. Far from an edge and in particular well above the *K* edge, the form factor has been shown to be accurate as an *atomic* form factor to within 1%.

A subset of these data sets are suitable or ideal for XAFS investigation, and are indicated as such in Table 1. This selection is illustrative and personal. It includes XAS data sets (*i.e.* absorption or transmission spectra) and fluorescence XAS data sets (labelled XFS to avoid confusion with the characteristic fluorescence spectra, but note that these both follow second-order Hamiltonian operators and selection rules instead of first order as for absorption/transmission XAS spectra). Most relate to *K*-edge XAFS, but some cover regions away from any edges, some cover *L* edges and some cover an edge but with sparse or limited energy steps in the XANES or XAFS region. The data sets cover examples of *K*-edge spectra, *L*-edge spectra, metal foils, elemental crystals, binary crystals, dilute solutions and cryostatic measurements.

Checklist-style columns in Table 1 are given for key aspects of data collection, analysis and possible sources of systematic errors. More details on these are provided below.

Column (A). All detectors have a dark current or signal in the absence of the beam, which is usually energy-dependent and time-dependent during an experiment. Regular dark-current measurements are generally critical for assessing detector linearity and accuracy for all samples, but particularly for thicker foil or solution samples. This requires regular measurement during a long data collection method or if the sample is relatively thick. This is characterized and corrected for in all these data sets (Chantler *et al.*, 2001*a*).

Column (B). Beamlines always have windows, air paths and an upstream detector, so it is important to regularly measure a 'blank' or take measurements with the sample absent to correct for background attenuation, especially in transmission measurements. For solutions one should use a solvent blank or cell to calibrate the sample. All these data sets have been corrected for this.

Column (C). For absorption measurements, what is actually measured is always attenuation with feedback from fluorescence into upstream and downstream detectors, so this should be measured and corrected for to obtain the actual attenuation (and from thence to be able to obtain the absorption coefficient to compare with theory) (Chantler *et al.*, 2001*b*). Conversely, for fluorescence measurements (XFS) the absorption and self-absorption corrections are often dominant and it is important to make these corrections before, for example, applying a spline to extract χ versus k values (Chantler *et al.*, 2012*b*; Trevorah *et al.*, 2019).

Column (D). If the data are not to have an arbitrary energy fitting offset they need to be calibrated using reference materials and not just a single edge (Rae *et al.*, 2010*c*; Tantau *et al.*, 2014). Where the energy or an uncertainty is determined, it has often been the case that a single reference edge defined by an inflection point defines a possible energy or energy offset with unknown error or uncertainty of the slope or the range of XAS. The energy and uncertainty can be defined directly by crystal or powder diffraction, or by multiple inflection points of reference materials; these each have their own accuracies and limitations.

Column (E). In the same manner, if the value of the attenuation or absorption is to be compared with theory or used to define the absorption profile with energy, it is important to characterize the samples both in the beam and off site, especially to measure and quantify distortions of amplitudes as a function of k (de Jonge *et al.*, 2004*a*; Islam *et al.*, 2010*a*; Rae *et al.*, 2010*b*).

Column (F). Harmonics affect the measured attenuation and absorption coefficients, especially in the upstream and downstream ion chambers and for thicker samples. In XFS, harmonics affect the upstream detector, but with suitable choice of regions of interest harmonics should not directly affect the fluorescence detector (Tran *et al.*, 2003*a*, 2004*b*; Glover & Chantler, 2009).

Column (G). The synchrotron bandwidth at the sample or upstream and downstream detectors particularly broadens the edge, pre-edge and white line at the beginning of the XANES, so acts somewhat like an augmented hole width, except that it is most significant in a critical region for chemical fingerprinting (de Jonge *et al.*, 2004*b*; Sier *et al.*, 2020).

Column (H). Sample roughness affects transmission measurements especially as a function of attenuation, so distorts high-k versus low-k oscillations and pre-edge versus above-edge structure (Glover *et al.*, 2009; Ekanayake *et al.*, 2021*a*).

The form of the material and factors like the temperature dictate the dominant systematic effects to be investigated or corrected for; there is certainly more than one approach to estimating an uncertainty or error or correcting for it. For an ideal solid metal foil, the blank normalization is particularly important for transmission (XAS) measurements; for a dilute liquid or frozen solution, the solvent measurement normalization is particularly critical for transmission (XAS) measurements; and for a fluorescence measurement (XFS), the absorption and self-absorption effects may be dominant. Some uncertainties may inevitably be unmeasured or unaccounted for or unknown. When a data set is deposited in a database or used as the basis of a study, these uncertainties should be noted where they may be significant. Whilst a summary checklist is provided in Table 1, there are potentially several other sources of systematic errors, including monochromator drift, Bragg glitches, thermal diffuse scattering *etc*., which may be important contributions in particular data sets.

In general, the data sets that are described in Sections 5 to 17 were presented as tables in pdf format in the associated publications, or deposited as text files and readme files (Section 8), or deposited as sets of pdfs of tabulated data of results (Sections 16 and 17). However, from Section 18 onwards (starting around 2018), following the work of Q2XAFS and the joint work of the IUCr Commission on XAFS and the International XAFS Society, it was seen to be important to develop some standard formats of data sets for direct input into XANES and XAFS fitting packages. Section 18 provides minimal examples of these for *mu2chi*, *iFEFFit* and *eFEFFit*. These examples were later developed much further, as described in the last sections of this chapter, to recommended formats for CIF and *eFEFFit*/*iFEFFit*.

5. Copper foils, 8.9–20.0 keV. XAS: systematic errors, portability and theory

The publication by Chantler *et al.* (2001*a*) is representative of some achievements of this early period (Table 2). The grid was designed for attenuation measurement and accuracy; with 84 points across an 11 keV energy range, the grid is far too coarse for XAFS or to determine any XAFS nanostructure. Nonetheless, it illustrates the need to provide an uncertainty in the energy E, the mass attenuation $[\mu/\rho]$ and the extracted form factors f''. This work investigated ideal copper metal foils, and used data from foils of nominal thicknesses of 5 µm, 10 µm, 15 µm, 20 µm, 30 µm and 100 µm, using at least three foils at each energy whether above or below the edge. Typical accuracies were 0.27% to 0.467%, *i.e.* well below 1%, which had proven nearly impossible to achieve before. The precision (reproducibility) was 0.024% to 0.58%, the latter typically at

Table 2

Copper, 8.9–20.0 keV (Chantler *et al.*, 2001*a*): copper bulk metal foil attenuation coefficients $[\mu/\rho]$ (cm^2 g^{-1}) and the imaginary part of the atomic form factors f'' with uncertainties.

Notes. (*a*) Precision, from repeated measurements at the same energies to give the reproducibility of the measurement ($\sigma_{\mu,\rm se}$ is the standard error). (*b*) Absolute standard error uncertainty in calibrated energy. (*c*) Percentage accuracy in sample thickness determination. (*d*) Percentage precision including uncertainty due to impurity, in quadrature. (*e*) $\sigma_{[\mu/\rho]_{\rm rel}} = \sigma_{\mu,\rm se} + \mu_i$. (*f*) Final percentage accuracy. (*g*) f'', after subtraction of scattering contribution following FFAST (Chantler, 1995). (*h*) f'', after subtraction of scattering contribution following XCOM (Hubbell *et al.*, 1980).

E (keV)	σ_E † (eV)	$[\mu/\rho]$ (cm^2 g^{-1})	$\sigma_{\mu,\rm se}$ (%) [Note (*a*)]	σ_t (%) [Note (*b*)]	$\sigma_{[\mu/\rho]_{\rm rel}}$ (%) [Note (*c*)]	$\sigma_{[\mu/\rho]}$ (%) [Note (*d*)]	$f''_{\rm FFAST}$ (e atom^{-1}) [Note (*e*)]	$f''_{\rm XCOM}$ (e atom^{-1}) [Note (*f*)]	$\sigma_{f''}$ (e atom^{-1})
8.8709	1.02	37.989	0.063	0.332	0.064	0.338	0.4861	0.4866	0.0016
8.9722	0.60	39.368	0.037	0.332	0.037	0.334	0.5089	0.5095	0.0017
8.9824	0.56	174.797	0.585	0.332	0.585	0.673	2.3570	2.3564	0.0159
9.0025	0.49	301.251	0.468	0.332	0.468	0.574	4.0711	4.0699	0.0234
9.0125	0.45	299.160	0.264	0.332	0.264	0.424	4.0473	4.0462	0.0172
9.0225	0.42	280.720	0.072	0.332	0.072	0.340	3.8020	3.8009	0.0129
9.0326	0.38	315.383	0.175	0.332	0.175	0.375	4.2762	4.2750	0.0160
9.0426	0.35	285.828	0.151	0.332	0.151	0.365	3.8797	3.8787	0.0142
9.0526	0.33	289.036	0.132	0.332	0.132	0.357	3.9275	3.9265	0.0140
9.0627	0.30	295.361	0.070	0.332	0.071	0.340	4.0179	4.0169	0.0136
9.0727	0.28	308.366	0.220	0.332	0.220	0.398	4.1994	4.1983	0.0167
9.0827	0.27	311.230	0.312	0.332	0.312	0.456	4.2430	4.2420	0.0193
9.0928	0.26	290.999	0.071	0.332	0.072	0.340	3.9715	3.9706	0.0135
9.1029	0.26	277.705	0.202	0.332	0.202	0.389	3.7943	3.7934	0.0147
9.1129	0.26	285.118	0.265	0.332	0.265	0.425	3.8998	3.8989	0.0166
9.1229	0.28	293.393	0.162	0.332	0.162	0.369	4.0173	4.0164	0.0148
9.1325	0.30	305.582	0.346	0.332	0.346	0.480	4.1886	4.1877	0.0201
9.1828	0.40	290.361	0.127	0.332	0.127	0.355	4.0016	4.0008	0.0142
9.2329	0.30	283.693	0.068	0.332	0.068	0.339	3.9308	3.9301	0.0133
9.2833	0.39	279.171	0.068	0.332	0.068	0.339	3.8890	3.8884	0.0132
9.3334	0.33	270.757	0.030	0.332	0.030	0.333	3.7919	3.7914	0.0126
9.3836	0.33	267.573	0.093	0.332	0.093	0.345	3.7673	3.7668	0.0130
9.4338	0.33	261.422	0.056	0.332	0.056	0.337	3.7001	3.6998	0.0125
9.6343	0.34	245.000	0.083	0.332	0.083	0.342	3.5406	3.5405	0.0121
9.8349	0.31	229.967	0.062	0.332	0.063	0.338	3.3918	3.3918	0.0115
9.8356	0.29	230.996	0.068	0.332	0.068	0.339	3.4072	3.4072	0.0115
10.0362	0.38	217.705	0.059	0.332	0.060	0.337	3.2759	3.2760	0.0111
10.4387	0.30	195.954	0.039	0.332	0.040	0.334	3.0656	3.0658	0.0103
10.6410	0.17	186.096	0.014	0.332	0.015	0.332	2.9671	2.9674	0.0099
10.8417	0.34	176.827	0.043	0.332	0.043	0.335	2.8719	2.8722	0.0096
11.0433	0.34	168.259	0.017	0.332	0.017	0.332	2.7830	2.7832	0.0093
11.2451	0.58	160.321	0.045	0.332	0.045	0.335	2.6996	2.6998	0.0090
11.4464	0.64	152.792	0.030	0.332	0.030	0.333	2.6184	2.6185	0.0087
11.6479	0.73	145.906	0.063	0.332	0.063	0.338	2.5438	2.5439	0.0086
11.8489	0.74	139.292	0.026	0.332	0.027	0.333	2.4699	2.4700	0.0082
12.0510	0.71	133.237	0.020	0.332	0.020	0.333	2.4023	2.4023	0.0080
12.4533	0.72	121.921	0.048	0.332	0.048	0.335	2.2706	2.2705	0.0076
12.6555	0.94	116.835	0.045	0.332	0.046	0.335	2.2107	2.2105	0.0074
12.8570	0.98	111.836	0.075	0.332	0.075	0.340	2.1493	2.1491	0.0073
13.0586	1.17	107.355	0.047	0.332	0.048	0.335	2.0950	2.0947	0.0070
13.2595	0.91	102.906	0.056	0.332	0.056	0.337	2.0387	2.0383	0.0069
13.4607	0.95	98.892	0.045	0.332	0.046	0.335	1.9884	1.9880	0.0067
13.6624	0.91	94.917	0.052	0.332	0.052	0.336	1.9366	1.9362	0.0065
13.8635	1.05	91.348	0.054	0.332	0.054	0.336	1.8908	1.8903	0.0064
14.0651	1.02	87.914	0.024	0.332	0.025	0.333	1.8457	1.8452	0.0061
14.2668	1.13	84.635	0.024	0.332	0.025	0.333	1.8020	1.8013	0.0060
14.4680	1.06	81.430	0.075	0.332	0.075	0.340	1.7577	1.7570	0.0060
14.6698	1.31	78.555	0.036	0.332	0.036	0.334	1.7190	1.7181	0.0057
14.8711	1.47	75.598	0.087	0.332	0.088	0.343	1.6765	1.6756	0.0058
15.0727	1.31	73.016	0.042	0.332	0.042	0.335	1.6407	1.6399	0.0055
15.2741	1.16	70.361	0.053	0.332	0.053	0.336	1.6019	1.6009	0.0054
15.4762	0.62	68.049	0.011	0.332	0.012	0.332	1.5694	1.5683	0.0052
15.4764	0.75	67.962	0.070	0.332	0.070	0.339	1.5674	1.5663	0.0053
15.5776	0.91	66.765	0.036	0.332	0.036	0.334	1.5496	1.5486	0.0052
15.6768	0.70	65.683	0.007	0.332	0.009	0.332	1.5340	1.5330	0.0051
15.6768	0.70	65.702	0.012	0.332	0.013	0.332	1.5345	1.5334	0.0051
15.6773	1.46	65.713	0.097	0.299	0.097	0.314	1.5348	1.5337	0.0048
15.8795	1.26	63.409	0.080	0.299	0.081	0.310	1.4997	1.4986	0.0046
16.0817	1.46	61.365	0.072	0.299	0.074	0.308	1.4694	1.4683	0.0045
16.2832	0.87	59.271	0.067	0.299	0.068	0.307	1.4367	1.4355	0.0044
16.4854	1.28	57.361	0.107	0.299	0.108	0.318	1.4073	1.4061	0.0045
16.6875	1.29	55.420	0.058	0.299	0.060	0.305	1.3760	1.3747	0.0042
16.8892	1.10	53.730	0.068	0.299	0.069	0.307	1.3499	1.3485	0.0041
17.0915	1.36	51.960	0.093	0.299	0.094	0.313	1.3207	1.3193	0.0041

Table 2 (continued)

E (keV)	σ_E † (eV)	$[\mu/\rho]$ (cm^2 g^{-1})	$\sigma_{\mu,\,\rm se}$ (%) [Note (*a*)]	σ_t (%) [Note (*b*)]	$\sigma_{[\mu/\rho]_{\rm rel}}$ (%) [Note (*c*)]	$\sigma_{[\mu/\rho]}$ (%) [Note (*d*)]	$f''_{\rm FFAST}$ (e atom^{-1}) [Note (*e*)]	$f''_{\rm XCOM}$ (e atom^{-1}) [Note (*f*)]	$\sigma_{f''}$ (e atom^{-1})
17.2929	1.17	50.392	0.072	0.299	0.073	0.308	1.2956	1.2941	0.0040
17.4954	1.45	48.758	0.074	0.299	0.075	0.308	1.2680	1.2664	0.0039
17.6967	0.64	47.393	0.023	0.299	0.026	0.300	1.2464	1.2447	0.0037
17.6967	0.64	47.401	0.048	0.299	0.050	0.303	1.2466	1.2449	0.0038
17.6972	1.26	47.337	0.055	0.271	0.056	0.277	1.2450	1.2432	0.0034
17.8995	1.75	45.875	0.063	0.271	0.064	0.278	1.2200	1.2182	0.0034
18.1004	0.99	44.519	0.042	0.271	0.044	0.275	1.1969	1.1951	0.0033
18.3022	1.03	43.158	0.068	0.271	0.069	0.280	1.1729	1.1711	0.0033
18.5049	1.37	41.913	0.042	0.271	0.044	0.275	1.1514	1.1495	0.0032
18.7054	0.82	40.723	0.031	0.271	0.034	0.273	1.1306	1.1286	0.0031
18.7054	0.82	40.725	0.023	0.271	0.027	0.272	1.1306	1.1286	0.0031
18.7060	1.02	40.682	0.043	0.271	0.045	0.275	1.1295	1.1275	0.0031
18.9061	1.17	39.494	0.050	0.271	0.051	0.276	1.1079	1.1059	0.0031
19.1049	1.53	38.372	0.028	0.271	0.031	0.273	1.0874	1.0853	0.0030
19.3001	1.74	37.318	0.023	0.271	0.027	0.272	1.0681	1.0660	0.0029
19.4919	2.37	36.301	0.018	0.271	0.022	0.272	1.0491	1.0468	0.0029
19.6777	3.14	35.373	0.066	0.271	0.067	0.279	1.0318	1.0295	0.0029
19.8558	4.01	34.525	0.012	0.271	0.017	0.272	1.0159	1.0135	0.0028
20.0286	0.84	33.761	0.034	0.271	0.037	0.274	1.0018	0.9994	0.0027
20.0286	0.84	33.750	0.023	0.271	0.026	0.272	1.0015	0.9991	0.0027

the rising slope of the edge, as expected. This enabled a range of studies of systematic errors, statistics at a typical synchrotron beamline, harmonic determination and direct observation of fluorescence in XAS measurements. Despite the sparseness of this XAFS data set, it could be modelled and provided insight for more advanced theory on XAFS (Witte *et al.*, 2006; Bourke & Chantler, 2010*a*) and photoelectron inelastic mean free paths (Bourke *et al.*, 2007). The data are available in the supporting information to this chapter as file bz5029sup1.pdf.

Table 3 illustrates the discussion of specific sources of uncertainty and systematic errors and their dominant or typical contribution in different regions of the spectrum, leading towards the detailed tabulation. In principle, this provides a basis for cross-portability between beamlines, samples or data sets. Table 4 illustrates the use of powder diffraction standards to calibrate the monochromated energy at the sample, in the potential presence of variations due to monochromator heat load, hysteresis, drift or detuning.

6. Silicon crystals, 5–20 keV. XAS: systematic errors, portability and theory

Another key example was presented in the work by Tran *et al.* (2003*b*,*c*) on silicon crystal samples (Table 5). In the X-ray energy range 5–20 keV there is no silicon edge and no XAFS, so this is both an XAS study and a study of attenuation coefficients and elemental form factors. The data are available in the supporting information to this chapter as file bz5029sup2.pdf. There were 123 measured data points.

These samples are near-perfect crystals, so Bragg diffraction from the sample was a key problem to be corrected for. Because of the low atomic number and the relatively high energies, these standard reference samples, which were also used for the IUCr Attenuation Project, covered the thickness range from to 50 µm to 4 mm, with three foils investigated at each energy.

Table 5 lists the energies and the corresponding uncertainties in columns 1 and 2, respectively. Columns 3, 4, 5 and 6

Table 3

Copper, 8.9–20.0 keV: uncertainties (standard errors) of the mass attenuation coefficient $[\mu/\rho]$, the photoelectric (mass absorption) coefficient $[\mu/\rho]_{\rm pe}$ and f'' (Chantler *et al.*, 2001*a*).

	% Contribution, ±1 standard deviation		
Source of uncertainty	Near edge, ~9 keV	Above edge, 12–20 keV	Notes
Energy drift (on edge)	0.04–0.59		±0.003% to ±0.011% in energy
Monochromator hysteresis		<0.06	δE = 1–4 eV at 19–20 keV
Energy calibration elsewhere	0.01–0.03	0.01–0.03	±0.003% to ±0.009% in energy
Overall system statistics	0.02	0.02	Reproducibility without sample
Experimental precision	0.03–0.59	0.007–0.107	Including above contributions
Sample thickness	0.33	0.27	With $\delta\rho$ = 0.04% and thickness transfer uncertainty
Impurity contamination	0.002–0.01	0.002–0.01	
Oxidation	<0.025	<0.003	±35 Å
Detector linearity and harmonic contamination	<0.03	<0.03	
Scattering	0.01	0.02	From theory and aperture tests
Rayleigh scattering (for $[\mu/\rho]_{\rm pe}$ and f'')	0.075	0.15	Variation in theory

Table 4

Copper, 8.9–20.0 keV: energy calibration.

Weighted sum and uncertainty of energies using Si and LaB$_6$ powder diffraction samples (uncertainties $\sigma \times \sqrt{\chi_r^2}$) (Chantler *et al.*, 2001*a*).

Si		LaB$_6$		Final average	
$E_{w=\sigma(\chi_r^2)^{1/2}}$ (keV)	$\sigma(\chi_r^2)^{1/2}$ (eV)	$E_{w=\sigma(\chi_r^2)^{1/2}}$ (keV)	$\sigma(\chi_r^2)^{1/2}$ (eV)	$E_{w=\sigma(\chi_r^2)^{1/2}}$ (keV)	$\sigma(\chi_r^2)^{1/2}$ (eV)
8.9817	0.38	8.9828	0.35	8.9823	0.56
9.1322	0.40	9.1328	0.35	9.1325	0.29
10.0386	1.23	10.0361	0.19	10.0362	0.37
11.0429	0.39	11.0433	0.16	11.0432	0.14
12.0500	0.37	12.0515	0.26	12.0510	0.70
13.0575	0.45	13.0588	0.26	13.0585	0.56
14.0638	0.40	14.0659	0.30	14.0651	1.01
15.6762	0.36	15.6776	0.39	15.6768	0.70
17.6959	0.59	17.6972	0.51	17.6967	0.64
18.7043	0.61	18.7060	0.47	18.7054	0.82
20.0279	0.55	20.0296	0.62	20.0286	0.84

Table 5

Silicon crystals, 5–20 keV (Tran *et al.*, 2003*b*,*c*): mass attenuation coefficients $[\mu/\rho]$ and the imaginary part of the atomic form factor f'' versus E.

Energy values marked with an asterisk are directly measured energies. Estimated uncertainties: σ_E – absolute uncertainty in calibrated energy (one standard error); $\sigma_{[\mu/\rho]_{\rm rel}}$ – percentage precision of repeated measurements (one standard error); σ_t – percentage accuracy in sample thickness determination; $\sigma_{[\mu/\rho]}$: total percentage accuracy in measured $[\mu/\rho]$. $f''_{\rm FFAST}$ – after subtraction of scattering contribution following FFAST (Chantler, 1995). $f''_{\rm XCOM}$: after subtraction of scattering contribution following XCOM (Berger & Hubbell, 1987; Hubbell *et al.*, 1975); $\sigma_{f''}$ – absolute uncertainty in f''.

E (keV)	σ_E (eV)	$[\mu/\rho]$ (cm^2 g^{-1})	$\sigma_{[\mu/\rho]_{\rm rel}}$ (%)	σ_t (%)	$\sigma_{[\mu/\rho]}$ (%)	$f''_{\rm FFAST}$ (e atom^{-1})	$f''_{\rm XCOM}$ (e atom^{-1})	$\sigma_{f''}$ (e atom^{-1})
5.0146*	1.52	244.247	0.321	0.139	0.350	8.170E-01	8.170E-01	2.856E-03
5.1133	1.31	231.275	0.292	0.139	0.323	7.888E-01	7.888E-01	2.551E-03
5.2126	1.29	218.775	0.327	0.139	0.356	7.606E-01	7.606E-01	2.705E-03
5.3120	1.30	207.209	0.313	0.139	0.343	7.341E-01	7.341E-01	2.516E-03
5.4116	1.30	197.271	0.307	0.139	0.337	7.119E-01	7.119E-01	2.399E-03
5.5113	1.28	186.718	0.316	0.139	0.345	6.862E-01	6.862E-01	2.369E-03
5.6115	1.24	177.229	0.319	0.139	0.348	6.632E-01	6.631E-01	2.305E-03
5.7111	1.19	168.356	0.145	0.139	0.200	6.411E-01	6.411E-01	1.285E-03
5.8111	1.13	159.869	0.138	0.139	0.195	6.194E-01	6.194E-01	1.210E-03
6.0110*	1.02	145.860	0.164	0.139	0.215	5.845E-01	5.845E-01	1.255E-03
6.1110	0.98	139.672	0.084	0.139	0.162	5.690E-01	5.689E-01	9.236E-04
6.2110	0.94	133.244	0.044	0.139	0.145	5.516E-01	5.516E-01	8.023E-04
6.3110	0.90	127.224	0.036	0.139	0.143	5.351E-01	5.351E-01	7.664E-04
6.4110	0.88	121.450	0.030	0.139	0.142	5.189E-01	5.189E-01	7.366E-04
6.5110	0.87	116.141	0.043	0.139	0.145	5.039E-01	5.039E-01	7.312E-04
6.6110	0.86	111.117	0.012	0.139	0.139	4.895E-01	4.895E-01	6.812E-04
6.7110	0.88	106.360	0.030	0.139	0.142	4.756E-01	4.755E-01	6.748E-04
6.8110	0.90	101.882	0.017	0.139	0.140	4.623E-01	4.623E-01	6.457E-04
6.9110	0.93	97.644	0.029	0.139	0.142	4.495E-01	4.495E-01	6.372E-04
7.0110*	0.97	93.625	0.021	0.139	0.140	4.372E-01	4.372E-01	6.131E-04
7.0110	0.97	93.578	0.020	0.139	0.140	4.370E-01	4.370E-01	6.123E-04
7.1117	0.87	89.788	0.057	0.139	0.150	4.253E-01	4.253E-01	6.384E-04
7.2061	0.80	86.627	0.009	0.139	0.139	4.157E-01	4.157E-01	5.777E-04
7.3131	0.76	83.143	0.144	0.139	0.200	4.049E-01	4.049E-01	8.099E-04
7.4138*	0.78	79.884	0.022	0.139	0.140	3.943E-01	3.943E-01	5.536E-04
7.5134	0.74	76.856	0.121	0.139	0.184	3.844E-01	3.844E-01	7.071E-04
7.6130*	0.35	73.826	0.080	0.139	0.160	3.741E-01	3.741E-01	5.980E-04
7.6130	0.35	73.827	0.052	0.139	0.148	3.741E-01	3.741E-01	5.545E-04
7.7130	0.27	71.168	0.167	0.139	0.217	3.654E-01	3.653E-01	7.944E-04
7.8135	0.22	68.509	0.021	0.139	0.140	3.563E-01	3.562E-01	4.997E-04
8.0134*	0.26	63.894	0.037	0.139	0.143	3.407E-01	3.406E-01	4.885E-04
8.0135	0.26	63.856	0.090	0.115	0.146	3.405E-01	3.404E-01	4.969E-04
8.1133	0.25	61.572	0.049	0.115	0.125	3.323E-01	3.323E-01	4.150E-04
8.2136	0.26	59.296	0.039	0.115	0.121	3.240E-01	3.239E-01	3.929E-04
8.3138	0.29	57.227	0.014	0.115	0.116	3.164E-01	3.164E-01	3.664E-04
8.4144	0.33	55.237	0.041	0.115	0.122	3.091E-01	3.090E-01	3.770E-04
8.5143	0.39	53.349	0.033	0.115	0.120	3.020E-01	3.020E-01	3.610E-04
8.6143	0.45	51.545	0.057	0.115	0.128	2.952E-01	2.951E-01	3.789E-04
8.7143	0.52	49.836	0.016	0.115	0.116	2.887E-01	2.886E-01	3.349E-04
8.8149	0.59	48.176	0.055	0.115	0.127	2.822E-01	2.822E-01	3.593E-04
8.9150	0.66	46.607	0.014	0.115	0.116	2.761E-01	2.760E-01	3.197E-04
9.0155*	0.74	45.184	0.147	0.115	0.186	2.707E-01	2.706E-01	5.040E-04
9.1159	0.66	43.697	0.076	0.115	0.138	2.646E-01	2.646E-01	3.654E-04
9.2159	0.59	42.342	0.028	0.115	0.118	2.592E-01	2.591E-01	3.069E-04
9.3158	0.53	41.081	0.072	0.115	0.135	2.541E-01	2.541E-01	3.443E-04

Table 5 (continued)

E (keV)	σ_E (eV)	$[\mu/\rho]$ (cm^2 g^{-1})	$\sigma_{[\mu/\rho]_{\rm rel}}$ (%)	σ_t (%)	$\sigma_{[\mu/\rho]}$ (%)	$f''_{\rm FFAST}$ (e atom^{-1})	$f''_{\rm XCOM}$ (e atom^{-1})	$\sigma_{f''}$ (e atom^{-1})
9.4156	0.46	39.737	0.081	0.115	0.141	2.484E-01	2.484E-01	3.498E-04
9.5159	0.40	38.486	0.087	0.115	0.144	2.431E-01	2.431E-01	3.509E-04
9.6158	0.36	37.306	0.091	0.115	0.147	2.381E-01	2.380E-01	3.497E-04
9.7164	0.32	36.273	0.120	0.115	0.166	2.339E-01	2.338E-01	3.884E-04
9.8164	0.30	35.151	0.074	0.115	0.137	2.289E-01	2.289E-01	3.128E-04
9.9171	0.31	34.112	0.125	0.115	0.170	2.244E-01	2.243E-01	3.816E-04
10.0168	0.33	33.104	0.027	0.115	0.118	2.199E-01	2.199E-01	2.598E-04
10.0172*	0.33	33.074	0.184	0.115	0.217	2.197E-01	2.197E-01	4.767E-04
10.0172	0.33	33.082	0.184	0.115	0.217	2.198E-01	2.197E-01	4.773E-04
10.1168	0.31	32.129	0.033	0.115	0.120	2.155E-01	2.155E-01	2.577E-04
10.2176	0.29	31.185	0.122	0.115	0.168	2.112E-01	2.112E-01	3.549E-04
10.3176	0.30	30.300	0.067	0.115	0.133	2.072E-01	2.071E-01	2.755E-04
10.4179	0.32	29.437	0.148	0.115	0.187	2.032E-01	2.032E-01	3.804E-04
10.5181	0.35	28.615	0.045	0.115	0.123	1.994E-01	1.993E-01	2.462E-04
10.6185	0.39	27.910	0.012	0.115	0.116	1.963E-01	1.962E-01	2.269E-04
10.7191	0.44	27.164	0.025	0.115	0.118	1.928E-01	1.928E-01	2.271E-04
10.8203	0.49	26.325	0.179	0.115	0.213	1.886E-01	1.885E-01	4.014E-04
10.9203	0.55	25.690	0.033	0.115	0.120	1.857E-01	1.856E-01	2.220E-04
11.0202*	0.61	24.972	0.138	0.115	0.179	1.821E-01	1.821E-01	3.266E-04
11.1197	0.56	24.326	0.114	0.115	0.162	1.790E-01	1.789E-01	2.901E-04
11.2199	0.52	23.667	0.014	0.115	0.116	1.757E-01	1.756E-01	2.035E-04
11.3198	0.50	23.018	0.205	0.115	0.235	1.723E-01	1.723E-01	4.047E-04
11.4203	0.50	22.428	0.088	0.115	0.145	1.693E-01	1.693E-01	2.456E-04
11.5200	0.52	21.958	0.165	0.115	0.201	1.672E-01	1.671E-01	3.358E-04
11.6203	0.56	21.364	0.021	0.115	0.117	1.641E-01	1.640E-01	1.918E-04
11.7199	0.61	20.859	0.135	0.115	0.177	1.615E-01	1.614E-01	2.858E-04
11.8202	0.68	20.260	0.017	0.115	0.116	1.582E-01	1.581E-01	1.838E-04
11.9211	0.76	19.823	0.068	0.115	0.134	1.561E-01	1.560E-01	2.085E-04
12.0209*	0.84	19.337	0.021	0.115	0.117	1.535E-01	1.534E-01	1.793E-04
12.0209	0.84	19.336	0.019	0.115	0.117	1.535E-01	1.534E-01	1.789E-04
12.1711	0.76	18.617	0.006	0.115	0.115	1.495E-01	1.495E-01	1.721E-04
12.3210	0.68	17.924	0.055	0.115	0.127	1.457E-01	1.456E-01	1.854E-04
12.4703	0.60	17.290	0.071	0.115	0.135	1.422E-01	1.421E-01	1.919E-04
12.6208	0.53	16.669	0.116	0.115	0.164	1.386E-01	1.386E-01	2.269E-04
12.7706	0.48	16.092	0.043	0.115	0.123	1.354E-01	1.353E-01	1.663E-04
12.9206	0.43	15.521	0.100	0.115	0.152	1.320E-01	1.320E-01	2.009E-04
13.0706	0.40	15.018	0.079	0.115	0.139	1.292E-01	1.291E-01	1.801E-04
13.2208	0.40	14.533	0.078	0.115	0.139	1.264E-01	1.263E-01	1.756E-04
13.3715	0.42	14.056	0.152	0.115	0.191	1.236E-01	1.235E-01	2.357E-04
13.5215*	0.45	13.559	0.109	0.115	0.159	1.205E-01	1.204E-01	1.911E-04
13.6713	0.41	13.137	0.082	0.115	0.141	1.180E-01	1.179E-01	1.666E-04
13.8220	0.39	12.755	0.038	0.115	0.121	1.157E-01	1.157E-01	1.402E-04
13.9721	0.39	12.314	0.104	0.115	0.155	1.129E-01	1.128E-01	1.748E-04
14.1224	0.41	11.983	0.153	0.115	0.192	1.110E-01	1.109E-01	2.128E-04
14.2723	0.45	11.551	0.137	0.115	0.179	1.081E-01	1.080E-01	1.931E-04
14.4228	0.50	11.222	0.240	0.115	0.266	1.060E-01	1.059E-01	2.819E-04
14.5744	0.56	10.903	0.085	0.115	0.143	1.040E-01	1.040E-01	1.490E-04
14.7240	0.63	10.544	0.194	0.115	0.225	1.016E-01	1.015E-01	2.290E-04
14.8759	0.70	10.254	0.346	0.115	0.365	9.976E-02	9.967E-02	3.641E-04
14.8722	0.70	10.173	0.174	0.115	0.209	9.893E-02	9.884E-02	2.064E-04
15.0231*	0.78	9.969	0.038	0.115	0.121	9.789E-02	9.781E-02	1.186E-04
15.2264	0.65	9.553	0.215	0.115	0.243	9.499E-02	9.491E-02	2.312E-04
15.4259	0.55	9.195	0.141	0.115	0.182	9.255E-02	9.247E-02	1.683E-04
15.6253	0.48	8.857	0.112	0.115	0.161	9.023E-02	9.015E-02	1.449E-04
15.8256	0.46	8.522	0.099	0.115	0.152	8.785E-02	8.777E-02	1.332E-04
16.0255	0.49	8.214	0.121	0.115	0.167	8.567E-02	8.559E-02	1.433E-04
16.2252*	0.56	7.921	0.053	0.115	0.126	8.356E-02	8.348E-02	1.057E-04
16.2257	0.56	7.913	0.055	0.115	0.127	8.348E-02	8.341E-02	1.064E-04
16.4246	0.50	7.647	0.037	0.115	0.121	8.159E-02	8.152E-02	9.850E-05
16.6252	0.46	7.390	0.096	0.115	0.150	7.974E-02	7.966E-02	1.196E-04
16.8272	0.47	7.116	0.138	0.115	0.180	7.763E-02	7.755E-02	1.395E-04
17.0274	0.51	6.865	0.176	0.115	0.210	7.571E-02	7.563E-02	1.593E-04
17.2278	0.59	6.633	0.049	0.115	0.125	7.393E-02	7.385E-02	9.226E-05
17.4276	0.68	6.405	0.051	0.115	0.126	7.214E-02	7.206E-02	9.076E-05
17.6276	0.79	6.174	0.125	0.115	0.170	7.025E-02	7.017E-02	1.191E-04
17.6284*	0.79	6.165	0.067	0.060	0.090	7.015E-02	7.007E-02	6.336E-05
17.8270	0.65	5.974	0.132	0.060	0.145	6.867E-02	6.859E-02	9.975E-05
18.0274	0.54	5.764	0.046	0.060	0.076	6.692E-02	6.683E-02	5.074E-05
18.2259	0.50	5.583	0.438	0.060	0.442	6.546E-02	6.538E-02	2.893E-04
18.4269	0.55	5.427	0.146	0.060	0.158	6.427E-02	6.418E-02	1.014E-04
18.6266	0.65	5.249	0.094	0.060	0.112	6.275E-02	6.266E-02	7.029E-05
18.6272*	0.65	5.229	0.105	0.060	0.121	6.250E-02	6.241E-02	7.576E-05
18.8253	0.57	5.079	0.084	0.060	0.104	6.129E-02	6.120E-02	6.358E-05

Table 5 (continued)

E (keV)	σ_E (eV)	$[\mu/\rho]$ ($\mathrm{cm^2\,g^{-1}}$)	$\sigma_{[\mu/\rho]_{\rm rel}}$ (%)	σ_t (%)	$\sigma_{[\mu/\rho]}$ (%)	$f''_{\rm FFAST}$ (e atom^{-1})	$f''_{\rm XCOM}$ (e atom^{-1})	$\sigma_{f''}$ (e atom^{-1})
19.0264	0.50	4.939	0.344	0.060	0.350	6.017E-02	6.008E-02	2.104E-04
19.2255	0.46	4.772	0.058	0.060	0.083	5.865E-02	5.856E-02	4.889E-05
19.4241	0.46	4.629	0.022	0.060	0.064	5.741E-02	5.732E-02	3.679E-05
19.6246	0.49	4.496	0.119	0.060	0.133	5.627E-02	5.618E-02	7.490E-05
19.8238	0.55	4.354	0.109	0.060	0.125	5.497E-02	5.488E-02	6.857E-05
20.0281*	0.63	4.228	0.084	0.060	0.103	5.385E-02	5.376E-02	5.573E-05

give the corresponding measured mass attenuation coefficient $[\mu/\rho]$, the experimental precision, the accuracy in the thickness determination and the total uncertainty of $[\mu/\rho]$, respectively. The last three columns list the imaginary part of the form factor after correction for scattering. Uncertainties in the theoretically calculated components of the scattering factor are indicated by the difference between the two model-dependent estimates of f''. This latter uncertainty is clearly insignificant in the lower-energy region, and contributes at most 0.05% as one approaches 20 keV. Above 5.6 keV, the experimental values of $[\mu/\rho]$ are the weighted mean of the measurements obtained with three thicknesses, excluding those points affected by Bragg diffraction. The final uncertainty in the mass attenuation coefficient $\sigma_{[\mu/\rho]}$ in this range is the root mean square of the contributions from the uncertainty in the thickness calibration σ_t, and from the consistency of the measurements of using different samples, $\sigma_{\rm se}$, defined as

$$\sigma_{\rm se} = \left(\frac{\sum_{\rm all} \left([\mu/\rho]_{t_i} - \overline{[\mu/\rho]} \right)^2 / \sigma_i^2}{\sum_{\rm all} 1/\sigma_i^2} \right)^{1/2}, \tag{1}$$

where $[\mu/\rho]_{t_i}$ are the mass attenuation coefficients measured using wafers of different thicknesses t_i, $\overline{[\mu/\rho]}$ is the weighted average of $[\mu/\rho]_{t_i}$ and σ_i are the corresponding statistical errors in the measurements of $[\mu/\rho]_{t_i}$. Between 5.0 keV and 5.6 keV the values of $[\mu/\rho]$ are corrected for (significant) harmonic contamination. In this energy range, the final uncertainty $\sigma_{[\mu/\rho]}$ is the root mean square of the contributions of σ_t and of the final error in the procedure of the harmonic correction $\sigma_{\rm har}$, calculated from

$$\sigma_{\rm har} = \left(\sigma_{\rm fit}^2 + \sigma_{\rm stat}^2 \right)^{1/2}, \tag{2}$$

where $\sigma_{\rm fit}$ is the fitting error and $\sigma_{\rm stat}$ is the minimum of the statistical errors σ_i. Mass attenuation coefficients and their uncertainties are not affected by the value of the density. It is for this reason that the mass attenuation coefficient $[\mu/\rho]$ rather than the linear attenuation coefficient μ should be used for comparisons of data from different sources.

Table 6 summarizes the major sources of uncertainty contributing to the final results. Major factors affecting the precision or the consistency of the measurements of $[\mu/\rho]$ using multiple foils are listed in the first part of Table 6. Apart from the intrinsic statistics – the intrinsic sources of statistical uncertainty of the system at the level of 0.02%, the other main factors affecting the consistency of the measurements in this experiment are Bragg diffraction and the harmonic contamination in the low-energy range of the measurements.

Table 6

Silicon crystals, 5–20 keV: uncertainties of the mass attenuation coefficient $[\mu/\rho]$, the (photoelectric) mass absorption coefficient $[\mu/\rho]_{\rm pe}$ and f'' (Tran *et al.*, 2003*b*,*c*).

	% Contribution (± 1 standard error)		
Source of uncertainty	5–5.6 keV	5.6–20 keV	Notes
Major contributions to precision:			
harmonic contamination	~0.3%		
Bragg diffraction		<0.44%	Maximal at 18.226 keV
monochromator hysteresis	<0.07%		$\sigma_E < 1.3$ eV at 5–6 keV
energy calibration elsewhere	0.01%	0.01%	$\sigma_E/E = \pm\,0.004\%$
system statistics	0.02%	0.02%	Reproducibility without sample
Major contributions to accuracy:			
experimental precision	0.3%	0.02–0.44%	Including all above contributions
sample thickness	0.139%	0.06–0.139%	Thickness calibration and transfer
Minor contributions:			
energy drift		0.00–0.008%	$\sigma_E/E = \pm 0.0026\%$ at 7.6 keV $\sigma_E/E = \pm 0.00175\%$ at 20 keV
Additional contributions:			
Compton scattering, thermal diffuse scattering (for $[\mu/\rho]_{\rm pe}$ and f'')	minor	0.05%	Variation in theory
Total final accuracy	0.323–0.350%	0.064–0.266%	Outliers 0.365% (at 14.879 keV) and 0.442% (at 18.226 keV) due to Bragg diffraction

Uncertainties from the fitting of the harmonic contamination of the incident beam below 5.6 keV are at the level of 0.3%. In the high-energy range, measurements that were significantly affected by Bragg diffraction (where the measured values of $[\ln(I/I_0)]$ were more than 0.5% higher than those from the other two specimens) were excluded from the calculations of the final results. The remaining points were consistent to better than 0.44% (the maximum discrepancy was at 18.226 keV, as in Tables 5 and 6).

Uncertainties in the correction of the (very significant) backlash hysteresis of the monochromator amounted to 1.3 eV or less between 5 keV and 6 keV. The effect of hysteresis is thus less than 0.07% in $[\mu/\rho]$ in this energy range. Errors in the energy determination of less than 1 eV elsewhere are equivalent to less than 0.01% in $[\mu/\rho]$. These main components of the factors affecting the experimental precision resulted in the final experimental precision listed in the second part of Table 6. This contributed to the total experimental accuracy at levels of 0.3% below 5.6 keV, and up to 0.44% in the higher-energy region.

Uncertainty from the determination of the thicknesses of the specimens increased from 0.06% (at 20 keV) to 0.139% (at 5 keV) due to the additional contribution from the thickness transfer procedure of Tran *et al.* (2004*a*). Mika *et al.* (1985) and Gerward *et al.* (1981) reported similar accuracies [3 µm (0.075%) and 2 µm (0.05%), respectively] for specimens of similar (4 mm) thickness. However, their results were for the local thickness measured with a micrometer and not for the absolute accuracy of the determination. Baltazar-Rodrigues & Cusatis (2001) reported 0.3 µm accuracy in the thickness determination of their silicon specimens of between 100 µm and 800 µm, but they appear to have used the average thicknesses of the specimens. Both methods (micrometry and average thickness) differ from the local mass per unit area actually seen by the X-ray beam and determined by our technique. The error can be significant (Tran *et al.*, 2004*a*).

This work led to a critical evaluation of how to account for Bragg/Laue reflections from the sample (Chantler *et al.*, 2010), as well as the nature of the elastic scattering contribution and its impact upon XAS measurement and the determination of the form factor. In particular, the replacement of a Rayleigh scattering coefficient with a prediction of thermal diffuse scattering was investigated. Approaches to absolute coefficient measurement and the calibration of energy using powder diffraction were also investigated.

7. Silver foils, 15–50 keV. XAS, towards XAFS

Tran *et al.* (2005) measured the X-ray mass attenuation coefficient of silver metal foils. In this case, the K edge was included. There were 146 data points in the data set, which was enough to see XAFS oscillations but only just enough to carry out standard XAFS analysis of the nanostructure. The energy range covered was 15.2–49.9 keV, so only about 60 data points covered a standard XAFS region, with a minimum energy step size of 5 eV. Whilst sufficient for a range of XAS applications, tests of theory and a simple analysis of the nanostructure, it is generally considered that analysis of sources of systematic errors and the many-body physics requires much closer point spacing near the edge.

Three foils were used at every energy, varying from 12 µm to 100 µm and 275 µm to cover an attenuation range of $0.1 < \ln(I_0/I) < 6.8$, well beyond the Nordfors criterion, in order to interrogate sources of systematic errors. Table 7 shows the results. Columns E and σ_E show the energies (in keV) and the corresponding uncertainties (in eV) at which attenuation measurements were carried out. The columns $[\mu/\rho]_{\rm meas}$, $\sigma_{[\mu/\rho]_{\rm rel}}$ and $\sigma_{[\mu/\rho]}$ show the measured mass attenuation coefficient $[\mu/\rho]_{\rm meas}$ (in cm^2 g^{-1}), the weighted deviation and the uncertainties of $[\mu/\rho]_{\rm meas}$. The uncertainty in the measured mass attenuation coefficient $\sigma_{[\mu/\rho]}$ is the root mean square of the contributions from the uncertainty in the thickness calibration σ_t and from the consistency of the measurements obtained with the different foils $\sigma_{[\mu/\rho]_{\rm rel}}$.

The column $[\mu/\rho]$ shows the total mass attenuation coefficients obtained by applying appropriate corrections to the $[\mu/\rho]_{\rm meas}$ values for the effects of fluorescence and scattering. Note that $[\mu/\rho]_{\rm meas}$ is ill-defined since it corrects for some of the sources of systematic errors but not, for example, scattering and fluorescence. However, it is an improvement compared with some earlier work. Columns f'' and $\sigma_{f''}$ list the imaginary part of the complex atomic form factor, f, and the corresponding absolute uncertainties. f'' was obtained from the optical theorem:

$$f'' = \frac{E\sigma_{\rm pe}}{2hcr_e} = \frac{EuA[\mu/\rho]_{\rm pe}}{2hcr_e}, \tag{3}$$

where E is the energy in eV, $\sigma_{\rm pe}$ is the (photoelectric) mass absorption cross section, h and c are Planck's constant and the speed of light, respectively, r_e is the classical electron radius, u is the atomic mass unit, A is the relative atomic mass, $m_a = uA$ is the (atomic) mass, and $[\mu/\rho]_{\rm pe}$ is the (photoelectric) mass absorption coefficient obtained by subtracting the total scattering coefficients $\left([\mu/\rho]_{\rm R} + [\mu/\rho]_{\rm C}\right)$ (following Chantler, 1995, 2000; Chantler *et al.*, 2000) from the mass attenuation coefficient $[\mu/\rho]$. The use of equation (3) in the region of XAFS is clearly affected by non-atomic, *i.e.* solid-state, effects and hence includes processes other than just those due to the atomic form factor. This also represented one of the first clear observations of the 'triangle effect' (Fig. 1): a discrepancy of absorption versus energy around the edge compared with all theory to date, which has the appearance of a triangle as a function of energy above the edge, or sometimes the appearance of a dispersion shape, like a double triangle (de Jonge *et al.*, 2005, 2007; Sier *et al.*, 2020). The data are available in the supporting information to this chapter as file bz5029sup3.pdf.

The tabulated values of the measured mass attenuation coefficients $[\mu/\rho]_{\rm meas}$ were calculated from the weighted mean of all the measurements obtained with combinations of the three foils and the three apertures. The total mass attenuation coefficients $[\mu/\rho]$ were obtained by applying corrections to the measured attenuation coefficients for the effects of scattering and fluorescence. As this correction is small (less than 0.05%),

Table 7

Silver, 15–50 keV, metal foil total mass attenuation coefficients $[\mu/\rho]$ and the imaginary part of the atomic form factor f'' versus E (Tran *et al.*, 2005), with uncertainties.

σ_E is the absolute uncertainty in calibrated energy (one standard error); $\sigma_{[\mu/\rho]_{\rm rel}}$ is the percentage precision of repeated measurements (one standard error); $\sigma_{[\mu/\rho]}$ is the total percentage accuracy in the mass attenuation coefficient $[\mu/\rho]$; f'' is the imaginary part of the complex atomic form factor, obtained using equation (3), where $[\mu/\rho]_{\rm pe} = [\mu/\rho] - ([\mu/\rho]_{\rm R} + [\mu/\rho]_{\rm C})$; and $\sigma_{f''}$ is the absolute uncertainty in f''. (Some rows of values have been omitted for brevity. The full version is available in the supporting information.)

E (keV)	σ_E (eV)	$[\mu/\rho]_{\rm meas}$ (cm^2 g^{-1})	$\sigma_{[\mu/\rho]_{\rm rel}}$ (%)	$\sigma_{[\mu/\rho]}$ (%)	$[\mu/\rho]$ (cm^2 g^{-1})	f'' (e atom^{-1})	$\sigma_{f''}$ (e atom^{-1})
15.291	2.3	38.006	0.08	0.28	38.008	1.423	0.007
15.791	2.1	34.778	0.07	0.27	34.779	1.342	0.007
16.289	2.0	31.915	0.03	0.27	31.916	1.267	0.007
16.688	2.0	29.871	0.05	0.27	29.873	1.212	0.007
17.087	1.9	27.994	0.06	0.27	27.995	1.161	0.007
17.485	1.8	26.283	0.05	0.27	26.284	1.113	0.007
17.883	1.7	24.716	0.04	0.27	24.717	1.068	0.007
18.280	1.7	23.265	0.07	0.27	23.266	1.026	0.007
18.678	1.6	21.944	0.08	0.28	21.945	0.987	0.007
19.076	1.6	20.675	0.03	0.27	20.676	0.947	0.006
19.473	1.6	19.542	0.07	0.27	19.544	0.912	0.006
19.870	1.6	18.489	0.07	0.27	18.490	0.879	0.006
20.267	1.7	17.539	0.14	0.30	17.540	0.848	0.006
20.267	1.7	17.524	0.02	0.27	17.526	0.848	0.006
20.663	1.7	16.592	0.15	0.31	16.594	0.816	0.006
21.060	1.8	15.742	0.12	0.29	15.743	0.788	0.006
21.457	2.0	14.946	0.12	0.29	14.948	0.760	0.006
21.853	2.1	14.210	0.15	0.31	14.211	0.734	0.006
22.250	2.3	13.515	0.15	0.30	13.516	0.709	0.006
22.646	2.5	12.864	0.20	0.34	12.865	0.686	0.006
23.438	3.0	11.717	0.05	0.28	11.718	0.643	0.006
23.834	3.2	11.175	0.02	0.28	11.176	0.622	0.006
24.230	3.5	10.664	0.04	0.28	10.665	0.602	0.006
24.626	3.7	10.190	0.04	0.28	10.191	0.583	0.006
25.022	4.0	9.749	0.02	0.28	9.750	0.566	0.006
25.219	4.2	9.571	0.02	0.28	9.572	0.559	0.006
25.317	4.2	9.523	0.05	0.28	9.524	0.558	0.006
25.378	14.8	9.547	0.17	0.40	9.548	0.562	0.006
25.383	4.3	9.543	0.03	0.28	9.544	0.561	0.006
25.383	4.3	9.552	0.06	0.28	9.553	0.562	0.006
25.407	14.8	9.626	0.15	0.39	9.627	0.567	0.006
25.427	14.8	9.720	0.18	0.40	9.722	0.574	0.006
25.437	14.8	9.788	0.20	0.41	9.789	0.579	0.006
25.447	14.8	9.905	0.15	0.39	9.907	0.587	0.006
25.456	14.8	10.054	0.29	0.46	10.055	0.597	0.006
25.466	14.8	10.295	0.17	0.40	10.296	0.613	0.006
25.476	14.8	10.714	0.19	0.40	10.715	0.640	0.006
25.486	14.8	11.596	0.20	0.41	11.597	0.698	0.006
25.496	14.8	14.277	0.25	0.44	14.279	0.874	0.007
25.506	14.8	32.122	1.08	1.14	32.128	2.041	0.024
25.516	14.8	56.986	0.31	0.48	56.997	3.669	0.018
25.526	14.8	55.765	0.32	0.48	55.778	3.590	0.018
25.535	14.8	58.655	0.40	0.53	58.670	3.781	0.021
25.545	14.8	60.144	0.25	0.44	60.160	3.880	0.018
25.555	14.7	55.361	0.32	0.48	55.377	3.568	0.018
25.565	14.7	59.342	0.17	0.40	59.361	3.831	0.016
25.575	14.7	62.748	0.60	0.70	62.769	4.056	0.029
25.585	14.7	57.981	0.17	0.40	58.003	3.745	0.016
25.595	14.7	57.038	0.38	0.52	57.060	3.684	0.020
25.605	14.7	59.332	0.29	0.46	59.357	3.836	0.019
25.615	14.7	60.431	0.22	0.42	60.458	3.910	0.017
25.624	14.7	59.705	0.19	0.40	59.733	3.864	0.017
25.634	14.7	58.327	0.25	0.44	58.355	3.775	0.017
25.644	14.7	58.481	0.34	0.49	58.511	3.787	0.020
25.654	14.7	59.420	0.52	0.63	59.450	3.850	0.025
25.664	14.7	59.529	0.19	0.40	59.559	3.859	0.017
25.674	14.7	58.717	0.35	0.50	58.747	3.807	0.020
25.684	14.7	58.474	0.19	0.40	58.503	3.792	0.016
25.693	14.7	57.909	0.22	0.42	57.938	3.757	0.017
25.703	14.7	57.930	0.19	0.40	57.959	3.759	0.016
25.713	14.7	58.591	0.25	0.44	58.620	3.804	0.018
25.723	14.7	58.631	0.41	0.54	58.660	3.809	0.022
25.733	14.7	58.448	0.41	0.54	58.477	3.798	0.021
25.743	14.7	57.720	0.42	0.55	57.749	3.751	0.021
25.753	14.7	57.105	0.26	0.44	57.133	3.712	0.017

Table 7 (continued)

E (keV)	σ_E (eV)	$[\mu/\rho]_{\rm meas}$ (cm^2 g^{-1})	$\sigma_{[\mu/\rho]_{\rm rel}}$ (%)	$\sigma_{[\mu/\rho]}$ (%)	$[\mu/\rho]$ (cm^2 g^{-1})	f' (e atom^{-1})	$\sigma_{f''}$ (e atom^{-1})
25.763	14.7	57.037	0.23	0.42	57.065	3.709	0.017
25.773	14.7	56.895	0.35	0.50	56.922	3.701	0.019
25.782	14.6	57.296	0.23	0.42	57.323	3.729	0.017
25.792	14.6	57.695	0.20	0.41	57.723	3.757	0.016
25.802	14.6	57.654	0.24	0.43	57.682	3.756	0.017
25.812	14.6	57.153	0.43	0.56	57.180	3.724	0.022
25.822	14.6	56.776	0.21	0.41	56.803	3.701	0.016
25.832	14.6	56.120	0.58	0.68	56.147	3.659	0.025
25.842	14.6	56.385	0.19	0.40	56.412	3.678	0.016
25.852	14.6	56.205	0.29	0.46	56.231	3.667	0.018
25.862	14.6	56.183	0.23	0.43	56.209	3.667	0.017
25.872	14.6	56.257	0.29	0.46	56.283	3.673	0.018
25.882	14.6	56.347	0.35	0.50	56.374	3.681	0.019
25.891	14.6	56.507	0.13	0.38	56.534	3.693	0.015
25.901	14.6	56.237	0.33	0.49	56.263	3.676	0.019
25.911	14.6	56.008	0.17	0.39	56.034	3.663	0.016
25.921	14.6	55.707	0.16	0.39	55.733	3.644	0.015
25.941	14.6	55.506	0.21	0.41	55.531	3.633	0.016
25.961	14.6	55.442	0.28	0.45	55.467	3.632	0.017
25.981	14.6	55.516	0.22	0.42	55.541	3.640	0.016
26.001	14.6	55.394	0.16	0.39	55.418	3.634	0.015
26.040	14.5	54.968	0.16	0.39	54.992	3.612	0.015
26.078	14.5	54.607	0.38	0.52	54.630	3.593	0.020
26.119	14.5	54.527	0.24	0.43	54.550	3.593	0.017
26.179	14.5	53.930	0.32	0.48	53.952	3.561	0.018
26.199	14.5	54.056	0.18	0.40	54.078	3.573	0.015
26.391	14.4	52.754	0.14	0.38	52.775	3.511	0.015
26.791	14.2	50.400	0.10	0.37	50.418	3.404	0.014
26.989	14.1	49.224	0.15	0.39	49.240	3.348	0.014
27.187	14.0	48.141	0.24	0.43	48.156	3.297	0.015
27.187	14.0	47.699	1.08	1.14	47.715	3.267	0.038
27.385	13.9	47.208	0.16	0.39	47.222	3.256	0.014
27.780	13.8	45.346	0.09	0.37	45.358	3.172	0.013
28.175	13.6	43.600	0.03	0.36	43.610	3.092	0.012
28.571	13.4	42.007	0.10	0.37	42.016	3.019	0.013
28.966	13.3	40.453	0.05	0.36	40.462	2.947	0.012
29.362	13.1	39.043	0.05	0.36	39.051	2.882	0.012
29.757	13.0	37.682	0.15	0.39	37.688	2.818	0.012
30.152	12.9	36.353	0.04	0.36	36.359	2.753	0.011
30.547	12.8	35.107	0.03	0.36	35.113	2.693	0.011
30.942	12.7	33.931	0.07	0.36	33.936	2.635	0.011
31.337	12.6	32.809	0.06	0.36	32.814	2.580	0.011
31.733	12.6	31.754	0.09	0.37	31.758	2.527	0.011
32.128	12.6	30.698	0.03	0.36	30.702	2.472	0.010
32.523	12.6	29.719	0.06	0.36	29.723	2.422	0.010
32.919	12.6	28.812	0.13	0.38	28.815	2.376	0.011
33.313	12.7	27.887	0.10	0.37	27.890	2.326	0.010
33.709	12.8	27.013	0.08	0.37	27.016	2.279	0.010
33.709	12.8	26.986	0.06	0.36	26.989	2.277	0.010
34.104	13.0	26.165	0.04	0.36	26.168	2.232	0.010
34.500	13.2	25.432	0.07	0.36	25.435	2.194	0.010
34.896	13.4	24.656	0.13	0.38	24.658	2.151	0.010
35.290	13.7	23.921	0.09	0.37	23.924	2.110	0.009
35.884	14.2	22.869	0.11	0.37	22.871	2.049	0.009
36.477	14.8	21.891	0.14	0.38	21.894	1.993	0.009
37.070	15.4	20.967	0.14	0.38	20.969	1.939	0.009
37.663	16.2	20.054	0.10	0.37	20.056	1.882	0.009
38.256	17.0	19.240	0.09	0.37	19.242	1.833	0.009
38.849	17.9	18.469	0.06	0.36	18.471	1.786	0.008
39.443	18.9	17.724	0.03	0.36	17.727	1.739	0.008
40.036	19.9	17.050	0.08	0.37	17.052	1.697	0.008
40.036	19.9	17.030	0.02	0.36	17.033	1.695	0.008
40.828	21.5	16.168	0.09	0.37	16.171	1.639	0.008
41.619	23.1	15.361	0.07	0.36	15.363	1.586	0.008
42.411	24.8	14.603	0.06	0.36	14.606	1.535	0.008
43.203	26.7	13.881	0.07	0.36	13.883	1.485	0.007
43.995	28.6	13.176	0.06	0.36	13.178	1.434	0.007
44.787	30.6	12.604	0.02	0.36	12.606	1.395	0.007
...							
49.146	43.3	9.759	0.06	0.36	9.760	1.178	0.006
49.531	44.5	9.578	0.08	0.37	9.579	1.165	0.006
49.918	45.7	9.381	0.10	0.37	9.382	1.150	0.006

Table 8
Silver, 15-50 keV, metal foils: uncertainties of the mass attenuation coefficient $[\mu/\rho]$, the (photoelectric) mass absorption coefficient $[\mu/\rho]_{\rm pe}$ and f'' (Tran *et al.*, 2005).

	% Contribution (±1 standard error)		
Source of uncertainty	Away from edge	At the K edge	Notes
Contributions to precision:			
energy calibration	0.01–0.02%	0.01–0.02%	σ_E = 0.007–0.08%
system statistics	0.02%	0.02%	Reproducibility without sample
Major contributions to accuracy:			
experimental precision	0.05–0.15%	0.2–0.5%	Including all above contributions
sample thickness	0.17–0.36%	0.17–0.36%	Thickness calibration and scaling
Minor contributions:			
secondary photons	0.003%	0.01%	20% of the correction
harmonic contamination	minor	minor	
detector linearity	minor	minor	
Additional contributions:			
Rayleigh, Compton (for $[\mu/\rho]_{\rm pe}$ and f'')	minor	0.05%	
Total final accuracy	0.27–0.4%	0.4–0.7%	

the difference between applying this correction before or after taking the average of $[\mu/\rho]_{\rm meas}$ is insignificant.

Table 8 summarizes the major sources of uncertainty contributing to the tabulated values of $[\mu/\rho]_{\rm meas}$. Major factors affecting the precision or the consistency of the measurements of $[\mu/\rho]_{\rm meas}$ using multiple foils are listed in the first part of Table 8. The main factors affecting the consistency of the measurements are the intrinsic sources of statistical errors of the system at the level of 0.02%, and the uncertainty in the energy.

The final uncertainty in $[\mu/\rho]$ (0.27–0.4% away from the K edge, 0.4–0.7% at the K edge) is dominated by the experimental precision (0.15% away from the K edge and 0.2% to 0.5% at the edge) and by the uncertainty in the local thickness (0.17–0.36%). Although limited in XAFS, this work was fully adequate for detailed comparison of advanced theoretical methods for computation of XAS and XAFS, including using *FDMNES* (Cosgriff *et al.*, 2005) and variable-cluster-size computations. It also was able to calibrate the energy using powder sample standards (Rae *et al.*, 2010*c*).

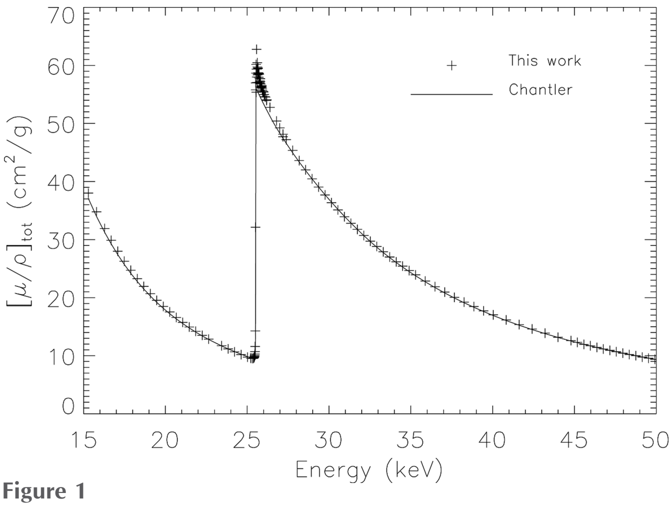

Figure 1
Silver foil mass attenuation coefficients $[\mu/\rho]$, experiment (15–50 keV; Tran *et al.*, 2005) and theory (Chantler, 1995, 2000; Chantler *et al.*, 2000), confirming the broad structure predicted by theory and detailed XAS. Copyright IOP Publishing. Reproduced with permission from Tran *et al.* (2005). All rights reserved.

8. Molybdenum foils, 13.5–41.5 keV. XAS, XAFS, bonding, nanostructure and theory

The article by de Jonge *et al.* (2005) was the first to provide an accurate XAS spectrum together with a detailed XAFS spectrum, in this case for molybdenum at and above the K edge at 20 keV. The foil thicknesses used were nominally 25 µm, 50 µm, 100 µm, 150 µm, 200 µm and 250 µm. Between three and five samples were used at each energy. This article defined significance as a measure of anomalies and unknown systematic errors, searched for a systematic error due to roughness, and found a systematic error due to bandwidth, allowing the bandwidth to be measured from the XAS data directly. This was the first example of its type to provide the pre-processed data as supplementary material – that is, the first to deposit a transferable data set. The data tabulated in the publication presented 94 points; the full set included 526 independent energies with 0.5 eV spacing above the edge. Hence this data set was the first high-accuracy data set amenable to detailed structural XAFS analysis and exploration of a range of independent systematic errors and new areas of physics.

Table 9 presents mass attenuation coefficients measured at 526 energies between 13.5 keV and 41.5 keV. The first column is the calibrated photon energy (in keV) with the uncertainty in the last significant figure presented in parentheses. The second column is the mass attenuation coefficient $[\mu/\rho]$ (in cm^2 g^{-1}; see Fig. 2) with uncertainty. The third column provides the percentage uncertainty in the mass attenuation coefficient. The values in the second and third columns were

Table 9

Molybdenum foils, 13.5–41.5 keV: mass attenuation coefficients $[\mu/\rho]$ and the imaginary component of the atomic form factor f'' as a function of X-ray energy.

One standard deviation uncertainties in the least significant digits are indicated in parentheses. The percentage uncertainty in the mass attenuation coefficients, $\sigma_{[\mu/\rho]}$, follows. The uncertainty in f'' includes the measurement uncertainty and the difference between major tabulations of the total Rayleigh plus Compton scattering cross sections. f'' in the energy range 19.9–20.9 keV is affected by solid-state effects. A further uncertainty, of the same order as the XAFS amplitude, may apply to these values when alternative atomic environments are investigated. (Some rows of values have been omitted for brevity. The full version is available in the supporting information.)

E (keV)	$[\mu/\rho]$ (cm^2 g^{-1})	$\sigma_{[\mu/\rho]}$ (%)	f'' (e atom^{-1})
13.50614 (31)	37.868 (25)	0.067	1.1125 (17)
13.80632 (31)	35.596 (35)	0.098	1.0671 (18)
14.10651 (30)	33.578 (24)	0.070	1.0267 (14)
. . .			
19.98279 (38)	15.739 (26)	0.17	0.6674 (13)
19.98330 (38)	15.906 (14)	0.087	0.67502 (87)
19.98380 (38)	16.058 (11)	0.070	0.68194 (78)
19.98430 (38)	16.2012 (92)	0.057	0.68848 (72)
19.98480 (38)	16.3753 (71)	0.043	0.69643 (67)
19.98530 (38)	16.603 (19)	0.12	0.7068 (11)
19.98581 (38)	16.818 (20)	0.12	0.7166 (11)
19.98631 (38)	17.098 (12)	0.069	0.72941 (79)
19.98681 (38)	17.256 (27)	0.16	0.7366 (14)
19.98781 (38)	17.940 (12)	0.069	0.76783 (81)
19.98832 (38)	18.204 (42)	0.23	0.7799 (20)
19.99083 (38)	20.843 (29)	0.14	0.9003 (14)
19.99133 (38)	21.762 (30)	0.14	0.9422 (15)
19.99183 (38)	23.067 (39)	0.17	1.0017 (18)
19.99233 (38)	24.407 (32)	0.13	1.0628 (16)
19.99278 (38)	26.111 (40)	0.15	1.1405 (19)
19.99329 (38)	28.012 (54)	0.19	1.2272 (25)
19.99379 (38)	30.395 (59)	0.20	1.3358 (28)
19.99429 (38)	32.545 (93)	0.28	1.4339 (43)
19.99479 (38)	34.825 (68)	0.19	1.5378 (31)
19.99530 (38)	36.881 (59)	0.16	1.6316 (27)
19.99580 (38)	38.756 (49)	0.13	1.7171 (23)
19.99630 (38)	40.559 (43)	0.11	1.7994 (20)
19.99680 (38)	42.134 (67)	0.16	1.8712 (31)
19.99731 (38)	43.791 (40)	0.092	1.9469 (19)
19.99781 (38)	45.378 (56)	0.12	2.0193 (26)
19.99831 (38)	47.089 (60)	0.13	2.0973 (28)
19.99881 (38)	48.682 (41)	0.085	2.1700 (20)
19.99932 (38)	50.403 (32)	0.064	2.2485 (16)
19.99982 (38)	52.108 (23)	0.045	2.3263 (12)
20.00032 (38)	53.827 (44)	0.081	2.4048 (21)
20.00082 (38)	55.429 (29)	0.052	2.4779 (14)
20.00133 (38)	57.022 (26)	0.046	2.5506 (13)
20.00183 (38)	58.753 (55)	0.094	2.6296 (26)
20.00233 (38)	60.596 (35)	0.058	2.7137 (17)
20.00283 (38)	62.472 (51)	0.082	2.7993 (24)
20.00334 (38)	64.636 (27)	0.041	2.8981 (13)
20.00384 (38)	67.038 (90)	0.13	3.0077 (41)
20.00429 (38)	69.699 (88)	0.13	3.1292 (40)
20.00480 (38)	72.541 (58)	0.080	3.2588 (27)
20.00530 (38)	75.252 (47)	0.062	3.3826 (22)
20.00580 (38)	78.274 (44)	0.057	3.5205 (21)
20.00631 (38)	81.16 (15)	0.18	3.6521 (67)
20.00681 (38)	83.88 (10)	0.12	3.7762 (47)
20.00731 (38)	85.898 (70)	0.081	3.8686 (32)
20.00781 (38)	87.590 (61)	0.070	3.9458 (28)
20.00832 (38)	88.884 (52)	0.059	4.0050 (24)
20.00882 (38)	89.919 (44)	0.049	4.0523 (21)
20.00933 (38)	90.532 (40)	0.044	4.0803 (19)
20.00983 (38)	90.944 (34)	0.038	4.0993 (17)
20.01033 (38)	90.997 (28)	0.031	4.1017 (14)
20.01083 (38)	90.708 (25)	0.028	4.0887 (13)
20.01134 (38)	90.231 (42)	0.047	4.0670 (20)
20.01184 (38)	89.535 (39)	0.044	4.0354 (19)
20.01234 (38)	88.537 (40)	0.045	3.9899 (19)
20.01285 (38)	87.372 (33)	0.037	3.9369 (16)
20.01330 (38)	86.318 (24)	0.028	3.8888 (12)
20.01380 (38)	85.365 (16)	0.019	3.84548 (90)
20.01431 (38)	84.410 (51)	0.060	3.8020 (24)
20.01934 (38)	85.541 (46)	0.054	3.8546 (21)
20.01985 (38)	86.007 (36)	0.042	3.8759 (17)
20.02035 (38)	86.418 (33)	0.039	3.8948 (16)
20.02085 (38)	86.651 (32)	0.037	3.9055 (15)
20.02131 (38)	86.832 (30)	0.034	3.9139 (14)
20.02181 (38)	86.934 (28)	0.032	3.9186 (14)
20.02231 (38)	86.990 (27)	0.031	3.9213 (13)
20.02282 (38)	86.950 (25)	0.029	3.9196 (12)
20.02332 (38)	86.881 (23)	0.026	3.9165 (11)
20.02383 (38)	86.830 (20)	0.023	3.9143 (10)
20.02433 (38)	86.804 (45)	0.051	3.9132 (21)
20.02483 (38)	86.631 (64)	0.073	3.9054 (29)
20.02534 (38)	86.626 (60)	0.070	3.9053 (28)
20.02584 (38)	86.633 (56)	0.065	3.9057 (26)
20.02635 (38)	86.696 (53)	0.061	3.9087 (25)
20.02685 (38)	86.819 (49)	0.056	3.9144 (23)
20.02735 (38)	86.997 (44)	0.051	3.9226 (21)
20.02786 (38)	87.277 (41)	0.046	3.9355 (19)
20.02831 (38)	87.588 (35)	0.040	3.9498 (16)
20.02882 (38)	88.000 (27)	0.031	3.9687 (13)
20.02932 (38)	88.482 (29)	0.033	3.9908 (14)
20.02982 (38)	88.786 (37)	0.042	4.0048 (18)
20.03033 (38)	89.176 (36)	0.041	4.0227 (17)
20.03083 (38)	89.574 (35)	0.039	4.0410 (16)
20.03134 (38)	89.971 (34)	0.037	4.0592 (16)
20.03184 (38)	90.382 (32)	0.035	4.0781 (15)
20.03234 (38)	90.737 (29)	0.032	4.0944 (14)
20.03285 (38)	91.138 (29)	0.032	4.1128 (14)
20.03336 (38)	91.560 (28)	0.030	4.1322 (13)
20.03386 (38)	91.990 (24)	0.026	4.1520 (12)
20.03436 (38)	92.522 (33)	0.035	4.1764 (16)
20.03482 (38)	92.891 (41)	0.044	4.1933 (19)
20.03532 (38)	93.345 (40)	0.043	4.2142 (19)
20.03583 (38)	93.825 (38)	0.040	4.2362 (18)
20.03633 (38)	94.226 (37)	0.039	4.2546 (17)
20.03683 (38)	94.582 (33)	0.035	4.2710 (16)
20.03734 (38)	94.890 (32)	0.033	4.2852 (15)
20.03784 (38)	95.115 (29)	0.031	4.2956 (14)
20.03835 (38)	95.202 (27)	0.029	4.2996 (13)
20.03885 (38)	95.103 (31)	0.032	4.2952 (15)
20.03936 (38)	95.001 (28)	0.029	4.2907 (13)
20.03986 (38)	94.653 (93)	0.099	4.2749 (43)
20.04037 (38)	94.139 (90)	0.096	4.2515 (42)
20.04082 (38)	93.578 (87)	0.093	4.2260 (40)
20.04133 (38)	92.906 (82)	0.089	4.1954 (38)
20.04183 (38)	92.175 (82)	0.089	4.1621 (38)
20.04234 (38)	91.382 (76)	0.084	4.1260 (35)
20.04284 (38)	90.620 (74)	0.082	4.0913 (34)
20.04335 (38)	89.858 (69)	0.077	4.0565 (32)
20.04385 (38)	89.131 (69)	0.077	4.0234 (32)
20.04436 (38)	88.533 (42)	0.048	3.9962 (20)
20.04935 (38)	85.379 (38)	0.045	3.8530 (18)
20.04986 (38)	85.333 (60)	0.071	3.8510 (28)
20.05037 (38)	85.339 (59)	0.069	3.8514 (27)
20.05087 (38)	85.382 (59)	0.069	3.8535 (27)
20.05133 (38)	85.514 (59)	0.070	3.8596 (27)
20.05183 (38)	85.595 (60)	0.070	3.8634 (28)
20.05234 (38)	85.753 (60)	0.070	3.8707 (28)
20.05284 (38)	85.916 (61)	0.071	3.8782 (28)
20.05335 (38)	86.113 (61)	0.071	3.8874 (28)
20.05385 (38)	86.383 (63)	0.073	3.8998 (29)
20.05436 (38)	86.618 (52)	0.060	3.9106 (24)
20.05936 (38)	87.835 (29)	0.034	3.9673 (14)
20.05987 (38)	87.817 (70)	0.080	3.9666 (32)
20.06038 (38)	87.706 (77)	0.088	3.9616 (35)
20.06088 (38)	87.639 (98)	0.11	3.9586 (45)
20.06134 (38)	87.51 (12)	0.13	3.9528 (53)
20.06184 (38)	87.41 (10)	0.12	3.9485 (47)
20.06235 (38)	87.297 (68)	0.078	3.9433 (31)

Table 9 (continued)

E (keV)	$[\mu/\rho]$ (cm^2 g^{-1})	$\sigma_{[\mu/\rho]}$ (%)	f'' (e atom^{-1})
20.06285 (38)	87.202 (66)	0.076	3.9390 (30)
20.06336 (38)	87.059 (68)	0.078	3.9326 (31)
20.06387 (38)	86.887 (65)	0.075	3.9248 (30)
20.06437 (38)	86.797 (28)	0.033	3.9208 (13)
20.06938 (38)	85.628 (40)	0.046	3.8683 (19)
20.06989 (38)	85.553 (72)	0.085	3.8650 (33)
20.07034 (38)	85.543 (69)	0.081	3.8646 (32)
20.07085 (38)	85.600 (69)	0.081	3.8673 (32)
20.07136 (38)	85.694 (67)	0.078	3.8717 (31)
20.07186 (38)	85.820 (66)	0.077	3.8776 (30)
20.07237 (38)	85.983 (64)	0.074	3.8851 (29)
20.07288 (38)	86.180 (62)	0.072	3.8942 (29)
20.07338 (38)	86.411 (61)	0.071	3.9049 (28)
20.07389 (38)	86.688 (60)	0.069	3.9176 (27)
20.07434 (38)	87.032 (46)	0.052	3.9335 (21)
20.07936 (39)	90.212 (69)	0.076	4.0801 (32)
20.07987 (39)	90.340 (81)	0.090	4.0860 (37)
20.08037 (39)	90.498 (81)	0.090	4.0934 (37)
20.08088 (39)	90.617 (81)	0.089	4.0989 (37)
20.08139 (39)	90.645 (79)	0.087	4.1003 (36)
20.08189 (39)	90.683 (76)	0.083	4.1021 (35)
20.08235 (39)	90.665 (76)	0.083	4.1014 (35)
20.08286 (39)	90.572 (73)	0.081	4.0973 (34)
20.08336 (39)	90.429 (75)	0.082	4.0908 (34)
20.08387 (39)	90.300 (74)	0.082	4.0850 (34)
20.08438 (39)	90.056 (47)	0.052	4.0739 (22)
20.08940 (39)	86.406 (45)	0.053	3.9078 (21)
20.08986 (39)	86.043 (65)	0.076	3.8912 (30)
20.09036 (39)	85.763 (65)	0.075	3.8785 (30)
20.09087 (39)	85.589 (64)	0.075	3.8707 (30)
20.09138 (39)	85.405 (63)	0.074	3.8623 (29)
20.09188 (39)	85.233 (63)	0.074	3.8546 (29)
20.09239 (39)	85.122 (65)	0.076	3.8496 (30)
20.09290 (39)	85.029 (64)	0.075	3.8454 (29)
20.09336 (39)	84.966 (62)	0.073	3.8426 (29)
20.09386 (39)	84.973 (62)	0.073	3.8430 (29)
. . .			
40.5598 (26)	12.4559 (32)	0.026	1.10821 (30)
41.0614 (28)	12.0437 (22)	0.018	1.08396 (21)
41.5630 (29)	11.6535 (29)	0.025	1.06082 (28)

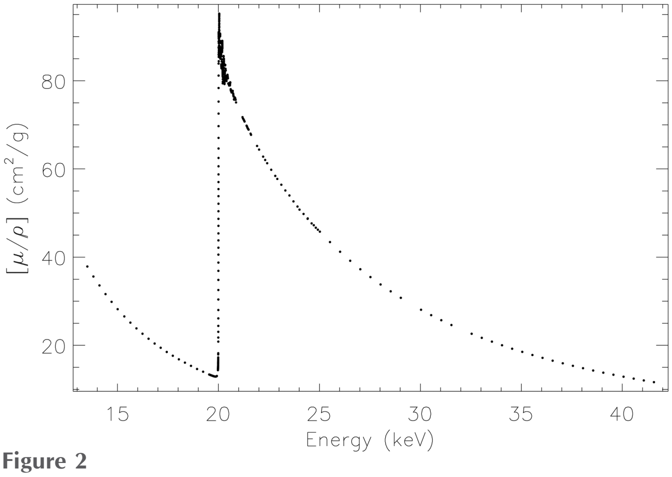

Figure 2

Molybdenum foil mass attenuation coefficients, 13.5–41.5 keV. Reprinted with permission from de Jonge *et al.* (2005). Copyright (2005) by the American Physical Society.

determined from the weighted mean of the measurements made with a variety of apertures and foil thicknesses, and using the values determined from the counts recorded in both of the downstream ion chambers. The weighted mean typically involved between 18 and 30 determinations. The uncertainty in the mass attenuation coefficient was evaluated from $\sigma_{\rm se}$. The imaginary component of the atomic form factor f'' was evaluated using equation (3). $[\mu/\rho]_{\rm pe}$ was evaluated by subtracting the average of the Rayleigh plus Compton contributions, as tabulated in XCOM (Scofield, 1973; Berger & Hubbell, 1987; Gerward *et al.*, 2004) and FFAST (Chantler, 1995, 2000; Chantler *et al.*, 2000).

In parentheses following the reported values are the uncertainties in f'', evaluated from

$$\sigma_{f''} = \frac{EuA}{2hcr_e}(\sigma^2_{[\mu/\rho]} + \Delta^2_{\rm RC})^{\frac{1}{2}}, \tag{4}$$

which includes an uncertainty contribution of half of the difference $\Delta_{\rm RC}$ between the tabulated values of the Rayleigh plus Compton contributions. The use of the photoelectric component of the attenuation determined in this manner is appropriate when Rayleigh and Compton scattering are the only significant other contributions to the total attenuation. This is the case apart from near the absorption edge and in the region of the XAFS. Near the edge, the influence of solid-state and bonding effects is difficult to evaluate or estimate. Values of f'' in the energy range from 19.9–20.9 keV should be subject to a further uncertainty (hence correction) of the same order as the XAFS amplitude when alternative atomic environments are investigated. The mass attenuation coefficient can be written as a sum of the photoelectric absorption $[\mu/\rho]_{\rm pe}$, Rayleigh scattering $[\mu/\rho]_{\rm R}$ and Compton scattering $[\mu/\rho]_{\rm C}$ according to

$$\left[\frac{\mu}{\rho}\right] \simeq \left[\frac{\mu}{\rho}\right]_{\rm pe} + \left[\frac{\mu}{\rho}\right]_{\rm R} + \left[\frac{\mu}{\rho}\right]_{\rm C}. \tag{5}$$

Further attenuating processes are negligible in the energy region of this experiment. The results of atomic form factor calculations can be assessed by comparing the calculated photoelectric absorption coefficients with the measured values. The authors estimated the Rayleigh plus Compton cross section to be equal to the average of the values reported by the FFAST and XCOM tabulations, and estimated the uncertainty in the Rayleigh plus Compton cross section to be half of the difference between these tabulations. They subtracted these scattering components from the measured values to determine the photoelectric absorption coefficients.

The information deposited with the original publication consisted of two text files: a README file representing header information, as required for portability to *iFEFFit*, *eFEFFit* or CIF formats (available in the supporting information for this present chapter as file bz5029sup4.txt); and the actual tabulation of data (file bz5029sup5.txt). In the interests of a compact notation for ease of use by other researchers, there were only four columns of data, but with uncertainties in the last significant figures of three of these given in parentheses (as is conventional). It is clearly important to report the evaluated mass attenuation coefficient (column 2 in Table 9), yet in much XAFS work the mass absorption coefficient is a more relevant quantity. This can be obtained from the fourth

Table 10
Uncertainty contributions to the data in Table 9 for molybdenum foils, 13.5–41.5 keV (de Jonge *et al.*, 2005).

Quantity	Estimated magnitude	Contributions and comments
$[\mu/\rho]$ away from the absorption edge	0.028%	Accuracy limited by the full-foil mapping technique
	0.02–0.15%	Precision, limited by counting statistics and foil replacement errors
	<0.03%	Unidentified systematic component: one quarter of correction
$[\mu/\rho]$ near the absorption edge (19.99–21 keV)	0.01–0.06%	X-ray bandwidth
	0.003–0.006%	Sample roughness
	<0.01%	Harmonic components
	0.005–0.01%	Secondary photons
Total accuracy near edge	0.03–0.1%	
E	0.0015–0.007%	Accuracy of monochromator dispersion function interpolation
f''	0.2–0.5%	Inconsistency of subtracted scattering components

column, f'', which represents the photoabsorption. Another potential deficiency of these data was the absence of the relative uncertainty versus the total absolute uncertainty of the mass attenuation coefficient. Often it is more useful to use the relative quantity in, for example, fitting of XAFS, as it separates independent point errors (uncertainties) from overall scaling or normalization uncertainties. This format is compact and in ASCII, but the use of parentheses for uncertainties does make the processing of the raw data for fitting by other researchers slightly more complicated. The separation of the header from the deposited spectrum also means that the two files could become separated or one could be lost, perhaps especially without direct connection to the details in the published manuscript.

Table 10 presents estimates of contributions of the individual errors to the reported values. One significant concern was the comparison of inflection points versus Bragg diffraction for the determination of energy. The accuracy of the energy determination can be assessed by comparing the absorption edge energy with the most accurate value in the literature. The first point of inflection of the mass attenuation coefficient on the absorption edge occurs at 19.9944 ± 0.0002 ± 0.0003 keV, where the first uncertainty reflects the ability to locate the position of the point of inflection and the second is the uncertainty in determining the energy. Comparison with the value reported by Kraft *et al.* (1996), 20.00036 ± 0.00002 keV, indicates a discrepancy of 6 eV, or 0.03%. The most likely causes of this discrepancy are a difference in the interpretation of the absorption-edge location, chemical or thermal effects on the edge location, or further errors in the energy determination. de Jonge *et al.* (2005) considered an upper limit on the accuracy of the determined energies to be half of the difference between these absorption-edge locations, at about 0.015%.

As it stands, this implies agreement with FFAST to within a quoted uncertainty of 1% well above the edge, and 3–5% near the edge, and a confirmation of the triangle effect of magnitude 3–5% around the edge. Conversely, it suggests FFAST (Chantler, 1995, 2000) is significantly more accurate than XCOM (Berger & Hubbell, 1987; Berger *et al.*, 1999) and Henke *et al.* (1993). This work also led to further investigations and publications on bandwidth, the integrated column density, and especially investigation of standard theoretical approaches and anomalies in theoretical broadening (Smale *et al.*, 2006), advanced investigations of beamline-independent spectra and structure (Glover & Chantler, 2007), advanced investigations of theory using *FDMX*, and the development of experimental investigations of inelastic mean free paths of the photoelectron and plasmons (Chantler & Bourke, 2010, 2014*b*,*c*; Bourke & Chantler, 2015; Chantler & Bourke, 2019). It also led to detailed investigations of theory with the program *FEFF* (Kas *et al.*, 2010).

9. Tin foils, 29–60 keV. XAS, XAFS, bonding, nanostructure and theory

The work of de Jonge *et al.* (2007) was unique in that for this single experiment the team implemented the energy calibration for the setup *in situ* and also installed a unique four-bounce monochromator particularly for the higher energies. This was a credit to these researchers and the beamline staff. The Sn foil thicknesses were nominally 25 µm, 50 µm, 100 µm, 150 µm, 200 µm, 250 µm and 500 µm. Sample thicknesses spanned the range of attenuation $(0.1–0.9) \leq [\mu/\rho] \leq (2–7.5)$ across the wide range of energies. Accuracies were 0.04–3%, and typically in the range 0.1–0.2%. This was used as a test case for new theory (Bourke *et al.*, 2016*a*).

The X-ray energy was selected by tuning the upstream monochromator crystal so that the X-rays reflected from the (444) planes of silicon were of the desired energy. When this is done, X-rays of all allowed harmonic energies are also transmitted into the beam. Unwanted harmonic energies are then removed by reflecting this partially monochromated beam from the (333) planes of a second, downstream silicon crystal. The downstream channel-cut monochromator crystal was tuned to optimize the reflected X-ray intensity by scanning it through a small range of angles about the Bragg angle corresponding to the (333) planes. The peak intensity was identified from the scan, and the crystal was then set at the angle corresponding to the peak intensity.

Table 11 presents some of the data that were collected at 293 energies across and above the *K* edge of Sn (Fig. 3). The full data set is available as supporting information to this chapter as file bz5029sup6.pdf. The calibrated photon energy

Table 11

Tin metal foils, 29–60 keV: mass attenuation coefficients $[\mu/\rho]$ and the imaginary component of the atomic form factor f'', with one standard error uncertainties in the least significant digits indicated in parentheses.

The percentage uncertainty in the mass attenuation coefficients, $\sigma_{[\mu/\rho]}$, is also given. Uncertainty in f'' includes the measurement uncertainty and the difference between major tabulations of the total Rayleigh plus Compton scattering cross sections. f'' in the energy range 29.1–30 keV is affected by solid-state effects. (Some rows of values have been omitted for brevity. The full version is available in the supporting information.)

E (keV)	$[\mu/\rho]$ (cm^2 g^{-1})	$\sigma_{[\mu/\rho]}$ (%)	f'' (e atom^{-1})
29.00351 (92)	7.8285 (97)	0.12	0.5740 (23)
29.02351 (92)	7.856 (68)	0.86	0.5767 (59)
29.04350 (92)	7.859 (56)	0.71	0.5774 (51)
29.06348 (92)	7.877 (19)	0.24	0.5794 (27)
29.08347 (92)	7.915 (59)	0.75	0.5829 (53)
29.10345 (92)	8.018 (46)	0.57	0.5918 (43)
29.12345 (92)	8.167 (28)	0.34	0.6045 (31)
29.13344 (92)	8.288 (22)	0.27	0.6147 (28)
29.14344 (92)	8.416 (89)	1.1	0.6254 (76)
29.15342 (92)	8.627 (83)	0.96	0.6431 (72)
29.16341 (92)	9.004 (78)	0.87	0.6743 (68)
29.16442 (92)	9.2723 (97)	0.10	0.6964 (23)
29.16542 (92)	9.395 (76)	0.81	0.7065 (66)
29.16642 (92)	9.422 (75)	0.80	0.7088 (65)
29.16742 (92)	9.526 (75)	0.78	0.7174 (65)
29.16841 (92)	9.586 (74)	0.77	0.7223 (65)
29.16942 (92)	9.704 (74)	0.76	0.7321 (64)
29.17041 (92)	9.758 (73)	0.75	0.7365 (64)
29.17142 (92)	9.868 (73)	0.74	0.7456 (64)
29.17241 (92)	9.991 (13)	0.13	0.7558 (24)
29.17342 (92)	10.109 (72)	0.71	0.7655 (63)
29.17541 (92)	10.395 (71)	0.68	0.7891 (62)
29.17641 (92)	10.568 (70)	0.66	0.8034 (62)
29.17741 (92)	10.776 (70)	0.65	0.8206 (61)
29.18041 (92)	11.481 (14)	0.12	0.8787 (24)
29.18241 (92)	12.079 (69)	0.57	0.9280 (61)
29.18340 (92)	12.476 (68)	0.54	0.9607 (60)
29.18441 (92)	12.887 (68)	0.53	0.9945 (60)
29.18540 (92)	13.413 (67)	0.50	1.0379 (59)
29.18640 (92)	14.041 (66)	0.47	1.0896 (59)
29.18741 (92)	14.762 (67)	0.45	1.1491 (59)
29.18840 (92)	15.803 (18)	0.12	1.2349 (26)
29.18941 (92)	16.711 (66)	0.39	1.3096 (58)
29.19040 (92)	18.226 (65)	0.36	1.4344 (58)
29.19140 (92)	20.067 (65)	0.32	1.5861 (58)
29.19241 (92)	22.202 (65)	0.29	1.7620 (58)
29.19340 (92)	24.943 (65)	0.26	1.9878 (58)
29.19440 (92)	28.765 (65)	0.23	2.3026 (58)
29.19540 (92)	33.208 (67)	0.20	2.6687 (59)
29.19640 (92)	38.36 (11)	0.28	3.0930 (92)
29.19740 (92)	43.214 (70)	0.16	3.4930 (61)
29.19839 (92)	47.893 (70)	0.15	3.8785 (62)
29.19940 (92)	51.164 (72)	0.14	4.1481 (63)
29.20040 (92)	53.026 (80)	0.15	4.3016 (69)
29.20139 (92)	53.771 (84)	0.16	4.3632 (73)
29.20240 (92)	53.433 (76)	0.14	4.3354 (66)
29.20340 (92)	52.616 (76)	0.14	4.2683 (66)
29.20439 (92)	51.020 (78)	0.15	4.1369 (67)
29.20839 (92)	47.343 (72)	0.15	3.8346 (63)
29.20939 (92)	46.753 (73)	0.16	3.7861 (64)
29.21039 (92)	46.190 (67)	0.15	3.7398 (59)
29.21139 (92)	45.895 (69)	0.15	3.7156 (61)
29.21239 (92)	45.567 (43)	0.095	3.6888 (41)
29.21339 (92)	45.626 (71)	0.16	3.6937 (62)
29.21439 (92)	45.678 (66)	0.14	3.6982 (58)
29.21539 (92)	45.829 (67)	0.15	3.7107 (59)
29.21739 (92)	46.352 (71)	0.15	3.7541 (62)
29.21839 (92)	46.528 (65)	0.14	3.7687 (58)
29.21939 (92)	46.725 (68)	0.14	3.7851 (60)
29.22038 (92)	46.754 (54)	0.12	3.7876 (49)
29.22238 (92)	46.994 (66)	0.14	3.8077 (58)
29.22338 (92)	46.987 (66)	0.14	3.8072 (59)
29.22438 (92)	46.748 (62)	0.13	3.7876 (56)
29.22639 (92)	46.641 (64)	0.14	3.7791 (57)
29.22738 (92)	46.402 (66)	0.14	3.7595 (58)
29.22838 (92)	45.891 (54)	0.12	3.7175 (49)
29.23038 (92)	45.443 (65)	0.14	3.6808 (58)
29.23138 (92)	45.199 (64)	0.14	3.6609 (57)
29.23238 (92)	45.095 (64)	0.14	3.6524 (57)
29.23338 (92)	45.026 (63)	0.14	3.6469 (56)
29.23438 (92)	45.092 (63)	0.14	3.6524 (56)
29.23538 (92)	45.311 (65)	0.14	3.6706 (58)
29.23638 (92)	45.439 (42)	0.092	3.6813 (41)
29.23738 (92)	45.708 (64)	0.14	3.7036 (57)
29.23837 (92)	45.938 (63)	0.14	3.7227 (56)
29.23938 (92)	46.161 (63)	0.14	3.7412 (56)
29.24037 (92)	46.349 (63)	0.14	3.7569 (56)
29.24137 (92)	46.617 (64)	0.14	3.7791 (57)
29.24237 (92)	46.839 (64)	0.14	3.7976 (57)
29.24337 (92)	47.037 (63)	0.13	3.8140 (56)
29.24437 (92)	47.267 (32)	0.067	3.8331 (34)
29.24537 (92)	47.532 (64)	0.13	3.8551 (57)
29.24636 (92)	47.741 (64)	0.13	3.8725 (57)
29.24736 (92)	47.879 (63)	0.13	3.8840 (56)
29.24837 (92)	48.022 (64)	0.13	3.8959 (57)
29.24936 (92)	48.097 (65)	0.13	3.9022 (58)
29.25037 (92)	48.133 (65)	0.13	3.9053 (57)
29.25137 (92)	47.982 (64)	0.13	3.8930 (57)
29.25237 (92)	47.749 (88)	0.18	3.8739 (76)
29.25337 (92)	47.721 (64)	0.13	3.8718 (57)
29.25436 (92)	47.512 (65)	0.14	3.8547 (58)
29.25536 (92)	47.169 (65)	0.14	3.8265 (58)
29.25636 (92)	46.988 (65)	0.14	3.8117 (58)
29.25736 (92)	46.739 (66)	0.14	3.7912 (58)
29.25836 (92)	46.464 (66)	0.14	3.7687 (59)
29.25936 (92)	46.223 (65)	0.14	3.7489 (58)
29.26035 (92)	45.859 (61)	0.13	3.7190 (55)
29.26136 (92)	45.773 (66)	0.14	3.7121 (58)
29.26236 (92)	45.616 (67)	0.15	3.6992 (60)
29.26336 (92)	45.399 (66)	0.15	3.6815 (58)
29.26436 (92)	45.365 (67)	0.15	3.6788 (59)
29.26535 (92)	45.262 (68)	0.15	3.6704 (60)
29.26636 (92)	45.262 (68)	0.15	3.6705 (60)
29.26736 (92)	45.303 (70)	0.15	3.6740 (61)
29.26836 (92)	45.254 (44)	0.098	3.6701 (42)
29.26935 (92)	45.364 (69)	0.15	3.6793 (61)
29.27035 (92)	45.516 (70)	0.15	3.6920 (61)
29.27135 (92)	45.646 (73)	0.16	3.7029 (64)
29.27236 (92)	45.790 (70)	0.15	3.7149 (62)
29.27335 (92)	45.994 (71)	0.15	3.7318 (62)
29.27435 (92)	46.218 (74)	0.16	3.7505 (65)
29.27535 (92)	46.485 (76)	0.16	3.7727 (66)
29.27635 (92)	46.643 (20)	0.043	3.7859 (27)
29.27735 (92)	46.874 (77)	0.16	3.8050 (67)
29.27934 (92)	47.113 (73)	0.15	3.8251 (64)
29.28335 (92)	47.631 (75)	0.16	3.8684 (66)
29.28435 (92)	47.53 (10)	0.21	3.8599 (85)
29.28534 (92)	47.498 (76)	0.16	3.8577 (67)
29.28734 (92)	47.425 (78)	0.16	3.8519 (68)
29.29134 (92)	47.012 (80)	0.17	3.8184 (70)
29.29234 (92)	46.776 (54)	0.11	3.7989 (49)
29.29334 (92)	46.715 (81)	0.17	3.7941 (70)
29.29434 (92)	46.681 (82)	0.18	3.7914 (71)
29.29534 (92)	46.595 (82)	0.18	3.7844 (71)
29.29634 (92)	46.604 (85)	0.18	3.7852 (74)
29.29734 (92)	46.434 (84)	0.18	3.7713 (73)
29.29833 (92)	46.417 (83)	0.18	3.7701 (72)
29.29934 (92)	46.379 (84)	0.18	3.7671 (73)
29.30033 (92)	46.236 (39)	0.085	3.7553 (39)
29.30134 (92)	46.257 (86)	0.19	3.7572 (74)
. . .			
58.6641 (31)	7.01 (20)	2.9	1.102 (34)
59.3636 (33)	6.814 (66)	0.97	1.084 (12)
60.0632 (34)	6.558 (96)	1.5	1.054 (17)

Table 12
Tin metal foils, 29–60 keV: error contributions.

Quantity	Estimated magnitude	Contributions and comments
$[\mu/\rho]$ away from the absorption edge	0.04%	Accuracy limited by the full-foil mapping technique
	<3%	Precision, limited by counting statistics
	<0.03%	Incorrectly estimated dark current
$[\mu/\rho]$ near the absorption edge (29.15–30 keV)	<0.01%	X-ray bandwidth
E	0.003–0.007%	Monochromator dispersion function interpolation
f''	0–0.2–0.4%	Inconsistency of subtracted scattering components

(in keV) is followed by the uncertainty in the last significant figures presented in parentheses. The mass attenuation coefficient $[\mu/\rho]$ (in cm^2 g^{-1}) is similarly given with its uncertainty. The third column is the percentage uncertainty in the mass attenuation coefficient. The second and third columns are determined from the weighted mean of the measurements made with a variety of apertures and foil thicknesses. The weighted mean typically involved about ten individual measurements, and hence if each had similar statistical quality and consistency, the precision of the pooled result could be reduced by just over a factor of three. At a number of energies in the XAFS region only one measurement is used for efficiency, and these naturally have larger uncertainties. The uncertainty in the mass attenuation coefficient was generally evaluated from $\sigma_{\rm sd}$ defined in equations A2 and A3 of the article by de Jonge *et al.* (2007).

The imaginary component of the atomic form factor f'' was evaluated from equation (3) and $[\mu/\rho]_{\rm pe}$ has been evaluated by subtracting the average of the Rayleigh plus Compton contribution as tabulated in XCOM (Scofield, 1973; Berger & Hubbell, 1987; Gerward *et al.*, 2004) and FFAST (Chantler, 1995, 2000; Chantler *et al.*, 2000). In parentheses following the reported values are uncertainties in f'', evaluated from equation (4), which include an uncertainty contribution of half of the difference $\Delta_{\rm RC}$ between the two tabulated values of the Rayleigh plus Compton contribution.

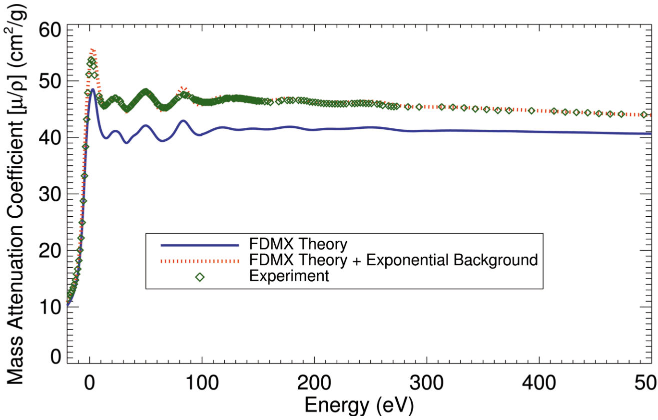

Figure 3
Tin, 29–60 keV. XAFS measured with high absolute accuracy (de Jonge *et al.*, 2007) (green diamonds), where the energy is given as $E - E_0$ above the absorption edge with E_0 = 29.195 keV (see the original paper for the full spectrum), compared with predicted values from the *FDMX* package with default physical parameters (solid blue line) and with an added exponential background function (dotted red line) (Bourke *et al.*, 2016*a*).

The use of the photoelectric component of the attenuation determined in this manner is appropriate when Rayleigh and Compton scattering are the only significant other contributions to the total attenuation. This is certainly the case in the energy range covered by this experiment apart from near the absorption edge and in the region of the XAFS. In these regions the influence of solid-state and bonding effects is naturally substantial. Table 12 presents estimates of the individual error contributions to the reported values.

10. Copper foils revisited, 5–20 keV. XAS, XAFS, bonding, portability and theory

Glover *et al.* (2008) attempted to test the beamline independence of earlier copper metal foil measurements of XAS and also attempted to investigate the XAFS structure directly. A total of 108 data points were collected across, above and below the *K* edge compared with the previous best synchrotron data set, which had 84 points across the energy range 8.9–20 keV. Samples of nominal thicknesses of 5 µm, 10 µm, 15 µm, 30 µm and 100 µm were used with three samples for every measured energy, as given in Table 13. The measurements are accurate to between 0.09% and 4.5%, with most measurements being accurate to better than 0.12%. A key systematic error due to monochromator drift during the measurements was characterized accurately. This enabled development of advanced theory of XAFS (Bourke & Chantler, 2010*a*), the development of the field of extracting photoelectron inelastic mean free paths from XAFS data sets (Bourke & Chantler, 2010*b*) and development of the theory of the inelastic mean free path of electrons (IMFP theory) (Bourke & Chantler, 2012; Chantler & Bourke, 2014*a*). It also allowed detailed exploration of developments of XAS theory (Kas *et al.*, 2010).

Table 13
Nominal thicknesses of copper metal foils for 5–20 keV study.

The samples were changed at 16 keV, 8.5 keV, 8 keV and 6 keV. Samples where $[\rho t]$ was determined using the full-foil mapping technique are indicated in bold.

	Sample		
Energy range (keV)	Position 1	Position 2	Position 3
20–18	**100** µm (sample a)	**100** µm (sample b)	30 µm
18–16	**100** µm (sample a)	10 µm	30 µm
16–8.5	15 µm	10 µm	5 µm
8.5–8	15 µm	**100** µm (sample b)	5 µm
8–6	15 µm	10 µm	30 µm
6–5	15 µm	10 µm	5 µm

Table 14

Copper metal foils, 5–20 keV: mass attenuation coefficients and form factors at 108 energies, with one standard deviation uncertainties in the least significant digit(s) given in parentheses.

f'' values between 8.95 keV and 9.5 keV are affected by solid-state effects.

E (keV)	$[\mu/\rho]$ (cm^2 g^{-1})	$\sigma_{[\mu/\rho]}$ (%)	f'' (e atom^{-1})
5.0053 (6)	193.5 (3)	0.136	1.440 (2)
5.1060 (6)	182.97 (19)	0.106	1.3883 (15)
5.2063 (6)	173.10 (18)	0.101	1.3383 (14)
5.3069 (6)	164.00 (16)	0.095	1.2916 (13)
5.4073 (6)	155.57 (15)	0.095	1.2475 (12)
5.5079 (6)	147.69 (14)	0.095	1.2055 (12)
5.6085 (6)	140.24 (14)	0.100	1.1648 (12)
5.7089 (6)	133.47 (13)	0.099	1.1276 (12)
5.8096 (6)	127.08 (14)	0.112	1.0917 (13)
5.9100 (6)	121.13 (14)	0.112	1.0578 (12)
6.0105 (6)	115.76 (11)	0.093	1.0274 (10)
6.1111 (6)	110.77 (11)	0.094	0.9989 (10)
6.2114 (6)	106.16 (11)	0.100	0.9724 (10)
6.3117 (5)	101.41 (10)	0.094	0.9432 (9)
6.4123 (5)	96.95 (9)	0.095	0.9153 (9)
6.5128 (5)	92.62 (9)	0.096	0.8874 (9)
6.6130 (5)	88.52 (8)	0.094	0.8605 (9)
6.7136 (5)	84.83 (9)	0.109	0.8365 (10)
6.8142 (5)	81.23 (9)	0.108	0.8122 (10)
6.9148 (5)	78.46 (8)	0.106	0.7957 (10)
7.0151 (5)	74.78 (7)	0.098	0.7685 (9)
7.1156 (5)	71.80 (7)	0.096	0.7478 (8)
7.2160 (5)	68.98 (7)	0.094	0.7280 (8)
7.3168 (5)	66.32 (7)	0.098	0.7090 (8)
7.4171 (5)	63.77 (7)	0.105	0.6906 (8)
7.5174 (5)	61.30 (6)	0.095	0.6721 (8)
7.6180 (5)	59.04 (7)	0.110	0.6555 (9)
7.7184 (5)	56.89 (6)	0.105	0.6394 (8)
7.8190 (5)	54.80 (5)	0.098	0.6233 (8)
7.9195 (5)	52.78 (5)	0.097	0.6075 (8)
8.0200 (4)	50.95 (5)	0.100	0.5933 (8)
8.1204 (4)	49.18 (5)	0.106	0.5794 (8)
8.2212 (4)	47.48 (5)	0.098	0.5658 (8)
8.3215 (4)	45.90 (4)	0.097	0.5531 (7)
8.4222 (4)	44.38 (4)	0.101	0.5407 (8)
8.5220 (4)	42.95 (4)	0.097	0.5289 (8)
8.6226 (4)	41.50 (4)	0.104	0.5166 (8)
8.7231 (4)	40.10 (5)	0.122	0.5045 (9)
8.8236 (4)	38.76 (4)	0.109	0.4928 (8)
8.9229 (4)	37.91 (4)	0.104	0.4870 (8)
8.9431 (4)	38.06 (10)	0.268	0.4902 (15)
8.9529 (4)	38.32 (11)	0.277	0.4944 (16)
8.9578 (4)	38.61 (10)	0.258	0.4985 (15)
8.9629 (4)	39.04 (13)	0.331	0.5046 (19)
8.9680 (4)	39.9 (2)	0.517	0.517 (3)
8.9732 (4)	41.5 (5)	1.297	0.539 (7)
8.9782 (4)	58.6 (7)	1.218	0.771 (10)
8.9830 (4)	157.2 (5)	0.340	2.108 (7)
8.9880 (4)	193.2 (7)	0.378	2.598 (10)
8.9930 (4)	282.3 (5)	0.165	3.810 (6)
8.9981 (4)	293.6 (7)	0.232	3.966 (9)
9.0032 (4)	311.0 (5)	0.171	4.204 (7)
9.0084 (4)	291.7 (6)	0.189	3.944 (8)
9.0134 (4)	276.6 (5)	0.187	3.741 (7)
9.0183 (4)	288.7 (5)	0.178	3.908 (7)
9.0232 (4)	309.3 (4)	0.116	4.190 (5)
9.0283 (4)	315.4 (5)	0.155	4.277 (7)
9.0332 (4)	295.2 (4)	0.139	4.003 (6)
9.0384 (4)	287.3 (3)	0.120	3.898 (5)
9.0436 (4)	291.0 (3)	0.102	3.951 (4)
9.0486 (4)	291.9 (3)	0.119	3.965 (5)
9.0537 (4)	296.0 (4)	0.129	4.024 (5)
9.0635 (5)	306.2 (5)	0.151	4.167 (6)
9.0735 (5)	318.0 (5)	0.161	4.334 (7)
9.0836 (5)	298.3 (4)	0.149	4.068 (6)
9.0935 (5)	285.3 (3)	0.114	3.894 (5)
9.1034 (5)	279.7 (4)	0.144	3.822 (6)
9.1138 (5)	294.4 (4)	0.132	4.028 (5)
9.1237 (5)	299.0 (4)	0.146	4.095 (6)
9.1334 (5)	317.7 (5)	0.150	4.359 (7)
9.1438 (5)	306.7 (5)	0.165	4.212 (7)
9.1539 (5)	279.8 (5)	0.181	3.844 (7)
9.1638 (5)	271.3 (5)	0.168	3.730 (6)
9.1738 (5)	289.9 (3)	0.110	3.992 (4)
9.1841 (5)	290.8 (3)	0.112	4.009 (5)
9.1941 (5)	288.2 (4)	0.125	3.978 (5)
9.2038 (5)	291.8 (4)	0.122	4.031 (5)
9.2140 (5)	298.8 (4)	0.146	4.134 (6)
9.2241 (5)	291.1 (5)	0.160	4.031 (7)
9.2340 (4)	278.3 (3)	0.094	3.858 (4)
9.2440 (5)	274.5 (3)	0.106	3.808 (4)
9.2541 (5)	275.6 (3)	0.113	3.828 (4)
9.2643 (5)	277.3 (3)	0.122	3.855 (5)
9.2742 (5)	280.1 (3)	0.117	3.899 (5)
9.2842 (5)	281.5 (3)	0.104	3.923 (4)
9.2945 (5)	282.5 (3)	0.110	3.941 (4)
9.3045 (5)	280.9 (4)	0.150	3.923 (6)
9.3144 (5)	276.1 (3)	0.120	3.860 (5)
9.3251 (5)	272.7 (3)	0.101	3.816 (4)
9.3758 (4)	269.1 (2)	0.091	3.786 (4)
9.4257 (4)	263.2 (2)	0.093	3.723 (4)
9.4758 (4)	257.8 (2)	0.092	3.665 (3)
9.5268 (4)	255.4 (3)	0.099	3.651 (4)
9.6267 (4)	246.6 (3)	0.126	3.561 (5)
9.7275 (4)	238.5 (2)	0.092	3.480 (3)
9.8279 (4)	231.8 (2)	0.093	3.417 (3)
9.9282 (4)	225.3 (2)	0.091	3.353 (3)
10.0284 (3)	219.0 (2)	0.094	3.294 (3)
11.0334 (3)	168 (6)	3.417	2.78 (10)
12.0385 (3)	131 (6)	4.384	2.36 (10)
13.0442 (3)	108.00 (10)	0.096	2.104 (2)
14.0496 (3)	88.42 (9)	0.100	1.853 (2)
15.0559 (3)	73.42 (7)	0.098	1.6466 (18)
16.0619 (4)	61.60 (6)	0.093	1.4715 (16)
17.0699 (4)	52.20 (5)	0.093	1.3233 (15)
18.0768 (5)	44.69 (4)	0.094	1.1977 (13)
19.0836 (5)	38.51 (4)	0.099	1.0878 (12)
20.0885 (6)	33.45 (3)	0.092	0.9927 (10)

The imaginary component of the form factor quantifies the photoelectric absorption of a material. Photoelectric absorption is the dominant contributor to the X-ray mass attenuation coefficient for copper for the energies in Table 14, with scattering contributing less than 5%. The photoelectric mass absorption was calculated from the measured total mass attenuation coefficient by subtracting the contribution to the attenuation from Rayleigh and Compton scattering. The scattering contribution was calculated by taking the average of the FFAST (Chantler, 2000) and XCOM (Berger & Hubbell, 1987) tabulations of the Rayleigh plus Compton attenuation coefficient with the uncertainty assumed to be the difference between the two tabulations divided by $\sqrt{2}$. The scattering uncertainty contributed between 0.05% and 0.13% to the photoelectric absorption and is only significant in the region just below the edge. The imaginary component of the atomic form factor f'' was calculated using equation (3).

This study used samples of metallic (solid-state) copper, but these gave an excellent approximation to the atomic values outside the edge regions. The equivalence of the solid-state and atomic mass attenuation coefficients outside the edge and XAFS regions has been suggested and illustrated for

Table 15
Copper metal foils, 5–20 keV: uncertainty contributions to the mass attenuation coefficient, imaginary component of the form factor and energy.

Quantity	Uncertainty	Comment
$[\mu/\rho]$	0.092%	Accuracy of the full-foil mapping
	<0.11%	5.0–5.3 keV due to harmonics
	<1.4%	Uncertainty due to energy drift in the edge and XAFS region
	4%	At 11 and 12 keV due to detector saturation
f''	0.09–4.5%	Contribution from $[\mu/\rho]$
	<0.15%	Scattering contribution uncertainty, largest just below edge
E	0.3–0.6 eV	Accuracy limited by powder diffraction determination
	<0.15 eV	Energy drift uncertainty between 8 keV and 10 keV

cadmium (Kodre *et al.*, 2006). Therefore, this measurement of the form factor approximates the atomic form factor of copper, except at the edge and in the XAFS region between 8.9 keV and 9.5 keV where solid-state effects are dominant.

Measurements of the mass attenuation coefficient prove useful for XAFS and as a standard XAFS spectrum. XAFS analysis does not require absolute measurements of the mass attenuation coefficient; for current modelling it conventionally requires high-accuracy relative measurements. Therefore the uncertainty due to the absolute thickness determination (0.092%) can be subtracted from the total uncertainty when the data from Table 14 are used in XAFS analyses. The uncertainty in the mass attenuation coefficient was dominated by the contribution due to the absolute calibration, so subtracting this reduces the uncertainty greatly. The data are available as supporting information to this chapter as file bz5029sup7.pdf.

A particular success of this work was the proof of consistency within uncertainty to the earlier extensive XAS measurement, proving that stability and accuracy can be correctly measured and consistently determined. This was not a full proof of beamline portability and transferability but was a very welcome demonstration. Another useful development was the identification of effective harmonic contributions versus relative harmonic probability, its measurement and the determination of its impact (Glover & Chantler, 2009).

Table 14 gives the calibrated X-ray energy in keV with the uncertainty in the last significant digit(s) given in parentheses. The second column gives the value of the mass attenuation coefficient in cm^2 g^{-1} with the uncertainty in parentheses. Column three gives the uncertainty in the mass attenuation coefficient as a percentage of its value. The fourth column lists the imaginary component of the form factor along with its uncertainty in parentheses. Table 15 gives a breakdown of the contributions to the uncertainty of the energy, mass attenuation coefficient and imaginary component of the form factor.

11. Zinc foils, 7.2–15.2 keV. XAS, accuracy and relative (XAFS) accuracy

Rae *et al.* (2010*a*) reported a short XAS spectrum with a very large grid spacing and no XAFS. This had only 19 energy points across the energy range with an absolute accuracy of between 0.044% and 0.197%. This was the most accurate determination of any attenuation coefficient on a bending-magnet beamline at that time and reduced the absolute uncertainty by a factor of 3 compared with earlier work by

Table 16
Zinc metal foils, 7.2–15.2 keV (Rae *et al.*, 2010*a*): mass attenuation coefficients $[\mu/\rho]$ and the imaginary component of the form factor, f'', with one standard deviation uncertainties in parentheses.

The relative absolute accuracy of the mass attenuation coefficient $\sigma_{[\mu/\rho]_{\rm rel}}$ and the percentage (absolute) accuracy $\sigma_{[\mu/\rho]}$ are given. The (photoelectric) mass absorption coefficient $[\mu/\rho]_{\rm pe}$ is derived by subtracting the mass attenuation due to Raleigh and Compton scattering $[\mu/\rho]_{\rm R+C}$ from the total mass attenuation coefficient, to derive the form factor f''. The uncertainty in $[\mu/\rho]_{\rm R+C}$ estimated by half the discrepancy between tabulations in XCOM and FFAST is included in the uncertainty of f''.

E (keV)	$[\mu/\rho]$ (cm^2 g^{-1})	$\sigma_{[\mu/\rho]_{\rm rel}}$ (% relative)	$\sigma_{[\mu/\rho]}$ (% absolute)	$[\mu/\rho]_{\rm pe}$ (cm^2 g^{-1})	$[\mu/\rho]_{\rm R+C}$ (cm^2 g^{-1})	f'' (e atom^{-1})
15.2255 (12)	78.397 (41)	0.029	0.053	77.335 (97)	1.062 (71)	1.83 (12)
14.6257 (11)	87.284 (57)	0.049	0.066	86.172 (84)	1.111 (66)	1.95 (11)
14.0222 (11)	97.767 (67)	0.053	0.069	96.601 (67)	1.165 (56)	2.10 (10)
13.4208 (10)	109.924 (62)	0.035	0.056	108.6997 (41)	1.224 (49)	2.267 (92)
12.8180 (11)	124.249 (64)	0.026	0.051	122.9607 (90)	1.288 (45)	2.449 (86)
12.4176 (11)	135.243 (85)	0.045	0.063	133.9091 (33)	1.334 (43)	2.584 (84)
12.0148 (12)	147.907 (71)	0.019	0.048	146.5242 (73)	1.383 (43)	2.736 (86)
11.6143 (13)	161.699 (77)	0.017	0.047	160.2643 (92)	1.434 (45)	2.893 (91)
11.2139 (14)	177.92 (11)	0.050	0.067	176.4381 (81)	1.489 (48)	3.07 (10)
10.8124 (15)	195.946 (87)	0.006	0.044	194.3975 (63)	1.548 (53)	3.26 (11)
10.4116 (16)	218.12 (30)	0.130	0.138	216.5165 (83)	1.611 (60)	3.50 (13)
10.0108 (18)	247.32 (34)	0.133	0.141	245.6427 (16)	1.678 (70)	3.82 (15)
9.6098 (19)	34.826 (30)	0.075	0.087	33.075 (26)	1.750 (64)	0.494 (18)
9.2089 (20)	38.848 (31)	0.068	0.081	37.020 (48)	1.827 (57)	0.529 (16)
8.8081 (21)	44.102 (87)	0.192	0.197	42.192 (02)	1.910 (52)	0.577 (16)
8.4069 (23)	50.290 (31)	0.042	0.061	48.290 (90)	1.999 (51)	0.631 (16)
8.0065 (24)	57.711 (72)	0.117	0.126	55.615 (11)	2.095 (53)	0.692 (17)
7.6056 (26)	66.672 (43)	0.047	0.064	64.473 (72)	2.199 (41)	0.762 (14)
7.2048 (27)	77.376 (91)	0.110	0.118	75.059 (76)	2.317 (36)	0.840 (13)

Table 17
Gold foils, 38–50 keV: $[\mu/\rho]$ in the energy range 37.95–49.86 keV with $[\rho t]_c$ determined from a comparison with the reference foil.

Numbers in parentheses are the standard deviations of the parameter in the least significant digits. $\sigma_{[\mu/\rho]_{\rm rel}}$ is the percentage uncertainty from the standard deviations of the measurements. $\sigma_{[\mu/\rho]}$ is the total percentage uncertainty including the contribution from the uncertainty in the absolute value of $[\rho t]_c$, where $\%\sigma_{[\rho t]_c} = 0.1\%$. The (photoelectric) mass absorption coefficient $[\mu/\rho]_{\rm pe}$ and the imaginary part of the atomic scattering factor f'' are also given.

E (keV)	$[\mu/\rho]$ (cm^2 g^{-1})	$\sigma_{[\mu/\rho]_{\rm rel}}$ (% relative)	$\sigma_{[\mu/\rho]}$ (% absolute)	$[\mu/\rho]_{\rm pe}$ (cm^2 g^{-1})	f'' (e atom^{-1})
37.95137 (29)	14.6962 (32)	0.022%	0.102%	13.6625 (158)	2.4275 (28)
38.94325 (30)	13.7352 (17)	0.012%	0.101%	12.7327 (165)	2.3214 (30)
39.95217 (31)	12.8518 (13)	0.010%	0.101%	11.8865 (140)	2.2223 (26)
40.92519 (32)	12.0540 (18)	0.015%	0.101%	11.1168 (145)	2.1299 (28)
41.92506 (35)	11.3171 (30)	0.027%	0.102%	10.4104 (133)	2.0430 (27)
43.90285 (51)	10.0214 (15)	0.015%	0.101%	9.1678 (126)	1.8843 (26)
45.88667 (62)	8.9164 (16)	0.018%	0.102%	8.1138 (104)	1.7430 (23)
47.87059 (94)	7.9821 (19)	0.024%	0.103%	7.2234 (99)	1.6188 (22)
49.8545 (11)	7.1685 (10)	0.014%	0.101%	6.4499 (89)	1.5054 (21)

using advances in integrated column density determination and the full-foil mapping technique.

Four zinc foils of nominal thicknesses of 10 µm, 25 µm, 50 µm and 100 µm provided a range of log attenuation values $0.5 \leq \ln[I_0/I] \leq 6$ across the experimental energy range. This work defined and presented a ‘relative accuracy’ of 0.006%, which is not the same as either the precision or the absolute accuracy. Relative accuracy is the appropriate parameter for standard implementation of analysis of near-edge spectra, so can be called the ‘XAFS accuracy’. These additional data are therefore particularly relevant for XAFS analysis. This work also provided estimates of the assumed (Rayleigh and Compton) scattering so that any errors in that assumption could be clarified or corrected for in later work, and clarified methods for absolute determination of the integrated column density and thickness, and hence for the mass attenuation coefficient (Rae *et al.*, 2010*b*). The data are shown in Table 16 and are also available as supporting information to this chapter as file bz5029sup8.pdf.

12. Gold foils, 38–50 keV. XAS study

Islam *et al.* (2010*b*) reported an XAS spectrum with 9 points between the K and L edges, hence with no points covering XAFS. This data set is not useful for edge determination, reference calibration or for studying bonding and dynamic structure, and many other good sets of relative data are available along with a high-accuracy set of absolute data (Glover *et al.*, 2010). However, the data set given by Islam *et al.* (2010*b*) represented a detailed study of systematic errors and XAS at higher energies, and gold metal foils give a good approximation to atomic form factors for use as a reference standard and for calibration. Four gold foils with nominal thicknesses of 9.3 µm, 100.6 µm, 116.5 µm and 275 µm were used for the measurements. The study clarified methods for the absolute determination of the integrated column density and thickness, especially for foil samples (Islam *et al.*, 2010*a*). The method for energy analysis using powder diffraction standards was also detailed (Rae *et al.*, 2010*c*). The data are shown in Table 17 and are also available as supporting information to this chapter as the file bz5029sup9.pdf.

13. Gold foils, 14.2–21.1 keV. $L_{\rm I}$ edge XAS, XAFS and bonding

Glover *et al.* (2010) provided a detailed XAS and XAFS data set for gold metal foils across the $L_{\rm I}$ edge, accurate to between 0.08% and 0.10%, dominated by the absolute calibration uncertainty. Four gold foil thicknesses were used, nominally 5 µm, 9 µm, 15 µm and 25 µm. This helped to develop the absolute method for integrated column density determination for foils: the multiple independent foil technique (Chantler *et al.*, 2012*b*).

An analysis of the $L_{\rm I}$ edge XAFS showed excellent agreement between the measured and simulated XAFS and yielded highly accurate values of the bond lengths of gold. This data set included 91 points across the $L_{\rm I}$ edge, and the study included comparison with *eFEFFit* analysis following *iFEFFit* (*i.e.* providing and fitting input data uncertainties). This data set measured nanoroughness in 5 µm gold foils inside the spot size of the synchrotron beam (Glover *et al.*, 2009), which is very important for nanostructure quality control, and modelled the fluorescence signature (Fig. 4).

The photoelectric mass absorption coefficient was calculated by subtracting the contribution from Rayleigh and Compton scattering. The scattering attenuation coefficient

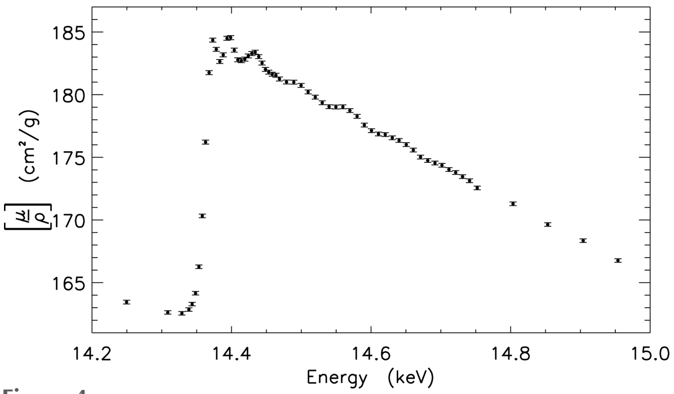

Figure 4
Mass attenuation coefficients for gold metal, 14.2–21.1 keV, plotted with experimental error bars (Glover *et al.*, 2010). The gold $L_{\rm I}$ absorption edge can be seen at 14.35 keV with the associated XAFS from 14.35 keV to 14.75 keV. Copyright IOP Publishing. Reproduced with permission. All rights reserved.

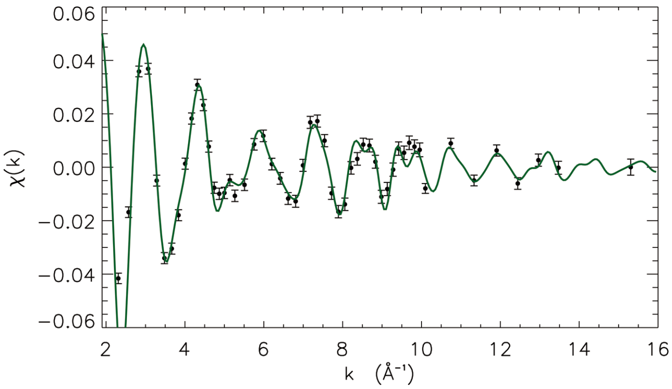

Figure 5
Gold metal, 14.2–21.1 keV (Glover *et al.*, 2010), experiment and fitted structure of the XAFS above the $L_{\rm I}$ edge. The standard XAFS signal $\chi(k)$ is plotted. Experimental measurements in are in black with error bars for experimental uncertainties. The *FEFF* fit is the dark green line. The agreement is excellent ($\chi^2_{\rm r} = 1.94$). Copyright IOP Publishing. Reproduced with permission. All rights reserved.

was calculated from the average of the FFAST (Chantler, 2000) and XCOM (Berger & Hubbell, 1987) tabulations and the uncertainty was assumed to be the difference between the two tabulations divided by $\sqrt{2}$. The uncertainty in the scattering attenuation contributed less than 0.03% to the photoelectric absorption and was not a major source of error. These measurements should provide a good approximation to the imaginary part of the atomic form factor of gold, except at the edge and in the XAFS region between about 14.3 keV and 15 keV, where solid-state effects are significant. The data are available as supporting information to this chapter as file bz5029sup10.pdf. The experimental and fitted structure of the XAFS above the edge are shown in Fig. 5.

Table 18 gives the values and uncertainties of the calibrated X-ray energy, mass attenuation coefficient, photoelectric mass absorption coefficient and imaginary component of the form factor. Column four lists the accuracy of the mass attenuation coefficient measurement excluding the contribution from the

Table 18
Gold foils, 14.2–21.1 keV: mass attenuation coefficients tabulated at 91 energies with one standard deviation uncertainties in the least significant digit(s) given in parentheses.

$\sigma_{[\mu/\rho]_{\rm rel}}$ is the precision of the mass attenuation coefficient measurements (the uncertainty excluding the contribution from full-foil mapping), which is useful for XAFS research. f'' is the imaginary component of the form factor of gold with uncertainties in parentheses. f'' values between 14.35 keV and 14.8 keV (at and above the edge) include solid-state effects.

E (keV)	$[\mu/\rho]$ (cm^2 g^{-1})	$\sigma_{[\mu/\rho]}$ (%)	$\sigma_{[\mu/\rho]_{\rm rel}}$ (cm^2 g^{-1})	$[\mu/\rho]_{\rm pe}$ (cm^2 g^{-1})	f'' (e atom^{-1})
14.2496 (6)	163.45 (15)	0.09	0.06	160.01 (15)	10.672 (10)
14.3087 (6)	162.62 (14)	0.08	0.03	159.20 (14)	10.662 (9)
14.3289 (4)	162.55 (14)	0.08	0.03	159.13 (14)	10.673 (9)
14.3389 (4)	162.85 (14)	0.08	0.02	159.44 (14)	10.701 (9)
14.3436 (3)	163.29 (14)	0.08	0.03	159.87 (14)	10.734 (9)
14.3484 (3)	164.15 (14)	0.08	0.03	160.74 (14)	10.795 (10)
14.3533 (3)	166.27 (14)	0.08	0.04	162.85 (14)	10.941 (10)
14.3581 (3)	170.32 (15)	0.08	0.04	166.91 (15)	11.217 (10)
14.3628 (3)	176.21 (16)	0.08	0.06	172.80 (16)	11.617 (11)
14.3679 (3)	181.76 (16)	0.08	0.05	178.35 (16)	11.994 (11)
14.3731 (3)	184.35 (16)	0.08	0.04	180.94 (16)	12.173 (11)
14.3781 (3)	183.62 (16)	0.08	0.04	180.21 (16)	12.128 (11)
14.3832 (3)	182.65 (16)	0.08	0.04	179.24 (16)	12.067 (11)
14.3881 (3)	183.18 (16)	0.08	0.04	179.77 (16)	12.107 (11)
14.3935 (3)	184.50 (16)	0.08	0.04	181.09 (16)	12.201 (11)
14.3987 (3)	184.55 (16)	0.08	0.04	181.15 (16)	12.209 (11)
14.4040 (3)	183.55 (16)	0.08	0.04	180.15 (16)	12.146 (11)
14.4091 (3)	182.79 (16)	0.08	0.04	179.39 (16)	12.099 (11)
14.4141 (3)	182.71 (16)	0.08	0.04	179.32 (16)	12.098 (11)
14.4190 (3)	182.84 (16)	0.08	0.04	179.44 (16)	12.111 (11)
14.4241 (3)	183.09 (16)	0.08	0.04	179.69 (16)	12.132 (11)
14.4292 (3)	183.28 (16)	0.08	0.04	179.89 (16)	12.150 (11)
14.4339 (3)	183.39 (16)	0.08	0.04	180.00 (16)	12.161 (11)
14.4390 (3)	183.04 (16)	0.08	0.04	179.64 (16)	12.141 (11)
14.4437 (3)	182.53 (16)	0.08	0.04	179.14 (16)	12.111 (11)
14.4487 (3)	182.01 (16)	0.08	0.04	178.62 (16)	12.080 (11)
14.4534 (3)	181.80 (16)	0.08	0.04	178.41 (16)	12.070 (11)
14.4583 (3)	181.63 (16)	0.08	0.04	178.24 (16)	12.063 (11)
14.4636 (3)	181.55 (16)	0.08	0.04	178.16 (16)	12.062 (11)
14.4687 (3)	181.25 (16)	0.08	0.04	177.87 (16)	12.046 (11)
14.4788 (4)	181.01 (16)	0.08	0.04	177.63 (16)	12.038 (11)
14.4892 (4)	181.00 (16)	0.08	0.04	177.62 (16)	12.046 (11)
14.4997 (4)	180.74 (16)	0.08	0.04	177.36 (16)	12.037 (11)
14.5098 (4)	180.22 (16)	0.08	0.04	176.84 (16)	12.011 (11)
14.5201 (4)	179.80 (16)	0.08	0.04	176.43 (16)	11.991 (11)
14.5300 (4)	179.35 (16)	0.08	0.04	175.99 (16)	11.969 (11)
14.5398 (4)	179.04 (15)	0.08	0.04	175.68 (16)	11.956 (11)
14.5496 (4)	179.02 (15)	0.08	0.04	175.65 (15)	11.962 (11)
14.5596 (4)	179.03 (15)	0.08	0.04	175.67 (15)	11.972 (11)
14.5696 (4)	178.73 (15)	0.08	0.04	175.37 (15)	11.960 (11)
14.5799 (4)	178.27 (15)	0.08	0.04	174.91 (15)	11.937 (11)

Table 18 (continued)

E (keV)	$[\mu/\rho]$ (cm^2 g^{-1})	$\sigma_{[\mu/\rho]}$ (%)	$\sigma_{[\mu/\rho]_{\rm rel}}$ (cm^2 g^{-1})	$[\mu/\rho]_{\rm pe}$ (cm^2 g^{-1})	f'' (e atom^{-1})
14.5903 (4)	177.57 (15)	0.08	0.04	174.22 (15)	11.898 (11)
14.6006 (4)	177.13 (15)	0.08	0.04	173.78 (15)	11.876 (10)
14.6106 (4)	176.87 (15)	0.08	0.04	173.52 (15)	11.867 (10)
14.6203 (4)	176.82 (15)	0.08	0.04	173.47 (15)	11.871 (10)
14.6304 (4)	176.56 (15)	0.08	0.04	173.22 (15)	11.862 (10)
14.6401 (4)	176.35 (15)	0.08	0.04	173.01 (15)	11.856 (10)
14.6504 (4)	176.01 (15)	0.08	0.04	172.67 (15)	11.841 (10)
14.6606 (4)	175.58 (15)	0.08	0.04	172.25 (15)	11.820 (10)
14.6709 (4)	175.02 (15)	0.08	0.04	171.69 (15)	11.790 (10)
14.6812 (4)	174.74 (15)	0.08	0.04	171.42 (15)	11.779 (10)
14.6916 (4)	174.54 (15)	0.08	0.04	171.22 (15)	11.774 (10)
14.7016 (4)	174.36 (15)	0.08	0.04	171.04 (15)	11.770 (10)
14.7116 (4)	174.02 (15)	0.08	0.04	170.70 (15)	11.755 (10)
14.7212 (4)	173.79 (15)	0.08	0.04	170.47 (15)	11.746 (10)
14.7311 (4)	173.46 (15)	0.08	0.04	170.14 (15)	11.732 (10)
14.7411 (4)	173.13 (15)	0.08	0.04	169.81 (15)	11.717 (10)
14.7521 (4)	172.56 (15)	0.08	0.02	169.25 (15)	11.687 (10)
14.8034 (6)	171.29 (15)	0.08	0.02	167.99 (15)	11.640 (10)
14.8531 (6)	169.64 (14)	0.08	0.02	166.35 (14)	11.565 (10)
14.9040 (6)	168.35 (14)	0.08	0.02	165.08 (14)	11.516 (10)
14.9538 (6)	166.77 (14)	0.08	0.02	163.51 (14)	11.445 (10)
15.0046 (6)	165.42 (14)	0.08	0.02	162.18 (14)	11.390 (10)
15.0559 (6)	163.89 (14)	0.08	0.02	160.65 (14)	11.321 (10)
15.2573 (12)	158.54 (13)	0.08	0.02	155.35 (13)	11.094 (10)
15.4578 (12)	153.30 (13)	0.08	0.02	150.16 (13)	10.864 (9)
15.6583 (12)	148.38 (13)	0.08	0.02	145.27 (13)	10.647 (9)
15.8599 (12)	143.58 (12)	0.08	0.02	140.52 (12)	10.431 (9)
16.0616 (12)	139.04 (12)	0.08	0.01	136.02 (12)	10.226 (9)
16.2631 (12)	134.71 (12)	0.08	0.03	131.73 (12)	10.028 (9)
16.4639 (12)	130.53 (11)	0.08	0.03	127.60 (11)	9.833 (9)
16.6652 (12)	126.59 (11)	0.08	0.03	123.70 (11)	9.649 (9)
16.8676 (12)	122.72 (11)	0.08	0.03	119.87 (11)	9.464 (8)
17.0688 (12)	119.10 (10)	0.08	0.03	116.28 (10)	9.290 (8)
17.2708 (12)	115.53 (10)	0.08	0.03	112.75 (10)	9.115 (8)
17.4720 (12)	112.19 (10)	0.08	0.03	109.45 (10)	8.951 (8)
17.6730 (12)	108.92 (10)	0.08	0.02	106.21 (10)	8.786 (8)
17.8735 (13)	105.83 (9)	0.08	0.02	103.16 (9)	8.631 (8)
18.0754 (13)	102.83 (9)	0.08	0.01	100.19 (9)	8.477 (7)
18.2752 (13)	99.95 (9)	0.08	0.02	97.35 (9)	8.328 (7)
18.4766 (13)	97.18 (8)	0.08	0.02	94.61 (8)	8.182 (7)
18.6781 (13)	94.51 (8)	0.08	0.02	91.97 (8)	8.041 (7)
18.8782 (13)	91.94 (8)	0.08	0.02	89.44 (8)	7.903 (7)
19.0795 (13)	89.45 (8)	0.08	0.01	86.98 (8)	7.768 (7)
19.2818 (13)	87.05 (7)	0.08	0.01	84.61 (8)	7.636 (7)
19.4833 (13)	84.76 (7)	0.08	0.01	82.35 (7)	7.510 (7)
19.6832 (13)	82.55 (7)	0.08	0.01	80.18 (7)	7.387 (7)
19.8848 (15)	80.37 (7)	0.08	0.01	78.03 (7)	7.263 (7)
20.0881 (13)	78.34 (7)	0.08	0.02	76.03 (7)	7.149 (7)
20.5894 (6)	73.47 (6)	0.08	0.01	71.21 (6)	6.863 (6)
21.0919 (6)	69.02 (6)	0.08	0.02	66.79 (6)	6.594 (6)

absolute calibration. This quantity is useful for XAFS, since most researchers use and analyse attenuation data on a relative scale. This quantity is referred to as $\sigma_{\rm rel}$. A breakdown of the various contributions to the uncertainty in the energy, mass attenuation coefficient and imaginary part of the form factor is given in Table 19.

14. Silver foils, 5.0–20.1 keV. XAS study

Islam *et al.* (2014) measured the XAS spectra from silver foils for 84 discrete energies between the $L_{\rm I}$ and the K edges, hence their data showed no XAFS. Silver foils were used with nominal thicknesses of 5 µm (2 foils), 10 µm (2 foils), 12 µm, 50 µm (2 foils), 100 µm (2 foils) and 275 µm. The data had an accuracy of 0.01–0.2% on a relative scale down to 5.3 keV, and

Table 19

Gold foils, 14.2–21.1 keV: contributions to the uncertainty in the mass attenuation coefficient, imaginary component of the form factor and the X-ray energy.

Uncertainties due to impurities, roughness and energy drift were appreciable only for selected measurements. The final results used a weighted mean.

Quantity	Uncertainty	Comment
$[\mu/\rho]$	0.083%	Accuracy of the full-foil mapping
	<0.06%	Impurities in the 99.9% foils
	<0.06%	Roughness of the 5 µm foil
	<0.03%	Uncertainty due to energy drift
f''	0.08–0.1%	Contribution from $[\mu/\rho]$ uncertainty
	<0.03%	Scattering contribution uncertainty, largest just below $L_{\rm I}$ edge
E	0.3–1.3 eV	Accuracy limited by powder-diffraction results
	<0.1 eV	Uncertainty due to energy drift

Table 20
Silver, 5.0–20.1 keV: X-ray mass attenuation coefficients $[\mu/\rho]$, the photoelectric mass absorption coefficients $[\mu/\rho]_{\rm pe}$, the imaginary components of the form factor f'' and the mass attenuation coefficients for Raleigh and Compton scattering $[\mu/\rho]_{\rm R+C}$, with uncertainties.

The mass attenuation coefficients for Rayleigh and Compton scattering were taken as the average of the tabulated FFAST and XCOM values and determined by interpolation at the measured energies. The uncertainty of $[\mu/\rho]_{\rm R+C}$ was determined from half of the variation between the tabulated FFAST and XCOM values. The uncertainty of $[\mu/\rho]_{\rm pe}$ was determined from the uncertainty contributions of $[\mu/\rho]_{\rm R+C}$ and $[\mu/\rho]_t$.

E (keV)	$[\mu/\rho]$ (cm^2 g^{-1})	$\sigma_{[\mu/\rho]_{\rm rel}}$ (% relative)	$\sigma_{[\mu/\rho]}$ (% absolute)	$[\mu/\rho]_{\rm pe}$ (cm^2 g^{-1})	f'' (e atom^{-1})	$[\mu/\rho]_{\rm R+C}$ (cm^2 g^{-1})
20.06525 (58)	17.9785 (20)	0.011	0.088	16.740 (11)	0.86101 (56)	1.239 (13)
19.06124 (52)	20.6921 (36)	0.017	0.089	19.373 (11)	0.94660 (55)	1.319 (14)
18.05718 (46)	24.0298 (14)	0.006	0.087	22.622 (11)	1.04711 (49)	1.408 (15)
17.05313 (41)	28.1240 (28)	0.010	0.088	26.617 (10)	1.16355 (44)	1.507 (15)
16.55110 (39)	30.499 (22)	0.071	0.113	28.939 (24)	1.2278 (10)	1.561 (15)
16.04910 (36)	33.1993 (81)	0.024	0.090	31.582 (12)	1.29929 (49)	1.618 (14)
15.54701 (34)	36.2281 (66)	0.018	0.089	34.551 (10)	1.37697 (41)	1.677 (13)
15.04497 (33)	39.659 (12)	0.030	0.092	37.918 (14)	1.46237 (53)	1.741 (12)
14.84420 (32)	41.164 (19)	0.046	0.098	39.396 (20)	1.49911 (76)	1.767 (12)
14.64342 (31)	42.755 (11)	0.025	0.090	40.960 (12)	1.53753 (46)	1.794 (11)
14.44257 (31)	44.3646 (80)	0.018	0.089	42.5425 (98)	1.57503 (36)	1.822 (10)
14.24172 (30)	46.135 (16)	0.035	0.094	44.284 (17)	1.61670 (62)	1.8516 (95)
14.04092 (30)	47.954 (12)	0.026	0.091	46.074 (13)	1.65834 (47)	1.8797 (86)
13.84015 (30)	49.9145 (96)	0.019	0.089	48.005 (10)	1.70313 (37)	1.9096 (77)
13.63934 (29)	51.919 (17)	0.032	0.093	49.979 (17)	1.74743 (59)	1.9401 (67)
13.43850 (29)	54.074 (10)	0.019	0.089	52.102 (11)	1.79485 (37)	1.9715 (55)
13.23773 (29)	56.285 (84)	0.149	0.172	54.281 (84)	1.8420 (28)	2.0036 (42)
13.03687 (29)	58.743 (16)	0.027	0.091	56.707 (16)	1.89509 (54)	2.0365 (28)
12.83611 (29)	61.291 (28)	0.045	0.098	59.221 (28)	1.94864 (91)	2.0701 (11)
12.63525 (29)	64.020 (24)	0.037	0.094	61.916 (24)	2.00543 (76)	2.10460 (63)
12.43446 (29)	66.873 (20)	0.030	0.092	64.733 (20)	2.06338 (65)	2.1400 (25)
12.23364 (29)	69.933 (20)	0.029	0.092	67.756 (21)	2.12485 (64)	2.1766 (44)
12.03285 (29)	73.152 (20)	0.027	0.091	70.938 (20)	2.18812 (61)	2.2141 (64)
11.88227 (29)	75.687 (23)	0.030	0.092	73.444 (23)	2.23709 (70)	2.2430 (79)
11.73163 (30)	78.409 (24)	0.031	0.092	76.136 (25)	2.28969 (74)	2.2725 (95)
11.58104 (30)	81.158 (25)	0.031	0.092	78.856 (26)	2.34102 (76)	2.303 (11)
11.43044 (30)	84.149 (36)	0.042	0.097	81.815 (36)	2.3973 (11)	2.333 (13)
11.27979 (31)	87.181 (24)	0.027	0.091	84.817 (25)	2.45250 (71)	2.365 (15)
11.12919 (31)	90.540 (46)	0.051	0.101	88.143 (46)	2.5147 (13)	2.397 (17)
10.97859 (31)	93.897 (22)	0.023	0.090	91.467 (23)	2.57418 (65)	2.429 (19)
10.82801 (32)	97.485 (41)	0.042	0.097	95.022 (42)	2.6375 (12)	2.463 (21)
10.67736 (32)	101.250 (25)	0.025	0.091	98.753 (27)	2.70296 (74)	2.497 (24)
10.52679 (33)	105.358 (21)	0.020	0.089	102.827 (23)	2.77478 (63)	2.532 (26)
10.37618 (33)	109.663 (39)	0.036	0.094	107.096 (41)	2.8486 (11)	2.568 (28)
10.22556 (34)	114.133 (15)	0.013	0.088	111.529 (19)	2.92348 (50)	2.604 (31)
10.07496 (35)	118.853 (37)	0.031	0.092	116.211 (39)	3.0014 (10)	2.642 (33)
9.92435 (35)	123.792 (21)	0.017	0.089	121.112 (25)	3.08118 (63)	2.681 (36)
9.77371 (36)	129.140 (42)	0.032	0.093	126.420 (44)	3.1674 (11)	2.720 (38)
9.62312 (36)	134.677 (08)	0.006	0.087	131.916 (17)	3.25420 (41)	2.761 (41)
9.47253 (37)	140.651 (58)	0.041	0.096	137.850 (60)	3.3474 (15)	2.802 (43)
9.32192 (38)	146.798 (32)	0.021	0.090	143.954 (36)	3.44001 (85)	2.844 (46)
9.17131 (38)	153.554 (64)	0.041	0.096	150.667 (66)	3.5423 (15)	2.888 (49)
9.02069 (39)	160.660 (32)	0.020	0.089	157.727 (37)	3.64736 (85)	2.932 (52)
8.92029 (40)	165.237 (96)	0.058	0.105	162.275 (98)	3.7107 (22)	2.963 (54)
8.81988 (40)	170.545 (23)	0.013	0.088	167.552 (30)	3.78828 (67)	2.994 (56)
8.71947 (41)	175.848 (58)	0.033	0.093	172.822 (61)	3.8630 (14)	3.025 (58)
8.61909 (41)	181.513 (18)	0.010	0.088	178.455 (27)	3.94296 (60)	3.057 (60)
8.51867 (42)	187.243 (68)	0.037	0.094	184.153 (71)	4.0215 (16)	3.090 (62)
8.41826 (42)	193.382 (24)	0.012	0.088	190.259 (31)	4.10582 (67)	3.123 (64)
8.31785 (43)	199.733 (76)	0.038	0.095	196.576 (79)	4.1916 (17)	3.157 (66)
8.21747 (43)	206.406 (13)	0.006	0.087	203.214 (25)	4.28080 (52)	3.192 (68)
8.11704 (44)	213.266 (69)	0.032	0.093	210.039 (73)	4.3705 (15)	3.227 (70)
8.01663 (44)	220.693 (33)	0.015	0.088	217.430 (40)	4.46835 (82)	3.263 (72)
8.00711 (44)	221.235 (56)	0.025	0.091	217.969 (60)	4.4741 (12)	3.266 (72)
7.91623 (45)	228.262 (21)	0.009	0.088	224.963 (31)	4.56525 (63)	3.299 (74)
7.81584 (45)	236.089 (35)	0.015	0.088	232.752 (42)	4.66342 (84)	3.336 (76)
7.71542 (46)	244.576 (56)	0.023	0.090	241.202 (61)	4.7706 (12)	3.374 (78)
7.61504 (46)	253.292 (29)	0.012	0.088	249.879 (38)	4.87796 (73)	3.413 (80)
7.51462 (47)	262.520 (80)	0.031	0.092	259.068 (84)	4.9907 (16)	3.452 (82)
7.41422 (47)	271.873 (18)	0.006	0.087	268.381 (30)	5.10099 (57)	3.492 (84)
7.31381 (48)	282.11 (11)	0.040	0.096	278.57 (12)	5.2230 (22)	3.533 (86)
7.21342 (48)	292.731 (69)	0.024	0.090	289.156 (74)	5.3470 (14)	3.575 (88)
7.11301 (49)	304.17 (19)	0.065	0.108	300.55 (20)	5.4804 (36)	3.617 (90)
7.01258 (50)	316.101 (95)	0.030	0.092	312.440 (98)	5.6167 (18)	3.661 (92)
6.91218 (50)	328.37 (12)	0.036	0.094	324.67 (12)	5.7530 (22)	3.705 (94)
6.81178 (51)	341.17 (29)	0.084	0.121	337.42 (29)	5.8921 (50)	3.750 (96)

Table 20 (continued)

E (keV)	$[\mu/\rho]$ (cm^2 g^{-1})	$\sigma_{[\mu/\rho]_{\rm rel}}$ (% relative)	$\sigma_{[\mu/\rho]}$ (% absolute)	$[\mu/\rho]_{\rm pe}$ (cm^2 g^{-1})	f'' (e atom^{-1})	$[\mu/\rho]_{\rm R+C}$ (cm^2 g^{-1})
6.71138 (51)	354.71 (26)	0.072	0.113	350.91 (26)	6.0374 (44)	3.796 (98)
6.61096 (52)	368.63 (37)	0.101	0.134	364.79 (38)	6.1823 (64)	3.84 (10)
6.51058 (52)	383.96 (36)	0.095	0.129	380.07 (37)	6.3434 (61)	3.89 (10)
6.41016 (53)	400.29 (46)	0.114	0.143	396.34 (46)	6.5130 (75)	3.94 (10)
6.30977 (54)	416.86 (47)	0.112	0.142	412.87 (47)	6.6784 (76)	3.99 (11)
6.20935 (54)	434.79 (58)	0.133	0.159	430.75 (58)	6.8568 (92)	4.04 (11)
6.10894 (55)	454.13 (69)	0.151	0.174	450.04 (69)	7.047 (11)	4.09 (11)
6.00853 (55)	474.92 (59)	0.124	0.151	470.78 (59)	7.2515 (91)	4.14 (11)
5.90815 (56)	496.93 (97)	0.195	0.214	492.73 (97)	7.463 (15)	4.20 (11)
5.80774 (57)	518.90 (95)	0.183	0.203	514.64 (95)	7.662 (14)	4.25 (11)
5.70733 (57)	545 (1)	0.199	0.217	540 (1)	7.904 (16)	4.31 (11)
5.60692 (58)	569 (1)	0.194	0.212	565 (1)	8.120 (16)	4.37 (11)
5.50652 (58)	595 (1)	0.215	0.232	591 (1)	8.339 (18)	4.43 (11)
5.40611 (59)	623 (1)	0.175	0.196	618 (1)	8.566 (15)	4.49 (11)
5.30571 (60)	654 (1)	0.207	0.225	649 (1)	8.831 (18)	4.55 (12)
5.20530 (60)	687 (2)	0.273	0.286	682 (2)	9.107 (25)	4.61 (12)
5.10490 (61)	722 (3)	0.420	0.428	717 (3)	9.387 (40)	4.67 (12)
5.00449 (61)	746 (9)	1.217	1.220	741 (9)	9.50 (12)	4.73 (12)

of 0.09–1.22% on an absolute scale down to 5.0 keV. This was the first high-accuracy measurement of X-ray mass attenuation coefficients of silver in the low-energy range, indicating the possibility of obtaining high-accuracy X-ray absorption fine structure down to the $L_{\rm I}$ edge (3.8 keV) of silver. Comparison of these results with an earlier data set optimized for higher energies (Tran *et al.*, 2005) confirmed the accuracy to within one standard error of each data set collected and analysed using the principles of the X-ray extended-range technique (XERT). Comparison with theory showed a slow divergence towards lower energies in this region away from absorption edges.

This analysis indicated that high accuracy is obtainable at lower energies by using comparatively thin (*e.g.* 5 µm) foils and by using dilute solutions of silver compounds if accurate transfer of thickness or concentration is obtained. This work thus indicated that measurements of L-edge XAFS of silver (theoretically at and above 3.8 keV) are possible using XERT by making use of thinner silver foils at lower energies (3–6 keV). Perhaps just as significant is the independent verification of the accuracy of the earlier work (Tran *et al.*, 2005) to within one standard error, which confirms the potential accuracy of this technique and the portability and reproducibility across different diffracting monochromator crystals, energy ranges and foils. The data are shown in Table 20 and are available as supporting information to this chapter in the file bz5029sup11.pdf.

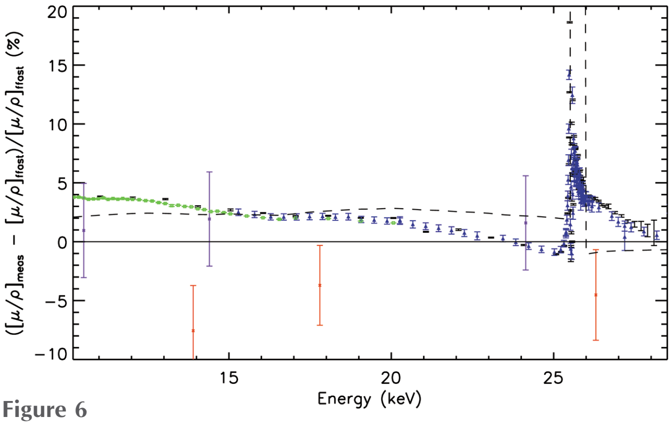

Figure 6
Silver, 11.0–28.1 keV. Comparison of $[\mu/\rho]$ with values from FFAST (Chantler, 1995, 2000; Chantler *et al.*, 2000) as the zero line; Tantau *et al.* (2015), black error bars; Tran *et al.* (2005), blue triangles; Islam *et al.* (2014), green boxes; Sandiago *et al.* (1997), purple stars; Tajuddin *et al.* (1995), red crosses; and the XCOM database (Berger *et al.*, 1999) as the dashed line. Copyright IOP Publishing. Reproduced with permission from Tantau *et al.* (2015). All rights reserved.

15. Silver foils, 11.0–28.1 keV. XAS, XAFS, bonding, nanostructure, theory and thermal behaviour

Tantau *et al.* (2015) investigated the XAFS region over 80 discrete energies including the K edge (Figs. 6 and 7), using six high-purity silver foils of nominal thicknesses 1 µm, 10 µm, 12.5 µm, 50 µm (2 foils) and 100 µm, chosen to ensure that for each energy at least one absorber would satisfy Nordfors' criterion (*i.e.* $2 < \ln(I/I_0) < 4$) for counting statistics. All thicknesses were used at most energies. This study showed extremely good consistency between different data sets with different systematic errors collected in different years and

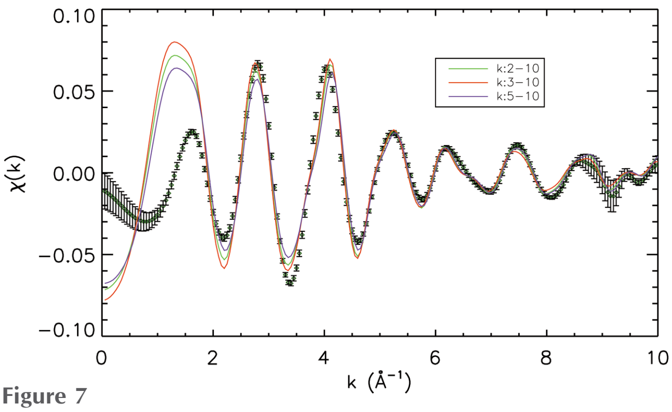

Figure 7
Silver, 11.0–28.1 keV. *eFEFFit* plots refined over different k windows, with uncertainties propagated. The structures are robust and appear well fitted, although the restricted k range leads to a respectable value of $\chi^2_{\rm r}$ for the reduced region of interest. Copyright IOP Publishing. Reproduced with permission from Tantau *et al.* (2015). All rights reserved.

Table 21

Silver, 11–28 keV: mass attenuation coefficients $[\mu/\rho]$ and the imaginary component of the atomic form factor f'', with one standard deviation uncertainties in the least significant digits indicated in parentheses.

Relative and absolute percentage uncertainty in the mass attenuation coefficients $\sigma_{[\mu/\rho]_{\rm rel}}$ and $\sigma_{[\mu/\rho]}$ are given. Uncertainties in $[\mu/\rho]_{\rm pe}$ and f'' include the measurement uncertainty and the difference between major tabulations of the total Rayleigh plus Compton scattering cross sections. f'' in the XAFS region is affected by solid-state effects.

E (keV)	$[\mu/\rho]$ (cm^2 g^{-1})	$\sigma_{[\mu/\rho]_{\rm rel}}$ (%)	$\sigma_{[\mu/\rho]}$ (%)	$[\mu/\rho]_{\rm R+C}$ (cm^2 g^{-1})	$[\mu/\rho]_{\rm pe}$ (cm^2 g^{-1})	f'' (e atom^{-1})
11.03599 (46)	92.743 (32)	0.01	0.03	2.417 (18)	90.33 (68)	2.555 (19)
12.04001 (47)	73.124 (54)	0.06	0.07	2.2126 (61)	70.91 (20)	2.1886 (63)
13.04339 (51)	58.876 (31)	0.04	0.05	2.0352 (30)	56.841 (89)	1.9005 (30)
14.04618 (56)	47.995 (29)	0.05	0.06	1.8788 (88)	46.12 (22)	1.6604 (78)
15.04851 (63)	39.761 (33)	0.07	0.08	1.740 (12)	38.02 (27)	1.467 (11)
16.05173 (70)	33.312 (13)	0.02	0.03	1.617 (14)	31.70 (28)	1.304 (12)
17.05414 (79)	28.163 (14)	0.03	0.04	1.507 (15)	26.66 (26)	1.165 (11)
18.05675 (87)	24.0872 (81)	0.01	0.03	1.408 (15)	22.68 (24)	1.050 (11)
19.06100 (96)	20.7471 (69)	0.01	0.03	1.319 (14)	19.43 (21)	0.949 (10)
20.0634 (11)	18.0557 (67)	0.02	0.03	1.239 (13)	16.82 (18)	0.8649 (92)
21.0676 (12)	15.6542 (62)	0.02	0.03	1.166 (12)	14.49 (15)	0.7824 (81)
22.0699 (13)	13.8502 (92)	0.05	0.06	1.101 (11)	12.75 (13)	0.7213 (74)
23.0731 (13)	12.2237 (48)	0.02	0.03	1.042 (10)	11.18 (11)	0.6614 (66)
24.0772 (14)	10.8552 (55)	0.04	0.05	0.9874 (97)	9.868 (97)	0.6090 (60)
25.0775 (15)	9.6768 (50)	0.04	0.05	0.9384 (93)	8.738 (86)	0.5617 (56)
25.2267 (16)	9.5448 (46)	0.03	0.04	0.9315 (92)	8.613 (86)	0.5570 (55)
25.3269 (16)	9.4963 (44)	0.03	0.04	0.9269 (92)	8.569 (85)	0.5564 (55)
25.3757 (16)	9.5290 (47)	0.03	0.04	0.9246 (92)	8.604 (86)	0.5597 (56)
25.4262 (16)	9.6595 (48)	0.03	0.04	0.9223 (92)	8.737 (87)	0.5695 (57)
25.4468 (16)	9.7641 (44)	0.03	0.04	0.9214 (92)	8.843 (88)	0.5768 (58)
25.4659 (16)	10.0110 (66)	0.05	0.06	0.9206 (91)	9.090 (91)	0.5934 (59)
25.4760 (16)	10.2158 (44)	0.03	0.04	0.9201 (92)	9.296 (93)	0.6071 (61)
25.4854 (16)	10.5658 (54)	0.04	0.05	0.9197 (92)	9.646 (96)	0.6302 (63)
25.4948 (16)	11.1115 (62)	0.04	0.05	0.9192 (92)	10.19 (10)	0.6661 (67)
25.5002 (16)	11.7262 (76)	0.05	0.06	0.9190 (92)	10.81 (11)	0.7064 (71)
25.5052 (16)	12.6870 (92)	0.06	0.07	0.9187 (91)	11.77 (12)	0.7694 (77)
25.5102 (16)	15.392 (36)	0.23	0.23	0.9184 (91)	14.47 (15)	0.9464 (96)
25.5150 (16)	21.829 (68)	0.30	0.31	0.9182 (91)	20.91 (22)	1.368 (14)
25.5197 (16)	34.01 (12)	0.36	0.36	0.9180 (91)	33.10 (35)	2.165 (23)
25.5244 (16)	46.38 (16)	0.34	0.34	0.9178 (91)	45.47 (48)	2.975 (31)
25.5298 (16)	55.213 (62)	0.10	0.11	0.9176 (91)	54.30 (54)	3.553 (35)
25.5351 (16)	57.552 (37)	0.05	0.06	0.9173 (91)	56.63 (56)	3.707 (37)
25.5399 (16)	55.817 (47)	0.07	0.08	0.9171 (91)	54.90 (54)	3.594 (36)
25.5449 (16)	56.432 (52)	0.08	0.09	0.9169 (91)	55.51 (55)	3.635 (36)
25.5508 (16)	60.625 (54)	0.08	0.08	0.9166 (91)	59.71 (59)	3.911 (39)
25.5559 (16)	61.568 (61)	0.09	0.09	0.9164 (91)	60.65 (60)	3.973 (39)
25.5615 (16)	57.879 (46)	0.07	0.07	0.9161 (91)	56.96 (56)	3.732 (37)
25.5666 (16)	55.877 (36)	0.05	0.06	0.9159 (91)	54.96 (54)	3.602 (36)
25.5767 (16)	59.030 (67)	0.11	0.11	0.9155 (91)	58.11 (58)	3.810 (38)
25.5868 (16)	62.475 (44)	0.06	0.06	0.9150 (91)	61.56 (61)	4.038 (40)
25.5969 (16)	58.847 (61)	0.10	0.10	0.9146 (91)	57.93 (58)	3.801 (38)
25.6068 (16)	57.402 (37)	0.05	0.06	0.9141 (91)	56.49 (56)	3.708 (37)
25.6163 (16)	59.234 (33)	0.04	0.05	0.9137 (91)	58.32 (58)	3.830 (38)
25.6262 (16)	60.492 (43)	0.06	0.07	0.9133 (91)	59.58 (59)	3.914 (39)
25.6357 (16)	60.048 (41)	0.06	0.06	0.9128 (91)	59.14 (59)	3.886 (39)
25.6456 (16)	58.714 (39)	0.05	0.06	0.9124 (91)	57.80 (57)	3.800 (38)
25.6557 (16)	58.626 (45)	0.07	0.07	0.9120 (91)	57.71 (57)	3.796 (38)
25.6653 (16)	59.650 (38)	0.05	0.06	0.9115 (91)	58.74 (58)	3.864 (38)
25.6752 (16)	59.631 (43)	0.06	0.07	0.9111 (91)	58.72 (59)	3.865 (39)
25.6860 (16)	59.027 (38)	0.05	0.06	0.9106 (91)	58.12 (58)	3.827 (38)
25.6959 (16)	58.484 (33)	0.04	0.05	0.9102 (91)	57.57 (57)	3.792 (38)
25.7064 (16)	58.133 (38)	0.05	0.06	0.9097 (91)	57.22 (57)	3.771 (38)
25.7173 (16)	58.175 (51)	0.08	0.08	0.9092 (91)	57.27 (57)	3.775 (38)
25.7272 (16)	58.819 (48)	0.07	0.08	0.9088 (91)	57.91 (58)	3.819 (38)
25.7425 (16)	58.872 (33)	0.04	0.05	0.9081 (91)	57.96 (58)	3.825 (38)
25.7570 (16)	57.794 (48)	0.07	0.08	0.9075 (91)	56.89 (57)	3.756 (38)
25.7718 (16)	57.114 (26)	0.03	0.04	0.9068 (91)	56.21 (56)	3.713 (37)
25.7860 (16)	57.248 (47)	0.07	0.08	0.9062 (91)	56.34 (56)	3.724 (37)
25.8008 (16)	57.765 (39)	0.05	0.06	0.9056 (91)	56.86 (57)	3.761 (38)
25.8157 (16)	57.61 (13)	0.22	0.22	0.9049 (91)	56.70 (58)	3.752 (38)
25.8312 (16)	57.02 (19)	0.33	0.33	0.9043 (91)	56.11 (59)	3.715 (39)
25.8463 (16)	56.44 (23)	0.40	0.40	0.9036 (91)	55.54 (60)	3.680 (40)
25.8624 (16)	56.846 (86)	0.14	0.15	0.9029 (91)	55.94 (57)	3.709 (38)
25.8780 (16)	56.460 (39)	0.06	0.06	0.9022 (91)	55.56 (56)	3.685 (37)
25.8984 (16)	56.681 (67)	0.11	0.11	0.9013 (91)	55.78 (56)	3.703 (37)
25.9179 (16)	56.59 (21)	0.36	0.36	0.9005 (91)	55.69 (60)	3.700 (40)

Table 21 (continued)

E (keV)	$[\mu/\rho]$ (cm^2 g^{-1})	$\sigma_{[\mu/\rho]_{\rm rel}}$ (%)	$\sigma_{[\mu/\rho]}$ (%)	$[\mu/\rho]_{\rm R+C}$ (cm^2 g^{-1})	$[\mu/\rho]_{\rm pe}$ (cm^2 g^{-1})	f'' (e atom^{-1})
26.0812 (16)	54.967 (52)	0.08	0.09	0.8935 (90)	54.07 (55)	3.615 (37)
26.1819 (17)	54.253 (48)	0.08	0.08	0.8892 (90)	53.36 (54)	3.582 (36)
26.2811 (17)	53.737 (48)	0.08	0.08	0.8850 (90)	52.85 (54)	3.561 (36)
26.3830 (17)	53.098 (35)	0.05	0.06	0.8807 (90)	52.22 (53)	3.531 (36)
26.4831 (17)	52.421 (44)	0.07	0.08	0.8765 (90)	51.54 (53)	3.499 (36)
26.5831 (17)	51.852 (39)	0.06	0.07	0.8724 (90)	50.98 (52)	3.474 (36)
26.6877 (17)	51.33 (10)	0.19	0.19	0.8682 (89)	50.46 (53)	3.452 (36)
26.8872 (17)	50.100 (49)	0.09	0.09	0.8601 (89)	49.24 (51)	3.394 (35)
27.0872 (17)	49.024 (52)	0.10	0.10	0.8522 (89)	48.17 (51)	3.345 (35)
27.2884 (18)	47.887 (64)	0.12	0.13	0.8444 (89)	47.04 (50)	3.291 (35)
27.4910 (18)	46.88 (11)	0.23	0.24	0.8367 (89)	46.04 (50)	3.244 (36)
27.6921 (18)	45.94 (18)	0.39	0.39	0.8291 (89)	45.11 (52)	3.202 (37)
27.8919 (18)	44.93 (24)	0.53	0.53	0.8217 (89)	44.11 (53)	3.154 (38)
28.0903 (19)	44.04 (47)	1.07	1.07	0.8145 (89)	43.22 (66)	3.112 (48)

with different experimental geometries, so presented a very strong argument for the possibility of beamline-independent, portable and reproducible measurements – that is, the potential to ask questions on an absolute and on a relative basis of theory.

The results are accurate to better than 0.1%, permitting critical tests of atomic and solid-state theory. This is one of the most accurate demonstrations of cross-platform accuracy in synchrotron studies up to now. The data set can be fully analysed by conventional XAFS analysis techniques, but the analysis can also be extended to include error propagation and uncertainty, yielding bond lengths accurate to approximately 0.24% and Debye–Waller parameters accurate to 30%. It also enabled the investigation of advanced theory (using *FDMX*) for accurate analysis of such data across the full XAFS spectrum, built on full-potential theory, yielding a bond-length accuracy of the order of 0.1% and demonstrating that a single Debye–Waller parameter is inadequate and inconsistent across the XAFS range. The first ten oscillations of XAFS are very clear. Two effective Debye–Waller parameters are determined: a high-energy value based on the highly correlated motion of bonded atoms [$\sigma_{\rm DW}$ = 0.1413 (21) Å] and an uncorrelated bulk value [$\sigma_{\rm DW}$ = 0.1766 (9) Å], in good agreement with that derived from room-temperature crystallography. The data are shown in Table 21 and are also available in the supporting information to this chapter as file bz5029sup12.pdf.

16. Dilute solutions of nickel(II) complexes with no long-range order. Hybrid technique, XAS, XAFS and nanostructure

The article by Chantler *et al.* (2015) presents a completely different type of study: the samples are dilute solutions of bis(*N*-isopropylsalicylaldiminato)nickel(II) (*i*-pr Ni for short) and bis(*N*-*n*-propylsalicylaldiminato)nickel(II) (*n*-pr Ni for short). Conventional wisdom would suggest measuring the XAS in fluorescence mode, but these data sets were measured in transmission mode, so in principle can yield an absolute measurement of XAS and XAFS without direct normalization to an additional reference standard.

However, the techniques of XERT are not appropriate for a solution or a dilute system. We cannot have several carefully calibrated thicknesses to check for systematic errors or the linearity of the detection chain. In principle, this can be addressed by using an ideal reference standard measured under identical conditions. Hence these were the first sets of data following the hybrid technique. This used different concentrations of a solution on the assumption that the local molecular structure would be unchanged (or at least similar), and, in principle, it can use a measurement of the solvent instead of (or as well as) an air path or blank measurement. The most important characteristic behind the accuracy, utility and success of these data sets is the concept of the signal-to-noise ratio versus the signal-to-background ratio. The signal-to-background ratio is very small in this case and in transmission mode in general, yet with good experimental design the signal-to-noise ratio can be very strong and such a study can provide useful insights. The hybrid technique can be used to collect data in either transmission or fluorescence mode. The data for this paper related to measurements collected in transmission mode. The measurements were made using a cryostat at *ca* 80 K. The solvent measurement was able to determine the solvent attenuation and that for the airpath, window adhesive (silicone), window (Kapton) and detector gas.

In this experiment, three samples provided three independent data sets: data for 226 discrete energies for 15.26 m*M* *i*-pr Ni, 199 independent energies for 1.515 m*M* *i*-pr Ni and 194 energies for 15.33 m*M* *n*-pr Ni were collected. A mixed solvent of 60% butyronitrile (BCN) + 40% acetonitrile (ACN) was used to prepare the solutions to avoid microcrystallization at low temperatures in the cryostat. Both complexes have the same composition, $NiN_2O_2C_{20}H_{24}$, so the ability to distinguish between the two isomers is ideally a matter for spectroscopy, isomer isolation and even machine learning. These complexes are already used as standards and reference materials by XAS researchers, because it is well believed that the *i*-pr Ni complex is tetrahedral and the *n*-pr Ni complex is square planar with identical coordination number at the Ni atom and identical atoms at very similar distances. However, it is perceived as potentially very hard or even impossible to establish the Ni conformation from XAFS.

Table 22

15m*M* *i*-pr Ni: measured X-ray mass attenuation coefficients $[\mu/\rho]_S$ from intensity measurements (I_0 and I) for a 15 m*M* solution of the complex and for its corresponding solvent.

Several possible sources of experimental errors, including energy calibration, dark current, solvent attenuation, harmonic contamination and thickness ratio [from the actual solvent attenuation and fitted background of the sample (solution)] were corrected to obtain the final results. The energies *E* are in eV with uncertainties in parentheses. Corrected X-ray mass attenuation coefficients $[\mu/\rho]_S$ of the solute S are given with the associated relative and percentage uncertainties and the absolute uncertainties including the uncertainty contributions from the thickness ratio, $t_{\rm ratio}$, and column density, $[\rho t]_c$, measurements. The (effective) photoelectric absorption coefficient $[\mu/\rho]_{\rm pe}$ is determined by subtracting the tabulated X-ray mass attenuation values of the complex for Rayleigh and Compton scattering from the total experimental X-ray mass attenuation coefficients $[\mu/\rho]_S$ at the measured energies, with uncertainties. The X-ray mass attenuation values for Rayleigh and Compton scattering are estimated, with the uncertainty of $[\mu/\rho]_{\rm R+C}$ determined from half of the variation between the FFAST and XCOM tabulated values. (Some rows of values have been omitted for brevity. The full version is available in the supporting information.)

E (eV)	$[\mu/\rho]_S$ (cm^2 g^{-1})	$\sigma_{[\mu/\rho]_{\rm rel}}$ (cm^2 g^{-1})	$\sigma_{[\mu/\rho]_{\rm rel}}$ (%)	$\sigma_{[\mu/\rho]}$ (cm^2 g^{-1})	$[\mu/\rho]_{\rm pe}$ (cm^2 g^{-1})	$\sigma_{[\mu/\rho]_{\rm pe}}$ (cm^2 g^{-1})	$[\mu/\rho]_{\rm R+C}$ (cm^2 g^{-1})
7016.75 (10)	21.5226	0.6013	2.79	0.6562	20.8524	0.6014	0.670 (11)
7618.05 (08)	14.8641	0.2674	1.80	0.3056	14.2368	0.2678	0.627 (14)
8019.31 (09)	12.4312	0.2454	1.97	0.2774	11.8503	0.2455	0.581 (08)
8019.36 (12)	13.4087	0.3431	2.56	0.3777	12.8278	0.3432	0.581 (08)
8059.16 (07)	13.4538	0.1749	1.30	0.2096	12.8818	0.1756	0.572 (15)
8099.42 (07)	12.7546	0.2021	1.58	0.2350	12.1916	0.2033	0.563 (22)
8139.14 (07)	12.9023	0.1640	1.27	0.1972	12.3479	0.1665	0.554 (29)
8179.60 (07)	10.7739	0.1630	1.51	0.1909	10.2290	0.1670	0.545 (36)
8219.50 (07)	11.6627	0.1525	1.31	0.1826	11.1280	0.1591	0.535 (45)
8259.75 (08)	11.6365	0.2348	2.02	0.2649	11.1113	0.2412	0.525 (55)
8259.80 (12)	11.0898	0.2378	2.14	0.2665	10.5647	0.2441	0.525 (55)
8299.69 (07)	12.1917	0.1382	1.13	0.1697	11.6760	0.1525	0.516 (64)
8328.92 (07)	13.0854	0.1353	1.03	0.1690	12.5592	0.1456	0.526 (54)
8329.93 (07)	13.1148	0.1287	0.98	0.1625	12.5849	0.1381	0.530 (50)
8330.88 (07)	13.6350	0.1367	1.00	0.1718	13.1015	0.1444	0.534 (47)
8331.95 (07)	13.4321	0.1420	1.06	0.1765	12.8946	0.1482	0.538 (43)
8332.78 (12)	13.5470	0.2232	1.65	0.2580	13.0065	0.2267	0.541 (40)
8332.84 (08)	13.6453	0.1582	1.16	0.1933	13.1045	0.1630	0.541 (39)
8333.73 (07)	14.1161	0.1316	0.93	0.1679	13.5771	0.1352	0.539 (31)
8334.75 (07)	14.5188	0.1273	0.88	0.1646	13.9762	0.1302	0.543 (27)
8335.70 (07)	14.7894	0.1555	1.05	0.1935	14.2434	0.1574	0.546 (24)
8336.65 (07)	14.7551	0.1332	0.90	0.1711	14.2058	0.1348	0.549 (21)
8337.71 (07)	14.6010	0.1266	0.87	0.1641	14.0481	0.1277	0.553 (17)
8338.72 (07)	15.3682	0.1310	0.85	0.1704	14.8119	0.1317	0.556 (14)
8339.21 (07)	15.4175	0.1297	0.84	0.1692	14.8596	0.1303	0.558 (12)
8339.63 (07)	15.7792	0.1323	0.84	0.1727	15.2200	0.1327	0.559 (11)
8340.10 (07)	16.2828	0.1353	0.83	0.1770	15.7220	0.1356	0.561 (09)
8340.64 (07)	17.2415	0.1331	0.77	0.1773	16.6791	0.1333	0.563 (08)
8341.11 (07)	17.9227	0.1334	0.74	0.1792	17.3588	0.1335	0.564 (06)
8341.65 (07)	19.4273	0.1291	0.66	0.1787	18.8618	0.1292	0.566 (05)
8342.12 (07)	20.5521	0.1233	0.60	0.1758	19.9852	0.1234	0.567 (03)
8342.60 (07)	21.9244	0.1209	0.55	0.1768	21.3561	0.1209	0.568 (02)
8343.13 (07)	23.8207	0.1322	0.55	0.1928	23.2509	0.1322	0.570 (00)
8343.73 (07)	26.0666	0.1338	0.51	0.2001	25.4951	0.1338	0.572 (02)
8344.20 (07)	28.8136	0.1365	0.47	0.2098	28.2408	0.1366	0.573 (03)
8344.69 (08)	32.4253	0.1787	0.55	0.2610	31.8512	0.1787	0.574 (04)
8344.75 (12)	32.4296	0.2346	0.72	0.3169	31.8554	0.2346	0.574 (04)
8345.23 (07)	35.3511	0.1262	0.36	0.2158	34.7757	0.1263	0.575 (05)
8345.64 (12)	39.1722	0.2157	0.55	0.3149	38.5958	0.2158	0.576 (06)
8345.70 (08)	39.1773	0.1620	0.41	0.2612	38.6007	0.1621	0.577 (07)
8346.18 (07)	42.7013	0.1275	0.30	0.2356	42.1235	0.1277	0.578 (08)
8346.71 (07)	46.9622	0.1311	0.28	0.2499	46.3833	0.1314	0.579 (09)
8347.25 (07)	51.2888	0.1239	0.24	0.2536	50.7087	0.1244	0.580 (10)
8347.72 (07)	56.6255	0.1597	0.28	0.3029	56.0444	0.1601	0.581 (11)
8348.26 (07)	61.1106	0.1254	0.21	0.2798	60.5284	0.1260	0.582 (12)
8348.80 (07)	65.9400	0.1305	0.20	0.2970	65.3568	0.1311	0.583 (13)
8349.39 (07)	70.2153	0.1241	0.18	0.3013	69.6311	0.1249	0.584 (14)
8349.88 (07)	73.7979	0.1271	0.17	0.3134	73.2128	0.1280	0.585 (15)
8350.36 (07)	76.1117	0.1342	0.18	0.3263	75.5259	0.1352	0.586 (16)
8350.83 (07)	77.8896	0.1229	0.16	0.3195	77.3032	0.1240	0.586 (16)
8351.31 (07)	78.5225	0.1256	0.16	0.3238	77.9354	0.1268	0.587 (17)
8351.85 (07)	78.9331	0.1277	0.16	0.3269	78.3455	0.1290	0.588 (18)
8352.32 (07)	78.7748	0.1275	0.16	0.3263	78.1867	0.1288	0.588 (18)
8352.92 (07)	79.0798	0.1280	0.16	0.3276	78.4911	0.1294	0.589 (19)
8353.40 (07)	78.4030	0.1299	0.17	0.3278	77.8140	0.1313	0.589 (19)
8353.81 (08)	77.4465	0.1663	0.21	0.3618	76.8572	0.1675	0.589 (19)
8353.87 (12)	77.4726	0.2153	0.28	0.4108	76.8834	0.2162	0.589 (19)
8354.35 (11)	76.8114	0.1996	0.26	0.3935	76.2219	0.2006	0.590 (20)
8354.41 (08)	76.7963	0.1536	0.20	0.3474	76.2068	0.1549	0.590 (20)
8354.96 (07)	75.8004	0.2431	0.32	0.4344	75.2107	0.2439	0.590 (20)
8355.43 (07)	75.6457	0.1676	0.22	0.3585	75.0561	0.1687	0.590 (20)

Table 22 (continued)

E (eV)	$[\mu/\rho]_{\rm S}$ (cm^2 g^{-1})	$\sigma_{[\mu/\rho]_{\rm rel}}$ (cm^2 g^{-1})	$\sigma_{[\mu/\rho]_{\rm rel}}$ (%)	$\sigma_{[\mu/\rho]}$ (cm^2 g^{-1})	$[\mu/\rho]_{\rm pe}$ (cm^2 g^{-1})	$\sigma_{[\mu/\rho]_{\rm pe}}$ (cm^2 g^{-1})	$[\mu/\rho]_{\rm R+C}$ (cm^2 g^{-1})
8355.91 (11)	73.8969	0.2174	0.29	0.4039	73.3073	0.2182	0.590 (20)
8355.97 (08)	74.1280	0.1601	0.22	0.3472	73.5384	0.1613	0.590 (20)
8356.45 (07)	73.0458	0.1318	0.18	0.3162	72.4564	0.1332	0.589 (19)
8356.92 (07)	71.7103	0.1272	0.18	0.3082	71.1211	0.1286	0.589 (19)
8357.40 (07)	70.4098	0.1397	0.20	0.3175	69.8210	0.1410	0.589 (19)
8357.82 (11)	69.6499	0.2141	0.31	0.3899	69.0614	0.2149	0.589 (19)
8357.88 (08)	69.6967	0.1501	0.22	0.3261	69.1083	0.1513	0.589 (18)
8358.36 (07)	68.4578	0.1323	0.19	0.3052	67.8698	0.1336	0.588 (18)
8358.83 (07)	66.8694	0.1308	0.20	0.2997	66.2821	0.1320	0.587 (17)
8359.37 (07)	66.4245	0.1245	0.19	0.2922	65.8379	0.1256	0.587 (17)
8359.79 (07)	65.0605	0.1301	0.20	0.2944	64.4747	0.1311	0.586 (16)
8360.27 (07)	64.0950	0.1381	0.22	0.3000	63.5101	0.1389	0.585 (15)
8360.82 (07)	62.9721	0.2144	0.34	0.3735	62.3883	0.2149	0.584 (14)
8361.35 (07)	62.9690	0.1239	0.20	0.2830	62.3865	0.1246	0.583 (13)
8361.77 (07)	61.5139	0.1411	0.23	0.2965	60.9325	0.1415	0.581 (11)
8362.25 (07)	60.7361	0.1252	0.21	0.2786	60.1561	0.1256	0.580 (10)
8362.73 (07)	60.4462	0.1273	0.21	0.2800	59.8678	0.1276	0.579 (08)
8363.21 (07)	59.8269	0.1398	0.23	0.2909	59.2501	0.1399	0.577 (07)
8363.68 (07)	58.6372	0.1299	0.22	0.2781	58.0621	0.1300	0.575 (05)
8364.10 (07)	57.9894	0.1467	0.25	0.2932	57.4160	0.1467	0.573 (03)
8364.58 (07)	58.0144	0.1262	0.22	0.2728	57.4430	0.1262	0.571 (01)
8365.18 (07)	56.9563	0.1258	0.22	0.2697	56.3877	0.1258	0.569 (01)
8365.60 (07)	56.2500	0.1321	0.23	0.2742	55.6834	0.1321	0.567 (03)
8366.09 (07)	55.2568	0.1351	0.24	0.2747	54.6927	0.1352	0.564 (06)
8366.56 (07)	54.5053	0.1260	0.23	0.2638	53.9438	0.1263	0.562 (09)
...							
9471.79 (14)	42.8257	0.2412	0.56	0.3496	42.2957	0.2415	0.530 (12)
9471.87 (10)	42.8325	0.1709	0.40	0.2794	42.3026	0.1713	0.530 (12)
9522.39 (08)	42.8316	0.1457	0.34	0.2542	42.3041	0.1463	0.528 (12)

Table 23

1.5mM *i*-pr Ni: measured X-ray mass attenuation coefficients $[\mu/\rho]_{\rm S}$ from intensity measurements (I_0 and I) for a 1.5 mM solution of the complex and for its corresponding solvent.

Several possible sources of experimental errors, including energy calibration, dark current, solvent attenuation, harmonic contamination and thickness ratio [from the actual solvent attenuation and fitted background of the sample (solution)] were corrected to obtain the final result. The energies E are in eV with uncertainties in parentheses. Corrected X-ray mass attenuation coefficients $[\mu/\rho]_{\rm S}$ of the solute S are given with the associated relative and percentage uncertainties and the absolute uncertainties including the uncertainty contributions from the thickness ratio, $t_{\rm ratio}$, and column density, $[\rho t]_{\rm c}$, measurements. The (effective) photoelectric absorption coefficient $[\mu/\rho]_{\rm pe}$ is determined by subtracting the tabulated X-ray mass attenuation values of the complex for Rayleigh and Compton scattering from the total experimental X-ray mass attenuation coefficients $[\mu/\rho]_{\rm S}$ at the measured energies, with uncertainties. The X-ray mass attenuation values for Rayleigh and Compton scattering are estimated, with the uncertainty of $[\mu/\rho]_{\rm R+C}$ determined from half of the variation between the FFAST and XCOM tabulated values. (Some rows of values have been omitted for brevity. The full version is available in the supporting information.)

E (eV)	$[\mu/\rho]_{\rm S}$ (cm^2 g^{-1})	$\sigma_{[\mu/\rho]_{\rm rel}}$ (cm^2 g^{-1})	$\sigma_{[\mu/\rho]_{\rm rel}}$ (%)	$\sigma_{[\mu/\rho]}$ (cm^2 g^{-1})	$[\mu/\rho]_{\rm pe}$ (cm^2 g^{-1})	$\sigma_{[\mu/\rho]_{\rm pe}}$ (cm^2 g^{-1})	$[\mu/\rho]_{\rm R+C}$ (cm^2 g^{-1})
8099.36 (07)	36.8201	1.6698	4.53	1.7699	36.2571	1.6699	0.563 (22)
8139.20 (07)	24.6351	2.8668	11.6	2.9351	24.0807	2.8669	0.554 (29)
8179.54 (07)	26.3899	1.4862	5.63	1.5592	25.8450	1.4867	0.545 (36)
8219.56 (07)	14.2868	2.0371	14.2	2.0786	13.7521	2.0376	0.535 (45)
8259.68 (07)	23.1324	1.3674	5.91	1.4319	22.6072	1.3685	0.525 (55)
8299.75 (07)	13.4084	1.6295	12.2	1.6687	12.8928	1.6308	0.516 (64)
8328.92 (07)	18.7673	1.2302	6.56	1.2833	18.2411	1.2314	0.526 (54)
8329.93 (07)	20.3898	1.2591	6.18	1.3165	19.8599	1.2601	0.530 (50)
8330.88 (07)	19.2183	1.2664	6.59	1.3207	18.6848	1.2672	0.533 (47)
8331.95 (07)	21.2500	1.1905	5.60	1.2501	20.7125	1.1913	0.537 (43)
8332.84 (07)	18.2139	1.2140	6.67	1.2657	17.6732	1.2146	0.541 (39)
8333.73 (07)	21.3961	1.3173	6.16	1.3772	20.8571	1.3176	0.539 (31)
8334.75 (07)	21.0412	1.2631	6.00	1.3222	20.4986	1.2634	0.543 (27)
8335.70 (07)	22.5559	1.2547	5.56	1.3177	22.0099	1.2550	0.546 (24)
8336.70 (07)	23.2202	1.2484	5.38	1.3131	22.6707	1.2486	0.549 (21)
8337.71 (07)	22.0860	1.2646	5.73	1.3264	21.5331	1.2647	0.553 (17)
8338.72 (07)	21.0854	1.2806	6.07	1.3397	20.5291	1.2806	0.556 (14)
8339.21 (07)	22.1303	1.2761	5.77	1.3380	21.5725	1.2762	0.558 (12)
8339.63 (07)	21.7090	1.3003	5.99	1.3610	21.1497	1.3003	0.559 (11)
8340.10 (07)	23.6257	1.2924	5.47	1.3582	23.0649	1.2924	0.561 (09)
8340.64 (07)	25.2605	1.2718	5.03	1.3418	24.6980	1.2718	0.562 (08)
8341.11 (07)	26.6212	1.3845	5.20	1.4580	26.0573	1.3845	0.564 (06)
8341.65 (07)	26.5812	1.2639	4.75	1.3373	26.0157	1.2639	0.566 (04)
8342.12 (07)	29.5081	1.2332	4.18	1.3143	28.9412	1.2332	0.567 (03)
8342.60 (07)	29.6686	1.2208	4.11	1.3022	29.1002	1.2208	0.568 (02)
8343.13 (07)	32.5808	1.2454	3.82	1.3344	32.0109	1.2454	0.570 (00)

Table 23 (continued)

E (eV)	$[\mu/\rho]_{\rm S}$ (cm^2 g^{-1})	$\sigma_{[\mu/\rho]_{\rm rel}}$ (cm^2 g^{-1})	$\sigma_{[\mu/\rho]_{\rm rel}}$ (%)	$\sigma_{[\mu/\rho]}$ (cm^2 g^{-1})	$[\mu/\rho]_{\rm pe}$ (cm^2 g^{-1})	$\sigma_{[\mu/\rho]_{\rm pe}}$ (cm^2 g^{-1})	$[\mu/\rho]_{\rm R+C}$ (cm^2 g^{-1})
8343.73 (07)	33.9700	1.3099	3.86	1.4026	33.3985	1.3099	0.572 (02)
8344.20 (07)	37.5385	1.2379	3.30	1.3399	36.9657	1.2379	0.573 (03)
8344.75 (07)	40.3905	1.2714	3.15	1.3807	39.8163	1.2714	0.574 (04)
8345.23 (07)	46.1060	1.2319	2.67	1.3562	45.5306	1.2320	0.575 (05)
8345.70 (07)	48.6691	1.1919	2.45	1.3228	48.0925	1.1919	0.577 (07)
8346.12 (07)	53.8558	1.1712	2.17	1.3156	53.2782	1.1712	0.578 (08)
8346.71 (07)	56.6905	1.1872	2.09	1.3390	56.1115	1.1873	0.579 (09)
8347.25 (07)	62.3970	1.3015	2.09	1.4681	61.8169	1.3015	0.580 (10)
8347.72 (07)	65.3705	1.1849	1.81	1.3592	64.7894	1.1849	0.581 (11)
8348.26 (07)	73.6468	1.1839	1.61	1.3798	73.0646	1.1840	0.582 (12)
8348.80 (07)	77.6169	1.2166	1.57	1.4228	77.0337	1.2167	0.583 (13)
8349.39 (07)	83.2275	1.2775	1.53	1.4983	82.6433	1.2776	0.584 (14)
8349.88 (07)	84.6464	1.1817	1.40	1.4062	84.0614	1.1818	0.585 (15)
8350.36 (07)	89.4259	1.2367	1.38	1.4736	88.8401	1.2368	0.586 (16)
8350.83 (07)	88.7259	1.2723	1.43	1.5074	88.1395	1.2724	0.586 (16)
8351.31 (07)	92.1816	1.2068	1.31	1.4509	91.5946	1.2069	0.587 (17)
8351.85 (07)	91.0746	1.3127	1.44	1.5539	90.4869	1.3129	0.588 (18)
8352.32 (07)	91.7652	1.2537	1.37	1.4967	91.1771	1.2538	0.588 (18)
8352.92 (07)	90.7730	1.2374	1.36	1.4778	90.1843	1.2375	0.589 (19)
8353.40 (07)	88.6976	1.2258	1.38	1.4608	88.1086	1.2259	0.589 (19)
8353.87 (07)	90.9187	1.2680	1.39	1.5088	90.3294	1.2682	0.589 (19)
8354.35 (07)	88.4200	1.2682	1.43	1.5025	87.8305	1.2683	0.589 (19)
8354.96 (07)	87.1118	1.2182	1.40	1.4491	86.5222	1.2184	0.590 (20)
8355.43 (07)	86.1762	1.2732	1.48	1.5017	85.5866	1.2734	0.590 (20)
8355.97 (07)	84.6883	1.2437	1.47	1.4683	84.0987	1.2438	0.590 (20)
8356.45 (07)	85.1552	1.2510	1.47	1.4768	84.5658	1.2512	0.589 (19)
8356.92 (07)	84.7208	1.5755	1.86	1.8001	84.1316	1.5756	0.589 (19)
8357.40 (07)	81.5294	1.2262	1.50	1.4426	80.9405	1.2263	0.589 (19)
8357.88 (07)	80.1758	1.2960	1.62	1.5089	79.5873	1.2962	0.588 (18)
8358.36 (07)	80.0005	1.2598	1.57	1.4722	79.4125	1.2599	0.588 (18)
8358.83 (07)	77.9530	1.1855	1.52	1.3925	77.3657	1.1856	0.587 (17)
8359.37 (07)	77.2138	1.2133	1.57	1.4184	76.6273	1.2134	0.587 (17)
8359.79 (07)	76.1148	1.2178	1.60	1.4201	75.5289	1.2179	0.586 (16)
8360.27 (07)	74.8982	1.2296	1.64	1.4287	74.3133	1.2297	0.585 (15)
8360.82 (07)	74.0557	1.2609	1.70	1.4578	73.4719	1.2609	0.584 (14)
8361.35 (07)	73.2283	1.2497	1.71	1.4445	72.6458	1.2498	0.583 (12)
8361.77 (07)	72.6399	1.2015	1.65	1.3948	72.0585	1.2016	0.581 (11)
8362.25 (07)	70.9479	1.1698	1.65	1.3587	70.3679	1.1699	0.580 (10)
8362.79 (07)	69.6480	1.2151	1.74	1.4006	69.0697	1.2152	0.578 (08)
8363.21 (07)	69.2431	1.2000	1.73	1.3844	68.6662	1.2000	0.577 (07)
8363.68 (07)	69.4906	1.2508	1.80	1.4359	68.9156	1.2508	0.575 (05)
8364.10 (07)	67.3170	1.2547	1.86	1.4341	66.7436	1.2547	0.573 (03)
8364.58 (07)	65.9459	1.2072	1.83	1.3831	65.3745	1.2072	0.571 (01)
8365.18 (07)	65.3861	1.2928	1.98	1.4672	64.8175	1.2928	0.569 (01)
8365.60 (07)	65.6587	1.1522	1.75	1.3273	65.0921	1.1522	0.567 (03)
8366.09 (07)	63.8118	1.3465	2.11	1.5168	63.2477	1.3465	0.564 (06)
…							
8990.29 (12)	55.1360	1.9125	3.47	2.0602	54.5844	1.9125	0.552 (11)
8990.36 (08)	49.9196	1.4712	2.95	1.6053	49.3680	1.4712	0.552 (11)
9020.47 (07)	63.1531	1.2094	1.91	1.3779	62.6029	1.2094	0.550 (11)

Table 24

15mM n-pr Ni: measured X-ray mass attenuation coefficients $[\mu/\rho]_{\rm S}$ determined from the intensity measurements (I_0 and I) for a 15 mM solution of the complex and for its corresponding solvent.

Several possible sources of experimental errors, including energy calibration, dark current, solvent attenuation, harmonic contamination and thickness ratio [from the actual solvent attenuation and fitted background of the sample (solution)] were corrected to obtain the final result. The energies E are in eV with uncertainties in parentheses. Corrected X-ray mass attenuation coefficients $[\mu/\rho]_{\rm S}$ of the solute S are given with the associated relative and percentage uncertainties and the absolute uncertainties including the uncertainty contributions from the thickness ratio, $t_{\rm ratio}$, and column density, $[\rho t]_{\rm c}$, measurements. The (effective) photoelectric absorption coefficient $[\mu/\rho]_{\rm pe}$ is determined by subtracting the tabulated X-ray mass attenuation values of the complex for Rayleigh and Compton scattering from the total experimental X-ray mass attenuation coefficients $[\mu/\rho]_{\rm S}$ at the measured energies, with uncertainties. The X-ray mass attenuation values for Rayleigh and Compton scattering are estimated, with the uncertainty of $[\mu/\rho]_{\rm R+C}$ determined from half of the variation between the FFAST and XCOM tabulated values. (Some rows of values have been omitted for brevity. The full version is available in the supporting information.)

E (eV)	$[\mu/\rho]_{\rm S}$ (cm^2 g^{-1})	$\sigma_{[\mu/\rho]_{\rm rel}}$ (cm^2 g^{-1})	$\sigma_{[\mu/\rho]_{\rm rel}}$ (%)	$\sigma_{[\mu/\rho]}$ (cm^2 g^{-1})	$[\mu/\rho]_{\rm pe}$ (cm^2 g^{-1})	$\sigma_{[\mu/\rho]_{\rm pe}}$ (cm^2 g^{-1})	$[\mu/\rho]_{\rm R+C}$ (cm^2 g^{-1})
7918.60 (11)	15.0026	0.3439	2.29	0.3566	14.3975	0.3440	0.605 (10)
7958.94 (10)	14.4521	0.1280	0.89	0.1404	13.8570	0.1280	0.595 (02)
7998.73 (10)	12.9877	0.2331	1.79	0.2446	12.4021	0.2331	0.586 (05)
8039.15 (10)	13.4378	0.1575	1.17	0.1693	12.8614	0.1579	0.576 (12)
8078.88 (12)	12.1499	0.2654	2.18	0.2765	11.5823	0.2661	0.568 (19)
8078.93 (17)	11.3425	0.2010	1.77	0.2117	10.7749	0.2019	0.568 (19)
8119.13 (10)	11.8420	0.1011	0.85	0.1120	11.2833	0.1043	0.559 (26)

Table 24 (continued)

E (eV)	$[\mu/\rho]_{\rm S}$ (cm^2 g^{-1})	$\sigma_{[\mu/\rho]_{\rm rel}}$ (cm^2 g^{-1})	$\sigma_{[\mu/\rho]_{\rm rel}}$ (%)	$\sigma_{[\mu/\rho]}$ (cm^2 g^{-1})	$[\mu/\rho]_{\rm pe}$ (cm^2 g^{-1})	$\sigma_{[\mu/\rho]_{\rm pe}}$ (cm^2 g^{-1})	$[\mu/\rho]_{\rm R+C}$ (cm^2 g^{-1})
8159.17 (09)	11.3740	0.1753	1.54	0.1859	10.8239	0.1782	0.550 (32)
8199.09 (09)	11.9725	0.1063	0.89	0.1173	11.4329	0.1137	0.540 (40)
8239.54 (09)	9.8658	0.2582	2.62	0.2680	9.3359	0.2631	0.530 (50)
8278.65 (09)	11.1380	0.0897	0.81	0.1002	10.6173	0.1075	0.521 (59)
8283.63 (09)	10.9600	0.1474	1.34	0.1578	10.4404	0.1593	0.520 (60)
8288.75 (09)	11.4219	0.0855	0.75	0.0962	10.9036	0.1055	0.518 (62)
8293.87 (09)	10.9533	0.1427	1.30	0.1532	10.4362	0.1560	0.517 (63)
8298.76 (09)	11.3262	0.0912	0.81	0.1018	10.8103	0.1115	0.516 (64)
8303.65 (05)	11.9663	0.0625	0.52	0.0735	11.4517	0.0905	0.515 (65)
8308.43 (09)	12.0490	0.0994	0.82	0.1104	11.5356	0.1197	0.513 (67)
8309.38 (09)	12.2179	0.0853	0.70	0.0965	11.7047	0.1084	0.513 (67)
8310.32 (09)	11.9839	0.0917	0.77	0.1027	11.4710	0.1136	0.513 (67)
8311.34 (09)	12.2849	0.0927	0.75	0.1039	11.7723	0.1146	0.513 (67)
8312.34 (09)	12.2484	0.1002	0.82	0.1113	11.7360	0.1208	0.512 (68)
8313.46 (09)	12.6040	0.0935	0.74	0.1049	12.0918	0.1156	0.512 (68)
8314.46 (09)	12.5348	0.0891	0.71	0.1004	12.0229	0.1122	0.512 (68)
8315.41 (09)	12.5665	0.0851	0.68	0.0965	12.0549	0.1092	0.512 (68)
8316.42 (09)	12.6117	0.0943	0.75	0.1057	12.1003	0.1166	0.511 (69)
8317.49 (09)	12.7160	0.0884	0.70	0.0998	12.2049	0.1121	0.511 (69)
8318.49 (09)	12.8593	0.0867	0.67	0.0982	12.3484	0.1109	0.511 (69)
8319.02 (09)	13.2490	0.0919	0.69	0.1036	12.7383	0.1151	0.511 (69)
8319.62 (09)	13.3094	0.0805	0.60	0.0922	12.7988	0.1063	0.511 (69)
8320.09 (09)	13.1921	0.0964	0.73	0.1081	12.6816	0.1189	0.510 (70)
8320.62 (09)	13.0655	0.1029	0.79	0.1145	12.5552	0.1243	0.510 (70)
8321.10 (09)	12.9936	0.1003	0.77	0.1119	12.4834	0.1222	0.510 (70)
8321.58 (09)	13.2144	0.1411	1.07	0.1528	12.7043	0.1575	0.510 (70)
8322.05 (09)	13.5160	0.0928	0.69	0.1047	13.0060	0.1163	0.510 (70)
8322.58 (09)	13.2740	0.1103	0.83	0.1220	12.7641	0.1307	0.510 (70)
8323.12 (09)	13.2916	0.0993	0.75	0.1110	12.7819	0.1217	0.510 (70)
8323.59 (09)	13.1612	0.0988	0.75	0.1104	12.6516	0.1213	0.510 (70)
8324.12 (09)	13.1028	0.0902	0.69	0.1019	12.5933	0.1145	0.509 (71)
8324.65 (09)	13.0729	0.0946	0.72	0.1062	12.5628	0.1177	0.510 (70)
8325.13 (09)	12.7662	0.0912	0.71	0.1026	12.2543	0.1138	0.512 (68)
8325.66 (09)	12.6681	0.1017	0.80	0.1131	12.1542	0.1214	0.514 (66)
8326.15 (09)	12.9941	0.0868	0.67	0.0983	12.4784	0.1080	0.516 (64)
8326.62 (09)	13.3032	0.0842	0.63	0.0960	12.7858	0.1049	0.517 (63)
8327.15 (09)	12.9793	0.0863	0.66	0.0979	12.4599	0.1054	0.519 (61)
8327.57 (09)	12.7948	0.0924	0.72	0.1039	12.2737	0.1096	0.521 (59)
8328.04 (09)	12.7191	0.0907	0.71	0.1021	12.1963	0.1072	0.523 (57)
8328.57 (09)	12.5894	0.0968	0.77	0.1082	12.0645	0.1114	0.525 (55)
8329.05 (09)	12.9246	0.0853	0.66	0.0968	12.3979	0.1006	0.527 (53)
8329.52 (09)	12.7369	0.0904	0.71	0.1018	12.2085	0.1041	0.528 (52)
8330.00 (09)	12.7613	0.1239	0.97	0.1353	12.2310	0.1335	0.530 (50)
8330.47 (09)	12.9064	0.1028	0.80	0.1143	12.3744	0.1135	0.532 (48)
8331.07 (09)	12.9967	0.0939	0.72	0.1055	12.4626	0.1045	0.534 (46)
8331.55 (09)	13.1421	0.0943	0.72	0.1060	12.6062	0.1041	0.536 (44)
8331.96 (09)	12.9859	0.0871	0.67	0.0987	12.4484	0.0969	0.537 (43)
8332.50 (09)	13.2308	0.0871	0.66	0.0988	12.6913	0.0960	0.539 (41)
8332.91 (09)	13.2972	0.0848	0.64	0.0965	12.7562	0.0933	0.541 (39)
8333.45 (09)	13.4960	0.0815	0.60	0.0933	12.9581	0.0875	0.538 (32)
8333.86 (09)	13.7092	0.0983	0.72	0.1102	13.1698	0.1029	0.539 (31)
8334.34 (09)	13.8201	0.0883	0.64	0.1003	13.2789	0.0929	0.541 (29)
8334.87 (09)	13.8094	0.1021	0.74	0.1141	13.2664	0.1056	0.543 (27)
8335.29 (09)	13.9741	0.0879	0.63	0.1000	13.4296	0.0915	0.545 (25)
8335.82 (09)	14.1363	0.0855	0.60	0.0977	13.5899	0.0887	0.546 (24)
8336.31 (09)	14.0868	0.0850	0.60	0.0972	13.5387	0.0878	0.548 (22)
8336.84 (09)	14.2042	0.1017	0.72	0.1140	13.6542	0.1037	0.550 (20)
8337.38 (09)	14.4006	0.0889	0.62	0.1012	13.8488	0.0907	0.552 (18)
8337.85 (09)	14.8022	0.0926	0.63	0.1052	14.2488	0.0941	0.553 (17)
8338.33 (09)	15.4063	0.0885	0.57	0.1015	14.8512	0.0898	0.555 (15)
8338.80 (09)	15.8844	0.0924	0.58	0.1057	15.3278	0.0934	0.557 (13)
8339.28 (09)	16.5746	0.0839	0.51	0.0975	16.0164	0.0847	0.558 (12)
8339.75 (09)	17.1886	0.0850	0.49	0.0990	16.6289	0.0857	0.560 (10)
8340.23 (09)	17.9072	0.0882	0.49	0.1025	17.3460	0.0886	0.561 (09)
8340.76 (09)	18.8303	0.0964	0.51	0.1113	18.2675	0.0966	0.563 (07)
8341.30 (09)	20.0802	0.0859	0.43	0.1015	19.5157	0.0861	0.565 (06)
8341.72 (09)	20.9746	0.0879	0.42	0.1041	20.4088	0.0880	0.566 (04)
8342.26 (09)	22.3591	0.0869	0.39	0.1038	21.7918	0.0870	0.567 (03)
8342.85 (09)	24.1739	0.0978	0.40	0.1158	23.6048	0.0978	0.569 (01)
8343.39 (09)	26.6625	0.0865	0.32	0.1059	26.0919	0.0865	0.571 (01)
8343.86 (09)	28.6822	0.0880	0.31	0.1085	28.1103	0.0880	0.572 (02)
8344.40 (09)	31.8424	0.0945	0.30	0.1168	31.2691	0.0946	0.573 (03)
8344.88 (09)	34.6921	0.0834	0.24	0.1074	34.1175	0.0836	0.575 (05)

Table 24 (continued)

E (eV)	$[\mu/\rho]_S$ (cm^2 g^{-1})	$\sigma_{[\mu/\rho]_{rel}}$ (cm^2 g^{-1})	$\sigma_{[\mu/\rho]_{rel}}$ (%)	$\sigma_{[\mu/\rho]}$ (cm^2 g^{-1})	$[\mu/\rho]_{pe}$ (cm^2 g^{-1})	$\sigma_{[\mu/\rho]_{pe}}$ (cm^2 g^{-1})	$[\mu/\rho]_{R+C}$ (cm^2 g^{-1})
8345.35 (09)	38.6115	0.0930	0.24	0.1192	38.0358	0.0932	0.576 (06)
8345.83 (09)	42.3968	0.0798	0.19	0.1081	41.8199	0.0801	0.577 (07)
8346.42 (09)	47.0804	0.0929	0.20	0.1239	46.5021	0.0933	0.578 (08)
8346.91 (09)	51.3041	0.0932	0.18	0.1266	50.7247	0.0936	0.579 (09)
8347.44 (09)	56.3805	0.0962	0.17	0.1325	55.7999	0.0968	0.581 (11)
8348.52 (09)	70.4395	0.0918	0.13	0.1361	69.8568	0.0927	0.583 (13)
8350.60 (09)	76.0340	0.0945	0.12	0.1420	75.4479	0.0958	0.586 (16)
8352.64 (09)	75.0248	0.0917	0.12	0.1386	74.4364	0.0935	0.588 (18)
8354.67 (09)	72.4205	0.0935	0.13	0.1389	71.8309	0.0955	0.590 (20)
8356.70 (09)	68.0119	0.0848	0.12	0.1278	67.4226	0.0870	0.589 (19)
8358.61 (09)	64.6053	0.1025	0.16	0.1434	64.0177	0.1040	0.588 (18)
8360.59 (08)	61.3634	0.0921	0.15	0.1313	60.7791	0.0932	0.584 (14)
8362.57 (08)	58.7797	0.0828	0.14	0.1204	58.2007	0.0833	0.579 (09)
8364.36 (08)	55.9661	0.0913	0.16	0.1274	55.3938	0.0914	0.572 (02)
8366.39 (08)	54.2395	0.0904	0.17	0.1254	53.6771	0.0907	0.562 (08)
8368.38 (08)	52.1884	0.0836	0.16	0.1175	51.6385	0.0860	0.550 (20)
8370.29 (08)	50.6032	0.0935	0.18	0.1265	50.0682	0.0998	0.535 (35)
8372.34 (08)	48.6696	0.0872	0.18	0.1191	48.1540	0.1028	0.516 (54)
8374.38 (08)	47.8563	0.1010	0.21	0.1325	47.3642	0.1276	0.492 (78)
8376.42 (08)	47.2438	0.0976	0.21	0.1287	46.7503	0.1240	0.494 (77)
8378.53 (08)	47.8057	0.1334	0.28	0.1648	47.3096	0.1525	0.496 (74)
8380.57 (08)	49.1540	0.0861	0.18	0.1183	48.6553	0.1118	0.499 (71)
8382.62 (08)	51.1068	0.0931	0.18	0.1264	50.6055	0.1157	0.501 (69)
8384.66 (08)	52.9162	0.0932	0.18	0.1275	52.4124	0.1143	0.504 (66)
8386.64 (08)	54.2970	0.1060	0.20	0.1411	53.7908	0.1237	0.506 (64)
...							
9380.95 (08)	40.7612	0.0887	0.22	0.1161	40.2269	0.0896	0.534 (12)
9471.67 (09)	40.6914	0.0795	0.20	0.1068	40.1615	0.0804	0.530 (12)
9521.81 (09)	40.2717	0.1644	0.41	0.1915	39.7442	0.1648	0.528 (12)

The data that were deposited as supporting information to the original publication are also available here in Tables 22 to 24 and also as supporting information to this chapter as file bz5029sup13.pdf. These tables of data have detailed column headings and header information, so can be used for diverse applications.

Fig. 8 shows a schematic of the experimental setup at the ANBF, Tsukuba, Japan, using the hybrid technique that was used to collect transmission and fluorescence XAS from these multiple dilute solutions of nickel(II) complexes and absorption spectra from a 5 µm Ni foil. Fig. 9 illustrates the multi-chambered solution cell suitable for cryostat use, and the filling of the chambers. This was the first implementation of the hybrid technique and led to further developments of the technique in later publications.

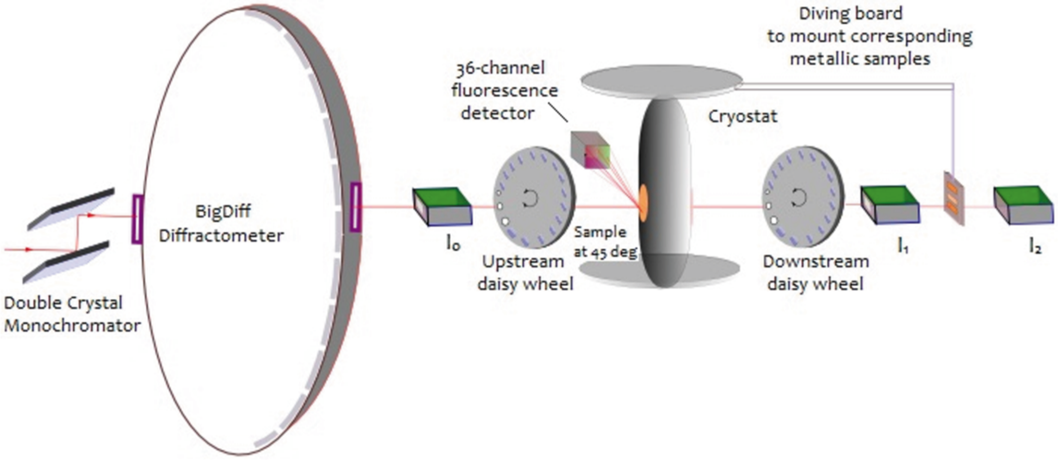

Figure 8

A schematic diagram of the experimental setup using the hybrid technique at the ANBF, Tsukuba, Japan. A multi-chambered solution cell was used in the cryostat containing two dilute solutions and the pure solvent in three chambers. The cryostat was translated vertically to record intensities attenuated by each of the solutions at each energy. Two daisy wheels containing 14 aluminium filters (of different thicknesses) were employed upstream and downstream to monitor harmonic contamination from higher-order reflections. Different aperture sizes on the daisy wheel allowed aperture-dependent measurements to be collected in order to characterize scattering effects for correction. Three ion chambers were employed to record unattenuated intensities, I_0, intensities attenuated by the dilute solutions, I_1, and intensities further attenuated by the corresponding metallic sample mounted with a cantilever as shown, I_2.

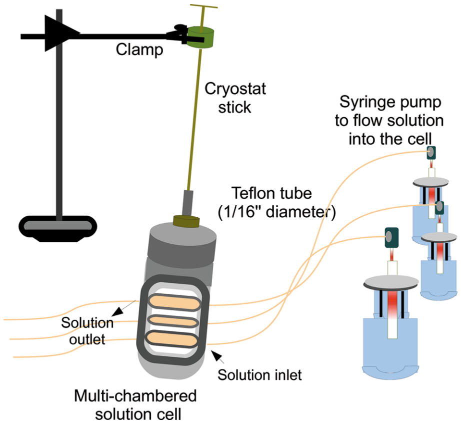

Figure 9
A three-chambered cryostat cell is filled with three solutions (15 m*M* and 1.5 m*M* nickel(II) complex, and pure solvent). A precise flow of solution into the chambers was achieved using three 10 ml syringe pumps, with fittings, and 1/16 inch Teflon tubes. The cell, mounted on a cryostat stick, was clamped in the horizontal plane. Each syringe pump was controlled by a stepper-motor controller programmed by software to pulse the syringe pumps.

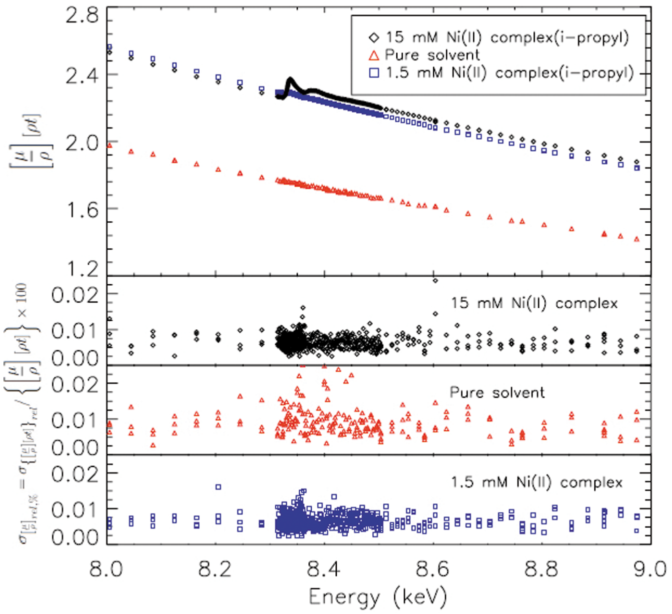

Figure 10
X-ray absorption spectra (top plot) and corresponding uncertainties (lower plots) using two solutions (15 m*M* and 1.5 m*M*) of the *i*-pr Ni complex, and the pure solvent. The black diamond markers represent the measurements with the 15 m*M* solution, and the measurements with the 1.5 m*M* solution and the pure solvent are represented by the blue square markers and the red triangles, respectively. Subplots indicate the percentage uncertainties underneath using the same coloured markers as for the solution spectra. A 0.005–0.06% variation in the uncertainties over the energy range represents the quality of data from the solutions. The variation in the background between the spectra was mainly due to the variation in the effective integrated column density $[m/A]_{\rm eff}$ of the solutions in different chambers.The well defined peaks confirm that there was negligible leaking between the solutions through the chambers. The pure solvent was not sucked uniformly during the filling, causing a linear offset from the background of the solutions. Modelling of the solvent (using the known experimental geometry) quantified and corrected for this background effect (Chantler *et al.*, 2015).

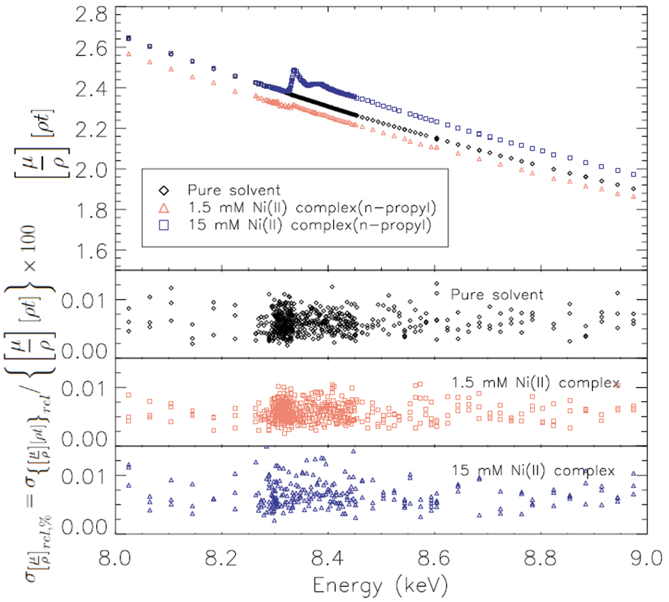

Figure 11
X-ray absorption spectra using two solutions (15 m*M*, 1.5 m*M*) of the *n*-pr Ni complex and the pure solvent used to prepare the solutions. As in Fig. 10, the corresponding uncertainties are presented in the plots underneath using the same coloured markers as for the solutions. Compared with the spectra obtained for the tetrahedral *i*-pr Ni complex, the variation between the backgrounds of the spectra for the square planar *n*-pr Ni complex are quite minor. The solvent absorption represented by the black diamonds was subtracted from the solution absorption.

Fig. 10 presents full plots of measured $[\mu/\rho][\rho t]$ values for the two *i*-pr Ni solutions and the pure solvent (top pane) and the statistical accuracy of these three data sets in the bottom panes. Despite the dilution and the very low signal-to-background ratio, the accuracy of each data set is at or below 0.01%, so the solvent can be subtracted to find the attenuation by the active species and the absorption edge. Similarly, Fig. 11 presents full plots of measured $[\mu/\rho][\rho t]$ values for the two *n*-pr Ni solutions and the pure solvent (top pane) with the statistical accuracy of these three in the bottom panes.

Because of the high signal-to-noise ratio and the characterization of the solvent and windows, highly accurate values for the attenuation due to the active species can be obtained (Figs. 12, 13). In these figures, the attenuation by the active species, *i.e.* the 15 m*M* solute, $\{[\mu/\rho][\rho t]\}_{\rm S}$, is plotted in the top panel, with four subpanels showing contributions to the total absolute uncertainty (second panel, $\delta_{\rm total}$) from the fitting/filling fraction (third panel, $\delta_{\rm frac}$), the statistical uncertainty from the sample and solvent measurements (fourth panel, $\delta_{[\mu/\rho][\rho t]{\rm S,stat}} = \sigma_{\{[\mu/\rho][\rho t]\}_{\rm S,stat}}$) and the contribution to the uncertainty from the background and dark current (bottom panel, $\delta_{\rm bkg+dc}$). Although the signals only correspond to a peak magnitude of 0.15 attenuation, or 0.12 above the below-edge value, the uncertainty is less than 0.0003 from statistical sources of error and about 0.0003 from statistical and system-related sources of error, so in fact the attenuation has an uncertainty of only about 0.2% across the edge, XANES and XAFS region.

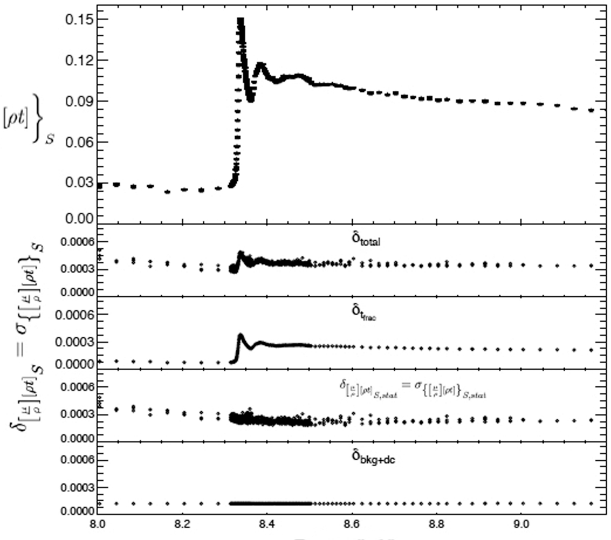

Figure 12
Corrected and normalized XAS (attenuation) of the *i*-pr Ni isomer (solute) $\{[\mu/\rho][\rho t]\}_S$ determined from the attenuations of 15 m*M* solutions following the solvent subtraction, as represented in the tabulated data sets. The corresponding total uncertainty (second panel, $\delta_{\rm total}$) was propagated from the uncertainty contributions of the fitting/filling solvent coefficient (third panel, $\delta_{\rm frac}$), the variance of repeated measurements with both the solution and the solvent (fourth panel, $\delta_{[\mu/\rho][\rho t]{\rm S,stat}} = \sigma_{\{[\mu/\rho][\rho t]\}_{\rm S,stat}}$), and the background and dark-current corrections (bottom panel, $\delta_{\rm bkg+dc}$). The accuracy allowed reliable structural analysis of *i*-pr Ni using XAFS. At each of the energies, three aperture-dependent measurements are in excellent agreement.

The *eFEFFit* package was used with weighting of the data derived from the experimental uncertainty, and in each case converged to a well defined XAFS model (Islam *et al.*, 2015). Structural refinement of the *i*-pr Ni complex gave an excellent fit to a tetrahedral geometry. *n*-pr Ni showed a distorted square planar geometry. This demonstrates the insight that can be obtained from the propagation of uncertainties in XAFS analysis and the consequent confidence in hypothesis testing and in the *ab initio* analysis of alternative structures (Fig. 14).

17. Dilute solutions with no long-range order: m*M* solutions of ferrocene and decamethylferrocene. Hybrid technique, XAS, XAFS and nanostructure

Islam *et al.* (2016) reported another example of the hybrid technique applied to the relatively small molecules ferrocene [Fc, $Fe(C_5H_5)_2$] and decamethylferrocene [DmFc or Fc*, $Fe(C_5(CH_3)_5)_2$], also as dilute solutions, at two concentrations and with a solvent measurement. Ferrocene has long been the archetypal metallocene and was the first known example of organometallic bonding. As well as having many applications and derivatives, it is also used as a key reference material for chemistry and XAS but, interestingly, one for which the structure is ill-determined. The experimental setup used by Islam *et al.* was equivalent to that described in Section 16 for hybrid measurement in transmission (and fluorescence) modes.

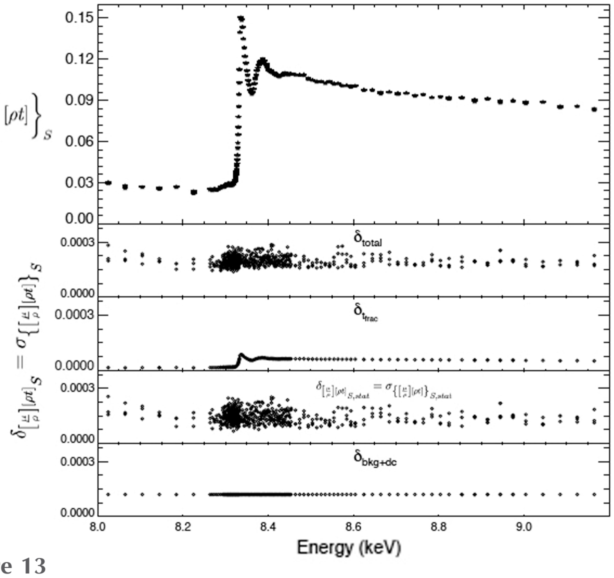

Figure 13
Corrected and normalized XAS (attenuation) of 15 m*M* *n*-pr Ni (solute) $\{[\mu/\rho][\rho t]\}_S$. The corresponding total uncertainty (second panel, $\delta_{\rm total}$) was propagated from the uncertainty contributions of the fitting/filling solvent coefficient (third panel, $\delta_{\rm frac}$), the variance of repeated measurements with both the solution and the solvent (fourth panel, $\delta_{[\mu/\rho][\rho t]{\rm S,stat}} = \sigma_{\{[\mu/\rho][\rho t]\}_{\rm S,stat}}$), and the background and dark-current corrections (bottom panel, $\delta_{\rm bkg+dc}$). Three to six aperture-dependent measurements were made at each energy and are in excellent agreement. High accuracy XAS for *n*-pr Ni was obtained for the path-length fraction ($t_{\rm frac}$ = 0.9804 ± 0.0006).

An earlier experiment looked at 10 m*M* Fc in fluorescence mode at 10–20 K (Chantler *et al.*, 2012*b*). This primarily led to development of the understanding of modelling absorption and self-absorption in multipixel fluorescence detectors.

Four data sets are presented in Tables 25–28, and also in the supporting information to this chapter as the file bz5029sup14.pdf. These are for nominal concentrations of 15 m*M* Fc, 3 m*M* Fc, 15 m*M* DmFc and 3 m*M* DmFc. The actual concentations were 15.26 m*M* and 3.07 m*M* (Fc) and 15.29 m*M* and 3.06 m*M* (DmFc), respectively. The columns of data and the header information for these tables were detailed, allowing use of the data for diverse applications.

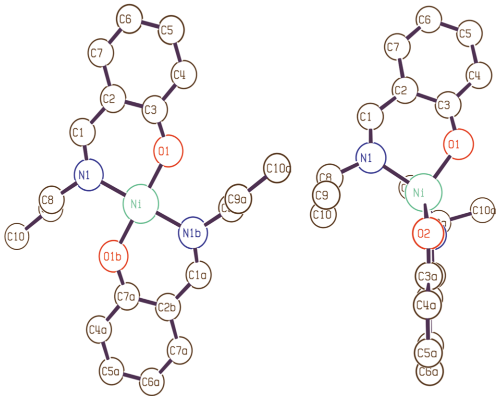

Figure 14
Room-temperature crystal structures (Fox *et al.*, 1964; Britton & Pignolet, 1989) for *n*-pr Ni with distorted square planar geometry and *i*-pr Ni with tetrahedral geometry, excluding hydrogen atoms.

Table 25
15m*M* Fc: X-ray mass attenuation coefficients $[\mu/\rho]_{\rm S}$ from the absolute intensities (I_0 and I) for a 15 m*M* Fc solution.

The energies E are in eV with uncertainties in parentheses. Corrected X-ray mass attenuation coefficients $[\mu/\rho]_{\rm S}$ of the solute S are given with associated relative and percentage uncertainties, and the absolute uncertainties including the uncertainty contributions from the thickness ratio $t_{\rm ratio}$ and column density $[\rho t]_{\rm c}$ measurements. The (effective) photoelectric absorption coefficient $[\mu/\rho]_{\rm pe}$ is determined by subtracting the tabulated X-ray mass attenuations of the complex for the Rayleigh and Compton scattering from the total experimental X-ray mass attenuation coefficients $[\mu/\rho]_{\rm S}$ at the measured energies, with uncertainties. The X-ray mass attenuation due to Rayleigh and Compton scattering is estimated, with the uncertainty of $[\mu/\rho]_{\rm R+C}$ determined from half of the variation between the FFAST and XCOM values. (Some rows of values have been omitted for brevity. The full version is available in the supporting information.)

E (eV)	$[\mu/\rho]_{\rm S}$ (cm^2 g^{-1})	$\sigma_{[\mu/\rho]_{\rm rel}}$ (cm^2 g^{-1})	$\sigma_{[\mu/\rho]_{\rm rel}}$ (%)	$\sigma_{[\mu/\rho]}$ (cm^2 g^{-1})	$[\mu/\rho]_{\rm pe}$ (cm^2 g^{-1})	$\sigma_{[\mu/\rho]_{\rm pe}}$ (cm^2 g^{-1})	$[\mu/\rho]_{\rm R+C}$ (cm^2 g^{-1})
6912.18 (13)	16.9302	0.2137	1.26	0.2416	16.0942	0.2144	0.836 (17)
7098.44 (17)	17.7364	0.3378	1.90	0.3668	16.9618	0.3388	0.775 (26)
7099.17 (17)	17.4919	0.2799	1.60	0.3086	16.7176	0.2811	0.774 (26)
7099.98 (17)	16.8730	0.2364	1.40	0.2642	16.0989	0.2378	0.774 (26)
7100.74 (17)	17.6435	0.2849	1.61	0.3138	16.8700	0.2861	0.774 (26)
7101.55 (17)	17.6649	0.3007	1.70	0.3296	16.8920	0.3018	0.773 (26)
7102.32 (17)	17.2871	0.5204	3.01	0.5488	16.5147	0.5210	0.772 (26)
7103.10 (17)	17.0115	0.2742	1.61	0.3022	16.2397	0.2754	0.772 (26)
7103.87 (17)	19.0457	0.2846	1.49	0.3155	18.2744	0.2857	0.771 (25)
7104.68 (17)	18.0019	0.2488	1.38	0.2782	17.2312	0.2501	0.771 (25)
7105.53 (17)	18.7994	0.3130	1.66	0.3435	18.0232	0.3136	0.776 (19)
7106.30 (17)	18.0965	0.2217	1.23	0.2512	17.3134	0.2220	0.783 (12)
7107.11 (17)	17.9869	0.2473	1.37	0.2767	17.1965	0.2473	0.790 (04)
7107.88 (17)	18.2976	0.3044	1.66	0.3342	17.5003	0.3044	0.797 (04)
7108.73 (17)	18.4132	0.2774	1.51	0.3074	17.6082	0.2777	0.805 (12)
7109.55 (17)	18.5824	0.5303	2.85	0.5605	17.7700	0.5307	0.812 (20)
7110.40 (17)	21.5751	0.2843	1.32	0.3188	20.7550	0.2858	0.820 (29)
7111.22 (17)	19.8999	0.2909	1.46	0.3230	19.0723	0.2932	0.828 (37)
7111.95 (21)	22.8657	0.2882	1.26	0.3245	22.0315	0.2916	0.834 (44)
7112.81 (17)	22.1592	0.2397	1.08	0.2750	21.3120	0.2443	0.847 (47)
7113.62 (17)	23.0609	0.3348	1.45	0.3714	22.2061	0.3393	0.855 (55)
7114.48 (17)	23.6683	0.3847	1.63	0.4222	22.8054	0.3898	0.863 (63)
7115.29 (17)	26.4959	0.2667	1.01	0.3082	25.6255	0.2758	0.870 (70)
7116.02 (17)	31.5720	0.2525	0.80	0.3012	30.6949	0.2640	0.877 (77)
7116.83 (17)	35.7122	0.2740	0.77	0.3286	34.8279	0.2867	0.884 (84)
7117.60 (21)	41.7340	0.9645	2.31	1.0277	40.8428	0.9688	0.891 (91)
7118.43 (17)	48.9884	0.3908	0.80	0.4643	48.0900	0.4030	0.898 (98)
7119.24 (17)	59.1354	0.2932	0.50	0.3812	58.2300	0.3115	0.91 (11)
7120.70 (17)	80.2569	0.4001	0.50	0.5181	79.3395	0.4169	0.92 (12)
7121.51 (17)	86.5154	0.5263	0.61	0.6532	85.5917	0.5406	0.92 (12)
7122.29 (17)	86.8350	0.2925	0.34	0.4199	85.9054	0.3199	0.93 (13)
7123.10 (17)	88.2233	0.2534	0.29	0.3828	87.2878	0.2873	0.94 (14)
7123.87 (17)	92.8486	0.2216	0.24	0.3575	91.9077	0.2625	0.94 (14)
7124.60 (17)	98.8125	0.2493	0.25	0.3937	97.8669	0.2887	0.95 (15)
7125.38 (17)	107.3455	0.3041	0.28	0.4607	106.3950	0.3392	0.95 (15)
7126.20 (17)	116.2921	0.3016	0.26	0.4709	115.3370	0.3391	0.96 (16)
7127.02 (17)	125.8179	0.2999	0.24	0.4828	124.8586	0.3395	0.96 (16)
7127.83 (17)	133.3888	0.2630	0.20	0.4567	132.4257	0.3094	0.96 (16)
7128.65 (17)	141.8578	0.3448	0.24	0.5505	140.8915	0.3828	0.97 (17)
7129.38 (17)	149.0124	0.3231	0.22	0.5390	148.0436	0.3644	0.97 (17)
7130.24 (17)	158.0056	0.2163	0.14	0.4450	157.0346	0.2756	0.97 (17)
7131.06 (17)	164.4201	0.2678	0.16	0.5056	163.4476	0.3185	0.97 (17)
7131.92 (17)	174.1914	0.3530	0.20	0.6047	173.2181	0.3932	0.97 (17)
7132.74 (17)	179.2747	0.2863	0.16	0.5453	178.3013	0.3346	0.97 (17)
7133.51 (17)	181.5503	0.2502	0.14	0.5124	180.5776	0.3039	0.97 (17)
7134.34 (17)	179.6495	0.3547	0.20	0.6142	178.6784	0.3937	0.97 (17)
7135.16 (17)	176.4352	0.2847	0.16	0.5396	175.4667	0.3308	0.97 (17)
7136.02 (17)	169.6654	0.2643	0.16	0.5096	168.7005	0.3114	0.97 (17)
7136.79 (17)	161.2584	0.2727	0.17	0.5060	160.2979	0.3163	0.96 (16)
7137.57 (17)	153.5846	0.2551	0.17	0.4775	152.6295	0.2985	0.96 (16)
7138.39 (17)	144.5699	0.3027	0.21	0.5123	143.6217	0.3370	0.95 (15)
7139.16 (17)	140.6419	0.2918	0.21	0.4958	139.7013	0.3238	0.94 (14)
7139.98 (21)	136.8569	0.2409	0.18	0.4395	135.9257	0.2742	0.93 (13)
7140.80 (17)	133.8604	0.3588	0.27	0.5531	132.9402	0.3783	0.92 (12)
7141.50 (17)	130.4616	0.2780	0.21	0.4675	129.5520	0.2987	0.91 (11)
7142.24 (17)	129.0538	0.2218	0.17	0.4093	128.1567	0.2420	0.897 (97)
7143.06 (17)	127.9076	0.2248	0.18	0.4107	127.0260	0.2391	0.882 (81)
…							
8013.25 (23)	92.0455	0.4397	0.48	0.5745	91.3074	0.4401	0.738 (19)
8513.46 (35)	77.2693	0.6532	0.85	0.7670	76.5672	0.6534	0.702 (17)
9013.43 (37)	60.0279	0.3438	0.57	0.4330	59.3555	0.3441	0.672 (13)

Table 26
3m*M* Fc: measured X-ray mass attenuation coefficients $[\mu/\rho]_S$ obtained from the absolute intensities for a 3 m*M* Fc solution and its corresponding solvent.

Several experimental sources of error including energy calibration, dark current, solvent attenuation, harmonic contamination and thickness ratio [from the actual solvent attenuation and fitted background of the sample (solution)] were corrected for to obtain the final result. The columns are as in Table 25. (Some rows of values have been omitted for brevity. The full version is available in the supporting information.)

E (eV)	$[\mu/\rho]_S$ (cm^2 g^{-1})	$\sigma_{[\mu/\rho]_{rel}}$ (cm^2 g^{-1})	$\sigma_{[\mu/\rho]_{rel}}$ (%)	$\sigma_{[\mu/\rho]}$ (cm^2 g^{-1})	$[\mu/\rho]_{pe}$ (cm^2 g^{-1})	$\sigma_{[\mu/\rho]_{pe}}$ (cm^2 g^{-1})	$[\mu/\rho]_{R+C}$ (cm^2 g^{-1})
6912.18 (16)	16.2859	1.4756	9.06	1.5072	15.4499	1.4757	0.836 (17)
7098.44 (17)	21.5930	0.7112	3.29	0.7518	20.8183	0.7117	0.775 (26)
7099.17 (17)	20.4647	0.9276	4.53	0.9663	19.6903	0.9280	0.774 (26)
7100.74 (17)	19.8954	0.6268	3.15	0.6645	19.1218	0.6273	0.774 (26)
7101.55 (17)	20.9026	0.8263	3.95	0.8657	20.1297	0.8267	0.773 (26)
7102.32 (17)	19.9726	1.2683	6.35	1.3062	19.2002	1.2686	0.772 (26)
7103.10 (17)	22.2456	1.2100	5.44	1.2517	21.4738	1.2103	0.772 (26)
7103.87 (17)	20.2890	0.8569	4.22	0.8953	19.5177	0.8573	0.771 (25)
7104.68 (17)	18.3027	0.7293	3.98	0.7643	17.5320	0.7297	0.771 (25)
7105.53 (17)	20.2956	0.7486	3.69	0.7869	19.5194	0.7488	0.776 (19)
7106.34 (17)	21.8373	0.9134	4.18	0.9544	21.0538	0.9135	0.783 (11)
7107.11 (17)	18.6017	0.8735	4.70	0.9090	17.8113	0.8736	0.790 (04)
7107.88 (17)	20.5142	0.7131	3.48	0.7519	19.7169	0.7132	0.797 (04)
7108.73 (17)	19.2439	0.6022	3.13	0.6388	18.4389	0.6024	0.805 (12)
7109.55 (17)	22.6475	1.8813	8.31	1.9237	21.8351	1.8814	0.812 (20)
7110.40 (17)	20.9884	0.8097	3.86	0.8492	20.1682	0.8102	0.820 (29)
7111.22 (17)	23.1301	1.0821	4.68	1.1252	22.3026	1.0827	0.828 (37)
7111.95 (17)	22.6661	0.8341	3.68	0.8765	21.8319	0.8353	0.834 (44)
7112.81 (17)	20.9731	0.8075	3.85	0.8470	20.1259	0.8088	0.847 (47)
7113.62 (17)	24.1558	1.1368	4.71	1.1818	23.3010	1.1382	0.855 (55)
7114.48 (17)	22.4814	0.9759	4.34	1.0180	21.6185	0.9779	0.863 (63)
7115.25 (17)	25.7762	1.3678	5.31	1.4155	24.9062	1.3696	0.870 (70)
7116.02 (17)	26.2477	0.8704	3.32	0.9189	25.3706	0.8738	0.877 (77)
7116.83 (17)	29.5644	1.1207	3.79	1.1749	28.6801	1.1239	0.884 (84)
7117.64 (17)	31.4720	1.0444	3.32	1.1018	30.5804	1.0484	0.892 (92)
7118.43 (21)	35.8397	0.8274	2.31	0.8922	34.9413	0.8333	0.898 (98)
7119.24 (17)	37.4569	1.0165	2.71	1.0840	36.5516	1.0219	0.91 (11)
7119.97 (17)	45.0492	1.1954	2.65	1.2759	44.1378	1.2006	0.91 (11)
7120.70 (17)	90.3340	0.8949	0.99	1.0522	89.4167	0.9025	0.92 (12)
7121.51 (17)	86.3696	0.9201	1.07	1.0707	85.4459	0.9283	0.92 (12)
7122.29 (17)	92.8384	0.8135	0.88	0.9751	91.9087	0.8238	0.93 (13)
7123.10 (17)	93.1584	1.3417	1.44	1.5038	92.2229	1.3485	0.94 (14)
7123.87 (17)	93.9028	1.2588	1.34	1.4222	92.9619	1.2666	0.94 (14)
7124.60 (17)	103.1289	0.7698	0.75	0.9489	102.1832	0.7835	0.95 (15)
7125.38 (17)	107.0117	1.0742	1.00	1.2599	106.0612	1.0847	0.95 (15)
7126.20 (17)	112.7076	0.7729	0.69	0.9683	111.7526	0.7883	0.96 (16)
7127.02 (17)	123.6424	0.6636	0.54	0.8776	122.6831	0.6824	0.96 (16)
7127.83 (17)	131.0334	0.8384	0.64	1.0650	130.0704	0.8541	0.96 (16)
7128.65 (17)	135.3651	0.8149	0.60	1.0488	134.3988	0.8317	0.97 (17)
7129.38 (17)	141.9209	1.1841	0.83	1.4291	140.9521	1.1960	0.97 (17)
7130.24 (17)	151.6987	1.3200	0.87	1.5816	150.7277	1.3310	0.97 (17)
7131.06 (17)	162.5304	0.7351	0.45	1.0151	161.5579	0.7550	0.97 (17)
7131.92 (17)	166.1009	0.7056	0.42	0.9917	165.1276	0.7266	0.97 (17)
7132.74 (17)	167.0337	0.6675	0.40	0.9552	166.0603	0.6896	0.97 (17)
7133.51 (17)	173.4009	0.8363	0.48	1.1348	172.4283	0.8540	0.97 (17)
7134.34 (17)	167.3626	0.7087	0.42	0.9969	166.3915	0.7290	0.97 (17)
7135.16 (17)	165.6996	0.7794	0.47	1.0648	164.7310	0.7974	0.97 (17)
7136.02 (17)	161.3311	1.3828	0.86	1.6608	160.3663	1.3926	0.97 (17)
7136.79 (17)	153.6411	0.8926	0.58	1.1575	152.6806	0.9068	0.96 (16)
7137.57 (17)	151.5031	1.9592	1.29	2.2205	150.5480	1.9654	0.96 (16)
7138.39 (17)	147.7561	0.8667	0.59	1.1216	146.8079	0.8792	0.95 (15)
7139.16 (17)	140.7466	1.0964	0.78	1.3395	139.8060	1.1054	0.94 (14)
7139.98 (17)	140.3181	1.5028	1.07	1.7451	139.3870	1.5084	0.93 (13)
7140.76 (17)	132.6806	0.9931	0.75	1.2224	131.7599	1.0003	0.92 (12)
7141.50 (17)	132.5578	0.8295	0.63	1.0586	131.6481	0.8367	0.91 (10)
7142.24 (17)	128.8725	0.7678	0.60	0.9906	127.9753	0.7739	0.897 (97)
7143.06 (17)	131.0553	1.4215	1.08	1.6481	130.1737	1.4239	0.882 (81)
7143.83 (17)	130.7432	1.0405	0.80	1.2666	129.8779	1.0426	0.865 (65)
. . .							
7792.25 (19)	111.8551	0.6581	0.59	0.8520	111.0951	0.6583	0.760 (15)
7796.34 (19)	111.5849	0.6816	0.61	0.8751	110.8253	0.6818	0.760 (15)
7800.44 (14)	112.6637	0.5423	0.48	0.7377	111.9046	0.5426	0.759 (15)

Table 27
15m*M* DmFc: X-ray mass attenuation coefficients $[\mu/\rho]_S$ using absolute intensities (I_0 and I) for a 15 m*M* DmFc solution and its corresponding solvent.

A number of key experimental sources of systematic errors including energy calibration, dark current, solvent attenuation, harmonic contamination and thickness ratio [from the actual solvent attenuation and fitted background of the sample (solution)] were corrected for to obtain the final results with the accuracy stated. The columns are as in Table 25. (Some rows of values have been omitted for brevity. The full version is available in the supporting information.)

E (eV)	$[\mu/\rho]_S$ (cm^2 g^{-1})	$\sigma_{[\mu/\rho]_{rel}}$ (cm^2 g^{-1})	$\sigma_{[\mu/\rho]_{rel}}$ (%)	$\sigma_{[\mu/\rho]}$ (cm^2 g^{-1})	$[\mu/\rho]_{pe}$ (cm^2 g^{-1})	$\sigma_{[\mu/\rho]_{pe}}$ (cm^2 g^{-1})	$[\mu/\rho]_{R+C}$ (cm^2 g^{-1})
7013.61 (14)	16.9045	0.1955	1.16	0.2370	16.1010	0.1956	0.803 (05)
7053.86 (18)	13.8405	0.3126	2.26	0.3494	13.0506	0.3130	0.790 (15)
7092.89 (14)	14.1715	0.1911	1.35	0.2283	13.3949	0.1926	0.777 (24)
7094.46 (18)	14.5341	0.4748	3.27	0.5126	13.7581	0.4754	0.776 (25)
7096.39 (18)	14.4981	0.3797	2.62	0.4175	13.7228	0.3805	0.775 (25)
7098.43 (18)	14.4291	0.4121	2.86	0.4497	13.6545	0.4129	0.775 (26)
7100.26 (18)	14.0643	0.3419	2.43	0.3790	13.2904	0.3429	0.774 (26)
7102.22 (18)	13.5240	0.2080	1.54	0.2442	12.7515	0.2096	0.772 (26)
7103.26 (18)	13.6449	0.4021	2.95	0.4385	12.8732	0.4029	0.772 (26)
7104.20 (18)	13.2912	0.3248	2.44	0.3607	12.5201	0.3258	0.771 (25)
7105.18 (18)	12.9506	0.2215	1.71	0.2568	12.1775	0.2226	0.773 (23)
7106.16 (18)	13.5975	0.2296	1.69	0.2660	12.8157	0.2300	0.782 (13)
7107.23 (18)	13.6265	0.2631	1.93	0.2995	12.8350	0.2631	0.791 (03)
7108.21 (18)	13.6584	0.2283	1.67	0.2647	12.8581	0.2284	0.800 (07)
7109.19 (18)	14.0397	0.9040	6.44	0.9411	13.2305	0.9042	0.809 (17)
7110.22 (18)	13.2739	0.2552	1.92	0.2910	12.4554	0.2566	0.819 (27)
7111.34 (18)	14.1007	0.3509	2.49	0.3880	13.2721	0.3529	0.829 (38)
7112.32 (18)	14.5485	0.4599	3.16	0.4977	13.7059	0.4619	0.843 (43)
7113.26 (18)	15.6962	0.2874	1.83	0.3271	14.8447	0.2920	0.851 (51)
7114.33 (18)	15.8825	0.3102	1.95	0.3501	15.0210	0.3162	0.861 (61)
7115.36 (18)	17.7570	0.4227	2.38	0.4655	16.8860	0.4286	0.871 (71)
7116.39 (18)	19.4299	0.1955	1.01	0.2410	18.5495	0.2114	0.880 (80)
7117.33 (18)	22.0806	0.7924	3.59	0.8419	21.1918	0.7973	0.889 (89)
7118.37 (18)	26.0627	0.2253	0.86	0.2810	25.1648	0.2456	0.898 (98)
7119.35 (18)	28.5142	0.2196	0.77	0.2791	27.6079	0.2439	0.91 (11)
7120.34 (18)	36.2972	0.8419	2.32	0.9135	35.3827	0.8497	0.91 (11)
7121.28 (18)	43.4113	0.2390	0.55	0.3217	42.4893	0.2683	0.92 (12)
7122.22 (18)	54.2665	0.2999	0.55	0.3993	53.3373	0.3265	0.93 (13)
7123.17 (18)	61.4214	0.6576	1.07	0.7682	60.4853	0.6715	0.94 (14)
7124.24 (18)	62.3121	0.6929	1.11	0.8049	61.3688	0.7075	0.94 (14)
7125.18 (18)	58.3692	0.3262	0.56	0.4321	57.4199	0.3587	0.95 (15)
7126.14 (18)	58.5089	0.2557	0.44	0.3617	57.5542	0.2988	0.96 (16)
7127.13 (18)	62.3881	0.2617	0.42	0.3738	61.4283	0.3066	0.96 (16)
7128.16 (18)	72.8083	0.2143	0.29	0.3426	71.8439	0.2701	0.96 (16)
7129.15 (18)	83.9086	0.2522	0.30	0.3977	82.9406	0.3030	0.97 (17)
7130.13 (18)	96.5867	0.2385	0.25	0.4037	95.6159	0.2932	0.97 (17)
7131.17 (18)	105.4872	0.6453	0.61	0.8243	104.5145	0.6679	0.97 (17)
7132.20 (18)	109.0172	0.2557	0.23	0.4402	108.0437	0.3089	0.97 (17)
7133.27 (18)	110.6909	0.4805	0.43	0.6676	109.7179	0.5107	0.97 (17)
7134.27 (18)	110.8168	0.2686	0.24	0.4559	109.8455	0.3185	0.97 (17)
7135.26 (18)	110.0281	0.2408	0.22	0.4268	109.0599	0.2936	0.97 (17)
7136.30 (18)	105.9835	0.2660	0.25	0.4457	105.0201	0.3121	0.96 (16)
7137.37 (18)	100.2688	0.3226	0.32	0.4935	99.3122	0.3585	0.96 (16)
7138.37 (18)	93.9911	0.2168	0.23	0.3779	93.0427	0.2626	0.95 (15)
7139.31 (18)	89.5080	0.2311	0.26	0.3852	88.5690	0.2695	0.94 (14)
7140.30 (18)	82.2477	0.5869	0.71	0.7298	81.3207	0.6005	0.93 (13)
7141.35 (18)	79.7142	0.3336	0.42	0.4726	78.8022	0.3519	0.91 (11)
7142.30 (18)	77.4903	0.2701	0.35	0.4056	76.5942	0.2866	0.896 (96)
7143.20 (18)	76.0592	0.8918	1.17	1.0251	75.1804	0.8953	0.879 (79)
7144.24 (18)	74.7426	0.8337	1.12	0.9650	73.8867	0.8356	0.856 (56)
7145.19 (18)	73.7873	0.2543	0.34	0.3841	72.9551	0.2563	0.832 (32)
7146.18 (18)	73.0971	0.4945	0.68	0.6232	72.2928	0.4945	0.804 (04)
. . .							
8006.89 (15)	55.7671	0.2257	0.40	0.3276	55.0285	0.2266	0.739 (19)
8014.40 (12)	53.7160	0.1507	0.28	0.2493	52.9780	0.1519	0.738 (19)
8514.68 (14)	50.6538	0.3389	0.67	0.4328	49.9517	0.3393	0.702 (17)

There are 297, 249, 234 and 236 independent energies across the Fe *K* edge, respectively, for these transmission XAS measurements of frozen solutions at 10–20 K, with accuracies (for the solute) from 0.2% to 2%, observing statistically significant fine structure to $k > 12$ Å^{-1}.

The solvent was 50% butyronitrile ($CH_3CH_2CH_2CN$) and 50% acetonitrile (CH_3CN), the mixture being less susceptible to crystallization during freezing. Uncertainties from the repeated measurements including the solvent were from 0.005% to 0.03%, indicating a very high signal-to-noise ratio (see Figs. 15 and 16), enabling extraction of the isolated solute spectra (see Figs. 17 and 18). Key challenges were the absolute calibration and characterization of the solvent and air path, and the volume change of freezing,

Table 28
3mM DmFc: measured X-ray mass attenuation coefficients $[\mu/\rho]_S$ from the intensity measurements (I_0 and I) for a 3 mM DmFc solution and its corresponding solvent.

A number of key experimental sources of systematic errors including energy calibration, dark current, solvent attenuation, harmonic contamination and thickness ratio [from the actual solvent attenuation and fitted background of the sample (solution)] were corrected for to obtain the final results. The columns are as in Table 25. (Some rows of values have been omitted for brevity. The full version is available in the supporting information.)

E (eV)	$[\mu/\rho]_S$ (cm^2 g^{-1})	$\sigma_{[\mu/\rho]_{rel}}$ (cm^2 g^{-1})	$\sigma_{[\mu/\rho]_{rel}}$ (%)	$\sigma_{[\mu/\rho]}$ (cm^2 g^{-1})	$[\mu/\rho]_{pe}$ (cm^2 g^{-1})	$\sigma_{[\mu/\rho]_{pe}}$ (cm^2 g^{-1})	$[\mu/\rho]_{R+C}$ (cm^2 g^{-1})
7013.74 (14)	19.2877	1.8703	9.70	1.9109	18.4843	1.8703	0.803 (05)
7013.82 (15)	18.2279	2.0515	11.25	2.0903	17.4245	2.0515	0.803 (05)
7013.86 (14)	14.6015	2.6684	18.27	2.7013	13.7982	2.6684	0.803 (05)
7053.73 (14)	12.0236	0.9659	8.03	0.9946	11.2336	0.9660	0.790 (15)
7092.89 (14)	12.0234	0.7216	6.00	0.7503	11.2468	0.7220	0.777 (24)
7094.46 (14)	11.8443	1.3380	11.30	1.3665	11.0683	1.3383	0.776 (25)
7096.39 (14)	9.4830	1.0604	11.18	1.0850	8.7076	1.0607	0.775 (25)
7098.43 (14)	10.2858	0.8354	8.12	0.8613	9.5112	0.8358	0.775 (26)
7100.26 (14)	12.4821	1.2650	10.13	1.2945	11.7082	1.2653	0.774 (26)
7102.22 (14)	8.6023	2.2564	26.23	2.2795	7.8298	2.2565	0.772 (26)
7103.26 (14)	10.3269	1.1878	11.50	1.2137	9.5551	1.1880	0.772 (26)
7104.20 (14)	8.6976	2.0845	23.97	2.1078	7.9266	2.0846	0.771 (25)
7105.18 (14)	9.0951	1.6256	17.87	1.6496	8.3220	1.6258	0.773 (23)
7106.16 (14)	10.7653	1.2149	11.28	1.2415	9.9834	1.2149	0.782 (13)
7107.23 (14)	12.0416	1.0559	8.77	1.0846	11.2502	1.0559	0.791 (03)
7108.21 (14)	8.4281	2.2616	26.83	2.2845	7.6278	2.2616	0.800 (07)
7109.19 (14)	7.8604	0.8995	11.44	0.9214	7.0512	0.8996	0.809 (17)
7110.22 (14)	9.8792	0.9563	9.68	0.9815	9.0607	0.9567	0.819 (27)
7111.34 (14)	13.4796	2.0357	15.10	2.0668	12.6510	2.0361	0.829 (38)
7112.32 (14)	9.8255	1.0104	10.28	1.0355	8.9829	1.0113	0.843 (43)
7113.26 (14)	11.0846	1.5017	13.55	1.5289	10.2332	1.5026	0.851 (51)
7114.33 (14)	12.2146	3.7302	30.54	3.7592	11.3531	3.7307	0.861 (61)
7115.36 (14)	13.0540	1.0726	8.22	1.1030	12.1830	1.0750	0.871 (71)
7116.39 (14)	13.8393	1.8121	13.09	1.8438	12.9588	1.8139	0.880 (80)
7117.33 (14)	17.6490	3.7778	21.41	3.8157	16.7601	3.7788	0.889 (89)
7118.37 (14)	21.6753	0.9104	4.20	0.9548	20.7774	0.9156	0.898 (98)
7119.35 (14)	26.5652	0.8487	3.19	0.9011	25.6589	0.8553	0.91 (11)
7120.34 (14)	33.4404	2.2750	6.80	2.3386	32.5260	2.2778	0.91 (11)
7121.28 (14)	43.3449	0.9385	2.17	1.0183	42.4230	0.9464	0.92 (12)
7122.22 (14)	54.0024	0.9725	1.80	1.0697	53.0733	0.9811	0.93 (13)
7123.17 (14)	61.1305	0.9237	1.51	1.0325	60.1945	0.9337	0.94 (14)
7124.24 (14)	58.4083	0.8755	1.50	0.9799	57.4649	0.8872	0.94 (14)
7125.18 (14)	55.4898	0.6933	1.25	0.7928	54.5405	0.7092	0.95 (15)
7126.14 (14)	59.0883	0.9788	1.66	1.0842	58.1335	0.9909	0.96 (15)
7127.13 (14)	65.8322	0.8855	1.35	1.0019	64.8723	0.8998	0.96 (16)
7128.16 (14)	75.6578	2.7892	3.69	2.9216	74.6934	2.7941	0.96 (16)
7129.15 (14)	89.0426	0.8074	0.91	0.9616	88.0746	0.8246	0.97 (17)
7130.13 (14)	100.0572	1.1378	1.14	1.3100	99.0864	1.1505	0.97 (17)
7131.17 (14)	113.0345	1.0223	0.90	1.2156	112.0618	1.0368	0.97 (17)
7132.20 (14)	113.6922	1.3928	1.23	1.5872	112.7188	1.4035	0.97 (17)
7133.27 (14)	115.1289	0.7664	0.67	0.9631	114.1559	0.7856	0.97 (17)
7134.27 (14)	116.4568	1.0702	0.92	1.2691	115.4856	1.0838	0.97 (17)
7135.26 (14)	114.6754	1.1792	1.03	1.3752	113.7072	1.1911	0.97 (17)
7136.34 (14)	112.1278	1.0690	0.95	1.2609	111.1646	1.0814	0.96 (16)
7137.37 (14)	105.4288	0.8999	0.85	1.0808	104.4722	0.9134	0.96 (16)
7138.37 (14)	98.8373	1.1089	1.12	1.2791	97.8888	1.1188	0.95 (15)
7139.31 (14)	93.9398	3.5450	3.77	3.7072	93.0008	3.5477	0.94 (14)
7140.30 (14)	85.6620	1.1122	1.30	1.2609	84.7350	1.1194	0.92 (13)
7141.35 (14)	82.8604	0.8452	1.02	0.9893	81.9483	0.8525	0.91 (11)
7142.30 (14)	79.2957	0.9438	1.19	1.0821	78.3996	0.9486	0.896 (96)
7143.20 (14)	77.3629	0.9679	1.25	1.1031	76.4841	0.9710	0.879 (79)
7144.24 (14)	75.4883	0.8876	1.18	1.0198	74.6324	0.8894	0.856 (56)
7145.19 (14)	75.8586	3.3343	4.40	3.4670	75.0265	3.3344	0.832 (32)
7146.18 (14)	75.0865	1.1261	1.50	1.2575	74.2822	1.1261	0.804 (04)
7147.13 (14)	72.5872	1.3103	1.81	1.4377	71.8129	1.3105	0.774 (26)
...							
8006.89 (14)	55.4844	0.7062	1.27	0.8058	54.7459	0.7065	0.739 (19)
8014.40 (14)	54.3576	0.6004	1.10	0.6981	53.6196	0.6007	0.738 (19)
8514.68 (14)	57.4075	1.2802	2.23	1.3829	56.7054	1.2804	0.702 (17)

together with the treatment of uncertainty within the hybrid technique.

There is moderately strong evidence for three crystal phases of Fc, but more challenging is the determination of their structures (Fig. 19). Note that in this study, it was not required that these frozen solutions (nor the higher-temperature solutions) should show the same structures as either an isolated molecule or a molecule in a crystal.

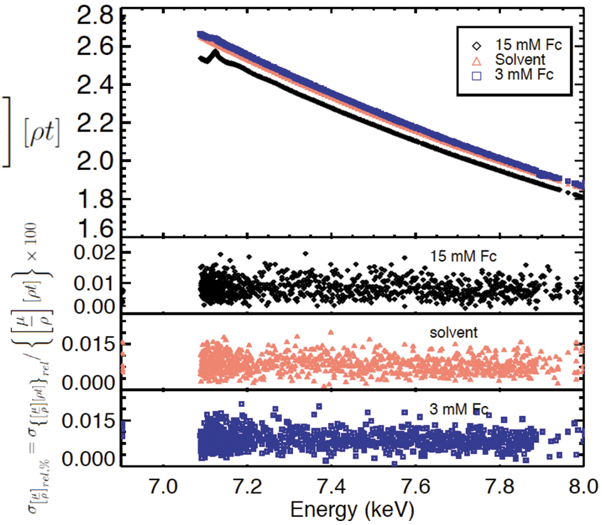

Figure 15
Attenuations of the 15 m*M* and 3 m*M* solutions of Fc, and of the pure solvent, represented respectively by black diamonds, blue squares and red triangle markers. The uncertainties determined from repeated measurements varied from 0.005% to 0.02%, reflecting the data quality. Well defined peaks from the 15 m*M* solution, relatively weak peaks from the 3 m*M* solution and no peaks from the pure solvent confirmed there was no cross contamination from leaking between the chambers. The solutions were confined to three chambers, each of 1.5 mm nominal path length. Reproduced with permission from Islam *et al.* (2016). Copyright (2016) American Chemical Society.

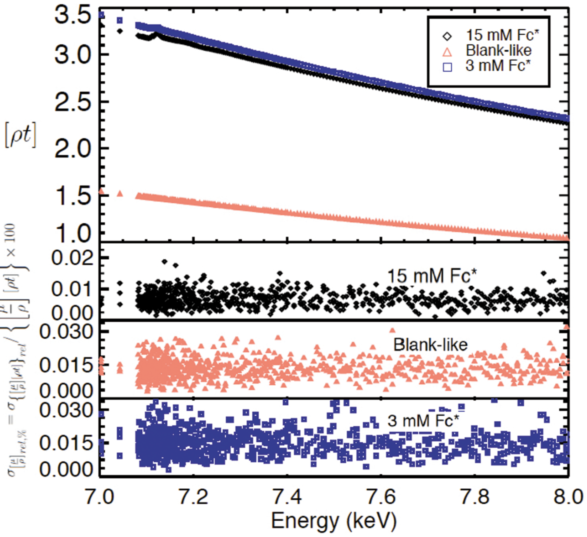

Figure 16
The attenuation from the 15 m*M* and 3 m*M* DmFc solutions (Fc*), and of a blank measurement using an empty chamber, are represented respectively by black diamond markers, blue squares and salmon triangles. The uncertainties determined from the repeated measurements varied from 0.005% to 0.03%, reflecting the data quality. The blank sample produced a smooth curve with substantially less attenuation, contributed primarily by components such as the sample holder, cryostat, detector windows and air path. Reproduced with permission from Islam *et al.* (2016). Copyright (2016) American Chemical Society.

The accuracy of these data sets was a major achievement of the hybrid technique and led to advanced theoretical investigations using the finite-difference method and the new theory *FDMX* (Bourke *et al.*, 2016*b*). However, there is still much more to understand about Fc and DmFc in crystalline and solution forms.

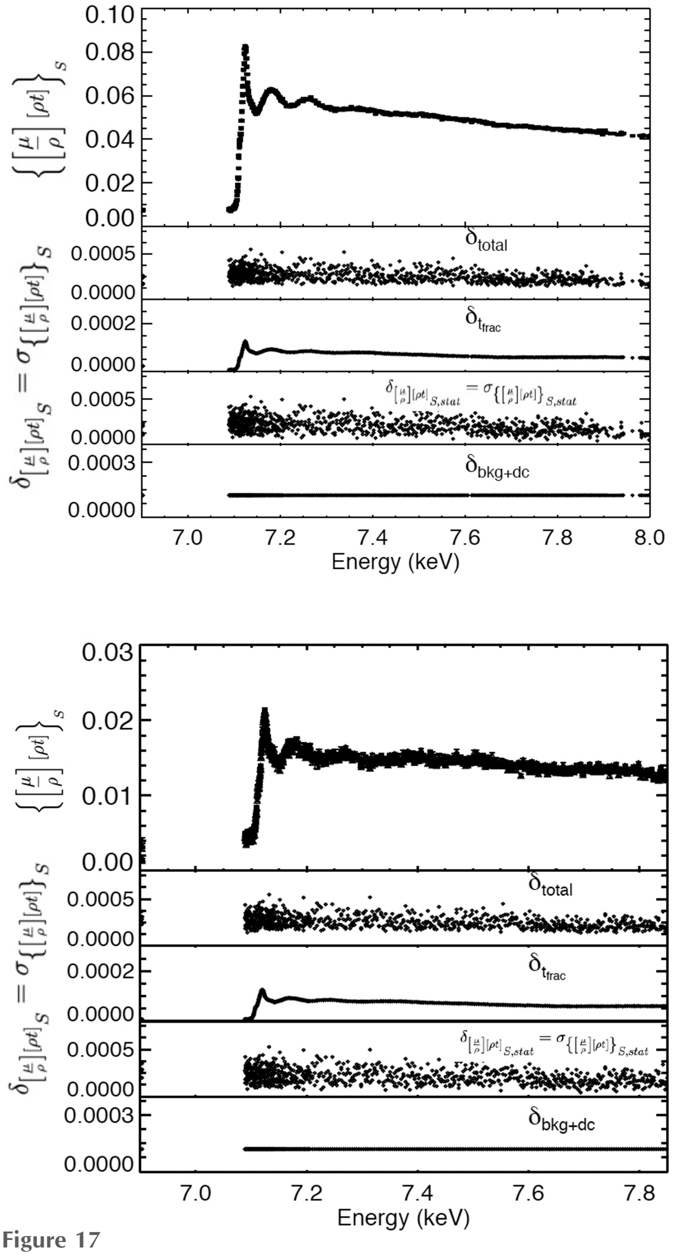

Figure 17
Normalized XAFS of 15 m*M* Fc (top) and 3 m*M* Fc (bottom) with total uncertainties ($\delta_{\rm total}$), uncertainties contributed by solvent path-length variation ($\delta_{t_{\rm frac}}$), statistical uncertainties ($\delta_{[\mu/\rho][\rho t]}$), and uncertainties due to background attenuation and dark current ($\delta_{\rm bkg+dc}$). Reproduced with permission from Islam *et al.* (2016). Copyright (2016) American Chemical Society.

18. *n*-pr Ni and *i*-pr Ni complexes, 7.9–9.5 keV. XAS, XAFS, structure, Ni conformation, error analysis and grid spacing

The study by Schalken & Chantler (2018) revealed one key problem of many data sets – the grid spacing in energy and the spacing translated to *k*-space are almost never uniform. Even if the spacing is more-or-less uniform in *k*-space, there are

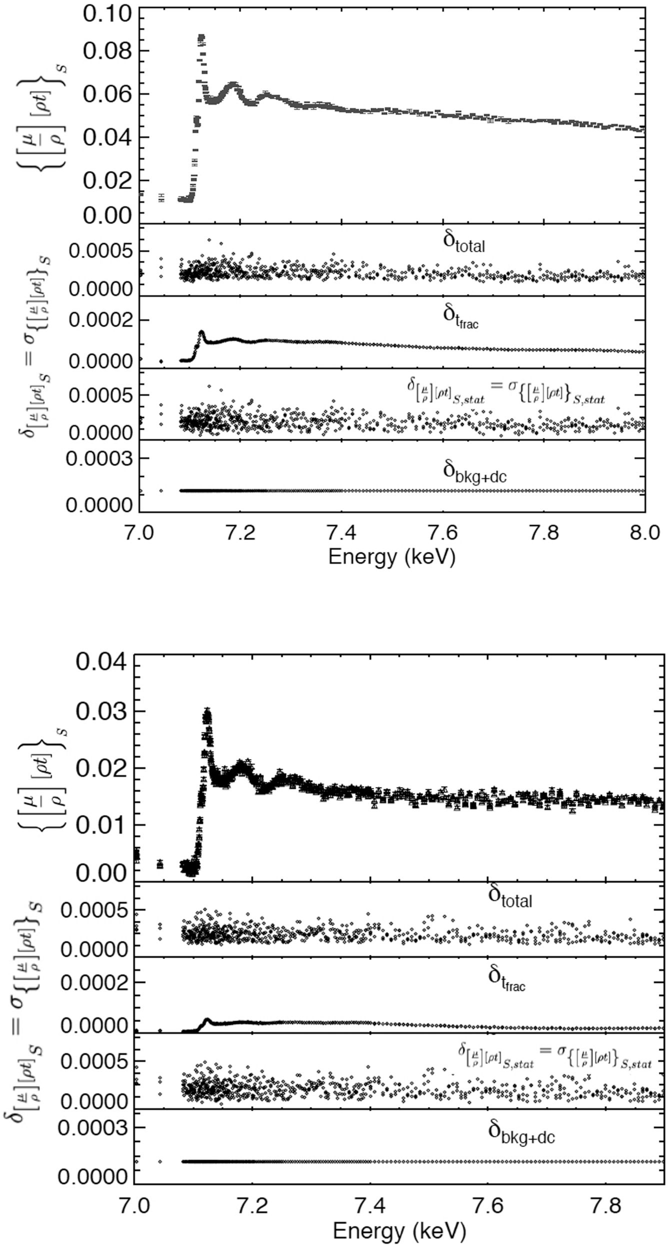

Figure 18

Normalized XAFS of 15 m*M* DmFc (top) and 3 m*M* DmFc (bottom) with total uncertainties ($\delta_{\rm total}$), uncertainties contributed by solvent path-length variation ($\delta_{t_{\rm frac}}$), statistical uncertainties ($\delta_{[\mu/\rho][\rho t]}$), and uncertainties due to background attenuation and dark current ($\delta_{\rm bkg+dc}$). Reproduced with permission from Islam *et al.* (2016). Copyright (2016) American Chemical Society.

likely to be some points missing due to data processing and removal due to Bragg glitches (three-beam interactions of the monochromator, unnormalized by an unmatched secondary detector). It is also assumed that the E_0 offset energy for the edge and continuum is defined exactly in the process of the transformation to *k*-space and hence that there is no need for an additional offset parameter for E_0. More commonly, the near-edge region has a finer spacing, *e.g.* 0.5 eV, increasing at some distance above the XANES region, so the grid is not uniform in *k*-space. Therefore to obtain data points with independent uncertainties and the (correct) propagation of errors, one must process each data point individually (Fig. 20). Then one can model the detailed structure with theory (Fig. 21). Conversely, this study also assessed how to interpolate the data, possibly onto a uniform grid in *k*-space, *post facto* with 'minimal' distortion of the data and well defined statistical significance. Quite often, and indeed for any current proces-

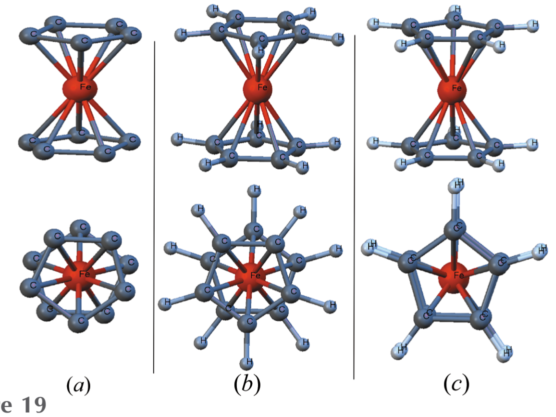

(*a*) (*b*) (*c*)

Figure 19

Models of reported crystal structures for Fc at three different temperatures [283 K (*a*), 173 K (*b*) and 98 K (*c*), from Dunitz *et al.* (1956), Brock & Fu (1997) and Seiler & Dunitz (1982), respectively] showing a range of predictions from conformation analysis. The higher-temperature structures clearly possess a staggered geometry for the cyclopentadienyl rings, while the 98 K measurement suggests a near-eclipsed structure with a relative rotation angle of 9°. Reproduced with permission from Islam *et al.* (2016). Copyright (2016) American Chemical Society.

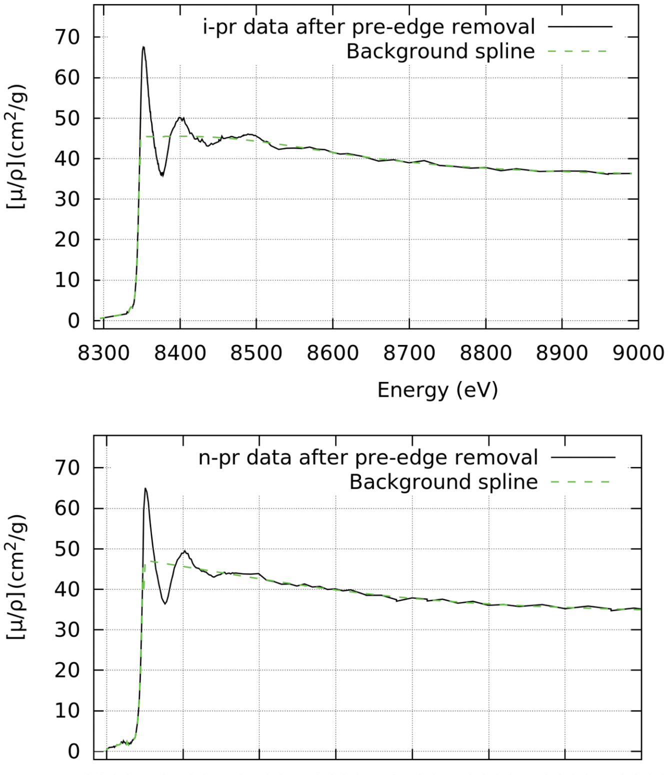

Figure 20

Quality of the data and background spline for the absorption spectrum with the solvent contribution removed for 15 m*M* *i*-pr Ni (top) and *n*-pr Ni (bottom) for the high-point-accuracy data sets.

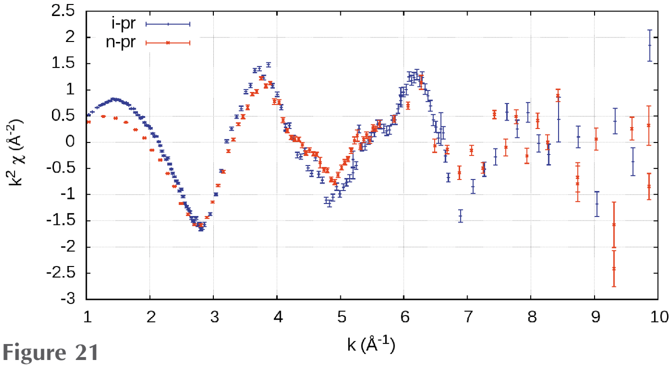

Figure 21
k^2-weighted *mu2chi* (non-interpolated) output for 15 m*M* *i*-pr Ni and *n*-pr Ni from the high-point-accuracy hybrid experiment.

sing in *R*-space, a fast Fourier transform (FFT) routine is used which assumes and requires a uniform grid in *k*-space. This study also discussed data sets where the beamtime was spent pursuing high-accuracy data points at fewer energies, versus a strategy where a much higher point density was pursued but with lower accuracy for each point.

Around this time, discussions arose through the joint Q2XAFS meetings coordinated by the IUCr Commission on XAFS and the International XAFS Society about appropriate data formats for deposition and tabulations for cross-platform portability (Ravel *et al.*, 2012; Chantler *et al.*, 2012*a*; Hester, 2016; Abe *et al.*, 2018; Chantler *et al.*, 2018, 2019). A key recommendation was that the format should be text-based and readable by humans, but also suitable for input to fitting, analysis and theory software. Secondly, it was recommended that information about the different columns and key issues should be noted in a header. Potential formats could be a .dat format similar to that used for *iFEFFit* or a format similar to the .cif format, already in use for the description of crystal structures and diffraction experiments. Other formats discussed included the binary HDF5 format, the European XDI format and later a XIF format (Sarangi, 2018).

Table 29
15 m*M* *n*-pr Ni: .dat tabulation of mass attenuation coefficients MU (= $[\mu/\rho]$).

E	MU	MU_ERR
7918.6	14.3975	0.344
7958.94	13.857	0.128
7998.73	12.4021	0.2331
8039.15	12.8614	0.1579
8078.88	11.5823	0.2661
8078.93	10.7749	0.2019
8119.13	11.2833	0.1043
8159.17	10.8239	0.1782
8199.09	11.4329	0.1137
8239.54	9.3359	0.2631
8278.65	10.6173	0.1075
8283.63	10.4404	0.1593
8288.75	10.9036	0.1055
8293.87	10.4362	0.156
8298.76	10.8103	0.1115
8303.65	11.4517	0.0905
8308.43	11.5356	0.1197
8309.38	11.7047	0.1084
8310.32	11.471	0.1136
8311.34	11.7723	0.1146
8312.34	11.736	0.1208
8313.46	12.0918	0.1156
8314.46	12.0229	0.1122
8315.41	12.0549	0.1092
8316.42	12.1003	0.1166
8317.49	12.2049	0.1121
8318.49	12.3484	0.1109
8319.02	12.7383	0.1151
8319.62	12.7988	0.1063
8320.09	12.6816	0.1189
8320.62	12.5552	0.1243
8321.1	12.4834	0.1222
8321.58	12.7043	0.1575
8322.05	13.006	0.1163
8322.58	12.7641	0.1307
8323.12	12.7819	0.1217
8323.59	12.6516	0.1213
8324.12	12.5933	0.1145
8324.65	12.5628	0.1177
8325.13	12.2543	0.1138
8325.66	12.1542	0.1214
8326.15	12.4784	0.108
8326.62	12.7858	0.1049
8327.15	12.4599	0.1054
8327.57	12.2737	0.1096
8328.04	12.1963	0.1072
8328.57	12.0645	0.1114
8329.05	12.3979	0.1006
8329.52	12.2085	0.1041
8330	12.231	0.1335
8330.47	12.3744	0.1135
8331.07	12.4626	0.1045
8331.55	12.6062	0.1041
8331.96	12.4484	0.0969
8332.5	12.6913	0.096
8332.91	12.7562	0.0933
8333.45	12.9581	0.0875
8333.86	13.1698	0.1029
8334.34	13.2789	0.0929
8334.87	13.2664	0.1056
8335.29	13.4296	0.0915
8335.82	13.5899	0.0887
8336.31	13.5387	0.0878
8336.84	13.6542	0.1037
8337.38	13.8488	0.0907
8337.85	14.2488	0.0941
8338.33	14.8512	0.0898
8338.8	15.3278	0.0934
8339.28	16.0164	0.0847
8339.75	16.6289	0.0857
8340.23	17.346	0.0886
8340.76	18.2675	0.0966
8341.3	19.5157	0.0861
8341.72	20.4088	0.088
8342.26	21.7918	0.087
8342.85	23.6048	0.0978
8343.39	26.0919	0.0865
8343.86	28.1103	0.088
8344.4	31.2691	0.0946
8344.88	34.1175	0.0836
8345.35	38.0358	0.0932
8345.83	41.8199	0.0801
8346.42	46.5021	0.0933
8346.91	50.7247	0.0936
8347.44	55.7999	0.0968
8348.52	69.8568	0.0927
8350.6	75.4479	0.0958
8352.64	74.4364	0.0935
8354.67	71.8309	0.0955
8356.7	67.4226	0.087
8358.61	64.0177	0.104
8360.59	60.7791	0.0932
8362.57	58.2007	0.0833
8364.36	55.3938	0.0914
8366.39	53.6771	0.0907
8368.38	51.6385	0.086
8370.29	50.0682	0.0998
8372.34	48.154	0.1028
8374.38	47.3642	0.1276
8376.42	46.7503	0.124
8378.53	47.3096	0.1525
8380.57	48.6553	0.1118
8382.62	50.6055	0.1157
8384.66	52.4124	0.1143
8386.64	53.7908	0.1237
8388.58	55.5608	0.1103
8390.56	56.4868	0.1096
8392.56	57.5525	0.0955
8394.43	57.9881	0.1524
8396.35	58.4913	0.1624
8398.35	59.2205	0.1015
8400.34	59.1963	0.1139
8402.33	59.8045	0.1027
8404.4	59.1507	0.1189
8406.45	59.1165	0.0928
8408.51	57.9148	0.1654
8410.63	57.7339	0.1247
8412.64	56.6799	0.1288
8414.69	56.0587	0.1063
8416.69	55.6385	0.1098
8418.58	55.5027	0.1178
8420.58	55.416	0.0891
8422.53	55.0891	0.1183
8424.35	54.6832	0.0918
8426.35	54.7478	0.1023
8428.37	54.5525	0.0864
8430.25	54.4688	0.0783
8432.26	54.0891	0.2069
8434.39	53.7708	0.0882
8436.34	53.7094	0.085
8438.54	53.3434	0.0847
8440.61	53.2192	0.0896
8442.56	53.425	0.0909
8444.65	53.6321	0.0801
8446.72	53.7605	0.0923
8448.62	53.812	0.0805
8450.57	54.0264	0.0857
8452.59	54.2818	0.1056
8454.49	54.3667	0.1727
8456.39	53.9618	0.0885
8458.48	54.1099	0.0858
8460.38	54.1696	0.0949
8462.4	53.9662	0.0903
8464.49	54.2245	0.0858
8466.45	54.1296	0.0725
8468.85	54.1731	0.0919
8479.07	53.9239	0.0819
8488.88	53.8575	0.082
8498.89	53.9639	0.1454
8509.12	52.3359	0.1244
8518.93	51.9634	0.0782
8528.96	51.2721	0.1145
8539.26	51.3383	0.0793
8548.96	50.7922	0.0801
8559	51.2728	0.0585
8569.31	50.5096	0.1136
8579.02	50.6278	0.0894
8589.07	49.8533	0.092
8599.33	49.9905	0.0904
8609.3	49.4738	0.0842
8619.42	49.707	0.065
8639.67	48.3695	0.1423
8639.73	48.3048	0.1748
8659.63	48.2793	0.1011
8679.37	47.1344	0.1903
8679.43	46.7633	0.1506
8699.71	47.5279	0.0892
8719.44	47.1829	0.1451
8719.5	46.7319	0.0967
8739.52	47.125	0.0836
8759.7	46.1062	0.0774
8779.37	46.5138	0.078
8799.67	45.492	0.0908
8819.54	45.6392	0.0779
8839.82	45.1138	0.1023
8870.07	45.5182	0.0568
8900.11	44.4451	0.1372
8930.22	45.013	0.0553
8960.14	44.2414	0.1012
8960.21	43.8138	0.0909
8990.12	44.4046	0.0601
9020.24	43.6004	0.1897
9060.44	43.9373	0.0634
9100.87	42.0694	0.1487
9140.95	42.2971	0.0788
9181.03	41.1502	0.1526
9221.1	41.3498	0.0779
9261.02	40.4682	0.2145
9261.09	39.9854	0.1472
9301.07	40.9859	0.1082
9341.17	39.8005	0.1166
9380.95	40.2269	0.0896
9471.67	40.1615	0.0804
9521.81	39.7442	0.1648

The data sets discussed in the previous sections of this chapter were presented as typeset tables of data within published articles (*e.g.* in pdf format), or deposited as text files and readme files (Section 8), or deposited as pdfs of tabulated data (Sections 16 and 17). However, by this point and in the following sections, discussions at the Q2XAFS meetings and the joint work of the IUCr Commission on XAFS and the International XAFS Society had shown that it was important to develop standard formats of data sets for direct input into XANES and XAFS fitting packages, for cross-platform portability and for deposition. For the study described in this section a minimalist template for *mu2chi*, *iFEFFit* and *eFEFFit* formats was used, as shown in Table 29, which is also available the supporting information to this chapter as the file bz5029sup15.txt. 'E' is the energy in eV; 'MU' is $[\mu/\rho]$ in cm^2 g^{-1} and 'MU_ERR' is $\sigma_{[\mu/\rho]}$ in cm^2 g^{-1}. The table contains no discussion of relative errors, but presents data for 194 independent energies for 15 m*M* *n*-pr Ni under the same conditions as discussed in Section 16. This template focused only on standard processing and packages, and not on the presentation of additional derived results. As a .txt file it was directly machine-readable. Comments, header information and metadata as recommended by the discussions at Q2XAFS are not included here, so the reader should refer to the article by Schalken & Chantler (2018) for these details. This template was later developed into the recommended formats of .cif and .dat (for *eFEFFit*/*iFEFFit*), as described in the sections below.

19. *n*-pr Ni and *i*-pr Ni complexes, 8.14–9.32 keV. XFS, XAFS, nanostructure, fluorescence reference data sets and Ni conformation

Trevorah *et al.* (2019) presented the first example of data sets collected using fluorescence detection. These data sets were of the same quality as the earlier transmission (XAS) data sets discussed in Section 16, and like them include detailed error analysis and uncertainty propagation. These data sets were presented in both *eFEFFit*/*iFEFFit* data format (.dat) and also in CIF (.cif) format. These potential ‘standard formats’ have not yet been agreed to by the international community, but are illustrative and can be used and ported as presented. In this section we explicitly present portable data with metadata and headers as discussed by the international community. We recommend this practice for future supplementary information, standards, deposition and storing of data as fulfilling the requirements decided upon during the Q2XAFS meetings.

X-ray absorption is a first-order process (in lowest order) in the Hamiltonian, whereas fluorescence is a second-order process (in lowest order) [see Chapters 2.8 by Chantler (2024) and 3.49 by Glatzel & Ghiringhelli (2024)]. Hence X-ray emission spectroscopy follows the same Hamiltonian whether it is detecting fluorescence in high-resolution fluorescence detection ‘XAS’ (HERFD-XAS) or observing emission fluorescence spectra, often called XES. Technologies such as resonant inelastic X-ray scattering also observe emission and are also types of X-ray emission spectroscopy, although conventionally one axis of the spectrum is labelled as the incident energy (‘XAS’ or perhaps ‘XFS’) and one is labelled as the emission energy (‘XES’).

The fluoresence data for 572 independent energies for 15 m*M* *n*-pr Ni are presented in Table 30 in .dat format. Table 31 shows the *i*-pr Ni fluorescence data in .cif format, with the same columns in the same order. Four files (one in .dat format and one in .cif format for each complex) are available the supporting information to this chapter as the files bz5029sup16.txt to bz5029sup19.txt.

One can convert a data file in .cif format to .dat format by commenting out some of the header items and perhaps clarifying some of the descriptions in other parts of the header. Similarly one can convert the .dat header fields into a CIF-like data format. In Tables 30 and 31, which correspond to Fig. 22, the energy E is in eV and is followed by $A[\mu/\rho]^*_{\rm pe}$ (for Ni) in cm^2 g^{-1}. $A[\mu/\rho]^*_{\rm pe}$ is not the same as $[\mu/\rho]$ for transmission or XAS experiments because there is intrinsically a scaling and efficiency correction, even if the results of this analysis are in excellent agreement with the results of the corresponding transmission experiments. The raw data for a transmission experiment are attenuation values, from which the photoelectric absorption coefficient $[\mu/\rho]_{\rm pe}$ may be extracted, whereas only a core–hole ionization can lead to fluorescence, so fluorescence measurements intrinsically measure the photoelectric coefficient $A[\mu/\rho]^*_{\rm pe}$. Similarly a transmission experiment will measure the attenuation or absorption from all shells and subshells, whereas fluorescence experiments will only measure the observed active edge or subshell, indicated by the label *. Because fluorescence measurements have significant nonlinearity from detector and self-absorption effects and directly measure I/I_0, the extracted values typically need to be scaled by a factor A to be consistent with attenuation or absorption measurements. Finally, the selection rules for a first-order process (attenuation) and a second-order process (fluorescence) are in general different. Additional columns in the tables give $\sigma_{\rm total}$ (cm^2 g^{-1}) or $\sigma_{[\mu/\rho]}$; $\sigma_{\rm Experimental}$ (cm^2 g^{-1}), *i.e.* $\sigma_{[\mu/\rho]_{\rm rel}}$; $\sigma_{\rm pixel}$ or the scaling/absolute transfer uncertainty or $\sigma_{[\mu/\rho]_{\rm cal}}$; and σ_E in eV.

These data were of sufficient quality to be used for nanostructural analysis, studies of the propagation of uncertainties and for reference standards (Trevorah *et al.*, 2020), see Fig. 23. For data deposition and processing, we recommend a

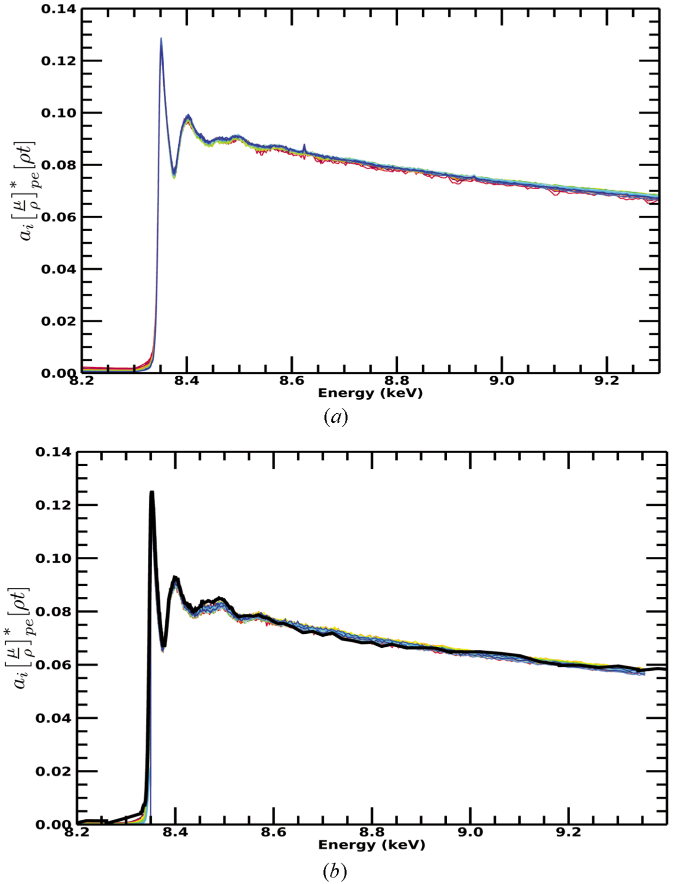

(*a*)

(*b*)

Figure 22

(*a*) Spectra for *n*-pr Ni corrected using *SeAFFluX* (Trevorah *et al.*, 2019). (*b*) Part (*a*) with scaled overplot of transmission XAS spectra. A dramatic reduction in dispersion is observed. Corrected fluorescence spectra display the expected decreasing trend at higher energies consistent with the absorption data (*b*). The fluorescence scale has one free parameter a_i corresponding to the pixel efficiency normalization.

Table 30
15 m*M* *n*-pr Ni, 7.9–9.5 keV, in *eFEFFit*/*iFEFFit* .dat format.

The energy E is in eV, followed by $A[\mu/\rho]^*_{\rm pe}$ (Ni) in cm^2 g^{-1}, $\sigma_{\rm total}$ (cm^2 g^{-1}) or $\sigma_{[\mu/\rho]}$, $\sigma_{\rm Experimental}$ (cm^2 g^{-1}) *i.e.* $\sigma_{[\mu/\rho]_{\rm rel}}$, $\sigma_{\rm pixel}$ or the scaling/absolute transfer uncertainty or $\sigma_{[\mu/\rho]_{\rm cal}}$, and σ_E in eV. The full version of this file is available in the supporting information.

```
# In this file, we provide the experimental data presented in 'Solving Self-Absorption
# in Fluorescence: Stereochemical Analysis in X-ray Absorption Spectroscopy of mM Ni
# Complexes' - Trevorah, Chantler and Schalken (2018).
# This data is presented post-SeAFFluX processing. This allows for verification of our
# results with complementary structural modelling techniques.
# This fluorescence data was taken at ANBF, KEK, Tsukuba, Japan in 2012.
# Fluorescence detector: 36 element Ge planar detector (EURYSIS EPIX 36-64-7-ER)
# Sample: bis(N-n-propyl-salicyladiminato) nickel (II)
# Chemical formula: C20H24N2NiO2
# Molarity: 15.33 +/- 0.06 mM
# Parts per million: 1137 +/- 4 w/w Ni
# Solvent: 60% butyronitrile (C3H7CN) + 40% acetonitrile (CH3CN)
# theta_inc: 45 degrees
# theta_out: 45 degrees
# absorber atom: Ni
# absorber edge: K
# source: KEK-PF
# source location: Tsukuba, Japan
#    detectors.label   detectors.position   detectors.type
# monitor      monitor    ionisation
# transmission detector   ionisation
# fluorescence detector   EURYSIS_EPIX_36-64-7-ER
#    ionisation_detector.gas_pressure_units   ionisation_detector.length_units
# 'atm'          'cm'
#    ionisation_detector.label    ionisation_detector.gas_pressure    ionisation_detector.length
#   ionisation_detector.amplifier_type   ionisation_detector.amplifier_gain
# monitor         1      19    'Keithley'    10
# transmission    1      19    'Keithley'    10
#Energy(eV), A\frac{\mu}{\rho}^*_{pe}(Ni)(cm^2/g), sigma_{total}(cm^2/g),
# sigma_{Experimental}(cm^2/g), sigma_{pixel}(cm^2/g), sigma_{Energy}(eV)
    8141.00  0.0007250    5.400E-05    3.896E-07    5.400E-05      0.09454
    8151.00  0.0006856    5.030E-05    2.083E-07    5.030E-05      0.09204
    8161.00  0.0006616    4.850E-05    1.583E-07    4.850E-05      0.09000
    8171.02  0.0006400    4.840E-05    4.127E-08    4.840E-05      0.09000
    8181.01  0.0006138    4.710E-05    2.624E-08    4.710E-05      0.09000
    8191.02  0.0005969    4.500E-05    4.572E-08    4.500E-05      0.09000
    8201.00  0.0005843    4.450E-05    5.928E-08    4.450E-05      0.09000
    8211.01  0.0005663    4.350E-05    1.030E-08    4.350E-05      0.09000
    8221.01  0.0005433    4.090E-05    4.824E-08    4.090E-05      0.09000
    8231.01  0.0005355    4.030E-05    8.780E-08    4.030E-05      0.09000
    8241.01  0.0005169    3.840E-05    8.609E-08    3.840E-05      0.09000
    8251.00  0.0005092    3.960E-05    6.487E-08    3.960E-05      0.09000
    8261.02  0.0004981    3.770E-05    1.629E-08    3.770E-05      0.09000
    8271.00  0.0004907    3.730E-05    2.278E-09    3.730E-05      0.09000
    8281.01  0.0004821    3.700E-05    4.460E-08    3.700E-05      0.09000
    8291.01  0.0004799    3.560E-05    1.383E-08    3.560E-05      0.09000
    8301.01  0.0004876    3.540E-05    4.967E-08    3.540E-05      0.07160
    8311.00  0.0007038    4.800E-05    8.242E-08    4.800E-05      0.09000
    8321.02   0.001033    6.700E-05    2.360E-07    6.700E-05      0.09000
    8321.02   0.001049    6.520E-05    3.189E-07    6.520E-05      0.09000
    . . .
```

column order with E first, then either $[\mu/\rho]$ for transmission measurements (*i.e.* the attenuation in XAS measurements) or $A[\mu/\rho]^*_{\rm pe}$ in cm^2 g^{-1} for fluorescence measurements. These are the typical data processed without uncertainties or uncertainty estimation. Then we recommend that the third column is $\sigma_{[\mu/\rho]}$, which is the uncertainty of the second column, also in cm^2 g^{-1} for simplicity of processing further with programs such as *mu2chi*, *eFEFFit*, *iFEFFit*, *Larch* or other programs that use this key uncertainty. The fourth column should then represent the estimate of the relative uncertainty $\sigma_{\rm Experimental}$ (cm^2 g^{-1}) or $\sigma_{[\mu/\rho]_{\rm rel}}$, also in cm^2 g^{-1}; subsequent columns could contain data related to particular contributions to the uncertainty from different sources of systematic error, *e.g.* $\sigma_{\rm pixel}$. For transmission XAS data there should be estimated values of $[\mu/\rho]_{\rm pe}$ and their uncertainties, possibly with an explicit scattering estimate; and perhaps the last column should be σ_E, preferably with an indication of how the energy was estimated. If values for the imaginary component of the atomic form factor are extracted from the data, these values should also be presented in a column with their uncertainties. Common usage of such data sets might not distinguish important terms. However, distinguishing the use of the term

Table 31
15 mM *i*-pr Ni, 7.9–9.5 keV, in .cif format.

The energy E is in eV, followed by $A[\mu/\rho]^{*}_{\rm pe}$ (Ni) in cm^2 g^{-1}, $\sigma_{\rm total}$(cm^2 g^{-1}) or $\sigma_{[\mu/\rho]}$, $\sigma_{\rm Experimental}$ (cm^2 g^{-1}) *i.e.* $\sigma_{[\mu/\rho]_{\rm rel}}$, $\sigma_{\rm pixel}$ or the scaling/absolute transfer uncertainty or $\sigma_{[\mu/\rho]_{\rm cal}}$, and σ_E in eV. The full version of this file is available in the supporting information.

```
data_ipr_15mM_xafs_fluorescence
# In this file, we provide the experimental data presented in 'Solving Self-Absorption
# in Fluorescence: Stereochemical Analysis in X-ray Absorption Spectroscopy of mM Ni
# Complexes' - Trevorah, Chantler and Schalken (2018).
# This data is presented post-SeAFFluX processing. This allows for verification of our
# results with complementary structural modelling techniques.
# This fluorescence data was taken at ANBF, KEK, Tsukuba, Japan in 2012.
# Fluorescence detector: 36 element Ge planar detector (EURYSIS EPIX 36-64-7-ER)
# Sample: bis(N-i-propyl-salicyladiminato) nickel (II)
# Chemical formula: C20H24N2NiO2
# Molarity: 15.26 +/- 0.03 mM
# Parts per million: 1133 +/- 2 w/w Ni
# Solvent: 60% butyronitrile (C3H7CN) + 40% acetonitrile (CH3CN)
# theta_inc: 45 degrees
# theta_out: 45 degrees
  _xafs_absorber.atom   Ni
  _xafs_absorber.edge    K
  _xafs_source.identification    'KEK-PF'
  _xafs_source.location           'Tsukuba, Japan'
loop_
    _xafs_detectors.label
    _xafs_detectors.position
    _xafs_detectors.type
monitor      monitor    ionisation
transmission detector   ionisation
fluorescence detector   EURYSIS_EPIX_36-64-7-ER

loop_
    _xafs_ionisation_detector.gas_pressure_units
    _xafs_ionisation_detector.length_units
'atm'          'cm'

loop_
    _xafs_ionisation_detector.label
    _xafs_ionisation_detector.gas_pressure
    _xafs_ionisation_detector.length
    _xafs_ionisation_detector.amplifier_type
    _xafs_ionisation_detector.amplifier_gain
monitor         1      19    'Keithley'    10
transmission    1      19    'Keithley'    10

loop_
    _xafs_reduced.energy_units
    _xafs_reduced.a_mu_rho_*_pe_ni_units
    _xafs_reduced.sigma_total_units
    _xafs_reduced.sigma_experimental_units
    _xafs_reduced.sigma_pixel_units
    _xafs_reduced.sigma_energy_units
'eV'   'cm^2/g'   'cm^2/g'   'cm^2/g'   'cm^2/g'   'eV'

loop_
    _xafs_reduced.energy
    _xafs_reduced.a_mu_rho_*_pe_ni
    _xafs_reduced.sigma_total
    _xafs_reduced.sigma_experimental
    _xafs_reduced.sigma_pixel
    _xafs_reduced.sigma_energy
8141.49  0.0003385    2.190E-05    2.796E-07    2.190E-05      0.07000
8151.49  0.0003195    2.060E-05    2.049E-07    2.060E-05      0.07000
8161.49  0.0003108    1.950E-05    9.257E-08    1.950E-05      0.07000
8171.51  0.0003034    1.920E-05    8.022E-08    1.920E-05      0.07000
8181.50  0.0002943    1.940E-05    1.804E-08    1.940E-05      0.07000
8191.51  0.0002881    1.810E-05    4.440E-08    1.810E-05      0.07000
8201.49  0.0002793    1.830E-05    5.666E-08    1.830E-05      0.07000
8211.50  0.0002757    1.780E-05    1.919E-08    1.780E-05      0.07000
8221.50  0.0002697    1.730E-05    3.146E-08    1.730E-05      0.07050
8231.50  0.0002631    1.690E-05    4.381E-08    1.690E-05      0.07298
...
```

'measured' from a mass attenuation measurement and from a measurement or extraction of a (photoelectric) mass absorption coefficient helps to clarify the importance of the terms, and is certainly important for comparison with and development of theory. The first two columns should be adequate for simple data processing, the first three for processing with uncertainties, and the later columns for investigating and interrogating this and other science more closely. Of course in CIF format every column is labelled, so the columns of data of interest can be easily extracted for any purpose. This is also the case for data in .dat format as long as the columns are labelled.

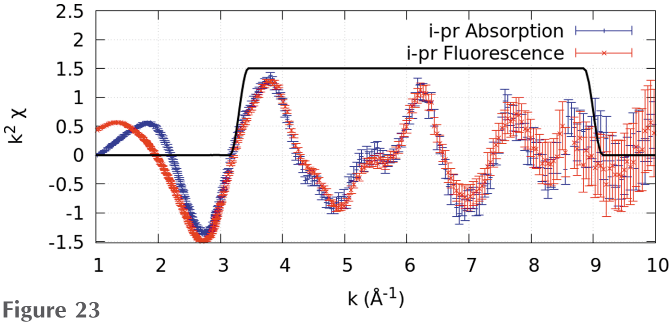

Figure 23
Transmission versus fluorescence spectra for *i*-pr Ni. The first peak within the Hanning window is in good agreement between the spectra; note the absorption spectrum has a larger amplitude than the fluorescence spectra elsewhere.

20. ZnSe crystal foils, 6.82–15.07 keV. XAS, XAFS, nanostructure

Sier *et al.* (2020) present XERT measurements and analysis of the binary crystal ZnSe, which has been the focus of a long-standing debate about the origin of anomalous Bijvoet ratios in its diffraction data. For a binary crystal, the concept of Rayleigh scattering is meaningless and instead Bragg/Laue diffraction or thermal diffuse scattering (TDS) dominate the elastic scattering with very different probabilities. Inelastic scattering might be thought of as conventional, but oriented crystals can also possess tensorial properties. The tensorial properties of ZnSe predict that there will be a major anomaly in the inelastic mean free path, especially with respect to the comparative additivity of the photoelectric mass absorption coefficient (Bourke & Chantler, 2014). This work derived and proved the dominance of thermal diffuse scattering (TDS) (Fig. 24) when Bragg/Laue scattering was avoided. There is, of course, another debate as to whether TDS is elastic or inelastic. Finding the answers to some of these questions will require further accurate experiments; other questions might turn out to be semantic.

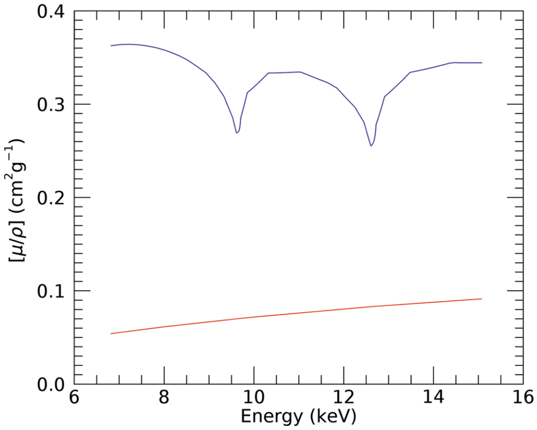

Figure 24
ZnSe binary crystal foils: attenuation of thermal diffuse scattering (blue) and Compton scattering (red) for zinc selenide across the measured energy range.

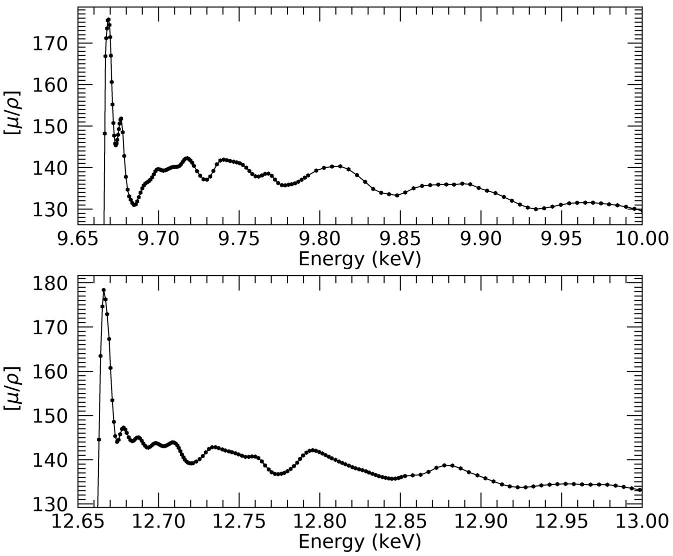

Figure 25
ZnSe binary crystal foils: absolute mass attenuation coefficients [μ/ρ] in cm^2 g^{-1} and structure in the XAFS regions of the zinc (top) and selenium (bottom) *K* edges.

Three high-purity zinc selenide foils were chosen for this experiment with nominal thicknesses of 25 µm, 50 µm and 100 µm. 561 attenuation coefficient data points were recorded in the energy range 6.818–15.073 keV, with measurements concentrated at the zinc and selenium pre-edge, near-edge and absorption fine-structure regions (Fig. 25). Steps of 0.5 eV were used near the edges.

There were two possible calibrations of the energy: that of 9.6638 (1) keV and 12.6578 (1) keV for the zinc and the selenium *K*-absorption edges, respectively, from external energy calibration, versus the values from Kraft *et al.* (1996) for zinc metal [9.66047 (8) keV] and pure selenium (Bearden, 1967; Bearden & Burr, 1967) [12.6578 (7) keV]; and taking the operational experimental edge energy as the lowest energy inflection point, yielding 9.6667 (12) keV and 12.6631 (13) keV for zinc and selenium, respectively. The accuracy was <0.13%, and led to detailed nanostructural analysis of room-temperature ZnSe with full propagation of the uncertainties. Systematic errors due to fluorescence, bandwidth, monochromator hysteresis and drift were all significant (Table 32).

This data set yielded detailed information on non-atomic and atomic behaviour across wide energy ranges compared with the theory current at that time (Fig. 26). The bond lengths, which were accurate to 0.003 Å to 0.009 Å, or 0.1% to 0.3%, are plausible and physically meaningful (Fig. 27). Importantly, the structures determined independently from the Zn and the Se *K* edges were in excellent agreement. Small variations from the structure determined by single-crystal diffraction suggest local dynamic motion beyond that usual for a crystal lattice (note that XAFS is sensitive to dynamic correlated motion). The results obtained in this work are the most accurate to date, and comparisons with theoretically determined values of the attenuation show discrepancies from theory of up to 4%, motivating further investigations into the origin of such discrepancies.

Table 32
Magnitudes of specific experimental systematic errors for ZnSe crystal foils and their correction, and effect of these on final results, absolute accuracy of the full-foil mapping technique and error in the fit of the energy calibration.

Notes: (1) Secondary photons from fluorescent scattering. Correction is highest directly above absorption edges, 0 directly below the Zn edge. (2) Correction for bandwidth. Highest at edge energies (9.6667 and 12.6631 keV). (3) Correction for monochromator drift. Highest at 9.3298 keV. (4) Dark current correction and corresponding uncertainty (± 2 counts). (5) Standard errors from counting statistics (variance including precision and systematic errors). (6) Sum of relative uncertainties. (7) Absolute accuracy of the full-foil mapping technique. (8) Blank current correction and corresponding uncertainty. Correction highest at low energies. (9) Error in the fit of the energy calibration data. Minimum 0.88 eV at 12.0503 keV, maximum 1.22 eV at 9.5892 keV.

	Magnitude		Uncertainty (± 1σ)		
Quantity	Near edge	Far edge	Near edge	Far edge	Contribution
$[\mu/\rho]_{\rm rel}$	0.046–0.118% (50 μm) – 0.67% (100 μm)		<0.01%	0	Fluorescence [Note (1)]
	<11.9%	0	<1.2%	0	Bandwidth [Note (2)]
	0	<0.15%	0	<0.016%	Monochromator drift [Note (3)]
	Up to 3.3% (25 μm) – 40.7% (100 μm)		0.00147–0.0185%		Dark current [Note (4)]
	0.328–7.237%		2.67×10^{-5}% – 4.82×10^{-4}%		Variance [Note (5)]
			0.00134–0.580%		Relative uncertainty [Note (6)]
$[\mu/\rho]_{\rm abs}$	–		0.129%		Full-foil mapping technique [Note (7)]
	7.6–25% (100 μm) – 51% (25 μm)		8.32×10^{-6}% – 3.6×10^{-5}%		Blank normalization [Note (8)]
E	0.223–0.385%		0.00655–0.0163%		Energy [Note (9)]

Five files, bz5029sup20.txt to bz5029sup24.txt, are available as supporting information to this chapter. bz5029sup20.txt is in .cif format and includes all of the data set across both edges, whereas .dat files conventionally relate to a single edge for processing by *mu2chi*, *eFEFFit*, *iFEFFit* or *Athena*, for example, so one file for each edge is provided in .dat format (bz5029sup21.txt, bz5029sup22.txt). Similarly the χ versus k spectra are specific to an edge and the relevant data depend on assumptions about E_0, spline fitting and background removal. The extracted χ versus k spectra for both the Zn and Se K edges are provided for comparison and fitting with different theoretical approaches (bz5029sup23.txt, bz5029sup24.txt).

Compared with Table 33, in the .cif and .dat format files the columns of data are in a different order, so that the values most usually used for data processing are in the earlier columns. For example, in the .cif format file the ordering is E, $[\mu/\rho]$, $\sigma_{[\mu/\rho]}$, $\sigma_{[\mu/\rho]_{\rm rel}}$, $[\mu/\rho]_{\rm pe}$, $\sigma_{[\mu/\rho]_{\rm pe}}$ and σ_E, where all coefficient values are given in cm^2 g^{-1}, *i.e.* in the same units as the coefficient for ease of processing and error propagation. Note that having multiple edges in the data raises a question about how best to deposit the data, as authors may wish to provide mutiple sets of data, for example one data set for each edge, data sets for $k^2\chi$ versus k or spectra transformed to R-space. Within the .cif format these could in principle all be in the one file, but it might be easiest to collect the data sets together in a dedicated folder or use a hierarchical data format (HDF) to include all processing information and outputs, even including fitting, for example.

21. Zinc metal foils, 8.51–11.59 keV: XAS, XAFS, nanostructure, edge jumps, theory

Ekanayake *et al.* (2021*a*) continued the detailed investigation of zinc metal, both as XAS and XAFS, with a detailed

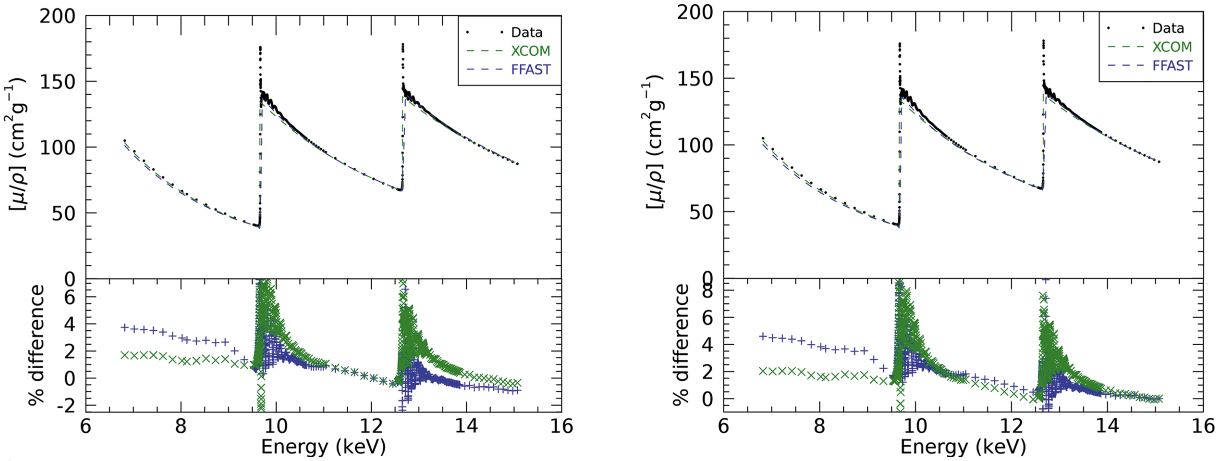

Figure 26
ZnSe binary crystal foils: comparison of the experimental mass absorption coefficient with two corresponding theoretical results. Left – density normalized at 12 keV; right – density normalized at 15 keV. Top – values of the mass attenuation coefficient as determined by this experiment and those predicted by the FFAST (Chantler, 2000) and XCOM (Berger & Hubbell, 1987) tabulations. Bottom – the percentage discrepancies between the measured data [zero line], FFAST [+] and XCOM [×].

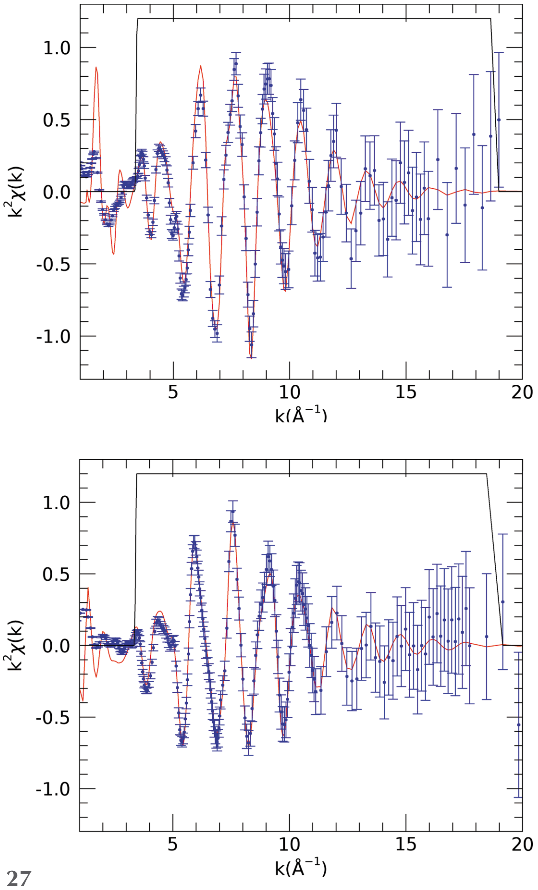

Figure 27
ZnSe binary crystal foils: fitted model output (red) with experimental data (blue) and uncertainties for the (top) zinc and (bottom) selenium *K* edges. The black box indicates the *k* Hanning window.

investigation across the *K* edge. The analysis of the nanostructure was described in Ekanayake *et al.* (2021*b*). This required a new model for and understanding of fluorescence and fluorescence scattering (Sier *et al.*, 2022). This was the first X-ray extended range technique (XERT)-like experiment carried out at the Australian Synchrotron, and high-accuracy measurements were recorded at 496 energies from 8.51 keV to 11.59 keV. The 'relative' accuracy (neglecting the absolute calibration) is better than 0.01–0.027%; the 'absolute' accuracy (including all pointwise and scaling uncertainties that were determined) is 0.023–0.036%. The XERT protocol requires that measurements related to dark-current nonlinearities, corrections for blank measurements, full-foil mapping to characterize the absolute value of the attenuation, scattering, harmonics and roughness are collected over an extended range of experimental parameter space.

This resulted in better data for analysis, culminating in measurement of mass attenuation coefficients across the zinc *K* edge to 0.023–0.036% accuracy (Table 34; Figs. 28, 29 and 30). Dark-current corrections are energy- and structure-dependent, and the magnitude of the corrections reached 57% for thicker samples, but was still large and significant for thin samples. Blank measurements scaled the thin-foil attenuation coefficients by 60% to 500%, and by up to even 90% for thicker foils. Full-foil mapping and characterization corrected discrepancies between foils of up to 20%, rendering the possibility of absolute measurements of attenuation. Fluorescence scattering was also significant. Harmonics, roughness and bandwidth were explored. These corrections are of course thickness-, sample-, composition-, energy-, temperature- and form-dependent, but are likely to be typical for most beamlines.

Table 33
ZnSe binary crystal foils (Sier *et al.*, 2020): mass attenuation and mass absorption coefficients $[\mu/\rho]$ and $[\mu/\rho]_{\rm pe}$ with one standard deviation.

Relative and total percentage uncertainties in the mass attenuation coefficients $\sigma_{[\mu/\rho]_{\rm rel}}$ and $\sigma_{[\mu/\rho]}$ are presented with the latter also given in absolute units. The percentage uncertainty in $[\mu/\rho]_{\rm pe}$ includes uncertainty in the measurements and in the calculations of thermal diffuse and Compton scattering attenuation. (Some rows of values have been omitted for brevity. The full version is available in the supporting information.)

E (eV)	σ_E (eV)	$[\mu/\rho]$ (cm^2 g^{-1})	$[\mu/\rho]_{\rm pe}$ (cm^2 g^{-1})	$\sigma_{[\mu/\rho]_{\rm rel}}$ (%)	$\sigma_{[\mu/\rho]}$ (%)	$\sigma_{[\mu/\rho]}$ (cm^2 g^{-1})	$\sigma_{[\mu/\rho]_{\rm pe}}$ (%)
6818.79	1.11	105.35	104.93	0.00193	0.129	0.136	0.169
7019.86	1.09	97.209	96.790	0.00205	0.129	0.126	0.172
7220.63	1.08	89.978	89.558	0.00195	0.129	0.116	0.176
7421.57	1.06	83.425	83.003	0.00181	0.129	0.108	0.180
7622.32	1.06	77.450	77.028	0.00166	0.129	0.100	0.184
7823.73	1.08	71.908	71.487	0.00175	0.129	0.0928	0.188
8024.10	1.09	67.008	66.588	0.00134	0.129	0.0865	0.192
8124.39	1.10	64.691	64.273	0.00159	0.129	0.0835	0.194
8325.44	1.12	60.479	60.064	0.00166	0.129	0.0781	0.198
8526.33	1.13	56.690	56.279	0.00171	0.129	0.0732	0.202
8727.16	1.15	53.065	52.659	0.00168	0.129	0.0685	0.206
8928.62	1.17	49.847	49.447	0.00210	0.129	0.0644	0.209
9129.51	1.18	46.689	46.298	0.00197	0.129	0.0603	0.213
9329.83	1.20	43.905	43.528	0.0384	0.135	0.0591	0.221
9529.07	1.21	41.394	41.039	0.00229	0.129	0.0534	0.215
9539.42	1.21	41.262	40.909	0.00224	0.129	0.0533	0.215
9549.31	1.21	41.145	40.794	0.00216	0.129	0.0531	0.214
9558.99	1.21	41.017	40.668	0.00249	0.129	0.0530	0.214
9569.01	1.22	40.887	40.540	0.00244	0.129	0.0528	0.214
9579.29	1.22	40.772	40.427	0.00234	0.129	0.0526	0.214
9589.18	1.22	40.689	40.346	0.00244	0.129	0.0525	0.213
9598.63	0.966	40.644	40.303	0.00264	0.129	0.0525	0.213
9600.53	0.966	40.637	40.296	0.00250	0.129	0.0525	0.213
9602.60	0.966	40.609	40.268	0.00243	0.129	0.0524	0.213
9604.67	0.966	40.594	40.253	0.00248	0.129	0.0524	0.213

Table 33 (continued)

E (eV)	σ_E (eV)	$[\mu/\rho]$ (cm^2 g^{-1})	$[\mu/\rho]_{\rm pe}$ (cm^2 g^{-1})	$\sigma_{[\mu/\rho]_{\rm rel}}$ (%)	$\sigma_{[\mu/\rho]}$ (%)	$\sigma_{[\mu/\rho]}$ (cm^2 g^{-1})	$\sigma_{[\mu/\rho]_{\rm pe}}$ (%)
9606.73	0.966	40.580	40.240	0.00229	0.129	0.0524	0.213
9608.72	0.966	40.575	40.235	0.00237	0.129	0.0524	0.213
9610.72	0.966	40.563	40.224	0.00251	0.129	0.0524	0.213
9612.87	0.966	40.558	40.219	0.00227	0.129	0.0524	0.213
9614.86	0.966	40.554	40.214	0.00264	0.129	0.0524	0.213
9616.77	0.966	40.548	40.209	0.00234	0.129	0.0524	0.213
9618.85	0.966	40.550	40.210	0.00255	0.129	0.0524	0.213
9620.93	0.966	40.555	40.215	0.00216	0.129	0.0524	0.213
9625.34	0.965	40.345	40.005	0.00326	0.129	0.0521	0.213
9626.30	0.965	40.356	40.016	0.00319	0.129	0.0521	0.213
9627.26	0.965	40.356	40.016	0.00329	0.129	0.0521	0.213
9628.22	0.965	40.364	40.024	0.00325	0.129	0.0521	0.213
9629.26	0.965	40.375	40.035	0.00326	0.129	0.0521	0.213
9630.22	0.965	40.375	40.036	0.00292	0.129	0.0521	0.213
9631.10	0.965	40.390	40.050	0.00342	0.129	0.0522	0.213
9632.22	0.965	40.402	40.063	0.00315	0.129	0.0522	0.213
9633.10	0.965	40.413	40.074	0.00317	0.129	0.0522	0.213
9634.06	0.965	40.434	40.095	0.00330	0.129	0.0522	0.213
9634.95	0.965	40.451	40.111	0.00295	0.129	0.0522	0.213
9635.90	0.965	40.473	40.133	0.00315	0.129	0.0523	0.213
9636.95	0.965	40.497	40.157	0.00329	0.129	0.0523	0.213
9637.91	0.965	40.514	40.175	0.00312	0.129	0.0523	0.213
9638.88	0.965	40.548	40.208	0.00321	0.129	0.0524	0.213
9639.91	0.965	40.580	40.240	0.00296	0.129	0.0524	0.213
9640.88	0.965	40.612	40.272	0.00320	0.129	0.0524	0.213
9641.84	0.965	40.657	40.318	0.00310	0.129	0.0525	0.213
9642.81	0.965	40.706	40.366	0.00321	0.129	0.0526	0.213
9643.84	0.965	40.757	40.417	0.00319	0.129	0.0526	0.213
9644.81	0.965	40.813	40.473	0.00326	0.129	0.0527	0.212
9645.86	0.965	40.871	40.531	0.00331	0.129	0.0528	0.212
9646.82	0.965	40.933	40.593	0.00309	0.129	0.0529	0.212
9647.87	0.965	41.015	40.675	0.00320	0.129	0.0530	0.212
9648.91	0.965	41.119	40.779	0.00326	0.129	0.0531	0.212
9649.88	0.965	41.218	40.878	0.00286	0.129	0.0532	0.212
9650.92	0.965	41.337	40.997	0.00291	0.129	0.0534	0.211
9651.89	0.965	41.472	41.132	0.00278	0.129	0.0536	0.211
9652.37	0.965	41.559	41.219	0.00292	0.129	0.0537	0.211
9652.93	0.964	41.663	41.322	0.00277	0.129	0.0538	0.211
9653.42	0.964	41.760	41.419	0.00267	0.129	0.0539	0.211
9653.98	0.964	41.880	41.540	0.00271	0.129	0.0541	0.210
9654.46	0.964	42.009	41.669	0.00311	0.129	0.0542	0.210
9654.94	0.964	42.166	41.826	0.00290	0.129	0.0545	0.210
9655.51	0.964	42.333	41.993	0.00314	0.129	0.0547	0.210
9656.07	0.964	42.521	42.181	0.00303	0.129	0.0549	0.209
9656.63	0.964	42.719	42.378	0.00280	0.129	0.0552	0.209
9657.20	0.964	42.991	42.651	0.00375	0.129	0.0555	0.208
9657.60	0.964	43.258	42.918	0.00367	0.129	0.0559	0.208
9658.16	0.964	43.570	43.229	0.00366	0.129	0.0563	0.207
9658.64	0.964	43.929	43.588	0.00431	0.129	0.0567	0.207
9659.13	0.964	44.435	44.094	0.00502	0.129	0.0574	0.206
9659.61	0.964	44.966	44.625	0.00519	0.129	0.0581	0.205
9660.09	0.964	45.608	45.267	0.00658	0.129	0.0590	0.204
9660.58	0.964	46.425	46.084	0.00887	0.129	0.0601	0.203
9661.07	0.964	47.492	47.151	0.0110	0.130	0.0615	0.201
9661.63	0.964	48.925	48.583	0.0169	0.130	0.0637	0.200
9662.11	0.964	50.832	50.490	0.0282	0.132	0.0672	0.199
9662.60	0.964	53.554	53.212	0.0523	0.139	0.0746	0.203
9663.08	0.964	57.691	57.350	0.0803	0.152	0.0877	0.211
9663.64	0.964	63.219	62.877	0.109	0.169	0.107	0.223
9664.20	0.964	71.136	70.795	0.180	0.222	0.158	0.270
9664.70	0.964	81.538	81.197	0.285	0.313	0.255	0.355
9665.18	0.964	95.272	94.931	0.383	0.404	0.385	0.440
9665.66	0.964	110.15	109.80	0.439	0.458	0.504	0.489
9666.14	0.964	125.20	124.86	0.420	0.439	0.550	0.466
9666.71	0.964	148.00	147.66	0.580	0.594	0.879	0.617
9667.11	0.964	166.54	166.20	0.568	0.582	0.969	0.603
9667.59	0.964	171.23	170.89	0.285	0.312	0.535	0.332
9668.09	0.964	174.18	173.84	0.0986	0.162	0.283	0.182
9668.57	0.964	176.01	175.67	0.0200	0.131	0.230	0.150
9669.05	0.964	176.25	175.91	0.00342	0.129	0.228	0.149
9669.61	0.964	174.99	174.65	0.0181	0.130	0.228	0.150
9670.10	0.964	171.90	171.56	0.0469	0.137	0.236	0.157
9670.50	0.964	167.40	167.06	0.0616	0.143	0.239	0.164

Table 33 (continued)

E (eV)	σ_E (eV)	$[\mu/\rho]$ (cm^2 g^{-1})	$[\mu/\rho]_{\rm pe}$ (cm^2 g^{-1})	$\sigma_{[\mu/\rho]_{\rm rel}}$ (%)	$\sigma_{[\mu/\rho]}$ (%)	$\sigma_{[\mu/\rho]}$ (cm^2 g^{-1})	$\sigma_{[\mu/\rho]_{\rm pe}}$ (%)
9670.99	0.964	160.81	160.46	0.0499	0.138	0.223	0.160
9671.47	0.964	155.44	155.10	0.0331	0.133	0.207	0.155
9672.04	0.964	150.76	150.42	0.0193	0.131	0.197	0.153
9672.52	0.964	147.74	147.39	0.0109	0.130	0.191	0.153
9673.09	0.964	145.77	145.43	0.00375	0.129	0.188	0.153
9673.49	0.964	145.38	145.03	0.00255	0.129	0.188	0.153
9673.98	0.964	145.80	145.45	0.00332	0.129	0.188	0.153
9674.46	0.964	146.66	146.32	0.00467	0.129	0.189	0.153
9674.94	0.964	147.90	147.56	0.00608	0.129	0.191	0.152
9675.43	0.964	149.27	148.92	0.00705	0.129	0.193	0.152
9675.84	0.964	150.55	150.21	0.00820	0.129	0.195	0.152
9676.40	0.964	151.54	151.20	0.00287	0.129	0.196	0.152
9676.88	0.964	151.82	151.47	0.00259	0.129	0.196	0.152
9677.86	0.964	148.48	148.14	0.00174	0.129	0.192	0.152
9678.74	0.964	142.83	142.48	0.00144	0.129	0.184	0.153
9679.80	0.964	137.76	137.42	0.00153	0.129	0.178	0.154
9680.85	0.963	134.68	134.34	0.00176	0.129	0.174	0.155
9681.82	0.963	133.06	132.72	0.00190	0.129	0.172	0.155
9682.79	0.963	132.24	131.90	0.00204	0.129	0.171	0.155
9683.76	0.963	131.47	131.12	0.00184	0.129	0.170	0.155
9684.73	0.963	131.00	130.65	0.00215	0.129	0.169	0.155
9685.87	0.963	131.13	130.79	0.00246	0.129	0.169	0.155
9686.77	0.963	131.82	131.47	0.00268	0.129	0.170	0.155
9687.81	0.963	132.87	132.52	0.00256	0.129	0.172	0.155
9688.87	0.963	133.96	133.61	0.00270	0.129	0.173	0.155
9689.92	0.963	135.00	134.65	0.00256	0.129	0.174	0.155
9690.90	0.963	135.68	135.33	0.00256	0.129	0.175	0.155
9691.87	0.963	136.15	135.80	0.00260	0.129	0.176	0.155
9693.01	0.963	136.45	136.10	0.00247	0.129	0.176	0.155
9694.06	0.963	136.72	136.37	0.00243	0.129	0.177	0.155
9694.95	0.963	137.07	136.72	0.00258	0.129	0.177	0.155
9696.09	0.963	137.66	137.31	0.00259	0.129	0.178	0.155
9697.14	0.963	138.36	138.01	0.00256	0.129	0.179	0.154
9698.12	0.963	139.11	138.76	0.00268	0.129	0.180	0.154
9699.09	0.963	139.52	139.17	0.00256	0.129	0.180	0.154
9700.07	0.963	139.61	139.26	0.00245	0.129	0.180	0.154
9701.12	0.963	139.47	139.12	0.00227	0.129	0.180	0.154
9702.26	0.963	139.29	138.94	0.00239	0.129	0.180	0.154
9703.15	0.963	139.25	138.90	0.00233	0.129	0.180	0.154
9704.21	0.963	139.34	138.99	0.00247	0.129	0.180	0.155
9705.20	0.963	139.49	139.13	0.00243	0.129	0.180	0.155
9706.25	0.963	139.70	139.34	0.00252	0.129	0.180	0.155
9707.23	0.963	139.87	139.52	0.00250	0.129	0.181	0.155
9708.12	0.963	140.02	139.66	0.00247	0.129	0.181	0.155
9709.18	0.962	140.11	139.75	0.00251	0.129	0.181	0.155
9710.15	0.962	140.13	139.78	0.00247	0.129	0.181	0.155
9711.05	0.962	140.14	139.78	0.00239	0.129	0.181	0.155
9712.03	0.962	140.22	139.86	0.00240	0.129	0.181	0.155
9713.17	0.962	140.42	140.07	0.00254	0.129	0.181	0.155
9714.06	0.962	140.84	140.48	0.00277	0.129	0.182	0.154
9715.04	0.962	141.34	140.98	0.00258	0.129	0.183	0.154
9715.94	0.962	141.83	141.47	0.00260	0.129	0.183	0.154
9716.84	0.962	142.15	141.79	0.00256	0.129	0.184	0.154
9717.89	0.962	142.24	141.88	0.00230	0.129	0.184	0.154
9718.88	0.962	142.04	141.68	0.00234	0.129	0.183	0.154
9719.85	0.962	141.66	141.30	0.00229	0.129	0.183	0.154
9720.92	0.962	141.15	140.80	0.00228	0.129	0.182	0.154
9721.98	0.962	140.36	140.00	0.00201	0.129	0.181	0.155
9723.94	0.962	139.09	138.73	0.00195	0.129	0.180	0.155
9725.90	0.962	138.02	137.66	0.00209	0.129	0.178	0.155
9727.94	0.962	137.15	136.79	0.00226	0.129	0.177	0.155
9730.07	0.962	137.07	136.71	0.00247	0.129	0.177	0.155
9732.11	0.962	137.84	137.48	0.00290	0.129	0.178	0.155
9734.07	0.962	139.17	138.81	0.00295	0.129	0.180	0.155
9736.20	0.961	140.78	140.42	0.00312	0.129	0.182	0.155
9738.33	0.961	141.67	141.31	0.00274	0.129	0.183	0.155
9740.46	0.961	141.89	141.53	0.00251	0.129	0.183	0.155
9742.43	0.961	141.75	141.39	0.00244	0.129	0.183	0.155
9744.48	0.961	141.55	141.19	0.00241	0.129	0.183	0.155
9746.61	0.961	141.39	141.03	0.00254	0.129	0.183	0.155
9748.58	0.961	141.22	140.86	0.00233	0.129	0.182	0.155
9750.47	0.961	141.02	140.66	0.00247	0.129	0.182	0.155
9752.36	0.961	140.60	140.23	0.00220	0.129	0.182	0.155

Table 33 (continued)

E (eV)	σ_E (eV)	$[\mu/\rho]$ (cm^2 g^{-1})	$[\mu/\rho]_{\rm pe}$ (cm^2 g^{-1})	$\sigma_{[\mu/\rho]_{\rm rel}}$ (%)	$\sigma_{[\mu/\rho]}$ (%)	$\sigma_{[\mu/\rho]}$ (cm^2 g^{-1})	$\sigma_{[\mu/\rho]_{\rm pe}}$ (%)
9754.41	0.961	139.98	139.62	0.00215	0.129	0.181	0.155
9756.38	0.961	139.15	138.79	0.00225	0.129	0.180	0.155
9758.19	0.961	138.42	138.06	0.00234	0.129	0.179	0.155
9760.17	0.961	137.88	137.52	0.00224	0.129	0.178	0.156
9762.14	0.961	137.82	137.45	0.00241	0.129	0.178	0.156
9764.20	0.960	138.10	137.74	0.00259	0.129	0.178	0.156
9766.09	0.960	138.46	138.09	0.00259	0.129	0.179	0.156
9768.15	0.960	138.51	138.14	0.00226	0.129	0.179	0.156
9770.30	0.960	138.00	137.63	0.00218	0.129	0.178	0.156
9772.28	0.960	137.07	136.70	0.00202	0.129	0.177	0.156
9774.26	0.960	136.26	135.89	0.00213	0.129	0.176	0.156
9776.49	0.960	135.75	135.39	0.00218	0.129	0.175	0.156
9778.55	0.960	135.71	135.34	0.00239	0.129	0.175	0.156
9780.62	0.960	135.84	135.47	0.00231	0.129	0.175	0.156
9782.60	0.960	135.97	135.60	0.00237	0.129	0.176	0.156
9784.67	0.960	136.20	135.83	0.00262	0.129	0.176	0.156
9786.73	0.960	136.56	136.19	0.00263	0.129	0.176	0.156
9788.81	0.960	137.06	136.69	0.00278	0.129	0.177	0.156
9790.80	0.960	137.55	137.18	0.00263	0.129	0.178	0.156
9792.78	0.959	138.10	137.73	0.00277	0.129	0.178	0.156
9797.83	0.959	139.26	138.88	0.00336	0.129	0.180	0.156
9802.65	0.959	139.91	139.54	0.00260	0.129	0.181	0.156
9807.64	0.959	140.23	139.86	0.00260	0.129	0.181	0.156
9812.78	0.959	140.28	139.91	0.00215	0.129	0.181	0.156
9817.86	0.959	139.58	139.20	0.00193	0.129	0.180	0.156
9823.11	0.958	138.14	137.76	0.00161	0.129	0.178	0.156
9828.21	0.958	136.56	136.18	0.00191	0.129	0.176	0.157
9833.21	0.958	134.79	134.41	0.00179	0.129	0.174	0.157
9838.14	0.958	133.92	133.54	0.00228	0.129	0.173	0.158
9843.00	0.958	133.57	133.19	0.00228	0.129	0.172	0.158
9848.02	0.957	133.29	132.91	0.00222	0.129	0.172	0.158
9853.05	0.957	134.00	133.62	0.00317	0.129	0.173	0.158
9858.26	0.957	134.99	134.61	0.00290	0.129	0.174	0.158
9863.47	0.957	135.57	135.19	0.00261	0.129	0.175	0.157
9868.51	0.957	135.77	135.38	0.00251	0.129	0.175	0.157
9873.56	0.957	135.89	135.50	0.00232	0.129	0.175	0.157
9878.54	0.956	135.92	135.53	0.00232	0.129	0.175	0.157
9883.34	0.956	135.88	135.50	0.00253	0.129	0.175	0.157
9888.41	0.956	136.12	135.73	0.00251	0.129	0.176	0.157
9893.40	0.956	135.94	135.56	0.00212	0.129	0.176	0.157
9898.65	0.956	135.09	134.71	0.00199	0.129	0.174	0.158
9903.81	0.955	134.40	134.01	0.00217	0.129	0.174	0.158
9908.99	0.955	133.85	133.47	0.00214	0.129	0.173	0.158
9914.26	0.955	132.90	132.51	0.00185	0.129	0.172	0.158
9919.19	0.955	132.00	131.62	0.00183	0.129	0.170	0.158
9924.20	0.955	131.07	130.68	0.00177	0.129	0.169	0.159
9929.06	0.955	130.37	129.98	0.00217	0.129	0.168	0.159
9934.09	0.954	129.98	129.59	0.00229	0.129	0.168	0.159
9939.21	0.954	130.19	129.80	0.00255	0.129	0.168	0.159
9944.33	0.954	130.59	130.20	0.00259	0.129	0.169	0.159
9949.55	0.954	131.02	130.64	0.00260	0.129	0.169	0.159
9954.78	0.954	131.39	131.00	0.00234	0.129	0.170	0.159
9959.66	0.953	131.50	131.12	0.00236	0.129	0.170	0.159
9964.72	0.953	131.54	131.16	0.00236	0.129	0.170	0.159
9969.53	0.953	131.54	131.15	0.00228	0.129	0.170	0.159
9974.51	0.953	131.37	130.98	0.00232	0.129	0.170	0.159
9979.51	0.953	131.15	130.76	0.00229	0.129	0.169	0.159
9984.68	0.953	130.91	130.52	0.00223	0.129	0.169	0.159
9990.03	0.952	130.54	130.15	0.00222	0.129	0.169	0.159
9995.21	0.952	130.05	129.66	0.00200	0.129	0.168	0.159
10000.4	0.952	129.55	129.16	0.00198	0.129	0.167	0.159
10005.2	0.952	129.08	128.69	0.00205	0.129	0.167	0.159
10010.2	0.952	128.67	128.28	0.00227	0.129	0.166	0.159
10015.3	0.951	128.15	127.76	0.00215	0.129	0.165	0.160
10020.1	0.951	127.63	127.24	0.00198	0.129	0.165	0.160
10025.2	0.951	127.26	126.87	0.00218	0.129	0.164	0.160
10030.3	0.951	127.01	126.62	0.00226	0.129	0.164	0.160
10035.7	0.951	126.74	126.35	0.00201	0.129	0.164	0.160
10045.8	0.950	126.36	125.97	0.00235	0.129	0.163	0.160
10055.7	0.950	126.52	126.13	0.00237	0.129	0.163	0.160
10065.7	0.950	126.48	126.08	0.00223	0.129	0.163	0.160
10075.9	0.949	126.37	125.98	0.00203	0.129	0.163	0.160
10086.2	0.949	126.11	125.72	0.00206	0.129	0.163	0.160

Table 33 (continued)

E (eV)	σ_E (eV)	$[\mu/\rho]$ (cm^2 g^{-1})	$[\mu/\rho]_{\rm pe}$ (cm^2 g^{-1})	$\sigma_{[\mu/\rho]_{\rm rel}}$ (%)	$\sigma_{[\mu/\rho]}$ (%)	$\sigma_{[\mu/\rho]}$ (cm^2 g^{-1})	$\sigma_{[\mu/\rho]_{\rm pe}}$ (%)
10096.2	0.949	125.64	125.25	0.00187	0.129	0.162	0.161
10105.9	0.948	125.03	124.63	0.00193	0.129	0.161	0.161
10115.9	0.948	124.31	123.91	0.00171	0.129	0.160	0.161
. . .							
14871.1	0.983	90.911	90.476	0.0114	0.130	0.118	0.177
14972.2	0.987	89.278	88.843	0.00285	0.129	0.115	0.178
15073.1	0.991	87.756	87.320	0.00311	0.129	0.113	0.179

Table 34

Zn metal foils, 8.51–11.59 keV: uncertainties of mass attenuation coefficients at several systematic correction stages, and the magnitudes of specific systematic corrections.

Contributions to measurements are labelled $[\mu/\rho]_{\rm rel}$ if they contribute in particular to the relative structure of adjacent points, *e.g.* the edge shape or the XAFS, and are labelled $[\mu/\rho]_{\rm abs}$ if they primarily scale all values with a slowly varying function. Hence there are two final uncertainties, relating to the absolute value of the mass attenuation coefficient $[\mu/\rho]$ and relating to the pointwise and local structure, *e.g.* for XAFS analysis, $[\mu/\rho]_{\rm rel}$. *Notes*: (1) Standard errors from counting statistics (variance including precision before systematic corrections). (2) Blank correction and net uncertainty. Large for thin foils. (3) Dark current correction and net uncertainty (0.5 counts). (4) Total dispersion of measurement precision after the corrections above. (5) The harmonic coefficient and contribution is very small in this case. (6) Secondary photons from fluorescent scattering. Correction large for 50 μm sample and directly above absorption edges, 0 below Zn edge. Maximum uncertainty only applies to 50 μm sample. (7) Effect of roughness is greatest for 10 μm sample when attenuation is large. (8) Bandwidth correction greatest for 50 μm sample along the edge where d$[\mu/\rho]$/dE is greatest. (9) Use of nominal thickness and corresponding uncertainty. (10) Use of local integrated column density (ICD) and corresponding uncertainty. (11) Absolute accuracy of the full-foil mapping technique. (12) Error in energy calibration data. Correction minimal at the absorption edge. (13) Relative measurements and uncertainties after correcting for systematic errors. (14) Absolute measurements and uncertainties after normalizing to absolute thickness with full-foil mapping.

Quantity	Magnitude of correction $[\mu/\rho]$	Uncertainty and variance $\sigma_{[\mu/\rho]}$	Comments
$[\mu/\rho]_{\rm rel}$		<0.319%	Variance [Note (1)]
	22–536% (10 μm foil)	<1.853% (10 μm)	Blank normalization [Note (2)]
	Up to 97% (50 μm foil)	<0.133% (100 μm)	
	Up to 57% ± 15% (100 μm)	0.00039–1.46%	Dark current [Note (3)]
	Up to 1.31% (10 μm)		
(total)		<0.042%	Total variance after corrections [Note (4)]
	1–5 × 10^{-3}%		Harmonic correction [Note (5)]
(50 μm)	<14.2%	<10.5%	Fluorescence correction [Note (6)]
(25 μm)	<0.101%	<0.003%	
(10 μm)	<0.0123%	<0.0003%	
(total)	<0.139%	<0.028%	
(10 μm)	<2.52%	<0.02%	Roughness [Note (7)]
(25 μm)	<0.815%	<0.015%	
(total)	<1.56%	<0.0037%	
(50 μm)	<9.89%	<0.239%	Bandwidth [Note (8)]
(25 μm)	<4.91%	<0.119%	
(10 μm)	<1.703%	<0.041%	
(total)	<7.24%	<0.0037%	
$[\mu/\rho]_{\rm abs}$		<0.037%	Nominal thicknesses [Note (9)]
	3.55–7.60%	0.000018–0.024237%	Average ICD [Note (10)]
	0.374–7.606%	0.024%	Full-foil map [Note (11)]
E (keV)	−1 to +3 eV ± 1–3 eV	<0.0038%	Energy [Note (12)]

Quantity	Magnitude range (cm^2 g^{-1})	Uncertainty range $\sigma_{[\mu/\rho]}$	Comments
$[\mu/\rho]_{\rm rel}$	34.765–325.321	0.000677–0.027%	After systematic corrections [Note (13)]
$[\mu/\rho]_{\rm abs}$	34.765–327.760	0.023–0.0357%	After normalizing to absolute thickness from full-foil map [Note (14)]

Four light-tight zinc foils from Goodfellow 25 mm × 25 mm in size with nominal thicknesses of 10 μm, 25 μm, 50 μm and 100 μm were chosen such that the log attenuation of the material fell between 0.5 and 6 over the energy range of the measurements at room temperature (Chantler *et al.*, 2001*a*). One could in principle present data sets for each of these thicknesses, either as 'raw' or 'corrected' data; however, the figures presented by Ekanayake *et al.* (2021*a*) prove that this would in no way be structurally consistent with one another, and of course therefore that none of the data sets would be accurate to the level needed for detailed analysis. Hence preprocessing is important. The mass attenuation coefficient of zinc metal and the mass absorption coefficient were determined to high accuracy using an advanced wiggler beamline, and are in good agreement with values from earlier data sets collected on a bending-magnet beamline. The imaginary

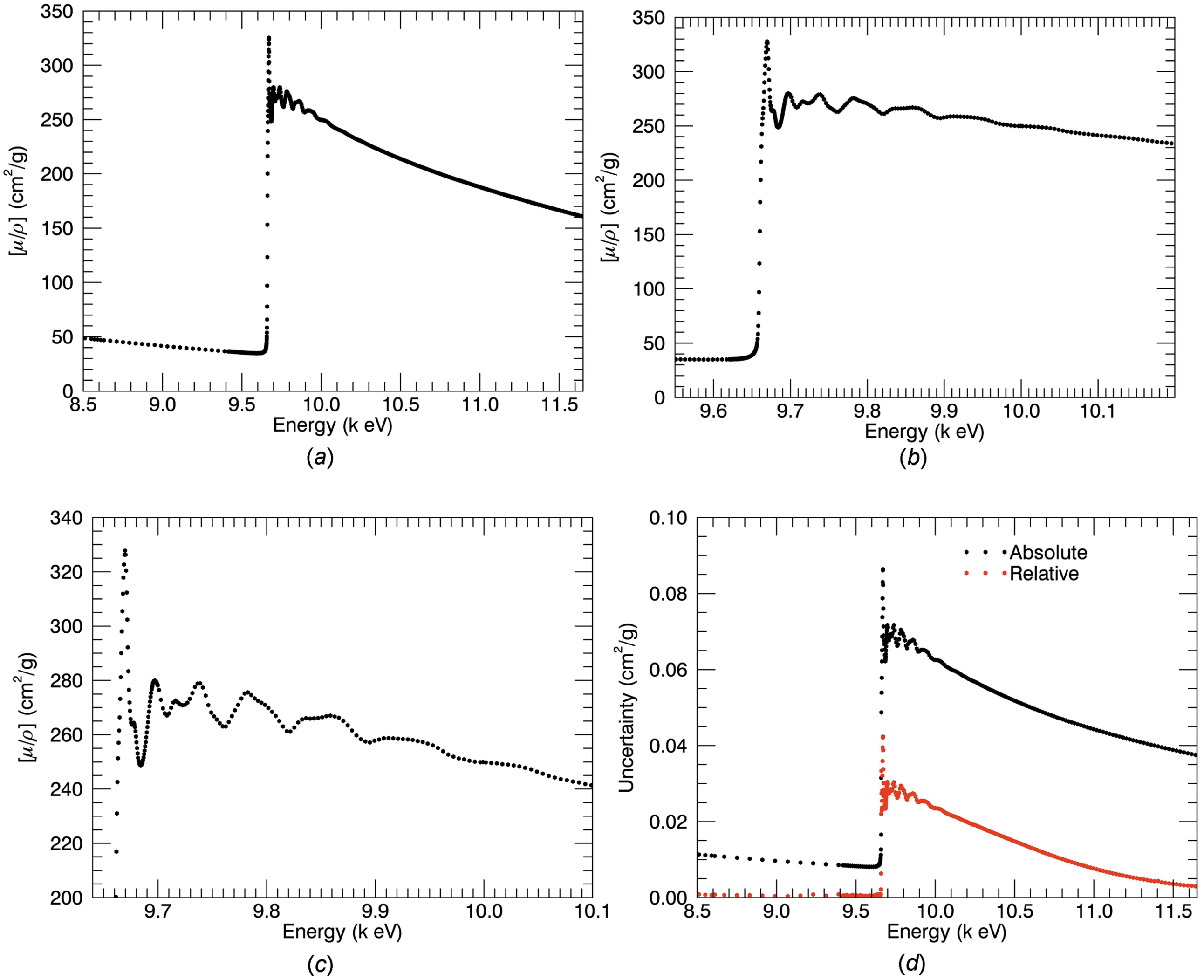

Figure 28
Zn metal foils 8.51–11.59 keV. Mass attenuation coefficients: (*a*) over the energy range 8.51 keV to 11.59 keV; (*b*) covering the edge and XAFS region; (*c*) in the central XAFS region; and (*d*) absolute and relative percentage uncertainties. The zinc *K* absorption edge is observed at 9.66 keV and the associated XAFS lies between 9.66 keV and 10.10 keV.

component of the atomic form factor and the zinc *K*-edge jump ratio and jump factor were determined and compared with widely varying results in the literature, representing two attempts at linking XAS and XAFS theory (for the linear or mass absorption coefficient or photoelectric effect) with experimental data. The XAFS analysis shows excellent agreement between the measured and tabulated values, and yields bond lengths and the nanostructure of zinc with uncertainties from 0.1% to 0.3%, or 0.003 Å to 0.008 Å. We observed significant variation from the reported crystal structure, suggesting local dynamic motion of the Zn atoms. XAFS is sensitive to dynamic correlated motion and in principle is capable of observing local dynamic motion beyond the reach of conventional crystallography.

Four files, bz5029sup25.txt to bz5029sup28.txt, are available as supporting information. The data shown in Table 35 are available in .dat format in bz5029sup25.txt. The file bz5029sup26.txt, also in .dat format, provides $[\mu/\rho]_{\rm tot}$ ($\rm cm^2\,g^{-1}$) versus E values with uncertainties suitable for input to *eFEFFit* (Smale *et al.*, 2006; Schalken & Chantler, 2018), *iFEFFit* (Newville, 2001), *Athena* (Ravel & Newville, 2005) and *mu2chi* (Schalken & Chantler, 2018). bz5029sup27.txt contains the data in .cif format, and bz5029sup28.txt contains χ versus k values with uncertainties for input to *eFEFFit*, *iFEFFit* and *Athena*.

22. XANES, pre-edge spectra and other modalities

All of the data sets which report detailed XAFS also report detailed XANES and pre-edge spectra. It might seem obvious that transmission (*i.e.* XAS) data sets with a fine grid spacing will provide the best XANES and pre-edge detail and structure. However, many XANES and pre-edge spectra are currently collected using fluorescence spectroscopy; care must be taken to define the region of interest explicitly or implicitly by the detector chain, and also the lower cut-off for onset of characteristic fluorescence. Many experiments measure and report XANES/pre-edge spectra only, especially in reaction or

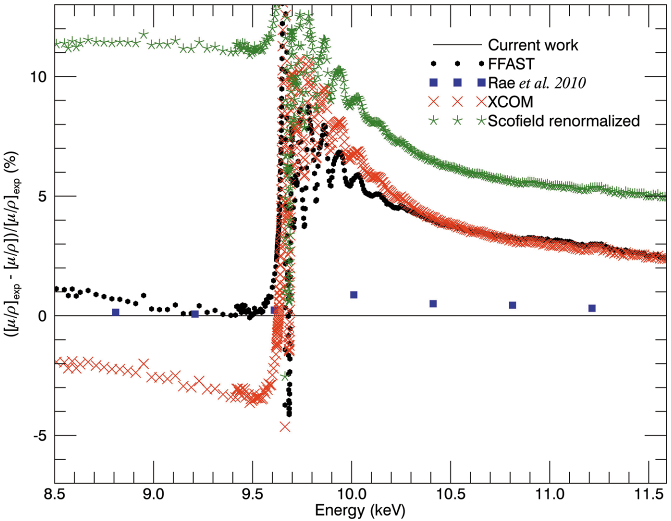

Figure 29
The percentage discrepancy between the derived mass attenuation coefficient and the tabulated FFAST values (black bullets) (Chantler, 2000) over the energy range 8.5 keV to 11.59 keV, and the percentage discrepancies between XCOM tabulated values with Hartree–Slater calculations (×) (Berger & Hubbell, 1987), Scofield tabulated values renormalized with Hartree–Fock calculations (*) (Scofield, 1973) and Rae *et al.* (2010*a*) measurements (filled squares). The near-edge region has a large discrepancy from current measurements due to the solid-state XAFS structure and the triangle effect. Renormalized Scofield (1973) values deviate dramatically everywhere, implying that the earlier belief that the correct theory lies between the unrenormalized and the renormalized predictions is not valid for these data.

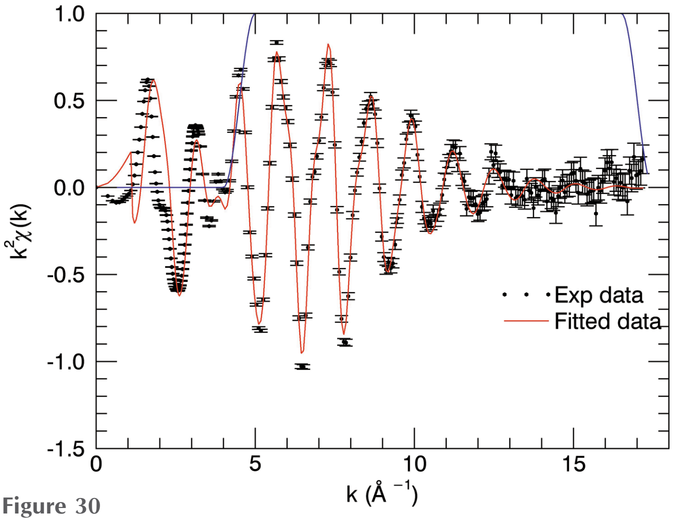

Figure 30
Zinc metal foils, 8.51–11.59 keV: data (black) with absolute uncertainties for the fine structure function above the zinc *K* edge produced by the *mu2chi* non-interpolation background subtraction software in *eFEFFit* and the fitted model (red) over a Hanning window $k = 4.5$ Å^{-1} to 17 Å^{-1}.

evolution environments, so while the individual data sets might be small, data collection results in a significant number of data files. These can be extremely valuable, if difficult to calibrate or normalize (Streltsov *et al.*, 2018). A key question about any data set, on a par with the challenge of spacing and grid uniformity, is the beamline or extracted resolution (the

Table 35
Zinc metal foils, 8.51–11.59 keV: mass attenuation coefficients $[\mu/\rho]$ and the imaginary component f'' of the form factor as a function of X-ray energy with one standard deviation.

Relative and total percentage uncertainties in the total mass attenuation coefficients $\sigma_{[\mu/\rho]_{\rm rel}}$ and $\sigma_{[\mu/\rho]}$ are presented with the latter also given in absolute units. The percentage uncertainty in $[\mu/\rho]_{\rm pe}$ includes uncertainty in the measurements and in the calculations of thermal diffuse and Compton scattering attenuation. (Some rows of values have been omitted for brevity. The full version is available in the supporting information.)

E (eV)	σ_E (eV)	$[\mu/\rho]$ (cm^2 g^{-1})	$\sigma_{[\mu/\rho]}$ (%)	$\sigma_{[\mu/\rho]_{\rm rel}}$ (%)	$[\mu/\rho]_{\rm pe}$ (cm^2 g^{-1})	$\sigma_{[\mu/\rho]_{\rm pe}}$ (%)	f'' (e atom^{-1})
8508.98	0.165	48.672	0.023	0.0026	46.695	0.060	0.617
8549.04	0.168	48.044	0.023	0.0026	46.076	0.061	0.612
8569.06	0.170	47.623	0.023	0.0014	45.660	0.062	0.608
8589.09	0.171	47.457	0.023	0.0034	45.498	0.062	0.607
8609.12	0.173	47.022	0.023	0.0057	45.068	0.063	0.603
8629.15	0.174	46.803	0.023	0.0014	44.854	0.063	0.601
8669.20	0.177	46.259	0.023	0.0034	44.318	0.064	0.597
8709.25	0.180	45.613	0.023	0.0012	43.681	0.065	0.591
8749.31	0.183	45.015	0.023	0.0032	43.092	0.067	0.586
8789.37	0.186	44.424	0.024	0.0010	42.510	0.068	0.581
8829.42	0.189	43.875	0.023	0.0030	41.969	0.069	0.576
8869.47	0.192	43.306	0.023	0.0009	41.409	0.070	0.571
8909.53	0.195	42.747	0.023	0.0047	40.858	0.071	0.566
8949.58	0.198	42.379	0.023	0.0013	40.498	0.072	0.563
8989.64	0.201	41.638	0.023	0.0040	39.766	0.074	0.555
9029.69	0.204	41.132	0.023	0.0021	39.268	0.075	0.551
9069.75	0.207	40.615	0.023	0.0032	38.759	0.076	0.546
9109.80	0.210	40.182	0.024	0.0013	38.334	0.077	0.543
9149.86	0.212	39.536	0.023	0.0032	37.696	0.078	0.536
9189.91	0.215	39.048	0.024	0.0024	37.216	0.080	0.531
9229.97	0.218	38.687	0.023	0.0043	36.864	0.080	0.529
9270.02	0.221	38.104	0.023	0.0015	36.288	0.082	0.523
9310.08	0.224	37.667	0.023	0.0054	35.859	0.083	0.519
9350.13	0.227	37.144	0.023	0.0016	35.344	0.084	0.513
9390.19	0.230	36.676	0.023	0.0029	34.883	0.085	0.509
9413.22	0.232	36.423	0.024	0.0019	34.635	0.086	0.507
9419.22	0.232	36.487	0.023	0.0033	34.700	0.086	0.508
9425.23	0.233	36.425	0.024	0.0013	34.639	0.086	0.507
9431.24	0.233	36.311	0.023	0.0021	34.527	0.086	0.506

Table 35 (continued)

E (eV)	σ_E (eV)	$[\mu/\rho]$ (cm^2 g^{-1})	$\sigma_{[\mu/\rho]}$ (%)	$\sigma_{[\mu/\rho]_{\rm rel}}$ (%)	$[\mu/\rho]_{\rm pe}$ (cm^2 g^{-1})	$\sigma_{[\mu/\rho]_{\rm pe}}$ (%)	f'' (e atom^{-1})
9437.25	0.234	36.283	0.023	0.0014	34.499	0.086	0.506
9443.26	0.234	36.131	0.023	0.0032	34.349	0.087	0.504
9449.27	0.234	36.178	0.023	0.0019	34.397	0.087	0.505
9455.27	0.235	36.037	0.023	0.0034	34.257	0.087	0.503
9461.28	0.235	36.038	0.023	0.0009	34.259	0.087	0.504
9467.29	0.236	35.872	0.023	0.0029	34.094	0.087	0.501
9473.30	0.236	35.827	0.023	0.0017	34.050	0.088	0.501
9479.31	0.237	35.779	0.023	0.0045	34.003	0.088	0.501
9485.32	0.237	35.598	0.023	0.0010	33.823	0.088	0.498
9491.32	0.238	35.591	0.023	0.0030	33.818	0.088	0.499
9497.33	0.238	35.504	0.023	0.0018	33.732	0.088	0.498
9503.34	0.238	35.462	0.023	0.0035	33.691	0.088	0.497
9509.35	0.239	35.480	0.024	0.0014	33.710	0.088	0.498
9515.36	0.239	35.358	0.023	0.0036	33.590	0.089	0.497
9521.36	0.240	35.299	0.023	0.0012	33.531	0.089	0.496
9527.37	0.240	35.240	0.023	0.0024	33.474	0.089	0.496
9533.38	0.241	35.184	0.023	0.0013	33.418	0.089	0.495
9539.39	0.241	35.148	0.023	0.0027	33.384	0.089	0.495
9545.40	0.242	35.040	0.024	0.0011	33.277	0.089	0.494
9551.41	0.242	34.991	0.023	0.0051	33.229	0.089	0.493
9557.41	0.242	35.041	0.023	0.0016	33.281	0.089	0.494
9563.42	0.243	34.941	0.023	0.0029	33.182	0.090	0.493
9569.43	0.243	34.973	0.023	0.0012	33.214	0.090	0.494
9575.44	0.244	34.873	0.023	0.0045	33.116	0.090	0.493
9581.45	0.244	34.900	0.024	0.0014	33.144	0.090	0.493
9587.46	0.245	34.819	0.023	0.0038	33.064	0.090	0.493
9593.46	0.245	34.765	0.023	0.0011	33.011	0.090	0.492
9599.47	0.245	34.844	0.023	0.0029	33.091	0.090	0.494
9605.48	0.246	34.881	0.024	0.0011	33.129	0.090	0.494
9611.49	0.246	34.920	0.023	0.0043	33.169	0.090	0.495
9617.50	0.247	34.962	0.024	0.0014	33.213	0.090	0.496
9620.70	0.247	35.031	0.023	0.0031	33.282	0.089	0.497
9621.20	0.247	35.066	0.023	0.0017	33.317	0.089	0.498
9621.70	0.247	35.046	0.023	0.0053	33.297	0.089	0.498
9622.20	0.247	35.078	0.024	0.0020	33.329	0.089	0.498
9622.70	0.247	35.079	0.023	0.0029	33.331	0.089	0.498
9623.20	0.247	35.129	0.023	0.0015	33.380	0.089	0.499
9623.71	0.247	35.121	0.023	0.0029	33.373	0.089	0.499
9624.21	0.247	35.196	0.024	0.0015	33.448	0.089	0.500
9624.71	0.247	35.155	0.023	0.0043	33.407	0.089	0.500
9625.21	0.247	35.194	0.023	0.0012	33.446	0.089	0.500
9625.71	0.247	35.197	0.023	0.0034	33.449	0.089	0.500
9626.21	0.247	35.222	0.023	0.0009	33.474	0.089	0.501
9626.71	0.247	35.238	0.023	0.0028	33.491	0.089	0.501
9627.21	0.248	35.268	0.024	0.0010	33.520	0.089	0.501
9627.71	0.248	35.268	0.023	0.0026	33.520	0.089	0.501
9628.21	0.248	35.314	0.023	0.0012	33.567	0.089	0.502
9628.71	0.248	35.290	0.023	0.0032	33.542	0.089	0.502
9629.21	0.248	35.237	0.023	0.0018	33.490	0.089	0.501
9629.71	0.248	35.294	0.023	0.0035	33.547	0.089	0.502
9630.21	0.248	35.276	0.023	0.0016	33.529	0.089	0.502
9630.71	0.248	35.322	0.023	0.0029	33.575	0.089	0.502
9631.21	0.248	35.344	0.023	0.0012	33.597	0.089	0.503
9631.71	0.248	35.367	0.023	0.0036	33.621	0.089	0.503
9632.22	0.248	35.396	0.023	0.0012	33.649	0.089	0.504
9632.72	0.248	35.420	0.023	0.0022	33.674	0.088	0.504
9633.22	0.248	35.450	0.023	0.0023	33.703	0.088	0.504
9633.72	0.248	35.475	0.023	0.0025	33.728	0.088	0.505
9634.22	0.248	35.488	0.023	0.0021	33.742	0.088	0.505
9634.72	0.248	35.552	0.023	0.0030	33.805	0.088	0.506
9635.22	0.248	35.556	0.023	0.0011	33.810	0.088	0.506
9635.72	0.248	35.636	0.023	0.0027	33.890	0.088	0.507
9636.22	0.248	35.649	0.023	0.0016	33.903	0.088	0.508
9636.72	0.248	35.721	0.023	0.0024	33.975	0.088	0.509
9637.22	0.248	35.700	0.023	0.0013	33.954	0.088	0.508
9637.72	0.248	35.811	0.023	0.0023	34.066	0.088	0.510
9638.22	0.248	35.814	0.023	0.0013	34.069	0.088	0.510
9638.72	0.248	35.930	0.023	0.0039	34.185	0.087	0.512
9639.22	0.248	35.931	0.023	0.0013	34.186	0.087	0.512
9639.73	0.248	36.062	0.023	0.0026	34.317	0.087	0.514
9640.23	0.248	36.070	0.023	0.0008	34.325	0.087	0.514
9640.73	0.249	36.180	0.023	0.0029	34.435	0.087	0.516
9641.23	0.249	36.198	0.024	0.0020	34.453	0.087	0.516

Table 35 (continued)

E (eV)	σ_E (eV)	$[\mu/\rho]$ (cm^2 g^{-1})	$\sigma_{[\mu/\rho]}$ (%)	$\sigma_{[\mu/\rho]_{\rm rel}}$ (%)	$[\mu/\rho]_{\rm pe}$ (cm^2 g^{-1})	$\sigma_{[\mu/\rho]_{\rm pe}}$ (%)	f'' (e atom^{-1})
9641.73	0.249	36.315	0.023	0.0026	34.570	0.086	0.518
9642.23	0.249	36.352	0.023	0.0014	34.607	0.086	0.518
9642.73	0.249	36.478	0.023	0.0046	34.733	0.086	0.520
9643.23	0.249	36.523	0.023	0.0016	34.778	0.086	0.521
9643.73	0.249	36.638	0.023	0.0026	34.894	0.086	0.523
9644.23	0.249	36.713	0.023	0.0011	34.969	0.085	0.524
9644.73	0.249	36.824	0.023	0.0044	35.079	0.085	0.526
9645.23	0.249	36.943	0.024	0.0022	35.198	0.085	0.527
9645.73	0.249	37.052	0.023	0.0049	35.308	0.085	0.529
9646.24	0.249	37.201	0.023	0.0021	35.457	0.084	0.531
9646.74	0.249	37.342	0.023	0.0025	35.598	0.084	0.534
9647.24	0.249	37.501	0.024	0.0015	35.757	0.084	0.536
9647.74	0.249	37.666	0.023	0.0029	35.922	0.083	0.538
9648.24	0.249	37.837	0.024	0.0010	36.094	0.083	0.541
9648.74	0.249	38.018	0.023	0.0029	36.274	0.083	0.544
9649.24	0.249	38.232	0.023	0.0016	36.488	0.082	0.547
9649.74	0.249	38.453	0.023	0.0028	36.710	0.082	0.550
9650.24	0.249	38.634	0.023	0.0011	36.891	0.081	0.553
9650.74	0.249	39.001	0.023	0.0032	37.258	0.081	0.559
9651.24	0.249	39.212	0.023	0.0011	37.469	0.080	0.562
9651.74	0.249	39.651	0.023	0.0026	37.908	0.079	0.568
9652.24	0.249	39.953	0.023	0.0009	38.210	0.079	0.573
9652.74	0.249	40.472	0.023	0.0026	38.729	0.078	0.581
9653.25	0.249	40.918	0.023	0.0010	39.175	0.077	0.588
9653.75	0.249	41.541	0.023	0.0027	39.798	0.076	0.597
9654.25	0.250	42.145	0.023	0.0019	40.402	0.075	0.606
9654.75	0.250	42.987	0.023	0.0040	41.244	0.074	0.619
9655.25	0.250	43.869	0.023	0.0040	42.127	0.072	0.632
9655.75	0.250	45.050	0.023	0.0064	43.307	0.070	0.650
9656.25	0.250	46.363	0.023	0.0096	44.621	0.069	0.669
9656.75	0.250	48.188	0.023	0.0177	46.446	0.066	0.697
9657.25	0.250	50.384	0.024	0.0227	48.642	0.064	0.730
9657.75	0.250	53.726	0.024	0.0271	51.984	0.060	0.780
9658.25	0.250	58.365	0.024	0.0218	56.623	0.056	0.850
9658.75	0.250	65.880	0.025	0.0185	64.138	0.052	0.963
9659.25	0.250	77.756	0.029	0.0137	76.015	0.048	1.141
9659.75	0.250	97.000	0.032	0.0122	95.258	0.045	1.430
9660.25	0.250	123.314	0.036	0.0100	121.573	0.043	1.825
9660.75	0.250	153.021	0.033	0.0098	151.279	0.038	2.271
9661.26	0.250	179.796	0.030	0.0096	178.055	0.035	2.673
9661.76	0.250	200.278	0.028	0.0098	198.537	0.031	2.980
9662.26	0.250	216.916	0.027	0.0099	215.175	0.030	3.230
9662.76	0.250	231.009	0.027	0.0102	229.268	0.030	3.442
9663.26	0.250	242.570	0.027	0.0104	240.829	0.030	3.616
9663.76	0.250	251.328	0.028	0.0108	249.587	0.030	3.747
9664.26	0.250	257.017	0.028	0.0112	255.276	0.030	3.833
9664.76	0.250	261.512	0.028	0.0115	259.772	0.030	3.901
9665.26	0.250	266.378	0.028	0.0119	264.637	0.031	3.974
9665.76	0.250	273.201	0.029	0.0122	271.461	0.031	4.077
9666.26	0.250	281.180	0.029	0.0126	279.439	0.031	4.197
9666.76	0.250	290.040	0.030	0.0129	288.299	0.032	4.330
9667.26	0.250	298.021	0.030	0.0130	296.281	0.032	4.450
9667.76	0.251	305.501	0.031	0.0131	303.760	0.032	4.563
9668.27	0.251	311.899	0.031	0.0131	310.159	0.033	4.659
9668.76	0.251	317.850	0.032	0.0129	316.110	0.033	4.749
9669.27	0.251	322.668	0.032	0.0124	320.928	0.033	4.821
9669.77	0.251	326.292	0.032	0.0120	324.552	0.033	4.876
9670.27	0.251	327.760	0.032	0.0115	326.021	0.033	4.898
9670.77	0.251	326.300	0.032	0.0111	324.560	0.033	4.877
9671.27	0.251	320.434	0.032	0.0108	318.694	0.033	4.789
9671.77	0.251	312.342	0.031	0.0106	310.602	0.033	4.667
9672.27	0.251	302.348	0.031	0.0105	300.609	0.032	4.517
9672.77	0.251	292.177	0.030	0.0104	290.437	0.032	4.365
9673.27	0.251	283.354	0.030	0.0103	281.615	0.031	4.232
9673.77	0.251	276.488	0.029	0.0103	274.748	0.031	4.130
9674.27	0.251	271.882	0.029	0.0103	270.143	0.031	4.060
9674.77	0.251	268.794	0.029	0.0103	267.056	0.031	4.014
9675.27	0.251	265.770	0.029	0.0103	264.031	0.031	3.969
9675.78	0.251	264.446	0.029	0.0103	262.707	0.031	3.949
9676.28	0.251	263.758	0.029	0.0102	262.019	0.031	3.939
9676.78	0.251	263.701	0.029	0.0103	261.962	0.031	3.939
9677.28	0.251	264.055	0.029	0.0101	262.317	0.031	3.944
9677.78	0.251	264.341	0.029	0.0101	262.603	0.031	3.949

Table 35 (continued)

E (eV)	σ_E (eV)	$[\mu/\rho]$ (cm^2 g^{-1})	$\sigma_{[\mu/\rho]}$ (%)	$\sigma_{[\mu/\rho]_{\rm rel}}$ (%)	$[\mu/\rho]_{\rm pe}$ (cm^2 g^{-1})	$\sigma_{[\mu/\rho]_{\rm pe}}$ (%)	f'' (e atom^{-1})
9678.28	0.251	264.352	0.029	0.0099	262.614	0.031	3.949
9678.78	0.251	263.832	0.029	0.0099	262.094	0.031	3.941
9679.28	0.251	262.828	0.028	0.0097	261.090	0.031	3.926
9679.78	0.251	261.288	0.028	0.0097	259.550	0.031	3.903
9680.28	0.251	259.323	0.028	0.0095	257.585	0.031	3.874
9680.78	0.251	257.207	0.028	0.0096	255.469	0.030	3.843
9681.28	0.252	255.076	0.028	0.0094	253.339	0.030	3.811
9681.78	0.252	253.091	0.028	0.0095	251.353	0.030	3.781
9682.28	0.252	251.428	0.028	0.0094	249.690	0.030	3.756
9682.79	0.252	250.293	0.028	0.0095	248.556	0.030	3.739
9683.29	0.252	249.463	0.028	0.0094	247.725	0.030	3.727
9683.79	0.252	248.980	0.028	0.0095	247.243	0.030	3.720
9684.29	0.252	248.797	0.028	0.0095	247.060	0.030	3.717
9684.79	0.252	248.749	0.028	0.0096	247.012	0.030	3.717
9685.29	0.252	248.872	0.028	0.0096	247.135	0.030	3.719
9685.79	0.252	249.254	0.028	0.0097	247.517	0.030	3.725
9686.29	0.252	249.760	0.028	0.0097	248.023	0.030	3.733
9686.79	0.252	250.666	0.028	0.0099	248.930	0.030	3.746
9687.29	0.252	251.597	0.028	0.0099	249.861	0.030	3.761
9687.79	0.252	252.847	0.028	0.0100	251.110	0.030	3.780
9688.29	0.252	254.156	0.028	0.0100	252.420	0.030	3.800
9688.79	0.252	255.713	0.028	0.0102	253.977	0.030	3.823
9689.29	0.252	257.254	0.028	0.0102	255.518	0.030	3.847
9689.80	0.252	259.052	0.028	0.0103	257.316	0.030	3.874
9690.29	0.252	260.823	0.028	0.0104	259.087	0.031	3.901
9690.80	0.252	262.804	0.028	0.0105	261.068	0.031	3.931
9691.30	0.252	264.602	0.028	0.0105	262.866	0.031	3.958
9691.80	0.252	266.601	0.029	0.0106	264.865	0.031	3.988
9692.30	0.252	268.482	0.029	0.0107	266.747	0.031	4.017
9692.80	0.252	270.467	0.029	0.0107	268.732	0.031	4.047
9693.30	0.252	272.209	0.029	0.0107	270.473	0.031	4.073
9693.80	0.252	273.937	0.029	0.0108	272.201	0.031	4.100
9694.30	0.252	275.389	0.029	0.0108	273.654	0.031	4.122
9694.80	0.253	276.746	0.029	0.0109	275.011	0.031	4.142
9695.30	0.253	277.786	0.029	0.0108	276.051	0.031	4.158
9695.80	0.253	278.692	0.029	0.0109	276.957	0.031	4.172
9696.30	0.253	279.296	0.029	0.0109	277.561	0.031	4.181
9696.80	0.253	279.768	0.029	0.0109	278.033	0.031	4.189
9697.30	0.253	279.890	0.029	0.0108	278.155	0.031	4.191
9697.81	0.253	279.911	0.029	0.0108	278.176	0.031	4.191
9698.31	0.253	279.760	0.029	0.0108	278.026	0.031	4.189
9698.81	0.253	279.508	0.029	0.0106	277.774	0.031	4.186
9699.31	0.253	279.152	0.029	0.0104	277.417	0.031	4.181
9699.81	0.253	278.671	0.029	0.0104	276.937	0.031	4.174
9700.31	0.253	278.190	0.029	0.0103	276.455	0.031	4.167
9701.51	0.253	276.463	0.029	0.0103	274.729	0.031	4.141
9703.31	0.253	272.857	0.029	0.0104	271.124	0.031	4.087
9705.12	0.253	269.696	0.029	0.0105	267.963	0.031	4.041
9706.92	0.253	267.840	0.029	0.0105	266.107	0.031	4.013
9708.82	0.254	267.054	0.029	0.0105	265.322	0.031	4.002
9710.82	0.254	267.835	0.029	0.0104	266.103	0.031	4.015
9712.83	0.254	269.905	0.029	0.0104	268.173	0.031	4.047
9714.83	0.254	271.851	0.029	0.0104	270.119	0.031	4.077
9716.83	0.254	272.548	0.029	0.0105	270.816	0.031	4.089
9718.93	0.254	271.871	0.029	0.0105	270.141	0.031	4.079
9721.04	0.254	271.163	0.029	0.0107	269.432	0.031	4.069
9723.24	0.255	270.873	0.029	0.0108	269.143	0.031	4.066
9725.44	0.255	271.018	0.029	0.0109	269.289	0.031	4.069
9727.65	0.255	271.775	0.029	0.0109	270.046	0.031	4.081
9729.95	0.255	273.198	0.029	0.0108	271.469	0.031	4.104
9732.25	0.255	275.314	0.029	0.0107	273.586	0.031	4.137
9734.66	0.255	277.576	0.029	0.0105	275.849	0.031	4.172
9737.06	0.256	278.807	0.029	0.0103	277.079	0.031	4.192
9739.46	0.256	278.906	0.029	0.0103	277.179	0.031	4.194
9741.96	0.256	277.365	0.029	0.0102	275.639	0.031	4.172
9744.47	0.256	274.397	0.029	0.0102	272.671	0.031	4.128
9746.97	0.256	270.897	0.029	0.0100	269.171	0.031	4.076
9749.58	0.257	268.168	0.029	0.0101	266.442	0.031	4.036
9752.18	0.257	266.777	0.029	0.0101	265.052	0.031	4.016
9754.78	0.257	265.579	0.029	0.0103	263.854	0.031	3.999
9757.49	0.257	264.219	0.028	0.0103	262.495	0.031	3.979
9760.29	0.257	263.063	0.028	0.0104	261.340	0.031	3.963
9762.99	0.258	263.024	0.028	0.0105	261.301	0.031	3.964

Table 35 (continued)

E (eV)	σ_E (eV)	$[\mu/\rho]$ (cm^2 g^{-1})	$\sigma_{[\mu/\rho]}$ (%)	$\sigma_{[\mu/\rho]_{\rm rel}}$ (%)	$[\mu/\rho]_{\rm pe}$ (cm^2 g^{-1})	$\sigma_{[\mu/\rho]_{\rm pe}}$ (%)	f'' (e atom^{-1})
9765.80	0.258	264.655	0.028	0.0107	262.933	0.031	3.990
9768.70	0.258	266.848	0.029	0.0107	265.126	0.031	4.024
9771.51	0.258	269.014	0.029	0.0107	267.293	0.031	4.058
9774.41	0.258	270.977	0.029	0.0106	269.257	0.031	4.089
9777.41	0.259	273.313	0.029	0.0106	271.593	0.031	4.126
9780.42	0.259	275.143	0.029	0.0105	273.424	0.031	4.155
9783.42	0.259	275.581	0.029	0.0106	273.862	0.031	4.163
9786.53	0.259	274.586	0.029	0.0104	272.867	0.031	4.149
9789.63	0.259	273.362	0.029	0.0104	271.644	0.031	4.132
9792.74	0.260	272.464	0.029	0.0102	270.746	0.031	4.119
9795.94	0.260	271.772	0.029	0.0102	270.056	0.031	4.110
9799.14	0.260	270.984	0.029	0.0100	269.268	0.031	4.100
9802.35	0.260	269.850	0.029	0.0100	268.134	0.031	4.084
9805.65	0.261	268.386	0.029	0.0099	266.671	0.031	4.063
9809.06	0.261	266.895	0.029	0.0101	265.180	0.031	4.041
9812.36	0.261	265.041	0.028	0.0101	263.327	0.031	4.015
9815.77	0.261	263.025	0.028	0.0102	261.311	0.031	3.985
9819.27	0.262	261.300	0.028	0.0102	259.587	0.031	3.960
9822.68	0.262	261.155	0.028	0.0102	259.443	0.031	3.959
9826.18	0.262	262.625	0.028	0.0102	260.913	0.031	3.983
9829.79	0.262	264.513	0.028	0.0103	262.802	0.031	4.014
9833.39	0.263	265.642	0.028	0.0102	263.932	0.031	4.032
9837.00	0.263	266.086	0.029	0.0103	264.377	0.031	4.041
9840.70	0.263	265.925	0.029	0.0103	264.216	0.031	4.040
9844.41	0.263	266.038	0.029	0.0103	264.330	0.031	4.043
9848.11	0.264	266.140	0.029	0.0102	264.432	0.031	4.046
9851.92	0.264	266.415	0.029	0.0103	264.708	0.031	4.052
9855.72	0.264	266.817	0.029	0.0101	265.111	0.031	4.060
9859.53	0.265	267.005	0.029	0.0101	265.299	0.031	4.064
9863.43	0.265	266.689	0.029	0.0099	264.985	0.031	4.061
9867.34	0.265	266.228	0.029	0.0099	264.524	0.031	4.055
9871.34	0.265	265.103	0.029	0.0098	263.399	0.031	4.040
9875.35	0.266	263.439	0.028	0.0099	261.736	0.031	4.016
...							
11570.56	0.390	163.799	0.024	0.0061	162.358	0.032	2.919
11582.58	0.391	163.366	0.024	0.0019	161.926	0.032	2.914
11594.60	0.392	162.914	0.024	0.0061	161.476	0.032	2.909

resolution after data-uncertainty determination and propagation, ready for fitting in k- or R-space). Separately, there are exciting developments for modalities such as RIXS or HERFD that are ongoing.

Acknowledgements

The author acknowledges all experimental and analytical coauthors and conceptual contributions to this work, and acknowledges the Australian National Beamline Facility, the Australian Synchrotron and the Advanced Photon Source in particular.

References

Abe, H., Aquilanti, G., Boada, R., Bunker, B., Glatzel, P., Nachtegaal, M. & Pascarelli, S. (2018). *J. Synchrotron Rad.* **25**, 972–980.

Aberdam, D. *et al.* (1980). Tech. Rep. European Synchrotron Research Facility. Grenoble, France.

Asakura, K., Abe, H. & Kimura, M. (2018). *J. Synchrotron Rad.* **25**, 967–971.

Baltazar-Rodrigues, J. & Cusatis, C. (2001). *Nucl. Instrum. Methods Phys. Res. B*, **179**, 325–333.

Bearden, J. A. (1967). *Rev. Mod. Phys.* **39**, 78–124.

Bearden, J. A. & Burr, F. A. (1967). *Rev. Mod. Phys.* **39**, 125–142.

Berger, M. J. & Hubbell, J. H. (1987). *XCOM: Photon Cross Sections on a Personal Computer*. Tech. Rep. NBSIR-87–3597. National Bureau of Standards, Washington, DC, USA.

Berger, M. J., Hubbell, J. H., Seltzer, S. M., Coursey, J. S. & Zucker, D. S. (1999). *XCOM: Photon Cross Section Database Version 1.2.* Tech. Rep. National Institute of Standards and Technology, Gaithersburg, USA. https://physics.nist.gov/xcom.

Best, S. P. & Chantler, C. T. (2024). *Int. Tables Crystallogr. I*, ch. 3.14, 375–394.

Bourke, J. D. & Chantler, C. T. (2010*a*). *Nucl. Instrum. Methods Phys. Res. A*, **619**, 33–36.

Bourke, J. D. & Chantler, C. T. (2010*b*). *Phys. Rev. Lett.* **104**, 206601.

Bourke, J. D. & Chantler, C. T. (2012). *J. Phys. Chem. A*, **116**, 3202–3205.

Bourke, J. D. & Chantler, C. T. (2014). *J. Electron Spectrosc. Relat. Phenom.* **196**, 142–145.

Bourke, J. D. & Chantler, C. T. (2015). *J. Phys. Chem. Lett.* **6**, 314–319.

Bourke, J. D., Chantler, C. T. & Joly, Y. (2016*a*). *J. Synchrotron Rad.* **23**, 551–559.

Bourke, J. D., Chantler, C. T. & Witte, C. (2007). *Phys. Lett. A*, **360**, 702–706.

Bourke, J. D., Islam, M. T., Best, S. P., Tran, C. Q., Wang, F. & Chantler, C. T. (2016*b*). *J. Phys. Chem. Lett.* **7**, 2792–2796.

Britton, D. & Pignolet, L. H. (1989). *Acta Cryst.* C**45**, 819–821.

Brock, C. P. & Fu, Y. (1997). *Acta Cryst.* B**53**, 928–938.

Bunker, G. (2010). *Introduction to XAFS: A Practical Guide to X-ray Absorption Fine Structure Spectroscopy.* Cambridge University Press.

Chantler, C. T. (1995). *J. Phys. Chem. Ref. Data*, **24**, 71–643.

Chantler, C. T. (2000). *J. Phys. Chem. Ref. Data*, **29**, 597–1056.

Chantler, C. T. (2024). *Int. Tables Crystallogr. I*, ch. 2.8, 88–99.

Chantler, C. T., Aquilanti, G., Diaz-Moreno, S. & Brois, V. (2019). *Mater. Struct. Chem. Biol. Phys. Technol.* **26**, 108–111.

Chantler, C. T., Barnea, Z., Tran, C. Q., Rae, N. A. & de Jonge, M. D. (2012*a*). *J. Synchrotron Rad.* **19**, 851–862.

Chantler, C. T. & Bourke, J. D. (2010). *J. Phys. Chem. Lett.* **1**, 2422–2427.

Chantler, C. T. & Bourke, J. D. (2014*a*). *J. Phys. Chem. A*, **118**, 909–914.

Chantler, C. T. & Bourke, J. D. (2014*b*). *J. Phys. Condens. Matter*, **26**, 145401.

Chantler, C. T. & Bourke, J. D. (2014*c*). *Phys. Rev. B*, **90**, 174306.

Chantler, C. T. & Bourke, J. D. (2019). *Ultramicroscopy*, **201**, 38–48.

Chantler, C. T., Bunker, B. A., Abe, H., Kimura, M., Newville, M. & Welter, E. (2018). *J. Synchrotron Rad.* **25**, 935–943.

Chantler, C. T., Islam, M. T., Best, S. P., Tantau, L. J., Tran, C. Q., Cheah, M. H. & Payne, A. T. (2015). *J. Synchrotron Rad.* **22**, 1008–1021.

Chantler, C. T., Olsen, K., Dragoset, R., Kishore, A., Kotochigova, S. & Zucker, D. (2000). *X-ray Form Factor, Attenuation and Scattering Tables*, Version 2.0. https://dx.doi.org/10.18434/T4HS32.

Chantler, C. T., Rae, N. A., Islam, M. T., Best, S. P., Yeo, J., Smale, L. F., Hester, J., Mohammadi, N. & Wang, F. (2012*b*). *J. Synchrotron Rad.* **19**, 145–158.

Chantler, C. T., Tran, C. Q. & Barnea, Z. (2010). *J. Appl. Cryst.* **43**, 64–69.

Chantler, C. T., Tran, C. Q., Barnea, Z., Paterson, D., Cookson, D. J. & Balaic, D. X. (2001*a*). *Phys. Rev. A*, **64**, 062506.

Chantler, C. T., Tran, C. Q., Paterson, D., Barnea, Z. & Cookson, D. J. (2001*b*). *Radiat. Phys. Chem.* **61**, 347–350.

Chantler, C. T., Tran, C. Q., Paterson, D., Cookson, D. & Barnea, Z. (2001*c*). *Phys. Lett. A*, **286**, 338–346.

Cosgriff, E., Chantler, C. T., Witte, C., Smale, L. F. & Tran, C. Q. (2005). *Phys. Lett. A*, **343**, 174–180.

Coster, D. & Veldkamp, J. (1931). *Z. Phys.* **70**, 306–316.

Creagh, D. C. (1999). In *International Tables for Crystallography*, Vol. C, edited by A. J. C. Wilson & E. Prince, Section 4.2.6, *X-ray dispersion corrections*, pp. 242–258. Dordrecht: Kluwer Academic Publishers.

Creagh, D. C. & Hubbell, J. H. (1987). *Acta Cryst.* A**43**, 102–112.

Creagh, D. C. & Hubbell, J. H. (1990). *Acta Cryst.* A**46**, 402–408.

Cullen, D. E., Hubbell, J. H. & Kissel, L. (1997). *Lawrence Livermore National Laboratory Report*, **6**, UCRL–50400 Rev 5. Lawrence Livermore National Laboratory, USA.

de Jonge, M. D., Barnea, Z., Tran, C. Q. & Chantler, C. T. (2004*a*). *Meas. Sci. Technol.* **15**, 1811–1822.

de Jonge, M. D., Barnea, Z., Tran, C. Q. & Chantler, C. T. (2004*b*). *Phys. Rev. A*, **69**, 022717.

de Jonge, M. D., Tran, C. Q., Chantler, C. T., Barnea, Z., Dhal, B. B., Cookson, D. J., Lee, W. & Mashayekhi, A. (2005). *Phys. Rev. A*, **71**, 032702.

de Jonge, M. D., Tran, C. Q., Chantler, C. T., Barnea, Z., Dhal, B. B., Paterson, D., Kanter, E. P., Southworth, S. H., Young, L., Beno, M. A., Linton, J. A. & Jennings, G. (2007). *Phys. Rev. A*, **75**, 032702.

Doniach, S., Hodgson, K., Lindau, I., Pianetta, P. & Winick, H. (1997). *J. Synchrotron Rad.* **4**, 380–395.

Dunitz, J. D., Orgel, L. E. & Rich, A. (1956). *Acta Cryst.* **9**, 373–375.

Ekanayake, R. S. K., Chantler, C. T., Sier, D., Schalken, M. J., Illig, A. J., de Jonge, M. D., Johannessen, B., Kappen, P. & Tran, C. Q. (2021*a*). *J. Synchrotron Rad.* **28**, 1476–1491.

Ekanayake, R. S. K., Chantler, C. T., Sier, D., Schalken, M. J., Illig, A. J., de Jonge, M. D., Johannessen, B., Kappen, P. & Tran, C. Q. (2021*b*). *J. Synchrotron Rad.* **28**, 1492–1503.

Fox, M. R., Orioli, P. L., Lingafelter, E. C. & Sacconi, L. (1964). *Acta Cryst.* **17**, 1159–1166.

Fricke, H. (1920). *Phys. Rev.* **16**, 202–215.

Gerward, L. (1981). *J. Phys. B At. Mol. Opt. Phys.* **14**, 3389–3395.

Gerward, L. (1989). *J. Phys. B At. Mol. Opt. Phys.* **22**, 1963–1969.

Gerward, L., Guilbert, N., Jensen, K. B. & Levring, H. (2004). *Radiat. Phys. Chem.* **71**, 653–654.

Glatzel, P. & Ghiringhelli, G. (2024). *Int. Tables Crystallogr. I*, ch. 3.49, 586–591.

Glover, J. L. & Chantler, C. T. (2007). *Meas. Sci. Technol.* **18**, 2916–2920.

Glover, J. L. & Chantler, C. T. (2009). *X-ray Spectrom.* **38**, 510–512.

Glover, J. L., Chantler, C. T., Barnea, Z., Rae, N. A. & Tran, C. Q. (2010). *J. Phys. B At. Mol. Opt. Phys.* **43**, 085001.

Glover, J. L., Chantler, C. T., Barnea, Z., Rae, N. A., Tran, C. Q., Creagh, D. C., Paterson, D. & Dhal, B. B. (2008). *Phys. Rev. A*, **78**, 052902.

Glover, J. L., Chantler, C. T. & de Jonge, M. D. (2009). *Phys. Lett. A*, **373**, 1177–1180.

Guda, A. A., Guda, S. A., Lomachenko, K. A., Soldatov, M. A., Pankin, I. A., Soldatov, A. V., Braglia, L., Bugaev, A. L., Martini, A., Signorile, M., Groppo, E., Piovano, A., Borfecchia, E. & Lamberti, C. (2019). *Catal. Today*, **336**, 3–21.

Guda, A. A., Guda, S. A., Martini, A., Bugaev, A. L., Soldatov, M. A., Soldatov, A. V. & Lamberti, C. (2020). *Radiat. Phys. Chem.* **175**, 108430–1.

Henke, B. L., Gullikson, E. M. & Davis, J. C. (1993). *At. Data Nucl. Data Tables*, **54**, 181–342.

Hester, J. R. (2016). *Data Sci. J.* **15**, 1–17.

Hubbell, J. H. (1994). NIST Internal Report 5437. National Institute of Standards and Technology, Gaithersburg, USA.

Hubbell, J. H. (1996). NIST Internal Report 5893. National Institute of Standards and Technology, Gaithersburg, USA.

Hubbell, J. H., Gimm, H. A. & Øverbø, I. (1980). *J. Phys. Chem. Ref. Data*, **9**, 1023–1148.

Hubbell, J. H. & Øverbø, I. (1979). *J. Phys. Chem. Ref. Data*, **8**, 69–106.

Hubbell, J. H., Veigele, W. J., Briggs, E. A., Brown, R. T., Cromer, D. T. & Howerton, R. J. (1975). *J. Phys. Chem. Ref. Data*, **4**, 471–538.

Islam, M. T., Best, S. P., Bourke, J. D., Tantau, L. J., Tran, C. Q., Wang, F. & Chantler, C. T. (2016). *J. Phys. Chem. C*, **120**, 9399–9418.

Islam, M. T., Chantler, C. T., Cheah, M. H., Tantau, L. J., Tran, C. Q. & Best, S. P. (2015). *J. Synchrotron Rad.* **22**, 1475–1491.

Islam, M. T., Rae, N. A., Glover, J. L., Barnea, Z. & Chantler, C. T. (2010*a*). *Nucl. Instrum. Methods Phys. Res. A*, **619**, 44–46.

Islam, M. T., Rae, N. A., Glover, J. L., Barnea, Z., de Jonge, M. D., Tran, C. Q., Wang, J. & Chantler, C. T. (2010*b*). *Phys. Rev. A*, **81**, 022903.

Islam, M. T., Tantau, L. J., Rae, N. A., Barnea, Z., Tran, C. Q. & Chantler, C. T. (2014). *J. Synchrotron Rad.* **21**, 413–423.

Joly, Y. (2001). *Phys. Rev. B*, **63**, 125120–125130.

Joly, Y., Cabaret, D., Renevier, H. & Natoli, C. R. (1999). *Phys. Rev. Lett.* **82**, 2398–2401.

Kas, J. J., Rehr, J. J., Glover, J. L. & Chantler, C. T. (2010). *Nucl. Instrum. Methods Phys. Res. A*, **619**, 28–32.

Kievit, B. & Lindsay, G. A. (1930). *Phys. Rev.* **36**, 648–664.

Kodre, A., Padežnik Gomilšek, J., Mihelič, A. & Arčon, I. (2006). *Radiat. Phys. Chem.* **75**, 188–194.

Kraft, S., Stümpel, J., Becker, P. & Kuetgens, U. (1996). *Rev. Sci. Instrum.* **67**, 681–687.

Lapeyre, C., Petiau, J., Calas, G., Gauthier, F. & Gombert, J. (1983). *Bull. Minéral.* **106**, 77–85.

Lindsay, G. A. (1931). *Z. Phys.* **71**, 735–738.

Lynch, D. W. (1997). *J. Synchrotron Rad.* **4**, 334–343.

Lytle, F. (1965). *Physics of Non-Crystalline Solids*, edited by J. Prins, pp. 12–30. Amsterdam: North Holland.

Lytle, F. (1966). *Advances in X-Ray Analysis*, Vol. 9, *Proceedings of the Fourteenth Annual Conference on Applications of X-Ray Analysis*, edited by G. R. Mallett, M. J. Fay & W. M. Mueller, pp. 398–409. New York: Springer.

Lytle, F., Sayers, D. & Stern, E. (1975). *Phys. Rev. B*, **11**, 4825–4835.

Martini, A., Guda, S. A., Guda, A. A., Smolentsev, G. A. A., Algasov, A., Usoltsev, O., Soldatov, M. A., Bugaev, A., Rusalev, Y., Lamberti, C. & Soldatov, A. V. (2020). *Comput. Phys. Commun.* **250**, 107064–1.

Mathew, K., Zheng, C., Winston, D., Chen, C., Dozier, A., Rehr, J. J., Ong, S. P. & Persson, K. A. (2018). *Sci. Data*, **5**, 180151.

Mika, J. F., Martin, L. J. & Barnea, Z. (1985). *J. Phys. C*, **18**, 5215–5223.

Newville, M. (2001). *J. Synchrotron Rad.* **8**, 96–100.

Newville, M. (2004). *Fundamentals of XAFS.* Consortium for Advanced Radiation Sources, University of Chicago, USA.

Nordfors, B. (1960). *Arkiv Fysik*, pp. 1–2.

Perkins, S. T., Cullen, D. E., Chen, M. H., Hubbell, J. H., Rathkopf, J. & Scofield, J. H. (1991). Lawrence Livermore Laboratory Report UCRL-50400. Lawrence Livermore Laboratory, USA.

Rae, N. A., Chantler, C. T., Barnea, Z., de Jonge, M. D., Tran, C. Q. & Hester, J. R. (2010*a*). *Phys. Rev. A*, **81**, 022904.

Rae, N. A., Glover, J. L. & Chantler, C. T. (2010*b*). *Nucl. Instrum. Methods Phys. Res. A*, **619**, 47–50.

Rae, N. A., Islam, M. T., Chantler, C. T. & de Jonge, M. D. (2010*c*). *Nucl. Instrum. Methods Phys. Res. A*, **619**, 147–149.

Ravel, B., Hester, J. R., Solé, V. A. & Newville, M. (2012). *J. Synchrotron Rad.* **19**, 869–874.

Ravel, B. & Newville, M. (2005). *J. Synchrotron Rad.* **12**, 537–541.

Sandiago, T. K. U., Umesh, T. K. & Gowda, R. (1997). *Pramana – J. Phys.* **48**, 1077–1090.

Sarangi, R. (2018). *J. Synchrotron Rad.* **25**, 944–952.

Schalken, M. J. & Chantler, C. T. (2018). *J. Synchrotron Rad.* **25**, 920–934.

Schaupp, D., Schumacher, M., Smend, F., Rullhusen, P. & Hubbell, J. H. (1983). *J. Phys. Chem. Ref. Data*, **12**, 467–512.

Scofield, J. H. (1973). Lawrence Livermore Laboratory Report UCRL-51326. Lawrence Livermore Laboratory, USA.

Seiler, P. & Dunitz, J. D. (1982). *Acta Cryst.* B**38**, 1741–1745.

Sier, D., Cousland, G. P., Trevorah, R. M., Ekanayake, R. S. K., Tran, C. Q., Hester, J. R. & Chantler, C. T. (2020). *J. Synchrotron Rad.* **27**, 1262–1277.

Sier, D., Ekanayake, R. S. K. & Chantler, C. T. (2022). *X-ray Spectrom.* **51**, 91–100.

Smale, L. F., Chantler, C. T., de Jonge, M. D., Barnea, Z. & Tran, C. Q. (2006). *Radiat. Phys. Chem.* **75**, 1559–1563.

Stanglmeier, F., Lengeler, B., Weber, W., Göbel, H. & Schuster, M. (1992). *Acta Cryst.* A**48**, 626–639.

Strange, R. W. & Feiters, M. C. (2008). *Curr. Opin. Struct. Biol.* **18**, 609–616.

Streltsov, V. A., Ekanayake, R. S., Drew, S. C., Chantler, C. T. & Best, S. P. (2018). *Inorg. Chem.* **57**, 11422–11435.

Tajuddin, A., Chong, C., Shukri, A., Bandyopadhyay, T. & Bradley, D. (1995). *Appl. Radiat. Isot.* **46**, 113–115.

Tantau, L. J., Chantler, C. T., Bourke, J. D., Islam, M. T., Payne, A. T., Rae, N. A. & Tran, C. Q. (2015). *J. Phys. Condens. Matter*, **27**, 266301.

Tantau, L. J., Islam, M. T., Payne, A. T., Tran, C. Q., Cheah, M. H., Best, S. P. & Chantler, C. T. (2014). *Radiat. Phys. Chem.* **95**, 73–77.

Timoshenko, J., Anspoks, A., Cintins, A., Kuzmin, A., Purans, J. & Frenkel, A. I. (2018). *Phys. Rev. Lett.* **120**, 225502–1.

Timoshenko, J., Lu, D., Lin, Y. & Frenkel, A. I. (2017). *J. Phys. Chem. Lett.* **8**, 5091–5098.

Tran, C. Q., Barnea, Z., de Jonge, M. D., Dhal, B. B., Paterson, D., Cookson, D. J. & Chantler, C. T. (2003*a*). *X-ray Spectrom.* **32**, 69–74.

Tran, C. Q., Chantler, C. T. & Barnea, Z. (2003*b*). *Phys. Rev. Lett.* **90**, 257401.

Tran, C. Q., Chantler, C. T., Barnea, Z. & de Jonge, M. D. (2004*a*). *Rev. Sci. Instrum.* **75**, 2943–2949.

Tran, C. Q., Chantler, C. T., Barnea, Z., de Jonge, M. D., Dhal, B. B., Chung, C. T. Y., Paterson, D. & Wang, J. (2005). *J. Phys. B At. Mol. Opt. Phys.* **38**, 89–107.

Tran, C. Q., Chantler, C. T., Barnea, Z., Paterson, D. & Cookson, D. J. (2003*c*). *Phys. Rev. A*, **67**, 042716.

Tran, C. Q., Jonge, M. D., Barnea, Z. & Chantler, C. T. (2004*b*). *J. Phys. B At. Mol. Opt. Phys.* **37**, 3163–3176.

Trevorah, R. M., Chantler, C. T. & Schalken, M. J. (2019). *IUCrJ*, **6**, 586–602.

Trevorah, R. M., Chantler, C. T. & Schalken, M. J. (2020). *J. Phys. Chem. A*, **124**, 1634–1647.

Wang, D., Ding, X., Wang, X., Yang, H., Zhou, H., Shen, X. & Zhu, G. (1992). *Nucl. Instrum. Methods Phys. Res. B*, **71**, 241–248.

Witte, C., Chantler, C. T., Cosgriff, E. C. & Tran, C. Q. (2006). *Radiat. Phys. Chem.* **75**, 1582–1585.

Wong, J. (1999). *Reference X-ray Spectra of Metal Foils*. EXAFS Materials, Inc., 871 El Cerro Blvd, Danville, CA, USA.

Zheng, C., Mathew, K., Chen, C., Chen, Y. M., Tang, H. M., Dozier, A., Kas, J. J., Vila, F. D., Rehr, J. J., Piper, L. F. J., Persson, K. A. & Ong, S. P. (2018). *npj Comput. Mater.* **4**, 12.